UNIVERSITY OF
THESSALY

DESIGN & DEVELOPEMENT OF AN AERODYNAMIC PACKAGE FOR A FSAE RACE CAR

Diploma Thesis
by

Ioannis Oxyzoglou

Supervisor: *Nikolaos Pelekasis*

Laboratory of Fluid Mechanics & Turbomachinery

Volos, Greece - May 2017

Approved by the tree-Member Committee of Inquiry:

1ˢᵗ Examiner: *Dr. Pelekasis Nikolaos*

Professor,
Computational Fluid Dynamics

pel@uth.gr

2ⁿᵈ Examiner: *Dr. Stamatelos Anastasios*

Professor,
Internal Combustion Engines

stam@uth.gr

3ʳᵈ Examiner: *Dr. Charalampous Georgios*

Assistant Professor,
Thermofluid Processes with Energy Applications
georgios.charalampous@uth.gr

ABSTRACT

This Thesis describes the process of designing and developing the aerodynamic package of the 2016 Formula Student race car (*Thireus 277*) of Centaurus Racing Team with the use of CAD Tools and Computational Fluid Dynamics (CFD). It further investigates the effects of aerodynamics on the vehicle's behavior and performance with regard to the Formula Student competition regulations. The methods used during the development are evaluated and put into context by investigating the correlation between the CFD results of the car model and the lap-time simulated counterpart. The aerodynamic package consists of a nosecone, two sidepods, an undertray, a front and a rear wing. The Thesis details all the stages involved in designing and optimizing these components to achieve the desired results and maximize the amount of performance enhancing aerodynamic downforce generated by the aerodynamic package, while maintaining drag force at low levels.

CONTENTS

1. INTRODUCTION

Aerodynamics is the science of how air flows around and inside objects. More generally, it can be labeled "*Fluid Dynamics*" because air is really just a very thin type of fluid. Above slow speeds, the air flow around and through a vehicle begins to have a more pronounced effect on the acceleration, top speed, fuel efficiency and handling. Therefore, to build the most efficient possible race car it is needed to understand and optimize how the air flows around and through the body, its openings and its aerodynamic devices. It is now established that aerodynamics has a key role in the performance and the efficiency of an open wheel racing car, even when it is moving at low speeds on the track like a FSAE car does. A well aerodynamically designed car is able to utilize the airflow around it in order to produce as much vertical to the ground force as possible while maintaining the air resistance force at low levels. The vertical force is known in Motorsport as *Downforce* and the resistance force is called *Drag*. In this way, the grip and thus the performance of the tires increases and the car is able to achieve higher cornering speeds while at the same time there is better fuel consumption due to the reduced air resistance.

Figure 1: *Mark's Webber accident at the Circuit de la Sarthes due to the car suffering of aerodynamic instabilities along the circuit's long high-speed straight sections, Le Mans 1999*

In order to keep the speed of the vehicles at low levels for safety reasons, most tracks at several FSAE Competitions consist primarily of repeated sharp turns and less of long straights. This fact led the majority of the FSAE teams to realize that the race can be won mainly by increasing the cornering performance of their cars. This makes the necessity of an efficient aerodynamic design even greater due to the significant difference that is made in the cornering speed, which can considerable reduce the lap-time of a FSAE car which uses aerodynamic devices. Moving at the same direction of thinking Centaurus Racing Team proceed for the first time since its foundation in the design and development of an efficient aerodynamic package for its 3rd race car *Thireus 277* for the season of *2015 - 2016*.

2. AERODYNAMICS OF A FSAE RACE CAR

2.1. Introduction to Race Car Aerodynamics

Each year FSAE cars become even more faster, which means that their power keeps increasing to. However, exactly such as there is a loss of energy from the engine being transferred to the transmission and wheels, thus there is also a limit to the amount of power that you can put from the tires on the ground. To increase this undesired limit, an extra force must be applied on the wheels, directing to ground. Increasing weight can do this, but weight makes the handling of the car worse while requires even more power and since FSAE cars become constantly lighter this downward force becomes even more important. By reducing the resistance (*Drag*) of the car through the air, it can achieve higher top speeds and go faster on straights while with the right design of its body shape a great amount of downward pressure (*Downforce*) can be transferred onto the tires and so the car will go even faster around the corners. Research into aerodynamics has allowed cornering speeds in "*high speed*" corners to be much higher than that which is possible without the use of aerodynamic aids, although it has reduced ultimate top speeds which is not that important for an FSAE competition.

2.1.1. Downforce

Every object travelling through air creates either a lifting or a downforce situation. A wing can make a plane to take off, but if we put it upside down, it can make a high-speed race car stay to the ground. The same principle that allows an airplane to rise off the ground by creating lift from its wings is used in reverse to apply force that presses the race car against the surface of the track. Typically, the term "lift" is used when talking about any kind of aerodynamically induced force acting on a surface. This is then given an indicator, either "*positive lift*" (*up*) or "*negative lift*" (*down*) as to its direction, since most aerodynamic devices were invented for aircraft and were designed to lift them into the air.

Figure 2: *Race cars use inverted airplane wings to produce downforce instead of lift*

In race car aerodynamics, the vertical downward force provided by aerodynamic devices mounted on a race car, pushes the tires onto the track surface to provide more grip, which in turn enables higher cornering speeds and faster braking. The grip between tires and track pavement provided entirely by aerodynamical forces is called "*aerodynamical grip*" and is distinguished from "*mechanical grip*" which is a function of the car mass repartition, tires and suspension. The creation of downforce by passive devices such as wings, bodywork, diffusers etc. almost always can only be achieved at the cost of increased aerodynamic drag (*or friction*), and the optimum setup is almost always a compromise between the two. Because it is a function of the flow of air over and under

the car, and because aerodynamic forces increase with the square of velocity, downforce increases with the square of the car's speed and requires a certain minimum speed in order to produce a significant effect.

2.1.2. Drag Force

When the fluid flows over a surface, the surface will resist its motion. In aerodynamics, drag is the fluid drag force that acts on any moving solid body in the direction of the fluid freestream flow. Aerodynamic drag on a race car is the sum of friction, form and pressure drag. Friction drag occurs as air particles pass over a car's surfaces and the layers of particles closest to the surface adhere. Skin friction drag is caused by the actual contact of the air particles against the surface of the moving object. The layer above these attached particles slides over them, but is consequently slowed down by the non-moving particles on the surface. The layers above this slowed layer move faster. As the layers get further away from the surface, they slow less and less until they flow at the free-stream speed. The area of slow speed, called the boundary layer, appears on every surface, and causes one of the three types of drag.

The force required to shift the molecules of air out of the way creates a second type of drag, form Drag. Due to this phenomenon, the smaller the frontal area of a vehicle, the smaller the area of molecules that must be shifted, and thus the less energy required to push through the air. With less engine effort being taken up in the moving air, more will go into moving the car along the track, and for a given engine power, the car will travel faster. Form drag and pressure drag are virtually the same type of drag. The separation of air creates turbulence and results in pockets of low and high pressure that leave a wake behind the car. This opposes forward motion and is a component of the total drag. Streamlining the moving object will reduce form drag, and parts of a race car(*mostly suspension parts*) that do not lend themselves to streamlining are enclosed in covers called fairings. So, drag in race car aerodynamics, is comprised primarily of three forces:

- *Frontal pressure*, or the effect created by a vehicle body pushing air out of the way.
- *Rear vacuum*, or the effect created by air not being able to fill the hole left by the vehicle body.
- Boundary *layer*, or the effect of friction created by slow moving air at the surface of the vehicle body.

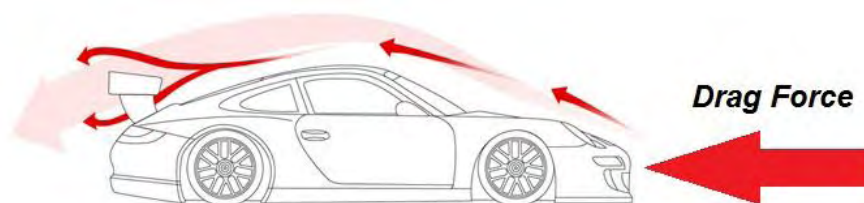**Figure 3:** *Drag force acting on a moving race car*

Flow detachment applies only to the "*rear vacuum*" portion of the drag forces and has a greater and greater negative effect as vehicle speed increases. In fact, the drag increase with the square of the vehicle speed, so more and more horsepower is needed to push a vehicle through the air as its speed rises. Therefore, when a vehicle reaches high

speeds it becomes important to design the car to limit areas of flow detachment. Understanding the relationship between speed and drag is important in calculating maximum endurance and the range of the race car. When drag is at a minimum, power required to overcome drag is also at a minimum.

2.1.3. C_L, C_D Coefficients

Lift coefficient (C_L, C_N *or* C_Z) is a dimensionless coefficient that relates the lift generated by a lifting body to the fluid density around the body, the fluid velocity and an associated reference area. The lift coefficient is a simple way that aerodynamicists use to represent a very complex idea and model all of the complex dependencies of shape, inclination, and some flow conditions on lift. This coefficient expresses the ratio of the lift force to the force produced by the dynamic pressure times the area. Lift coefficient is often found using computer generated models(*CFD*) or with wind tunnel testing. In certain ranges of operating conditions and when there is no stall, the lift coefficient has a constant value and the lift or downforce produced is then proportional to the square of airspeed and can be determined using the following equation:

$$L = \frac{1}{2} C_L \, \rho \, u^2 A \qquad \textbf{(2.1)}$$

where L is the lift force, A is the relevant plan area, ρ is the fluid density and u is the flow speed.

Drag coefficient (C_D *or* C_X) is a common measure in automotive design as it pertains to aerodynamics. The drag coefficient of an automobile impacts the way the automobile passes through the surrounding air. Aerodynamic drag increases with the square of speed therefore, it becomes critically important at higher speeds. Reducing the drag coefficient of a car improves the performance of the vehicle as it pertains to speed and fuel efficiency. C_D changes as a function of the shape of the body. Drag force changes as a function of C_D and flow direction, air density and viscosity, object size, speed and is proportional to the density of the air and to the square of the relative speed between the air and the object. One way to express this is by means of the drag equation:

$$F_D = \frac{1}{2} C_D \, \rho \, u^2 A \qquad \textbf{(2.2)}$$

where also **L** is the lift force, **A** is the relevant plan area, **ρ** is the fluid density and **u** is the flow speed. The reference area **A** depends on what type of drag coefficient is being measured. For automobiles and many other objects, the reference area is the projected frontal area of the vehicle. This may not necessarily be the cross-sectional area of the vehicle, depending on where the cross section is taken. For airfoils, the reference area is the nominal wing area. Since this tends to be large compared to the frontal area, the resulting drag coefficients tend to be low, much lower than for a car with the same drag, frontal area, and speed.

The drag coefficient of a vehicle is affected by the shape of body of the vehicle. In order to achieve a low drag coefficient, the boundary layer around the body must remain attached to the surface of the body for as long as possible, causing the wake to be narrow. A high *form drag* results in a broad wake. The boundary layer will transition from laminar

to turbulent if Reynolds number of the flow around the body is sufficiently great. Larger velocities, larger objects, and lower viscosities contribute to larger Reynolds numbers. Various other characteristics affect the coefficient of drag as well, some race cars may actually have higher drag coefficient, but this is to compensate for the amount of lift the vehicle generates, while others use aerodynamics to their advantage to gain speed and have much lower coefficients of drag. Other high performance race cars have a surprisingly high C_D, due to wider tires, extra wings and larger cooling systems as the usual cars have half size radiators with the remaining area blanked off to reduce cooling and engine bay drag.

Configuration	Description	C_D	C_L	C_D/C_L
	No aerodynamic devices	0.63	0.29	0.46
	Underbody channels (diffusers)	0.65	-0.79	-1.21
	Underbody channels, wings	0.66	-1.28	-1.94
	Underbody channels, wings with side fins	0.68	-1.56	-2.29
	Underbody channels, wings with side fins and flaps	0.90	-2.34	-2.60
	Underbody channels, multi-element wings	0.98	-2.58	-2.63
	Resized underbody, revised multi-element wings	1.30	-3.70	-2.85

Figure 4: *Drag and Lift coefficients of a FSAE car with different aerodynamic packages*

2.1.4. Wings Theory

Every wing in planar view has the shape of an airfoil. Low speed aerodynamics airfoils have a characteristic shape with a rounded leading edge, followed by a sharp trailing edge, often with a symmetric curvature of upper and lower surfaces. The geometry of the airfoil is described by three terms. The *leading edge* which is the point at the front of the airfoil that has maximum curvature and minimum radius, the *trailing edge* which is the point of minimum curvature at the rear of the airfoil, the *chord line* which is the straight line connecting leading and trailing edges. The chord length, is the length of the chord line and it is the reference dimension of the airfoil section. The shape of the airfoil is defined using the following two geometrical parameters. The mean *camber line* which is the locus of points midway between the upper and lower surfaces and the thickness distribution which

varies along the chord. Finally, two important concepts used to describe the airfoil's behavior when moving through a fluid, the *aerodynamic center* which is the chord-wise length about which the pitching moment is independent of the lift coefficient and angle of attack while the second one is the *center of pressure*, which is the chord-wise location about which the pitching moment is zero.
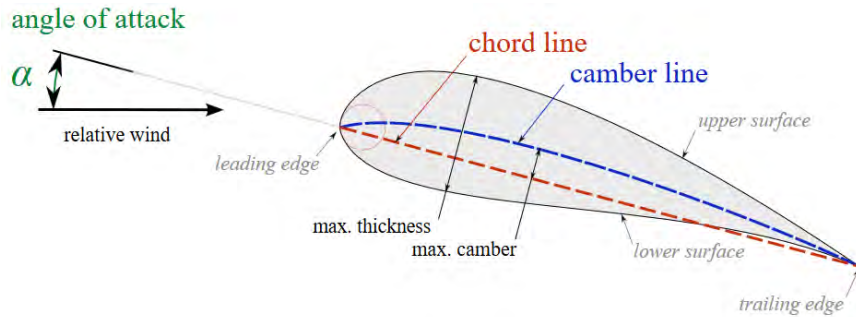

Figure 5: *Basic Airfoil characteristics*

Thanks to Newton's third law, we know that if the airfoil exerts a downward force on the air, the air will in turn exert an upward force on the wing. The lift on an airfoil is primarily the result of its angle of attack and shape. Wings are shaped so that that air flows faster over the top of the wing and slower underneath. Based to Bernoulli's principal, fast moving air equals low air pressure while slow moving air equals high air pressure. The high air pressure underneath the wings will therefore push the aircraft up through the lower air pressure. In aerodynamics, angle of attack specifies the angle between the chord line of the wing and the relative air flow. Since a wing can have twist, a chord line of the whole wing may not be definable, so an alternate reference line is simply defined. Often, the chord line of the root of the wing is chosen as the reference line. When oriented at a suitable angle, the airfoil deflects the oncoming air resulting in a force on the airfoil in the direction opposite to the deflection. This force is known as aerodynamic force and can be resolved into two components: lift and drag. Most airfoil shapes require a positive angle of attack to generate lift, but cambered airfoils can generate lift at zero angle of attack. This "*turning*" of the air in the vicinity of the airfoil creates curved streamlines, resulting in lower pressure on one side and higher pressure on the other. This pressure difference results to a flow field around the airfoil which has a higher average velocity on the upper surface than on the lower surface.
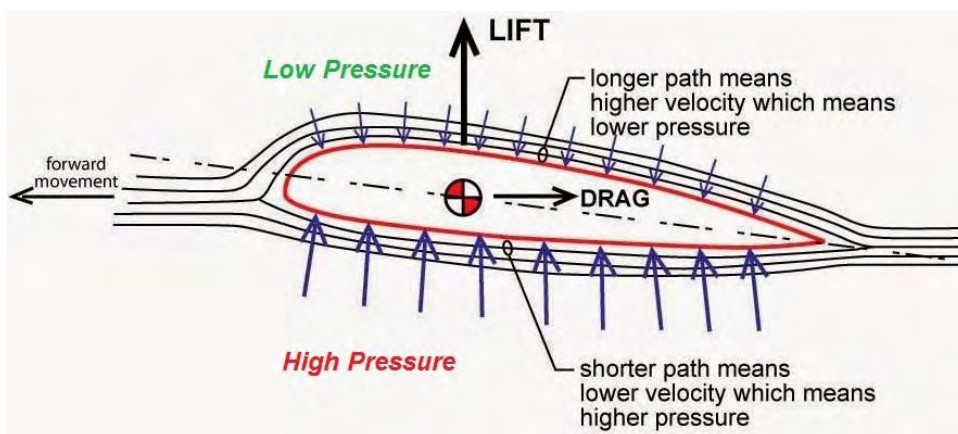

Figure 6: *How a moving airfoil works*

A symmetrical wing has zero lift at 0° degrees angle of attack. Increasing the angle of attack is associated with increasing the lift the airfoil creates and the lift coefficient up to the maximum limit. As the angle of attack keeps increasing, separation of the airflow from the upper surface of the wing becomes more pronounced and the separation point of the flow moves from the trailing edge towards the leading edge leading to a reduction in the rate of increase of the lift coefficient. The lowest pressure over the foil is found at a point on the hump near to the leading edge. In front of this low pressure point also known as the transition point, there exists laminar flow and behind it begins the turbulent flow. With the transition point being the lowest pressure area of the airfoil, there exists an adverse pressure gradient while the pressure of air there is lower than at trailing edge. The adverse pressure gradient therefore, acts against the regular flow of air over the airfoil. The normal skin friction drag acting on the airfoil, reduces the flow kinetic energy. So, there is no energy to act against the adverse. The lower levels of the boundary layer thus stop moving, while the upper layers overrun them. This causes the flow separation.

The critical angle of attack is the angle of attack which produces maximum lift coefficient. This is also called the "*stall angle of attack*". Below this critical angle of attack and as the angle of attack increases, the coefficient of lift C_L increases. Conversely, above the critical angle of attack the air begins to flow less smoothly over the upper surface of the airfoil and begins to separate. At the critical angle of attack, upper surface flow is more separated and the airfoil or wing is producing its maximum coefficient of lift. As angle of attack increases further, the upper surface flow becomes more and more fully separated with the wing producing even less lift, the C_L decreasing and coefficient of drag C_D rapidly increasing. The critical or stalling angle of attack is typically around 12° - 20° for many airfoils.
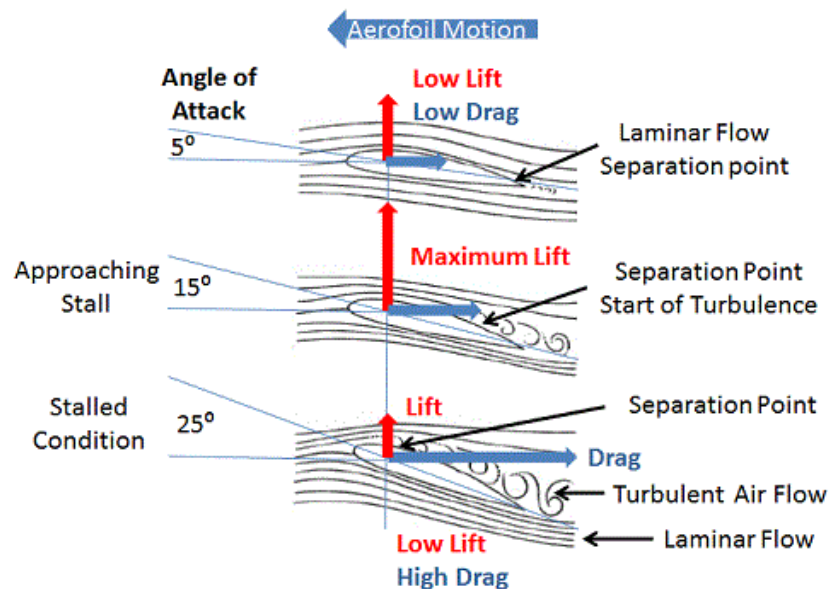
Figure 7: *Behavour of the airflow around an airfoil in differenet angles of attack*

Despite profile drag being large in the post stall regimes, a soft stall can extend the range of available performance at C_{Lmax}. So, one of the requirements is that a high downforce wing should possess a soft stall and sustain C_{Lmax} or perform close to it for a large angle of attack range to provide flexibility during car set up. Due to the very low

aspect ratios of race car wings, the primary source of drag comes from the induced component of overall drag. Therefore, the chief concern in motorsports airfoil design is not one of profile drag reduction. Instead it is a maximization of downforce and the ability of the designed airfoil to sustain the highest possible levels of downforce across a wide range of physical and aerodynamic adversities.

2.1.5. Venturi & Ground Effects

The Venturi effect is the phenomenon that occurs when a fluid that is flowing through a pipe is forced through a narrow section, resulting in a pressure decrease and a velocity increase. The effect is mathematically described through the Bernoulli equation and can be observed in both nature and industry. The Venturi effect is similar to the feeling one gets when the thumb is placed at the end of a garden hose with the water turned on. The water's velocity increases when the thumb is placed over the water. The pressure increases over the smaller surface area, however, the narrow flow then creates a vacuum in the water. In fluid dynamics, a fluid's velocity must increase as it passes through a constriction in accord with the principle of mass continuity, while its static pressure must decrease in accord with the principle of conservation of mechanical energy. Thus, any gain in kinetic energy a fluid may accrue due to its increased velocity through a constriction is balanced by a drop-in pressure. Referring to the adjacent diagram, using Bernoulli's equation in the special case of steady, incompressible, inviscid flows along a streamline, the theoretical pressure drop at the constriction is given by:

$$P_1 - P_2 = \frac{\rho}{2}(u_2^2 - u_1^2) \qquad \textbf{(2.3)}$$

where is ρ the density of the fluid, u_1 is the slower fluid velocity where the pipe is wider, u_2 is the faster fluid velocity where the pipe is narrower.
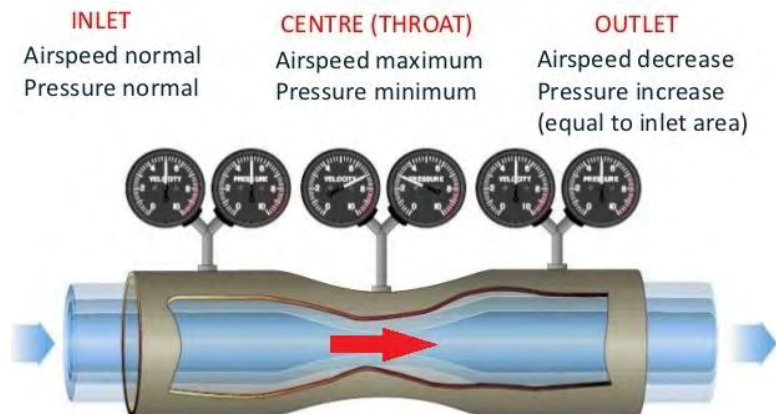
Figure 8: *Venturi effet Inside a Venturi tube*

A curved aerodynamic surface influences the airflow even a long way from that surface, bending the airflow in such a way that flow adjacent to the surface follows that surface almost perfectly. The further away from the surface you go, the straighter the flow becomes. When an aerodynamic surface is placed close to the ground, the presence of the ground determines where the flow becomes straight. This has the effect of speeding up the airflow between the surface and the ground, increasing the aerodynamic effect of the surface. It was discovered that large amounts of downforce could be generated from the

airflow between the underbody of the car and the ground plane. In particular, low pressure could be created underneath the car by using the ground plane almost like the floor of a Venturi duct. The ceiling of these Venturi ducts took the form of inverted wing profiles mounted in sidepods between the wheels of the car. The decreasing cross-sectional area in the throat of these ducts, and the inverted wing profile accelerated the airflow and created low pressure in accordance with the Bernoulli principle. Putting it simply as possible, Ground Effect is the art of creating a low pressure area underneath the car so that the atmospheric pressure pushes the car to the ground, which is the reverse of what happens with an aircraft wing. The way this can be achieved is by utilizing the Venturi Effect.
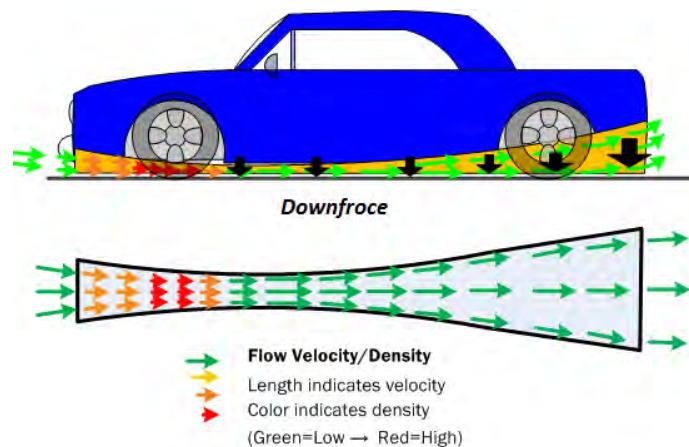

Figure 9: *Ground effect on a moving car*

The flow volume between the vehicle and the ground is strongly dependent on the car's attitude relative to the ground. Very small ground clearance results in positive lift, since there is almost no airflow between the underbody and the ground. With increasing ground clearance the airflow produces low pressures causing overall lift to be lowered to negative values and then to rise again as ground clearance continues to increase. This is due to the fact that the flow velocity under the car decreases as ground clearance increases. In this case, more downforce can be generated using a diffuser between the rear wheels.

The Ground effect works exactly the same for any type of wing. At a large height in ground effect, the flow is accelerated over the suction surface greater level than in a freestream, resulting in greater suctions on the suction surface. As the wing is brought closer to the ground, flow is accelerated to a higher degree, causing an increased peak suction and associated pressure recovery. At a height where the pressure recovery is sufficiently steep, boundary-layer separation was observed at the trailing edge of the suction surface. As the height is reduced beyond this, the wing still generates more downforce, but the rate of increase slows, and the downforce reaches a maximum, the downforce reduction phenomenon. Below this height, the down-force reduces sharply. As the height is reduced from the first height where flow separation was observed, the separation point moves forward steadily. At the maximum downforce, the boundary layer separates at approximately 80%c. Heights greater than the maximum downforce are known as the force enhancement region. Below the maximum downforce is known as the force reduction region.

2.2. FSAE Aerodynamic Devices

Aerodynamic upgrades are one of the key areas in a FSAE car development which can easily make the difference in the competition events, with direct effect on the top and cornering speed. Depending on the required goals of every team in question, they can either choose to reduce drag and increase top speed, increase down force and drag levels for cornering speeds, or aim for a balance between the two. Aerodynamic upgrades come in many different forms and have evolved mostly from the early days of FSAE competitions with a streamline design in the very beginning. This was in an attempt to increase overall top speeds and played a big impact on design directions. Most common devices and many others are used to make FSAE cars increase their aerodynamic efficiency, this in turn helps to keep the tires planted on the ground and maximize grip. There are many differences between "*open wheel*" and "*closed wheel*" aerodynamic designs and some components are not applicable in both specifications but they share the common goal to increase downforce levels with the minimal amount of drag. Producing downforce without creation of drag is impossible and it is always a balancing act to reach the best trade off and maximize aerodynamic efficiency.
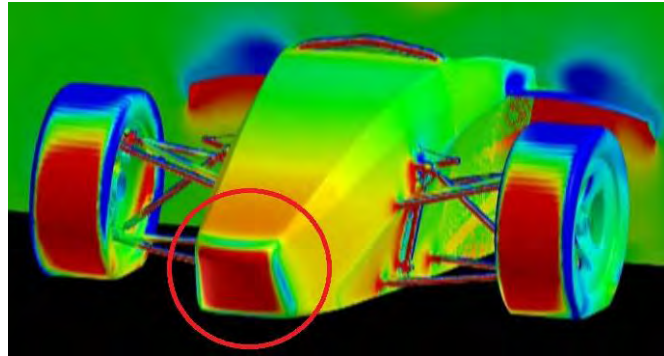
2.2.1. Nosecone

The nosecone is the aerodynamic bulkhead area in the front of the driver's feet. As seen on open wheel race cars, is an effective way to mount the front wing and minimize frontal area. Its design promotes undertray and diffuser's airflow optimization, promoting reduced drag and increasing downforce potential. Height and cross section in this area is critical as a minimal cross section is needed between the front wheels and as much space as possible underneath to fit bodywork to direct airflow around and

Figure 10: *Nosecone of a FSAE car, Tankia 2013 - TU Graz*

under the sidepods. So, most teams tend to raise nosecones as high as they can go. New nosecone designs tend to have an angled upper surface and a "*V*" cross section to the front bulkhead, to make the surfaces more aerodynamically efficient.

The front body work of the FSAE car usually experiences the highest pressure on the entire vehicle. This is because the fast-moving air stagnates (*slows*) when it hits the nosecone, causing a pressure rise. This stagnation pressure can be useful if the goal of the nose cone is downforce or undesirable if the goal is minimizing drag. For a downforce nose, the upper surface will show a low amount of curvature to maximize stagnation pressure. The angle between the upper surface of the nose and ground determines how much downforce and drag will be produced. A low drag nosecone will have convex curvature which lowers the drag, but also creates some lift. Low drag nosecones are probably the better option since a downforce nose will create both downforce and drag. The lift created by a low drag nosecone can be counteracted by the use of a front wing which can also provide downforce on the nose. Besides just adding additional downforce, front aerodynamic devices help to balance the car aerodynamically by providing a moving of the

center of pressure. A forward center of pressure creates oversteer and a rearward center of pressure creates understeer while it also moves rearward with increasing velocity.

Figure 11: *Stagnation point on the nosecone of a FSAE car, this type of nosecones produce great amounts of Drag*

The efficiency of a low-pressure area underneath the car is being seriously compromised by the low nose position at the front end of the car. Low nosecones effectively divert air sideways and upwards around the car's upper bodywork, and reduce dramatically the volume of air passing underneath the car. However, the generation of low pressures relies on increasing the speed of the air passing underneath the car, in relation to air passing over and around it. Having high nose allows air to go straight through under the nose instead of having to go around it. At first sight the higher nose is equal to less downforce as by itself it pushes less air up over the nose. However not only it can reduce drag but also all the air that passed under the nose is guided under the car or split to either side of the car by the splitters located in front of the sidepods. In simple terms, the more air that can be drawn underneath a car, the faster that air will have to be moving, and the faster the air is moving, the lower the pressure. Although rising the nosecone of the car increases the volume of air that passes underneath the car, the efficiency of the front wing decreases as far as it gets from the ground due to the ground effect. That means that during the design a compromise must be between the distance of the nosecone from the ground and the ride height of the front wing, so that the functionality of the first will not affect the aerodynamic efficiency of the other.

Figure 12: *One of the best aerodynamically designed bodywork and nosecone, Tankia 2010 - TU Graz*

2.2.2. Front wing

The first part of a FSAE car that comes in contact with the air is definitely the front wing. This means that it's the first part of the car that interacts with the air, therefore it has the important role to determine the under-stream flow through the rest of car. Front wings are normally mounted close to the suspension, or even on the mounts in order to transmit


Figure 13: *FSAE front wing, RP16c - Dynamics e.V.*

downward loads of force as effectively as possible and create downforce in order to press the tires of the front wheels into the ground and generate higher grip levels. The front wing generates up *20% - 30%* of the total downforce on the car. The basic design of a FSAE front wing is generally a multi-element airfoil which is typically closely coupled airfoils consisting of two or even four elements extended from both sides of the nosecone, with movable flaps incorporated in the design to adjust of the angle of attack. The wing's main element is usually a symmetric airfoil which is raised in the center in order to allow a slightly better airflow to the underfloor, but it also reduces the wings ride height sensitivity.

Front wings have a minimal effect on drag for the whole aerodynamic design, unlike small changes at the rear of the car, which can have drag penalties due to the wake being altered. The design of the front wing is critical in controlling the flow of air over the rear part of the car and allowing the air flow to the underfloor aerodynamic aids. A very common mistake that many teams do is that they choose to place three or four elements in the area between the inner side of the front wheels and the nosecone in order to achieve as much downforce as they can. This type of design prevents a great amount of air from flowing straight ahead into the side pods and therefore radiators receive less airflow and the car engine temperature can dramatically rise. Any aerodynamic issues at the front of the car has a huge impact on the rear of the car, so it is critical to get this right from the beginning of the design process.

The parts of the front wing, which tend to change most in design, are the endplates which are mounted at either end of the wing and their role is to aid the airflow to be forced over or under the wing further increasing its efficiency. The primary function of this feature is to stop the high-pressure air on the top of the wing from being encouraged to roll over the end of the wing to the low-pressure air beneath, causing induced drag. To increase front wing efficiency and maximize performance, the end-plates stop air spilling over the component and control airflow helping to make sure airflow is ducted to the rear wing and doesn't spill over the sides, while reducing drag. The rearward airflow coming of the device is smoothed out and helps to increase other aerodynamic devices efficiency. Additionally, another design aim of the endplates is to discourage the dirty air created by the front tires from getting under the floor of the car. Further to these, some teams use ''*splitters*'', which are vertical fences, attached to the undersurface of the front wing, to assist the endplate. This can also help to deal with the turbulences generated by the front wheels.
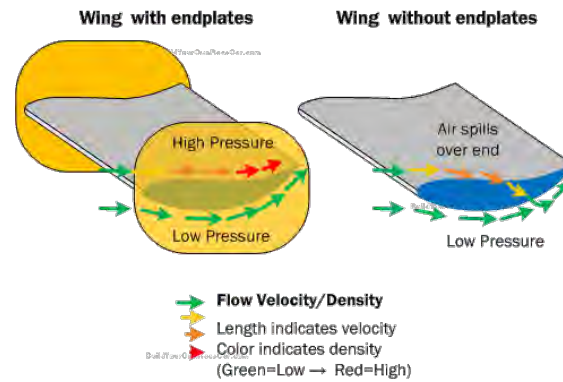
**Figure 14:** *How endplates improve the efficiency of a wing*

The exposed wheels of a FSAE car probably induce the most drag than any other part of the car. Since the FSAE rules prohibit any cover of the wheels an inevitable large separation of the flow takes place behind them and this causes the large amounts of formed drag. The amount of generated skin friction from the bodywork cannot even be compared to that type of drag. The interaction between the front wheels and the front wing makes it very difficult to come up with the best solution, however most teams are using a front wing in order to deflect the oncoming air around the front tires. Major design modification lies on the endplates and flaps of the wing, aiming to reduce tip vortex and wake of front wheel, either by making the inside edges of the front wing endplates curved to direct the air towards the chassis and the wheels or with sculpted outside edges to the endplates to direct the air from the outside of the front wheels.
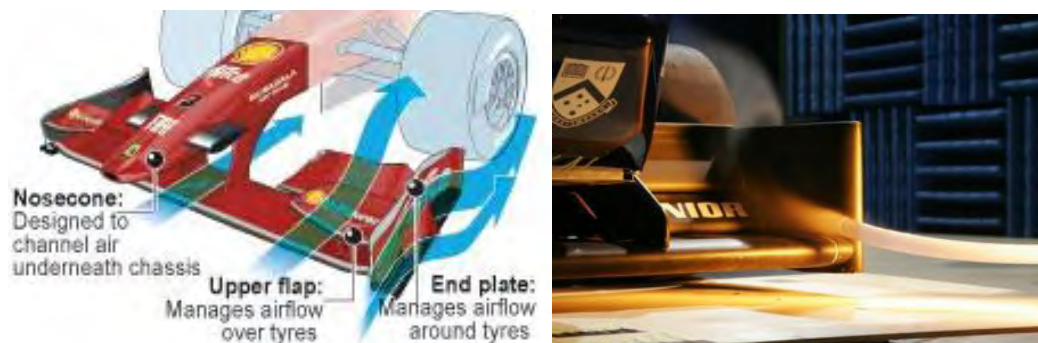
Figure 15: Left**,** *a well designed front wing prevents the incoming airflow from hitting direct on the front tires.* Right*, front wing endplate directs the airflow around the tires, Wind tunnel testing at Monash University.*
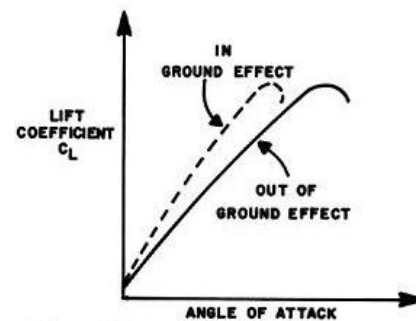
At the lower outside edges of the front wing endplates there are usually some semi-circular tunnels which called footplates. These tunnels are designed to help preventing airflow migrating from the outside of the endplate, underneath into the low-pressure region developed by the wing. As the higher-pressure airflow moves around and passes underneath the endplate, it trips over the lip of the endplate and flows into the low-pressure zone underneath the wing and this lateral mixing of high and low pressure airflow causes a small but powerful vortex to form just at inside of the endplate, hence footplates are also called vortex tunnels. When a vortex separates from a solid surface, it possesses a low-pressure core, in some sort of balance with the centrifugal "*force*" of the air spiraling around the vortex on helical trajectories. These vortexes act as air "*curtains*", sealing off other low pressure areas like the undertray and can also allow greater angles of attack for the front wing elements to be used, even right in front of the front tires and without the airflow stalling from their surface. This flow will then move onto the rear of the tire and if the footplate is correctly designed it will help to control front tire wake of the front wheels. If the front wing creates a turbulent wake or has a poor vortex generation, then every device that is developed downstream of the front wing must be optimized to work in that

environment, but often with less success. Many tests on different ride heights and wing angles of attack showed that these tunnels can significantly improve the downforce of a front wing up to 8%. However, due that footplates are considered part of the front wing, they must be located within the maximum allowable envelope for wings defined by the FSAE rules and cannot extend out of the front wheels. This means that the length of the wing must be reduced by a corresponding amount in order for the footplate to be compatible with the rules. Tests using different wings lengths showed that a loss up to 15% in total front wing downforce can result from the required reduction in wing length, and that is the main reason that most teams avoid the use of footplates in their wings.
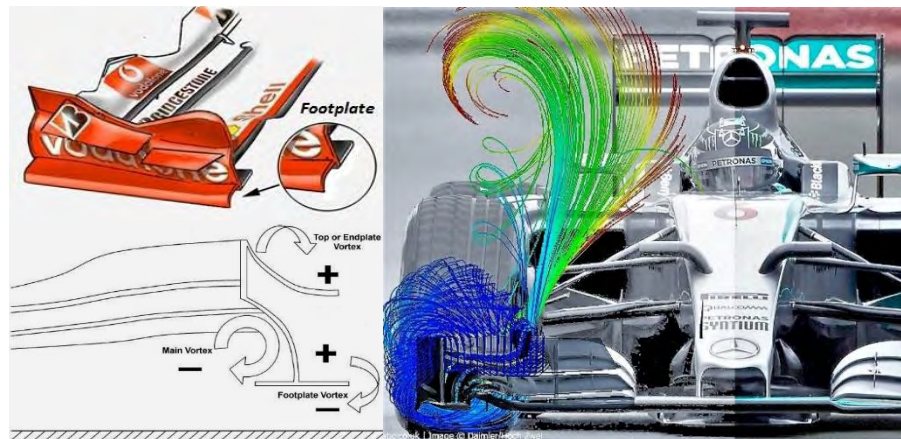
Figure 16: Left, *how footplate vortices are being created.* Right, *how a well-designed footplate operates*

The relationship between the front wing and the ground is a delicate one, with the wing generally being more efficient the closer it gets to the track due to the ground effect taking place. FSAE front wings usually operate most efficiently with ground effect typically at ride heights of about *40mm - 80mm,* depending on the wing design. Therefore, the front wing must be placed in a low position near to the ground to gain as much advantage from ground effect as possible. At higher ride heights, the wheels reduce wing downforce and increase wing drag, whereas the drag of the wheels themselves also rises. At low ride heights, however,

Figure 17: *When ground effect takes place in a front wing, higher C_L can be achieved until stall occurs*

the opposite happens and the wing performance improves, while the wheels produce less drag. The rear of the airfoil acts as a diffuser, the lower pressure region behind the airfoil assisting with increasing the speed of the airflow between the airfoil and the ground. Both these factors contribute to lowering the pressure beneath the airfoil and this is the reason that an inverted wing in ground effect has improved performance in comparison to an airfoil in free stream. As the angle of attack is increased, the lift also increases until stall is achieved at a much smaller angle in comparison to the free stream airfoil.

2.2.3. Rear Wing

The rear wing is a crucial component for the performance of a FSAE car. This device contributes to approximately one third of the car's total downforce, while it usually weights about *3 - 4kg*. The main function of the rear wing is to aid primarily in braking and cornering forces for the rear tires in order to eliminate oversteering. The rear wing is a multielement airfoil comprised usually of three or four sets of elements connected to each other by the wing endplates. Multiple wings and flaps are used to gain more downforce in the rear wing. Two wings will produce more downforce than one

Figure 18: *FSAE rear wing,* F0711-10 - *Rennteam*

wing, but not twice as much. The lift coefficient increases and lift/drag ratio decreases when increasing the number of airfoils. Multielement airfoils increase downforce by allowing greater total wing camber with high angle of attack and delaying flow separation near the trailing edge. This delay in flow separation on a deflected flap element is achieved by introducing a slot ahead of the flap nose for boundary layer control. The lower and biggest airfoil provide the most downforce while the 2-3 upper and smaller airfoils provide less downforce but can improve the efficiency of the lower one as they prevent airflow to stall. Sometimes an even lower extra airfoil is placed over the diffuser exit creating a low-pressure region just below the wing to help diffuser create more downforce below the car.

However, the airflow at the rear of the car can be affected by many different influences (*intake, bodywork, driver, etc.*) from the rest of the car at the front and so it is called "*dirty*" because it is mainly a separated flow with many turbulences. This causes the rear wing to be less aerodynamically efficient than the front wing, due to the disbursed airflow that it has to deal. There are many parameters including the gap width between elements, the orientation of each successive element and the span wise twist that must be properly designed to achieve maximum efficiency depending on the flow that reaches the rear wing. The position of the wings relative to each other is also important. If they are too close together, the resultant forces will be in opposite directions and thus cancel each other. The rear wing typically generates close to twice as much downforce as the front wing in order to maintain the handling balance of the car, but this also depends on the design and the suspension set up of each FSAE car. A larger aspect ratio or angle of attack, can be seen compared to the front wing and often two or more sections stacked are used on top of each other in order to create the amount of downforce needed and maximize available space. In rear-wheels cars, this is significant vital and the rear wing will not only add acceleration and braking abilities, but also cornering grip. A greater wing angle increases the downforce and produces more drag, thus reducing the cars top speed. So, when racing on FSAE tracks with long straights and few turns it is better to design the wings to have small angle of attack. Opposite to that, when the car is racing on FSAE tracks with many turns and few straights, more downforce is required thus it is better to design the wings to have greater angle of attack.
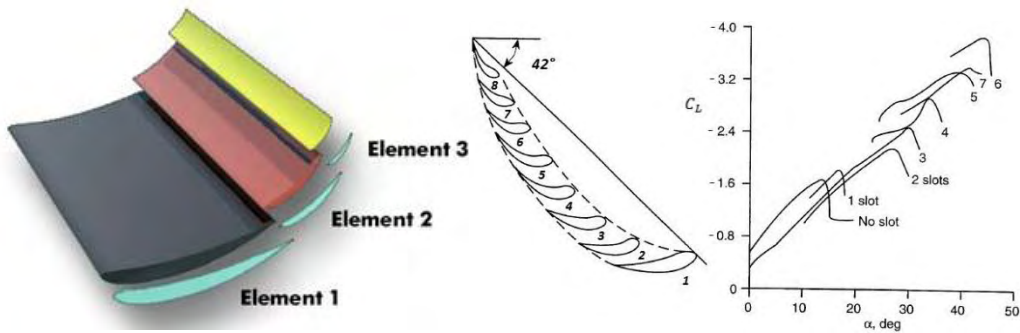
Figure 19: *Variation of lift coefficient with the number of elements*

As air flows over the wing, it is disturbed by the shape, causing a drag force. Although this force is designed to be less than the downforce, it can seriously limit top speed and cause the engine to use more fuel to get the car through the air. The design of the wings should reflect the need to generate enough grip to brake at speed without skidding. This allows more powerful brakes to be used with the same tires because the downforce increases the tires grip. The maximum speed of the car and the necessary rate of deceleration must be also taken under consideration. The wings should be optimized between the downforce needed for grip whilst braking and the drag they produce. The main problem at the designing of rear wing is the turbulence or the "*wake*" that is left behind of this device. To make sure wake is reduced to minimum, the air exiting the car cannot be turbulent with vortices. However, due to the Venturi tube effect under the car and the wing creating downforce above the car, the two exiting "*dirty*" air flows meet at the back of the car creating great vortices and affecting the aerodynamics of the car significantly by creating drag. Therefore, it is always an aim to make the two airflows meet as linearly as possible with minimal drag.

Rear wing endplates are designed with form and function in mind. Because of their form, they provide a convenient and sturdy way of mounting wings. The aerodynamic function of these endplates is to prevent air spillage around the wing tips and thus they delay the development of strongly concentrated trailing vortices. Trailing vortex or induced drag is the dominating drag on any kind of wings. An additional function of the rear endplates is to help reduce the influence of up flow from the wheels. The vortices start later on the wing with end plates because the airflow is forced to move in one direction of motion and can only start whirling after the rear wing. Splitting the airfoil into separate elements is one way to overcome the flow separation caused by adverse pressure gradients.
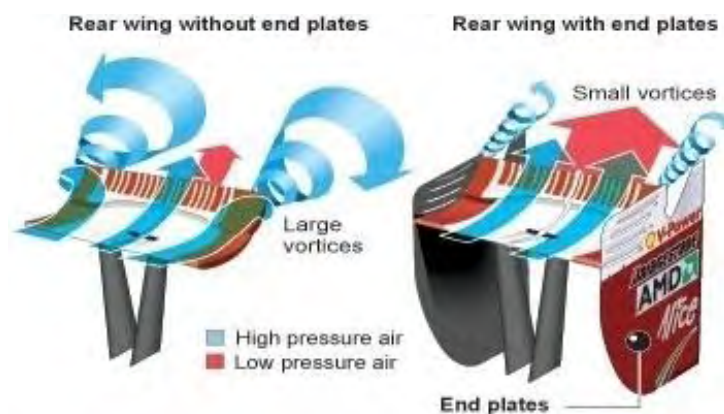

Figure 20: *How rear wing endplates reduce drag and improve the aerodynamic efficiency*

At high angles of attack, air is unable to follow the contour of the lower wing surface and can detach (*stall*), lowering the efficiency of the wing and adding drag. Adding a small lip on the trailing edge, causes a lower pressure just behind it which sucks the lower flow back up to the wing surface. The Gurney Flap (*or wickerbill*) is a small tab projecting from the trailing edge of a wing. Typically it is set at a higher angles of attack on the high pressure side surface of the airfoil, and it's height must be of the order of local boundary layer thickness or *1% - 4%* of the wing chord length in order to be effective. This trailing edge device can improve the performance of a simple airfoil to nearly the same level as a complex high-performance design. The device basically operates by increasing pressure on the pressure side of the wing, decreasing pressure on the suction side, and helping the boundary layer flow stay attached all the way to the trailing edge on the suction side of the airfoil. At the same time, a long wake downstream of the flap containing a pair of counter rotating vortices can delay or eliminate the flow separation near the trailing edge on the lower surface. Correspondingly, the total suction on the airfoil is increased. The designer has to get all the downforce possible out of the wing surfaces allowed by the rules. The Gurney flap surely causes some extra drag, but can generate more downforce from the allowable wings because of the higher angles of attack. Gurney flaps are also used as a quick way to fine tune the force a wing generates in order to adjust the way a car handles. Varying the height of the Gurney flap adjusts downforce (*and drag, of course*) and so most teams have devised ways of changing the Gurney quickly.
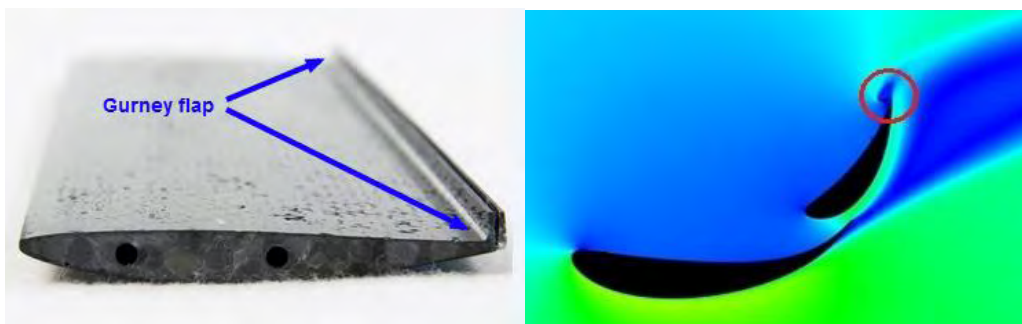
Figure 21: *Gurney flaps are usually placed on the trailing edge of the last element and can significantly increase the efficiency of the rear wing*

Generally, when the aim of top speed is the main consideration of the design, the reduction of the angle of attack is inevitable in order to minimize drag. Usually the rear wing elements are designed to have adjustability just like the front wings, each of these can be adjusted when the car is racing in different dynamic events (*Acceleration, Endurance etc.*) via small Allen keys to achieve the required downforce and drag levels of each event. In Acceleration event for example, many teams often choose to set their rear wings in low or even zero angle of attack in order to reduce the drag of the elements in minimum while until the car reaches at least 40km/h the rear wing doesn't produce enough downforce to give the required grip to the tires to avoid spinning. On the other hand in Endurance and Skidpad events where the downforce is vital for the ongoing turns, teams set their rear wings at the angle of attack that they have design them to operate and be most efficient. Some of the most advanced FSAE teams are also using a drag reduction system(*DRS*) operating with electronic actuators which give the ability to the driver with just the press of a button to level off the angle of attack, of the rear wing elements while driving, to reduce drag and downforce, thus increasing top speed. In the near future, active aerodynamic devices would be adjusted via computer calculations to

operate with specific way depending on speed, rpms, corner radius and track conditions giving thus huge performance gains compared to most static set-ups requiring adjustments that are being today. This would help to reach maximum performance levels for the tires while increasing fuel economy and the overall driving efficiency of the car.
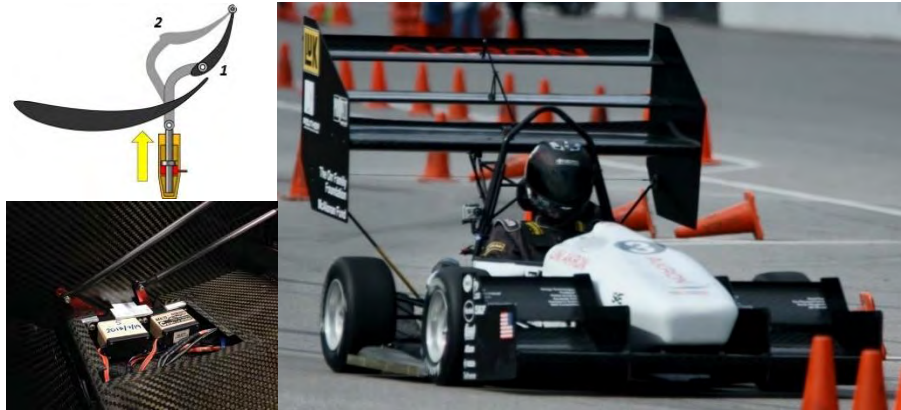
Figure 22: *FSAE Rear wing Drag Reduction System(DRS) on action*

2.2.4. Undertray Diffuser

The undertray is not only the largest aerodynamic component on a FSAE car, it's also the most aerodynamically efficient, producing nearly 9 times more downforce per unit of drag than a rear wing. Since the major rule changes in 2015 which heavily restrict the rear wing size, a focus on the optimization of the undertray has made it a critical part of the package. The location of the undertray is important


Figure 23: *FSAE Rear Diffuser*

because being in such a close proximity to the ground means it is able to take advantage of the phenomenon of ground effect, which essentially magnifies the suction force produced by airflow beneath the undertray surface. Bringing these surfaces closer together accelerates the flow, resulting in lower pressure and a greater amount of undertray downforce. Simple fluid dynamics says that when flow accelerates its pressure decreases. This is in fact the nozzle effect (*or Venturi effect*), when the flow in a convergent nozzle accelerates and drops its pressure and then recover in the diffuser. By shaping the underbody as an inverted wing, or with appropriate tunnels, or even with a simple scant angle that work with the Venturi effect, the overall pressure between the undertray and the ground decreases creating additional downforce. The key role of undertray is to accelerate the flow of air under the car, creating a greater difference in pressure between the upper and lower surfaces of the car, thus increasing downforce and aerodynamic grip, which literally sucks the car to onto the track creating much higher grip levels.

The Diffuser is the rear element at the underbody of a FSAE car close to the floor, from which air exits the car. This is the last components where air interacts with the car. The objective of the diffuser is to slow the flow back down again and to give the used air flow

from the undertray of the car as much possible space to exit from the rear end. This ultimately means that if the air can escape more easily from under the car, then more air at faster velocities can flow under the undertray of the car creating a lower pressure and therefore higher downforce. The diffuser increases in volume along its length, creating a void that has to be filled by the air passing under the body. This Venturi effect means that the flow is accelerated through the throat of the diffuser, creating the desired low pressure, then gradually returned to the same velocity at which it joined the wake. It is important to re-equalize the large pressure difference that the undertray creates between it and the ambient pressure which surrounds the car. Without a diffusion system in place to gradually slow the air down, significant drag would be induced by the forced, sudden mixture of high and low pressure airflow. Additionally, the expanding air exiting our diffuser is able to interact with the rear wing improving their combined performance.
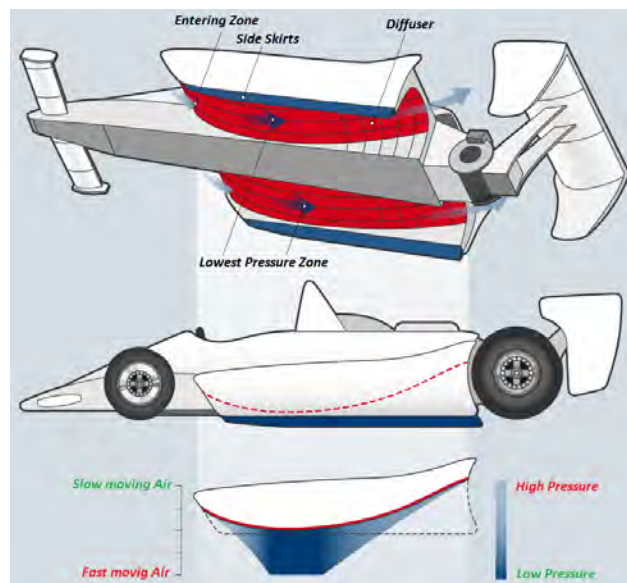

Figure 24: *The diffuser opperates as an inverted airfoil*

With the diffuser working, the car turns into a Venturi tube, being the most efficient aerodynamic package on an FSAE car. However, considering the diffuser has the potential to give an amount of 30-40% of the total downforce, the exit of the used air flow can sometimes be deemed much more significant. Diffusers leverage the low-pressure area behind the vehicle, and can sometimes leverage high speed exhaust gases ejected into the diffuser to create even lower pressure (*blown Diffusers*). The speed of air flow can significantly influence downforce, whereby the faster the flow exits, the more downforce is generated. With an increasing driving speed the airspeed will also increase. When this happens the proportional difference between the speed of the air on top of the undertray and underneath the undertray will get higher. This means the difference in pressure will be higher. So, the generated downforce and drag are completely dependent on the dimensions of the undertray diffuser and the speed of the air/speed of the car. When the incorrect dimensions are taken the undertray diffuser will generate a lot of drag and will generate a little amount of downforce or even positive lift. The diffuser doesn't directly produce downforce only to the rear end of the car but, in essence, it produces downforce along the whole of the car.
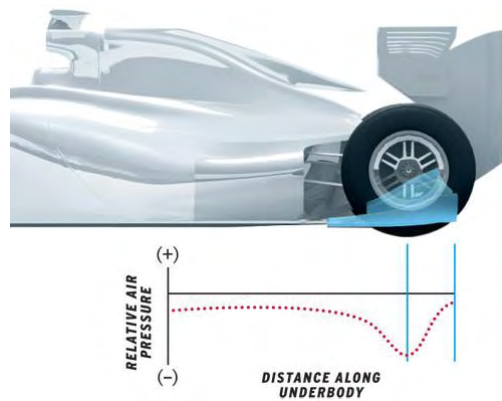
Figure 25: The lowest pressure occurs where the air moves the fastest, just immediately ahead of the diffuser.

The angle or slope of the diffuser is also important, the diffuser must have a gradual change of angle to prevent flow separation from its roof and sides. The angle of the diffuser relative to the ground affects the magnitude of downforce that is created. If the angle of the diffuser is close to zero the boundary layer flow will not detach, but the air speed will not be reduced enough to make a laminar transition of the air at the end of the car when to two airstreams meet. If the diffuser has a very large angle the boundary layer flow will detach and the airflow underneath the diffuser will be turbulent. In general, it is desired to have the highest angle without flow separation to generate maximum downforce. Once separation occurs the downforce is reduced and drag is greatly increased. Two-dimensional simulations of diffuser angle show that maximum downforce is reached with an angle of *8-12°*. However in reality there is another effect occurring that changes this statement. Starting at the diffuser entrance there is a vortex that forms that travels down the length of the diffuser. A vortex adds a rotational component to the velocity decreasing the pressure along its length. This vortex flow also adds energy to the flow and will delay separation allowing larger diffuser angles. Vortices can also be used on other parts of the undertray. Large vortex generators can be placed at the entrance of the undertray so that the vortices travel along the length of the vehicle, reducing the pressure and increasing downforce. These vortices can also be used along the sides of the undertray creating a "*false seal*" that also increases downforce.
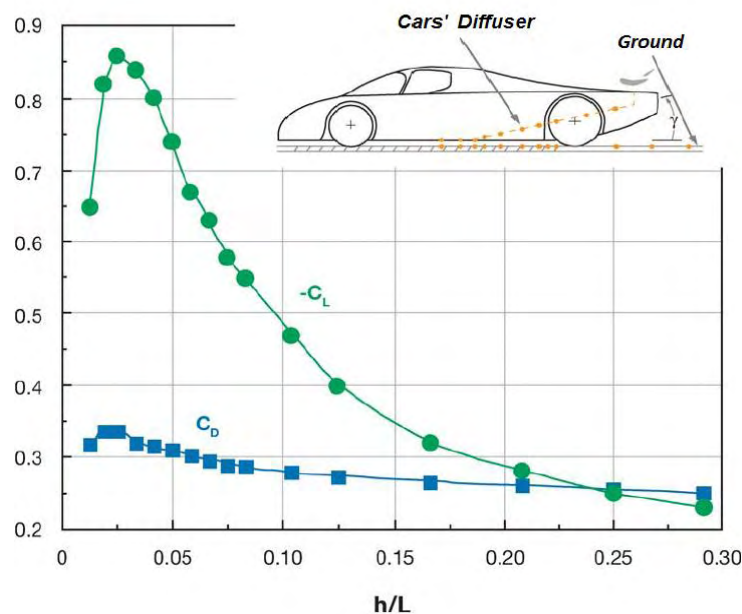
Figure 26: Lift and drag coefficient variation with ground clearance for a race car with underbody diffuser

26

2.2.5. Sidepods

Sidepod is the part alongside the cockpit that accommodates the radiator and often the engine exhaust and oil tank system. The main function of sidepods is to provide enough air for the cooling of the engine and to control underbody flow to generate desired downforce. The profile of sidepods are varied significantly on every car, based on the different aerodynamic designs. The internal shaping has to

Figure 27: *FSAE Sidepods, University of Auckland*

maximize thermal transfer rates and reduce drag penalties, which can be a balancing act in its self. The design normally incorporates chimneys and cooling louvres help to extract hot air as quickly as possible. General design of sidepods where quite tall and boxy in the beginning, but modern designs lend to be lower and sleeker, as teams strive for less drag and more downforce, at the rear of the car.

The width and height of the sidepods are determined by the need to accommodate the oil and water radiators for engine and exhaust cooling. The distribution of engine heat to water and oil will depend upon the detail philosophy of the engine design, but in total it will be similar for all the engines. Most teams aim to minimize engine heat rejection quantity and maximize coolant temperatures, in order to minimize the radiators sizes and airflow requirements for cooling system. However, for safety reasons bigger radiators than needed are selected, thus it takes all the space available in the sidepods to package radiators and their ducting to cool them. The bigger a radiator is, the greater its resistance in airflow and therefore increased drag. There is a parabolic growth of the flow resistance from an increasing Reynolds number. In this case, an increase of the Reynolds number means an increase of the velocity. So, the aim is to achieve the highest heat rejection with lowest possible drag. Heat transfer rate is also affected by the area of the sidepod inlet as it determines whether the flow into the sidepod is laminar or turbulent. Varying both outlet and inlet areas of the cooling system to give only the required amount of cooling under any given condition means that the cooling drag and fuel consumption are kept to a minimum.

The velocity distribution on the front face of the radiator must be uniform. This is the reason why the sidepod inlet is designed to ensure an even distributed velocity distribution on the front face of the radiator and at the same time balance the pressure distribution at the inlet and outlet in order to minimize the drag from a sufficient airflow through the radiator. The best way to design the ducting in order to avoid separation, which would decrease the efficiency of the radiator, is to have a smooth expansion after the inlet that has a smaller area than the front face of the radiator. To further increase the performance of the ducting and eliminate stall, the inlet edges can be rounded like a thin airfoil leading edge. Shortening the sidepods by moving the leading-edge rearwards, has not helped the task of providing enough cooling air to the radiators. The turbulent wake from the front wheel spreads as it moves downstream and so envelops the radiator intakes more, the further they are behind the wheels. A wide variety of barge-board arrangements has emerged since sidepods are shortened, to try and take control of both front wheel and

front wing wakes and move them to regions where they can do some good, instead of hurting the cooling by entering the radiator intake.
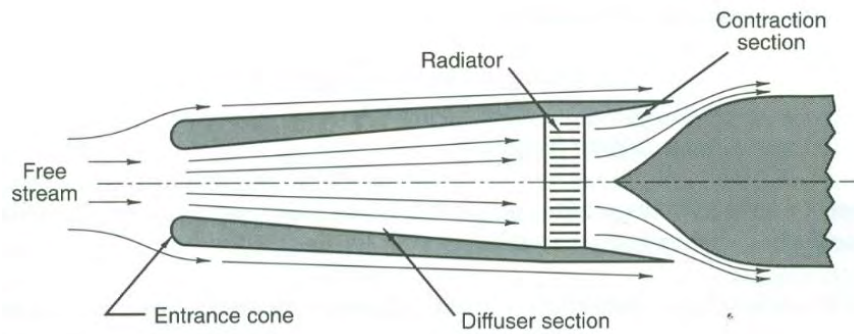
Figure 28: *Curved sidepod edges help to avoid stall on the inlet*

The aluminum radiator cores used in most FSAE cars are relatively thick and have high air pressure drop coefficients, and so do not require high velocity air to flow through them. Instead, the cooling air must be slowed efficiently, and the static pressure thereby raised, between the intake and the front face of the radiator. The internal ducting of the sidepods takes the form of a divergent duct to the one or more radiators in each sidepod. The pressure behind the radiator must be as low as possible to provide the greatest possible pressure difference across the core. Communicating the radiator exit ducts to the rear of the car ensures that the base pressure, lowered further by the rear wing underside, is used to "*pull*" air out of the radiator. The high pressure ahead of the wheels "*pushes*" air under the car, filling and decreasing the desirable low pressure generated there. The high velocity air flow around the inside edge and along the side of the wheel and tire creates low pressure, which is desirable as it inhibits the inflow under the floor area.

Setting the radiator at an angle of attack of *40-50°* inside the sidepod is another effective way to improve its functionality, as it increases the size of the radiator core for greater heat transfer and takes advantage of the natural convection of air. Once the lighter heated air exits the radiator, it travels directly upward toward the top surface of the sidepod due to the density difference. This restricts the airflow and creates low velocity regions inside the sidepod. In order to solve this problem, gills can be placed in the region where the sidepod is blocking the airflow assisting the expulsion of hot air from the radiator exit and allowing the sidepod to "*breathe*". However, regardless on fact that most of the hot air exits sidepods upwards and backwards, there is still great amount of up-force generated due to upper shape of the sidepods which isn't generating any downforce at all. All gain in downforce occurs only due to previously mentioned hot air outlets (chimneys, gills etc.) including the position and direction hot air and exhaust gasses.
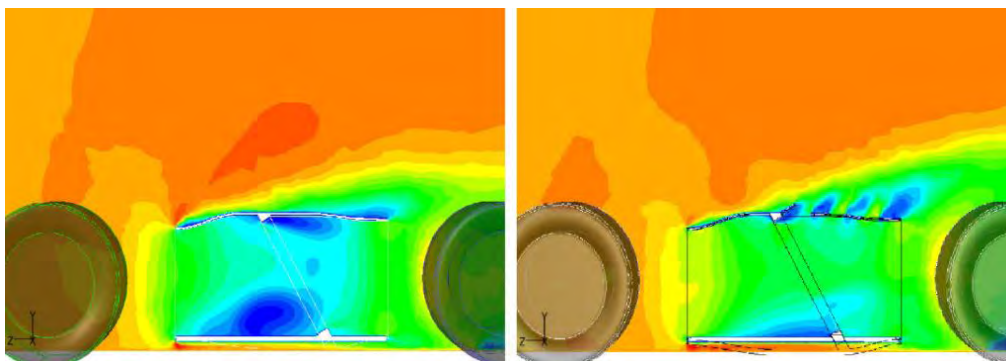
Figure 29: *Velocity field on the interior of a FSAE sidepod*

2.2.6. Brake Cooling Ducts

Under braking, the friction of the brake pads against the disc transfers the kinetic energy of the car into heat, which passes through the brake disc, pads and caliper. If this energy is not removed from these components, they will eventually fail. By far the most efficient method of heat transfer from the brakes is through convection. This is achieved by forcing cold air through the ducts and blowing it through the radial center vents of the hot disc, on the surface of the pads and calipers as well as any nearby electronic sensors. As flow passes through the large number of flow paths drilled or molded racially through the brake disc, heat is transferred from the hot disc into the colder air, and as this flow heads out of the wheel it can be up to 200°C hotter than when it went in.
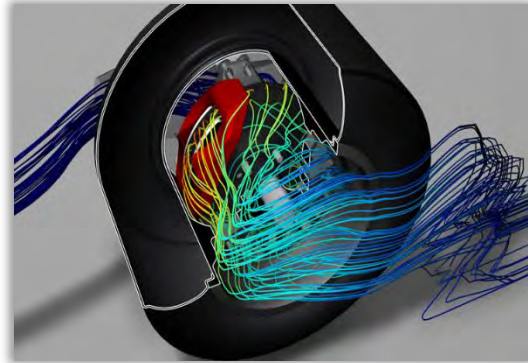
Figure 30: *Brake cooling duct*

The key for the inlet is to be in a high-pressure location which is usually the front surface of the car. Any inlet on the front of the car will work to a degree. They will be more effective the closer to the center of the wheel you can put them. As you move away from center, the air is traveling sideways over the wheel, not straight on, so inlets further to the sides are less effective. If a front wing is used, the duct inlet must be placed in such a way that the air passing from the front wing is driven directly to it. The amount of air is controlled by using different size ducts, which are smaller for circuits with less braking demand and larger for heavy braking circuits in order to manage the temperatures of the brakes and achieve the correct balance between high performance and acceptable wear rates. Moving from the smallest to largest cooling ducts can cost 1.5% in aerodynamic efficiency, which represents a loss of about 1km/h in top speed.
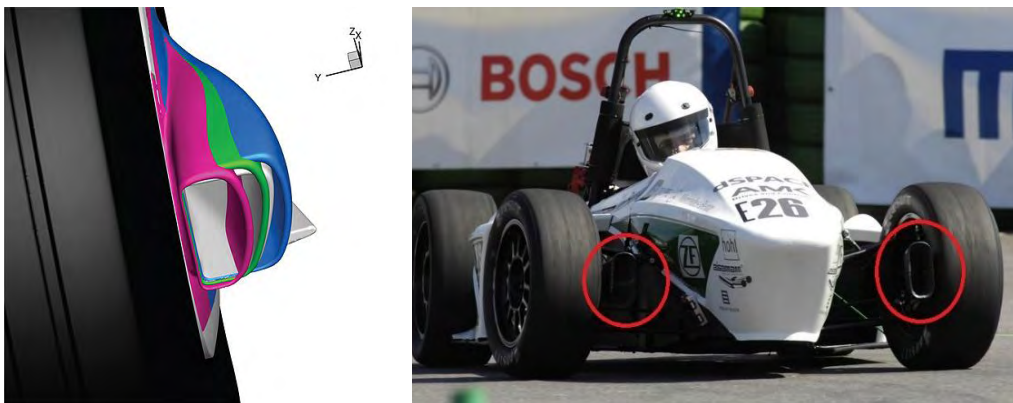

Figure 31: *FSAE Brake cooling ducts with different inlet sizes*

2.2.7. Flip-Ups

Exposed wheels are the anti-thesis of optimal aerodynamics in that they contribute significant drag and lift (the opposite of downforce). They also shed highly turbulent air in their wake, which is essentially useless as a feeder for other aerodynamic devices on the car. Lift due to exposed wheels is also a major problem for all open wheel racecars since regulations prohibit enclosing the wheels within the bodywork. Exposed wheels generate upward lift forces that decrease the downforce created by the wings and other structures. This positive lift may reduce the downforce of a FSAE car by approximately 11%. Plus, they disturb the air flow around rear wing. To resolve this problem, Flip-Ups are placed on the rear section of the sidepods, in front of the rear tires guiding air over the rear wheels while creating some downforce and shielding rear wing from influence of dirty air coming from front and rear wheels. Flip-Ups are also used to align the air with the wheel and thus reduce drag. Close by, and sometimes integrated into the Flip-Ups are winglets (*small airfoils with end plates*) to create additional downforce.
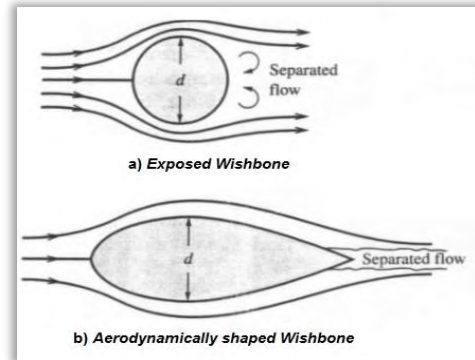

Figure 32: *FSAE Flip-Ups, Dynamis PRC - Politecnico di Milano*

Figure 33: *FSAE Flip-Ups, Rennteam* Uni Stuttgart *e.V.* - Universität Stuttgart

2.2.8. Suspension Wishbone Covers

Wishbones rods are in a direct contact with air for a wingless car or with the air coming through the front wing for a car with a full aerodynamic package. These parts are mainly circular or rectangular shaped, which makes them generate even more drag than an airfoil, therefore these bars and rods have an oval or airfoil envelope shape. Aerodynamic suspension helps to increase overall down force levels for the whole aerodynamic package. If there is airflow separation at the front of the car, this could easily reduce the whole aerodynamic package, or at least negate some of the down force generation potential. Their role is not to

Figure 34: *Streamlined wishbone improves the smoothness of the air flow for parts behind and reduces drag*

produce downforce but they are simply shaped that way to reduce the wishbone's drag and keep the flow heading to the sidepods relatively undisturbed as the stall behind the suspension components (*wishbones, dampers, rockers etc*.) can critically affect the efficiency of the radiator which is located inside the sidepod. These suspension arms are often made in a shape of a wing, although the upper surface is identical to the lower surface. Due to the manufacturing difficulties, most FSAE teams tend to design airfoil shaped shrouds in order to cover the cylindrical wishbones inside them, rather than making them as a single part like in a F1 car. Case **a**, represents an un streamlined suspension arm, and the lower one **b**, a suspension arm with an aerodynamic covering. Both have roughly the same cross sectional area, but **b** has a drag force up to ten times less than **a**.

**Figure 35:** *FSAE Suspension covers, RP16c - Dynamics e.V.*

Figure 36: *FSAE Suspension covers, TU* Darmstadt Racing *Team - DART* Racing

2.3. Aerodynamic Forces Distribution & Balance

On most FSAE cars downforce is produced largely (*about 40-50%*) by the undertray-diffuser while front and rear wings produce each about 20-30% of the total downforce, with the front and rear wings being the main tuning elements. Notice how the downforce is distributed at the front, middle and rear of the car. This results in a relatively even distribution of load between the front and rear tires. By tuning the front and rear downforce you alter the cars center of pressure. The center of pressure (C_P) is the balance of downforce at the front and rear axles, also known as the aerodynamic balance. The distance between C_P and center of gravity (C_g) is called static margin and it is typically required for the position of C_P to be as much closer to that of C_g. A slightly rearward aerodynamic package, where the C_P is behind the C_g is commonly used to ensure high speed stability. Designing for a good aerodynamic balance will ensure that the vehicle exhibits neutral handling characteristics rather than understeer or oversteer as a result of unevenly distributed aerodynamic loads.

Downforce has to be balanced between both the front and rear, left and right of the car. Due to the symmetry of the car, the balance between left and right can be easily achieved but achieving balance between front and rear is a different thing. Flow in the front greatly affects flow in the back of the car and vice versa. Downforce must be adjusted according to each racing track characteristics of the different FSAE events (*Endurance, Skidpad etc.*) and the dynamic behavior of the car. If a car has significantly more downforce at the rear than at the front or even if it has lift at the front, the front of the car can feel lighter under certain situations on the track. That lightness in the front of the car can lead to understeer, simply because the front wheels are lacking grip relative to rear grip. S most FSAE teams are trying to achieve an increase in front and rear downforce, while keeping the balance between the two forces correct, in order to avoid introducing any undesirable handling or grip issues by getting that balance wrong.
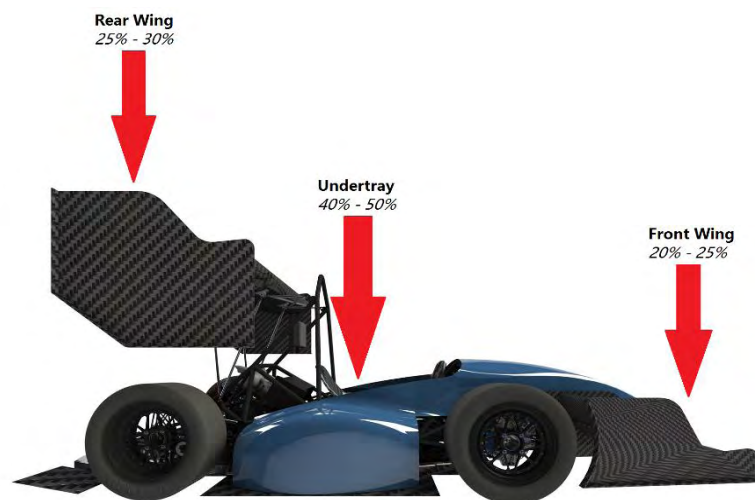
Figure 37: *Aerodynamic forces percentage distribution based on the efficiency of each device*

Another advantage of balancing downforce is that it can help reduce body roll while cornering and body pitch during braking or acceleration. This in turn helps reduce sudden variations in vertical forces applied to the tires at the limit, increasing vehicle stability in the wake of driver input. Vehicle behavior is also more linear near the limit of adhesion, contributing to increased driver control. Downforce not only increases dynamic performance, but also creates a more stable vehicle behavior environment for steering,

throttle, and braking inputs. In low-speed corners little power is needed to maintain speed, so reducing the drag has almost no effect. In high-speed corners the influence of drag can become quite significant however, it makes only *10%* of the difference than that which can be achieved by balancing downforce. In other words, creating downforce to press the vehicle onto the road as speed increases not only contributes to increased absolute cornering speed and thus absolute dynamic performance, but also significantly improves vehicle control quality as measured by response to driver inputs and vehicle stability at the limit.

Interference in the air flow results in increase of the pressure on the corresponding axle. This situation is especially evident during cornering. In the case where the rear axis carry more load, the front axle is not able to follow the path expected by a driver, thereby extending the radius-we deal with the effect of understeer. The opposite concept is oversteer where more susceptible to the occurrence of slip is a rear axle with much intense slip conditions. Increased pressure obtained through the interference with the flow of air results in more efficient acceleration, but a bad balance can lead to oversteer. Balance is determined by the addition of the moments produced due to both downforce and drag force over their perpendicular cantilever lengths about the design center of pressure, which in this case is taken as the ground position directly below the car's center of gravity which is usually at mid-wheelbase. For a FSAW car, a typical aerodynamic balance is approximately 45% downforce to the front and 55% to the rear.
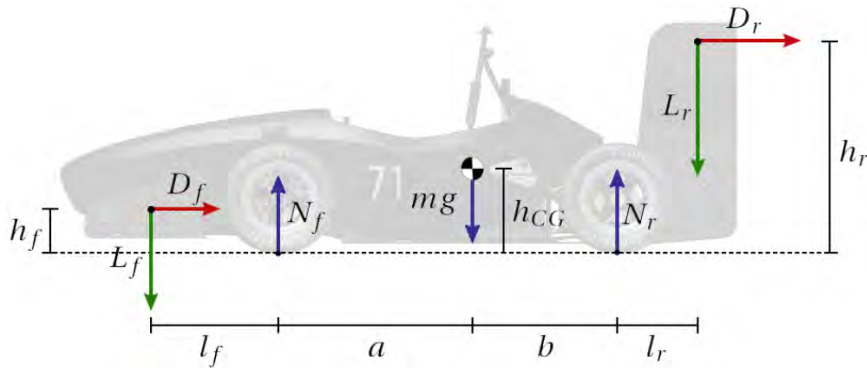

Figure 38: *Free body diagram of an FSAE car used for the estimation of the aerodynamic balance*

When both downforce and drag is already known for the front and rear of the car, an approximate calculation for the aerodynamic balance of the vehicle can be done based on the free body diagram, showing in *Figure 32* above. After the analysis of the applied forces and moments on the car, the force acting on rear tires (N_r) can be found using the equation below and respectively calculate the force for the front tires (N_f). Wing positions can be estimated by measuring the perpendicular distance from the balance point to the estimated center of pressure for each wing.
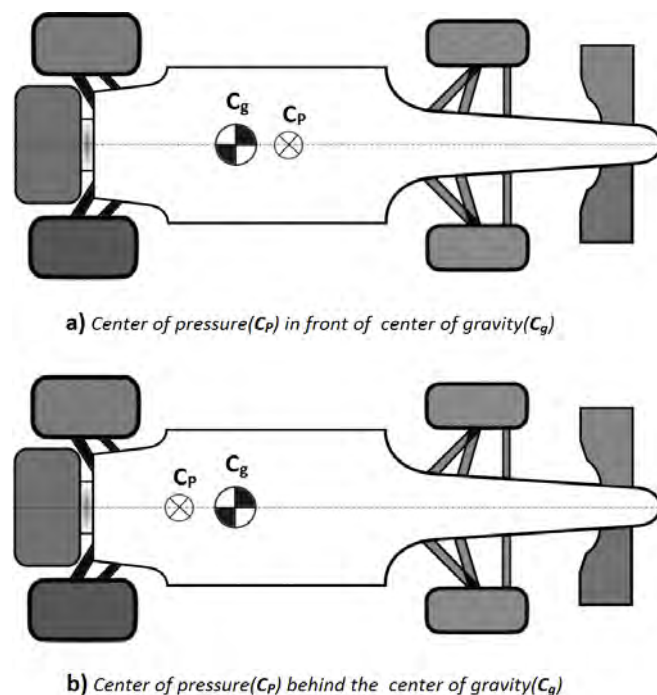
$$\uparrow: \quad \sum_i \mathbf{e}_z \cdot \mathbf{F}^{(i)} = 0 \qquad \Rightarrow \qquad N_f + N_r - mg - L_f - L_r = 0 \qquad \textbf{(2.4)}$$

$$\curvearrowleft: \quad \sum_i (\mathbf{r}^{(i)} - \mathbf{r}_{CG}) \times \mathbf{F}^{(i)} = 0 \qquad \Rightarrow \quad bN_r - aN_f - (l_r + b)L_r + (l_f + a)L_f$$

$$+(h_{CG} - h_r)D_r + (h_{CG} - h_f)D_f = 0 \qquad \textbf{(2.5)}$$

Rear tires Force:

$$N_r = \frac{amg + (l_r + a + b)L_r - l_f L_f + (h_r - h_{CG})D_r + (h_f - h_{CG})D_f}{a + b} \qquad \textbf{(2.6)}$$

FSAE cars are largely limited on corner entry by the rear grip available. In low to mid speed turns the car needs a slight rear bias to the C_P, this prevents the car suffering corner entry oversteer. Too much aggressive front wing in these corners will make the car too pointy and hinder lap-times while in faster turns the front wing can lead the car. The drivers turn in gentler in to fast turns, which creates less lateral acceleration at the rear axle. So, it is rare for the rear to step out on turn-in in to fast corners. Thus, at higher speeds it can be a C_g biased towards neutral or the front. Since applying downforce to a body will create better traction, we need to figure out how and where to apply it. Basically, a race car handling is described as oversteer, understeer or neutral. Oversteer in aerodynamic terms means more front downforce (*or less rear downforce*) while understeer would be more rear downforce (*or less front downforce*) and neutral would be a good combination of both.

a) *Center of pressure(C_P) in front of center of gravity(C_g)*

b) *Center of pressure(C_P) behind the center of gravity(C_g)*

Figure 39: a) *A C_P ahead of C_g is able to lead on an oversteering situation*
b) *When C_P is behind the C_g an understeering situation is expected*

Braking during cornering can easily put the car off-balance. Under the effect of deceleration, the front of the vehicle is more heavily loaded (*due to weight transfer on the front*), and because of the steering that extra load becomes unbalanced by acting of the centrifugal force on outer front corner of the car. This places a big load onto that suspension unit and creates a great deal of extra work for that tire to have to cooperate with. When this happens, even for rear-wheel drive vehicles, the rear of the car becomes lighter and with the dramatic unloading of the diagonally opposite wheel and suspension unit to that which has been unnaturally loaded. This braking effect being due to the retardation effect of the engine. This makes it more difficult for the rear tires to grip the road, due to the reduced amount of downforce and the rear of the car can more easily become provoked into oversteer and start to overtaking the front. Applying the brakes whilst cornering can even cause the rear tire, the one traveling on the inside of the bend, to lose contact with the road altogether.

The majority of the braking is done by the front wheels, but obviously all four wheels provide braking force. By increasing the rear grip without reducing the front grip it is possible to increase the overall grip under braking of the car as a whole, so additional rear downforce can have a positive effect on how much grip the rear wheels have under braking. Comparing a FSAE car running without a rear wing with a full aero car, the addition of a rear wing can produce downforce at the rear, helping to address the front downforce to rear downforce balance, but that balance requires to look at front downforce and rear downforce simultaneously. By creating a downforce with the same front to rear balance as vehicle weight, changes in steering characteristics from low to high speeds remain well under control. At higher speeds this translates into a more linear response. More precise control of the vehicle helps the driver delve further into the car's potential.

Even though FSAE wings do not see large changes in angle of attack during forward motion, it is necessary to have as wide an operating range as possible in order to have enough options when it comes to car setup. The rear wing is often used to balance the car after the front wing setup has been completed to compensate for any possible undesirable characteristics of the car endowed to it by pre-existing handling traits. The amount of downforce generated by current FSAE cars changes the load at the wheels by about 70% at the front and about 90% at the rear. For the suspension and tires, the car appears to be approximately two times as heavy at final speed than it is at low speeds. Combine this 100% increase in vertical load with the low ground clearance it can be clear how aerodynamics can affect the performance of a FSAE car even during braking.
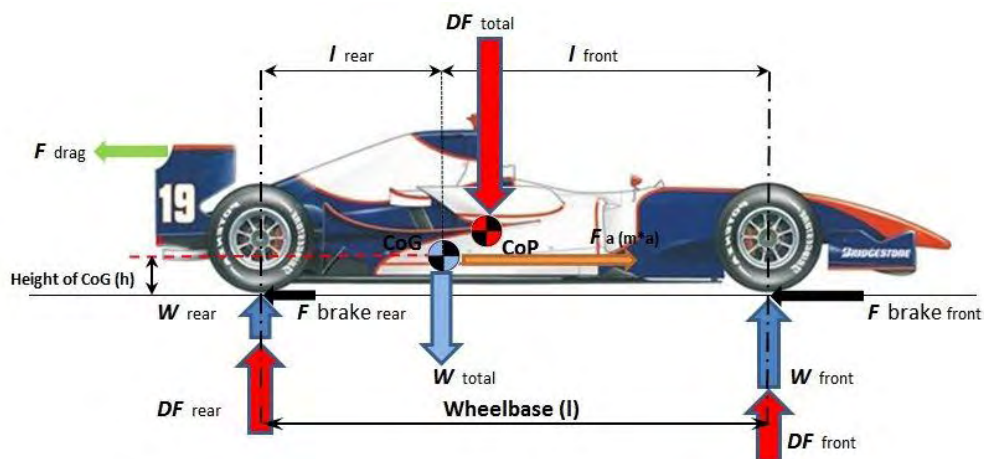
Figure 40: Free body diagram of a race car during Braking

3. SETUP OF THE CFD MODELS

This chapter gives a precise description of the straightforward and reliable way of how CFD simulations in the field of external aerodynamics of a FSAE car were made for the development of the aerodynamic package of Centaurus Racing Team's 2016 car *Thireus 277*. Comparing to the aerodynamic devices that were reported on Chapter 2, this aerodynamic package consisted of a low drag Nosecone, an Undertray with a rear Diffuser, two symmetric Sidepods and also a front and rear Wing which were not placed on the real car due to the lack of time. These aerodynamic devices were simulated and tested one by one until a complete CFD model be created and simulated giving the final aerodynamic characteristics of the whole vehicle. All the CAD models were designed with *Solidworks* software, by using mainly the Surfaces Tools while the powerful tool *ANSA* was used as *pre*-Processor in order to successfully deal with the "*cleaning*" of the highly complex geometries and generate high quality mesh with precise handling. The set up and solving of all the CFD cases was made with *ANSYS-Fluent* solver while for the visualization and estimation of the results was made using the advanced *post*-Processor, *mETA*. Items and approaches listed below do not claim to be complete nor optimized, they are just recommendations based on personal experience and recent comparable studies.

Computational Fluid Dynamics (CFD) is the use of applied mathematics, physics, numerical analysis and data structures to solve and analyze problems that involve fluid flows and visualize how a fluid(*air is the fluid for Aerodynamics*) flows as well as how it affects objects as the flow pass. Computational fluid dynamics is based on the Navier-Stokes equations. These equations describe how the velocity, pressure, temperature, and density of a moving fluid are related. Computers are used to perform the calculations required to simulate the interaction of liquids and gases with surfaces defined by boundary conditions. With high-speed supercomputers, better solutions can be achieved. Initial experimental validation of such software is performed using a wind tunnel with the final validation coming in full-scale testing. The current generation of CFD packages generally is capable of producing accurate solutions of simple flows. The codes are, however, designed to be able to handle very complex geometries and complex industrial problems. When used with care by a knowledgeable user CFD codes are an enormously valuable design tool.

An integrated CFD simulation consists of three main stages which are *pre*-Processing, Solving and *post*-Processing and are strictly performed in that order. In *pre*-Processing step the initial CAD geometry gets "cleaned" from any type of problematic surfaces and is divided into smaller fragments, called meshing or grid generation step. With mesh probe-points where the analysis has to be done are actually defined. Thus, at the Solving stage exactly as the geometry is discretized the same are the Navier-Stokes equations for each cell which are later solved giving on the *post*-Processing step the values that are obtained in the form of colorful contour plots using the visualization techniques that can give a very good insight to locate the hot-spots, recirculation and dead zones. So, it is not only the qualitative depiction of values that are generated but also the quantitative that can help the user to analyze the overall flow phenomena.
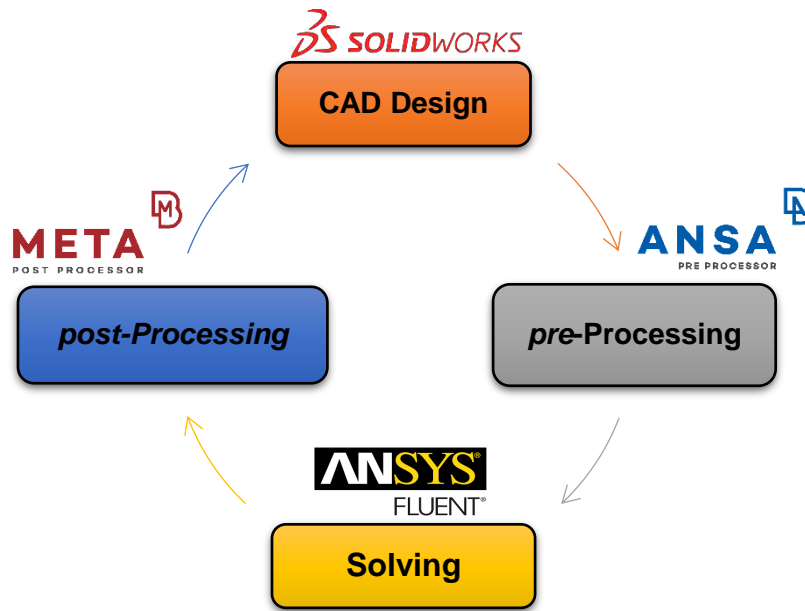
Figure 41: *Process followed for the correct execution of a complete CFD Simulation*

3.1. *pre*-Processing

3.1.1. Geometry "*Clean-up*"

When setting up a CFD model there is usually a geometry of interest which imported from a Computer Aided Design (CAD) package to use in the simulation. The complexity of each CAD geometry depends on the accuracy interest from the data imported and is directly connected with the available computing power. During the preparation for a CFD simulation, a consistent definition of fully connected geometry has to be ensured. Typically, the CAD geometry that is imported in the *pre*-Processor has not been created there but in one of many CAD packages. The first basic step after importing the CAD design, comprises of a "*Cleaning-up*" of the geometry in order to eliminate any kind of errors that may have occur during the CAD designing process. Many of these errors can be generalized as file translation issues. Exporting these files out of CAD software into a neutral file format (*IGES, STEP, SAT etc.*) accepted by the *pre*-Processor can introduce misrepresentations in the geometry. As a result of translation errors between CAD representations, errors or differences in the way the geometry is interpreted may occur.

Depending on the severity of the problem, sometimes a mesh can be generated even with a less than perfect geometric representation, however, in most cases, these should be resolved before meshing. In some cases, there exist small details in the geometry that if meshed, would result in very small elements and a potentially huge element budget. Small curves and surfaces can sometimes result from details in the design solid model that may not be necessary for analysis or may even be a result of careless construction of the CAD model. In either case, it is important to remove or modify these features before meshing. Assemblies of parts are often required to have a conformal mesh across their interface. The operations imprint and merge are often required to connect parts together so that when meshed, the representation will be a single continuous mesh. Modeling errors caused by the user in the CAD package is another problem that has to be fixed during

the *pre*-Process. In the CAD package, the user may not create the geometry correctly, causing some parts to overlap or introduce small gaps between parts that should touch. If also the meshing software's tolerance is finer than the CAD package's, this disparity in tolerance can cause subsequent geometry modification operations in the meshing package to inadvertently create sliver features, which tend to be difficult and tedious to deal with. This tolerance problem also causes misalignment issues between adjacent volumes of assemblies, hindering the sharing of coincident geometry in order to produce a conformal mesh.

3.1.2. Creation of Fluid Domain

During the *pre*-Processing the Fluid Domain inside which the CFD simulation is going to take place must be defined carefully to ensure the reliability of the results. In external aerodynamics the Fluid Domain has the shape of a rectangular box and represents a virtual wind tunnel in which the body of interest must be placed and must be ensured that there is always enough space between the inlet, the geometry and the outlet so, that the boundary conditions could be met with the geometry of the vehicle included thus the dissipation of vortices downstream from the vehicle does not disturb the solution upstream and the pressure at the stagnation point evolves reasonably. The entrance to the wind tunnel is typically placed about 4-5 times the characteristic length ahead of the geometry and an inlet velocity is defined on it. Respectively the exit of the wind tunnel is placed about 8-10 times the characteristic length behind the geometry and is considered as a pressure outlet while the side walls of the domain are placed about 2-3 times the characteristic length further. Typically, the ratio of the vehicle cross section to the wind tunnel cross section is within a certain range. This ratio is called blockage ratio and has to be less than 6% or even less than 2% depending on the inlet velocity and the kind of results that the user wants to examine on each case. As a result, the effects of the Fluid Domain walls on the pressure distribution and thus, the drag coefficient are small. Otherwise, the flow field around the car is disturbed by wall influences.

To reduce the total cell count, and therefore computing time, a symmetry plane was used down the center of all the geometries. Symmetric Computational domain may be used to reduce the computation effort without significant loss of accuracy and can save up to 50% or more in simulation turnaround time. Additionally, you can use the shortage memory to run more accurate simulations with more mesh cells clustered in areas of interest. However, it is not always given that a symmetric model will also have a symmetric flow field. For instance, the flow over a symmetric cylinder in a certain Reynolds number range exhibits vortex shedding that is clearly not a symmetric flow field. However, for external flow over FSAE cars the flow is symmetric enough to only run a simulation on symmetric half model. Symmetric simulations are also not applicable if the domain boundaries represent the walls of a real wind-tunnel. In this case the simulation should take into account the related wall effects. Simulations with complete vehicle domain is recommended when the car is tested in cornering or if a correlation with experimental data has to be done.

3.1.3. Mesh Creation

3.1.3.1. Surface Mesh

The first step in the surface meshing procedure is the imposing of the estimated average element size on the whole vehicle geometry. The most common type of elements that is used for a CFD simulation is the triangle elements. Triangle cells are shaped of 3 sides and is one of the simplest types of mesh. The faceted triangular surface resolution has to meet several requirements. For a typical FSAE car shape, pressure or form drag is dominant over skin friction, so the accuracy of the drag and lift predictions are largely determined by the accuracy of the predicted static pressure distribution on the body. This pressure distribution is strongly affected by the locations of flow separation and reattachment. Even though that the mesh must be very fine in the critical regions there is still the problem of knowing where these regions are and how fine the mesh should be. Along solid surfaces there will be a boundary layer and so there must be several points close to the surface in a direction normal to the surface. This allows the numerical solution to model the rapid variation in velocity through the boundary layer. Another example is where a surface has a large amount of curvature causing a rapid variation in pressure in the flow direction. However, large flow gradients also exist in areas of the flow away from the solid surfaces, like in the wake behind the car. Creating a suitable mesh in these areas is more difficult as the exact location of the critical areas is difficult to determine.
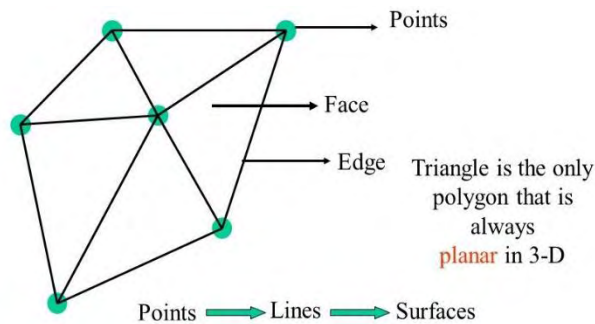
Figure 42: *Triangle surface mesh element*

The surface mesh of all models is created by using ANSA CFD algorithm which gives the user the possibility to identify locations where geometry simplifications have to be applied or a higher degree of mesh resolution is needed to capture the geometric details and accurately describe separation. There are also sharp angles between the wheels and the ground plane. This is a source for highly skewed cells. It is necessary to blunt this angle by introducing small faces connecting ground and tires and it can be made by using ANSA Fuse function. The surface meshing should result in a high quality, non-uniform triangular surface mesh that resolves all radii and geometrical details well. Therefore, it is important that the surface mesh resolves all relevant details of the geometry and satisfies the requirements of the physical models used in the simulation. To ensure high quality surface mesh for all the models, three quality criteria are used which are defined according to ANSYS-*Fluent* solver. The first and most important quality criterion is the Skewness of elements. According to the definition of Skewness, a value of 0 indicates an equilateral cell (*best*) and a value of 1 indicates a completely degenerate(*worst*) cell. Degenerate cells are characterized by nodes that are nearly coplanar. Cells with a skewness value above 1 are invalid. Highly skewed cells should be avoided as they can decrease solution accuracy and even destabilize the solution. The next criterion that is used is Wrapping which is the amount by which an element deviates from being planar. Since three points define a plane, this check only applies to quads. The quad is divided into two trias along its diagonal and

the angle between the trias' normal is measured. The maximum angle found between the planes is the warping of the element which for ANSYS-*Fluent* is 40°. Finally, the min and max angle criteria are used for shell elements, which is the maximum angle between adjacent edges and is computed by using corner node positions in 3-D space. The best possible triangle maximum angle, for an equilateral triangle, is 60° while Fluent sets the minimum angle limit at 30°. By using ANSA mesh quality improvement functions (*Fix Quality, Reconstruct, Smooth*) the surface mesh of all models results to compatible with all quality criteria. To illustrate the importance of mesh generation, it is worth mentioning that about 70% of the total time spent on a CFD case is devoted only to the creation of a high quality and accurate mesh. The quality of the mesh determines largely the accuracy and stability of the numerical computation.

Criteria	Calculation	Color	Failed
☐ aspect ratio	FLUENT	☐	3.
☑ skewness	FLUENT	☐	0.5
☑ warping	FLUENT	☐	40.
☐ min height	QUADS &	☐	0.
☐ squish		☐	0.5
☐ jacobian	ANSA	☐	0.4
☐ min length		☐	0.
☐ max length		☐	0.
☑ min angle quads	FLUENT	☐	45.
☑ max angle quads	FLUENT	☐	0.7
☑ min angle trias	FLUENT	☐	30.
☑ max angle trias	FLUENT	☐	0.7
☐ mesh distortion		☐	2.
☐ growth ratio		☐	3.
☐ h-ratio		☐	0.3

Figure 43: *Surface mesh quality criteria used in ANSA according to ANSYS-Fluent solver*
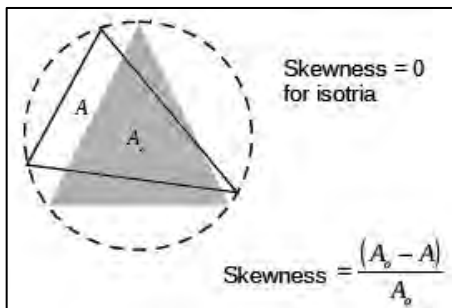
Figure 44: *Skewness criterion for surface mesh elements*
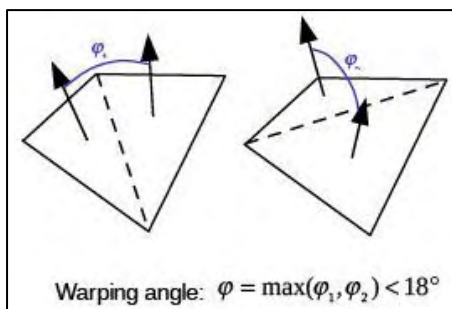
Figure 45: *Surface Warping criterion definition*
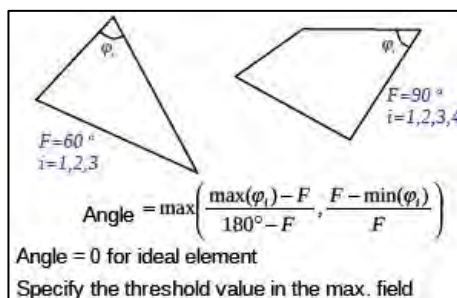
Figure 46: *min/max Angle criterion definition*

3.1.3.2. Layers

Properly resolving a boundary layer around any model requires a fine grid resolution close to the model surface. The actual cell density depends on several factors such as the boundary layer type (*laminar or turbulent*), the near wall function model used and, in case of turbulent flow, the implemented turbulence model. Compared with laminar flows, numerical results for turbulent flows are even more dependent on grid density due to the inherent strong interaction of mean flow and turbulence. First of all, the boundary layer mesh is extruded using the Advancing Front method, which extrude layers consisting of tetrahedral elements from the surface faces into the specified core zone. Therefore, the first layer height and the growth rate must be specified based on the estimated boundary thickness of each case. To accurately predict the estimated boundary thickness of each model, ANSA *Y+ Calculator* is used with a given velocity and the characteristic length of each geometry. This propagation is either determined by a specified number of element layers or by the constraint of a constant growth rate even in the adjacent element layers. The specified core zone is filled with uniform isotropic elements.

The surface mesh must be as smooth as possible to allow prism layers to be extruded from the surface of the examined geometry. Wall Layers are mesh element layers along all fluid-wall and fluid-solid interfaces. It augments the original mesh to produce a smooth distribution along all walls, which is critical for accurate flow and boundary layer thickness prediction. Wall Layers ensures adequate mesh across small gaps, which can be very difficult manually. Wall Layers creates layers before the 3D volume mesh is constructed. Diagnostic algorithms detect and avoid element clashes in small gaps automatically. Element layer height across each surface can be absolute or have an aspect ratio, and is based on the smallest length scale on a surface. For all models 6 layers in total are used with the first three having an absolute height and the next three a growth ratio of 1.2. A gradual transition between surfaces ensures gradual variations in element height throughout the model.
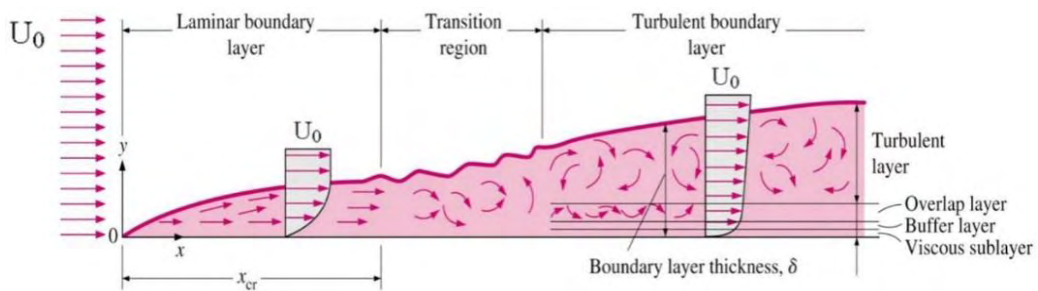
Figure 48: *Types of boundary layers*
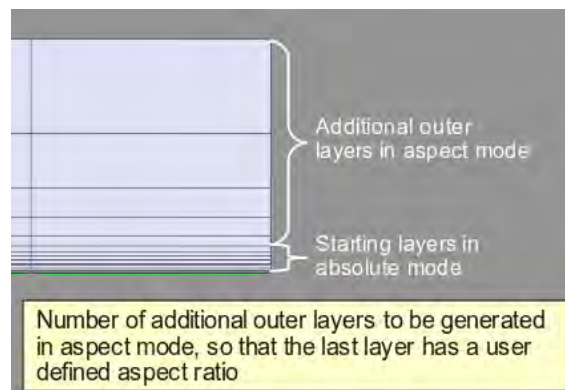
Figure 47: *Methodology used for Layers creation in ANSA*

41

3.1.3.3. Volume Mesh

The final step of the *pre*-Processing is the generation of the volume mesh which is going to fill in the fluid domain with Tetra volume elements. Tetrahedral(*Tetra*) elements are solid elements which have been extracted from 2D tria elements. As there are many complex geometries it is needed to have some mesh regions where a local volumetric control is used to captures the flow gradient vortex and wake, some of these important regions are the wake behind tires the wake in the rear end of the car and the underbody. In order to control the volume mesh near the car, extra size boxes may be created to refine mesh in critical regions where stall or strong vortices are expected to occur. These boxes should extend about half a characteristic length in front, to the sides and to the top, and about a characteristic length in the wake. Next, the whole fluid domain is filled with Tetra elements using the Tetra Rapid algorithm. An initial tetrahedron encloses the whole flow domain, and is successively refined, up to the boundary of the core zone. Thus, the required refinement in certain regions close to the bounding surfaces is ensured while larger elements in the majority of the flow domain are maintained.

Tetra Rapid is a volume meshing algorithm available in ANSA and was used for the creation of the volume mesh for all the models. The *Tetra Rapid* algorithm uses tetrahedral elements and pyramids if the surface mesh contains also quads. Most suited for geometries of thick Volumes or large domains with a significant variation in length along the surface mesh. This algorithm is specifically designed to handle large size CFD models and is bench marked to be 6 times faster than other algorithms (*patented*). The Maximum growth rate has to be defined, which is the approximate growth factor of volume element size from layer to layer while the generation moves towards the interior of the Volume. The values should range from 1.0 to 3.0 and for this project all models have the default value of 1.2. The standard method creates tetras from an enclosed volume of shell elements, plus several parameters. This provides the user with a lot of control over the final tetra mesh. The volume tetra mesher quickly and automatically creates a tetrahedral mesh on an enclosed volume of surfaces or solid geometry with only a few inputs. Finally, the quick tetra mesher creates a tetra mesh that maintains user specified quality requirements, but may sacrifice details in the shape of the part to do so.
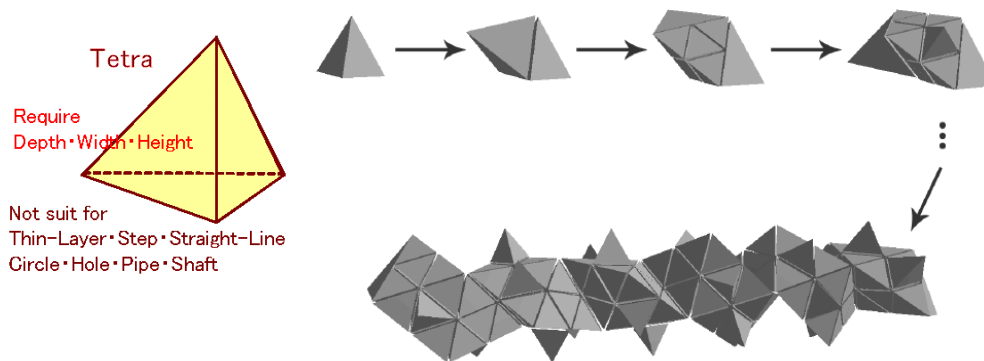
Figure 49: *Tetra volume mesh elements*

The user can select the quality criterion definition with respect to which the generated tetra. Specifying high quality threshold values results in a better-quality mesh but requires more time for its generation. Five mesh quality criteria are used for the volume mesh. The

Volume Aspect Ratio for tetrahedral elements is evaluated by finding the longest edge length and dividing it by the shortest height as measured from a node to its opposing face. Skewness is the difference between the shape of the cell and the shape of an equilateral cell of equivalent volume. This quality index is applied only to tetrahedral elements, all others are assigned value of zero. Volume Skewness is defined as 1-shape factor, so a value of 0 is perfect and a Skewness value of 1 is the worst possible value. The Warping criterion for volume elements is performed in the same way as for all faces of surface elements. Finally, the min/max angle of elements measures the deviation of an element from its ideal shape, such as a triangle's deviation from equilateral.

Criteria	Calculation	Color	Failed
☑ aspect ratio	FLUENT ▾	☐	20.
☑ skewness	FLUENT ▾	☐	0.92
☑ warping	FLUENT ▾	☐	50.
☐ squish		☐	0.95
☐ jacobian	ANSA ▾	☐	0.4
☐ min length		☐	0.
☐ max length		☐	0.
☑ min angle pentas	FLUENT ▾	☐	30.
☑ max angle pentas	FLUENT ▾	☐	0.92
☑ min angle hexas	FLUENT ▾	☐	30.
☑ max angle hexas	FLUENT ▾	☐	0.92
☐ non orthogonality	OPENFO. ▾	☐	70.
☐ growth ratio	ANSA ▾	☐	10.
☑ negative volume	PARTIAL ▾	☐	
☐ left handed		☐	
☐ min height		☐	0.
☐ h-ratio		☐	0.15
☐ determinant	OPENFO. ▾	☐	0.001
☐ layers quality		☐	1.
☐ face tetquality		☐	1.E-12
☐ min volume		☐	0.

Figure 50: *Volume mesh quality criteria used in ANSA, according to ANSYS-Fluent*
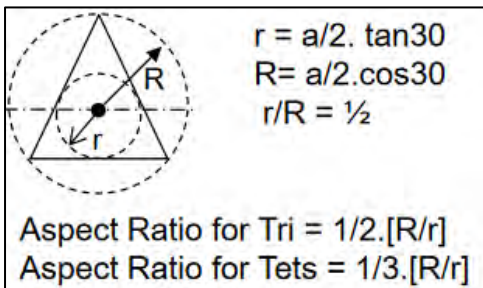
Figure 535: *Aspect Ratio criterion for volume elements*
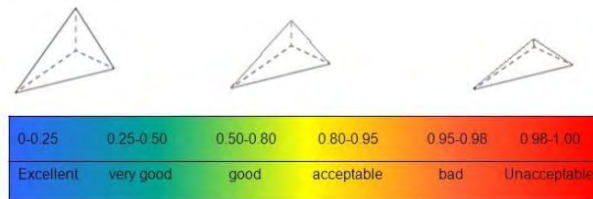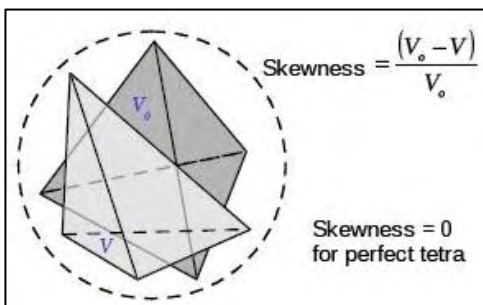
Figure 516: *Skewness criterion for volume elements*
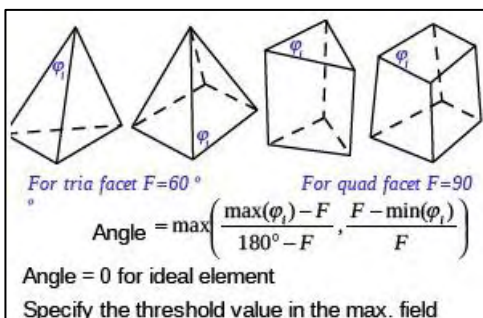
Figure 527: *min/max element Angle criterion for volume elements*

3.1.4. *pre*-Processing of the CFD Models for the Aerodynamic Package

3.1.4.1. Nosecone:

In order to properly setup a CFD model for the whole car, all parts of the aerodynamic package are tested one by one in order to optimize their features and assembly them to a final model. The first model is the nosecone of the car, which is the most front part of the car (*if there is not a front wing*) and due to the symmetry of the geometry, half of the nosecone is simulated. Assuming that the characteristic length of the nosecone is 1.2m, the Fluid Domain

Figure 54: *Nosecone's CAD model*

that is created for the CFD simulation is extended ten times the characteristic length (*12m*) to the rear, five times to the front (*6m*) and three times to the sides (*3.6m*). For the surface mesh of the model, ANSA CFD algorithm is used to create trias elements with a minimum target length of 50mm, a maximum target length of 150mm, a growth rate of 1.2, a distortion angle of 10° and a 30° angle limit for the sharp edges. Three rectangular size boxes are also used to refine mesh around the nosecone's surface with a maximum length of 25mm, 15mm and 25mm each. Using these parameters and with respect to the quality criteria that were referred earlier the surface mesh has a total of 230,248 elements while all elements are compatible with skewness criterion.

Figure 56: *Fluid Domain for the CFD simulation of the Nosecone*

Shell Skewness Graph

Classes	Ranges		Elements
Class 1:	< 0.00	0.00%	0
Class 2:	0.00 - 0.10	99.36%	228776
Class 3:	0.10 - 0.20	0.62%	1427
Class 4:	0.20 - 0.30	0.01%	17
Class 5:	0.30 - 0.40	0.01%	13
Class 6:	0.40 - 0.50	0.01%	15
Class 7:	0.50 - 0.60	0.00%	0
Class 8:	0.60 - 0.70	0.00%	0
Class 9:	0.70 - 0.80	0.00%	0
Class 10:	0.80 - 0.90	0.00%	0
Class 11:	0.90 - 0.92	0.00%	0
Class 12:	0.92 - 0.95	0.00%	0
Class 13:	0.95 - 0.98	0.00%	0
Class 14:	0.98 - 0.99	0.00%	0
Class 15:	0.99 - 1.00	0.00%	0
Class 16:	1.00 - 1.00	0.00%	0
Class 17:	> 1.00	0.00%	0
			Total: 230248

Figure 55: *Surface mesh used for Nosecone model*

After the successful generation of surface the mesh, layers are next to be created. To define the total height of layers it is first necessary to estimate the boundary layer's thickness. Using ANSA *Y+ Calculator* for a characteristic length of 1.2m and a velocity of 17m/s the estimated first layer height is about 6.3×10^{-4} m. So, a total number of six layers are created with the first three having an absolute height of 0.63mm and the next three a growth factor of 1.2. Finally, for the volume mesh tetras elements are created using ANSA *Tetra Rapid* algorithm with a growth rate of 1.2, while the maximum length for volume elements inside the three size boxes of is 35mm, 20mm and 35mm respectively resulting in a final model with 2,846,742 volume elements in total.
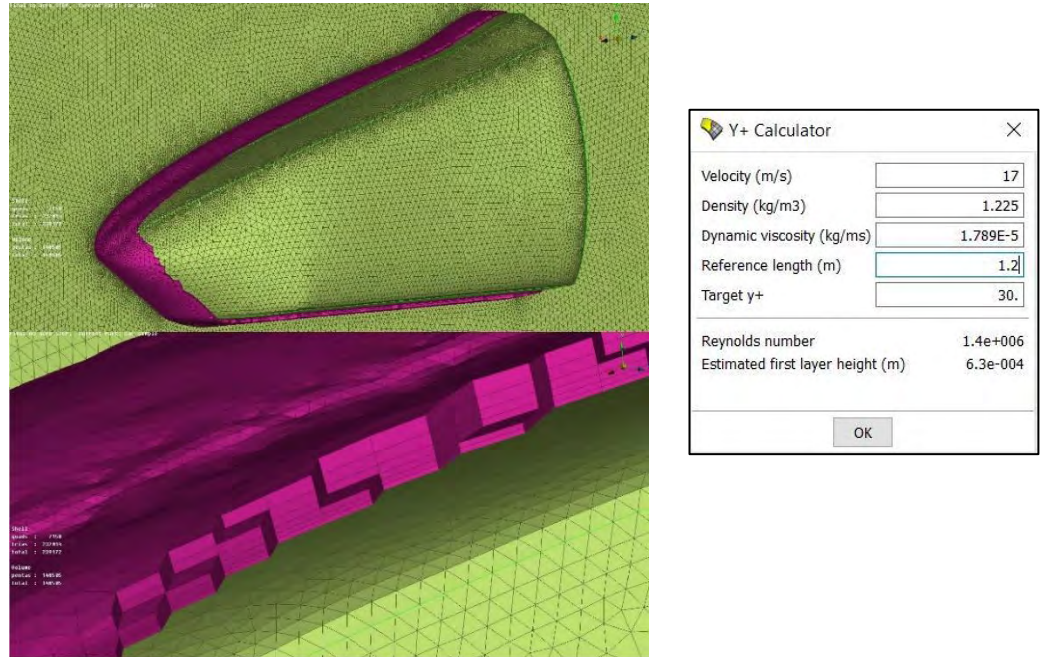
**Figure 58:** *Layers created for Nosecone model*
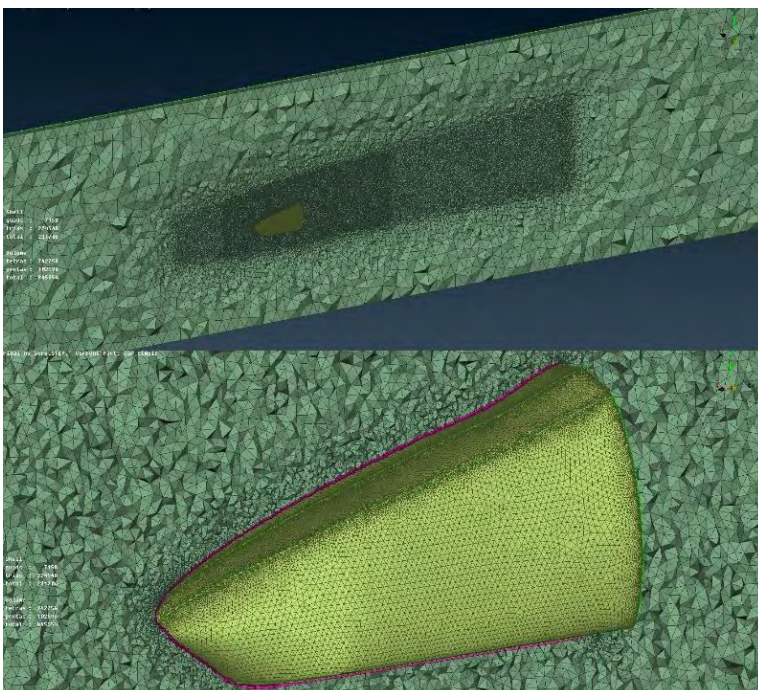
Figure 57: *Volume mesh elements generated for Nosecone model*

45
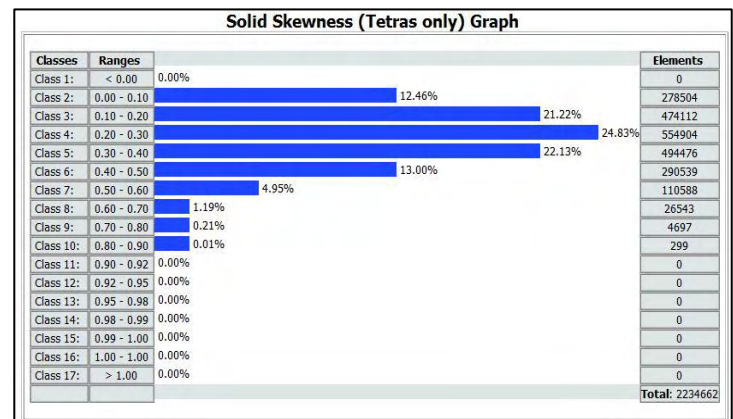
3.1.4.2. NACA Airfoils:

In order to design the front and rear wing of the aerodynamic package it is first necessary to select the most efficient and suitable NACA airfoil for each wing and estimate their optimal dimensions, position and angle. For the setup of the CFD model though, the Fluid Domain that is created is extended ten times the characteristic length ($6.7m$) to the rear, five times to the front

Figure 59: *CAD model of NACA airfoils*

($3.35m$) and three times to the sides ($2m$) assuming that the characteristic length of the whole model is about 0.67m. For the surface mesh of the model, ANSA CFD algorithm is used to create trias elements with a minimum target length of 50mm, a maximum target length of 100mm, a growth rate of 1.2, a distortion angle of 10° and a 30° angle limit for the sharp edges. Three rectangular size boxes are also used to refine mesh around the airfoils' surfaces with a maximum length of 20mm, 10mm and 20mm each. Using these parameters and with respect to the quality criteria that were referred earlier the surface mesh has a total of 157,892 elements while all elements are compatible with skewness criterion.

Figure 61: *Fluid Domain used for NACA airfoils model*
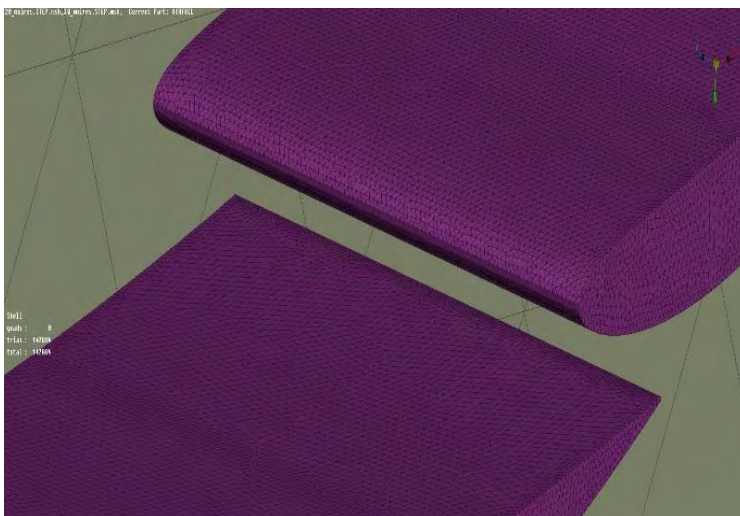
Figure 60: *Surface mesh created on NACA airfoils*

Shell Skewness Graph

Classes	Ranges		Elements
Class 1:	< 0.00	0.00%	0
Class 2:	0.00 - 0.10	97.56%	154035
Class 3:	0.10 - 0.20	0.90%	1414
Class 4:	0.20 - 0.30	0.01%	22
Class 5:	0.30 - 0.40	0.53%	829
Class 6:	0.40 - 0.50	1.01%	1590
Class 7:	0.50 - 0.60	0.00%	2
Class 8:	0.60 - 0.70	0.00%	0
Class 9:	0.70 - 0.80	0.00%	0
Class 10:	0.80 - 0.90	0.00%	0
Class 11:	0.90 - 0.92	0.00%	0
Class 12:	0.92 - 0.95	0.00%	0
Class 13:	0.95 - 0.98	0.00%	0
Class 14:	0.98 - 0.99	0.00%	0
Class 15:	0.99 - 1.00	0.00%	0
Class 16:	1.00 - 1.00	0.00%	0
Class 17:	> 1.00	0.00%	0
			Total: 157892

After the creation of the surface the mesh, layers are again next to be created. Using ANSA *Y+ Calculator* for a characteristic length of 0.67m and a velocity of 17m/s the estimated first layer height is about 5.9×10^{-4} m. So, a total number of seven layers are created with the first four having an absolute height of 0.59mm and the next three a growth factor of 1.2. Finally, for the volume mesh tetras elements are created using ANSA *Tetra Rapid* algorithm with a growth rate of 1.2, while the maximum length for volume elements inside the three size boxes of is 25mm, 15mm and 25mm respectively resulting in a model with 6,741,986 volume elements.
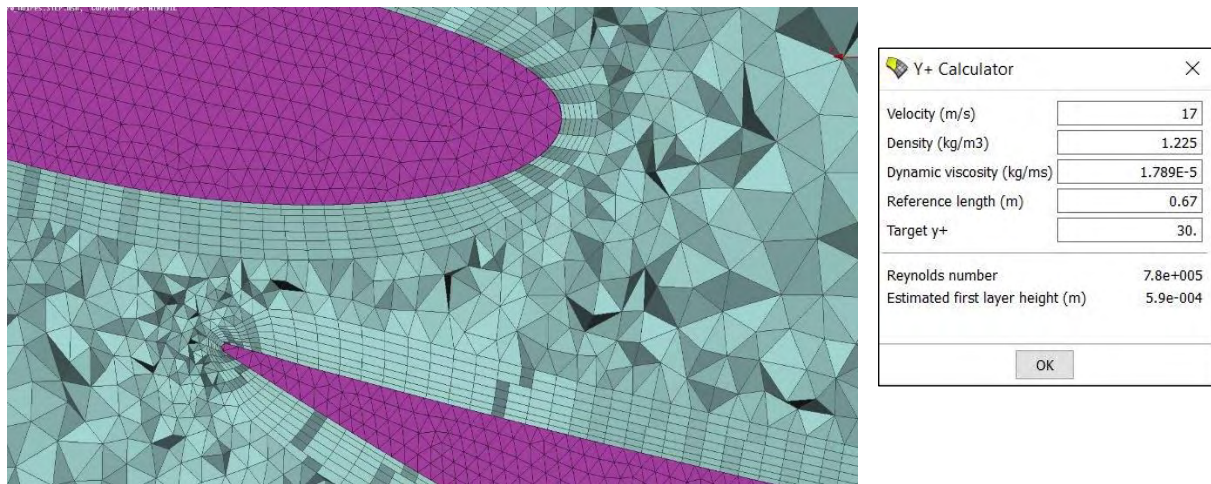
Figure 62: *Layers creation for NACA airfoils model*
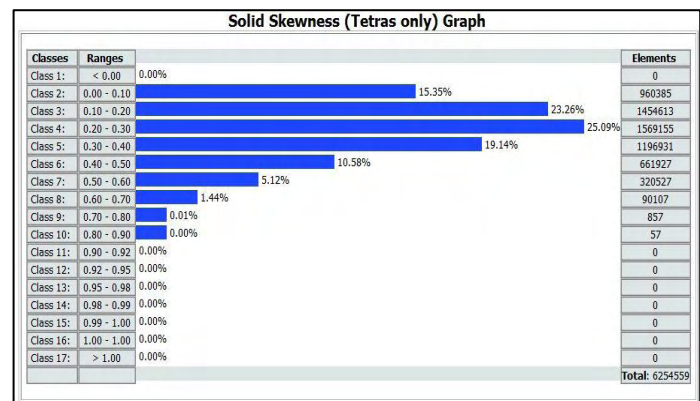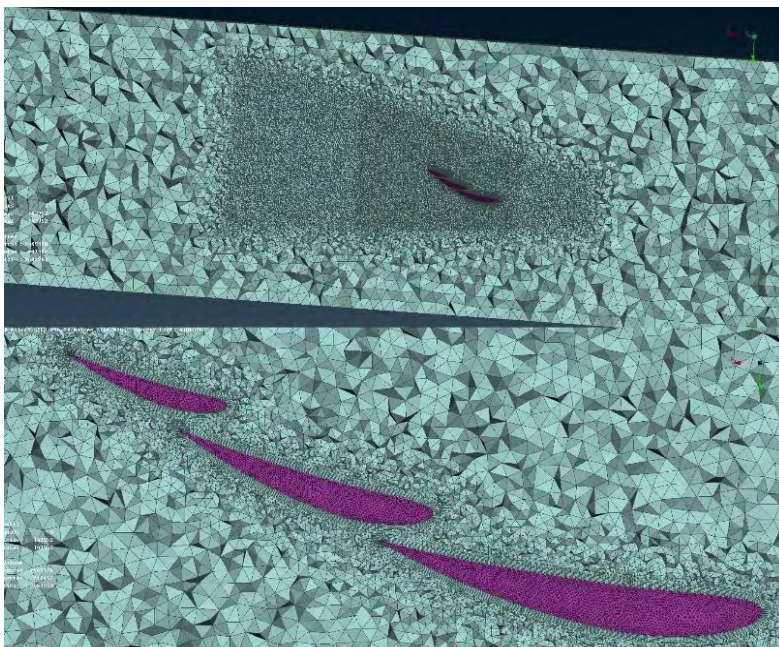
Figure 63: *Volume elements created for NACA Airfoils model*

3.1.4.3. Front Wing:

For the setup of the front wing's CFD model, again half of the wing's symmetric geometry is used while the Fluid Domain that is created and extended ten times the characteristic length ($6.5m$) to the rear, five times to the front ($3.25m$) and three times to the sides ($2m$) assuming that the characteristic length of the whole model is about 0.65m. For the surface mesh of the

Figure 64: *CAD model of the front wing*

model, ANSA CFD algorithm is used to create trias elements with a minimum target length of 50mm, a maximum target length of 150mm, a growth rate of 1.2, a distortion angle of 10° and a 30° angle limit for the sharp edges. Three rectangular size boxes are also used to refine mesh around the front wing's surface with a maximum length of 25mm, 15mm and 25mm each. Using these parameters and with respect to the quality criteria that were referred earlier the surface mesh has a total of 581,970 elements while all elements are compatible with skewness criterion.
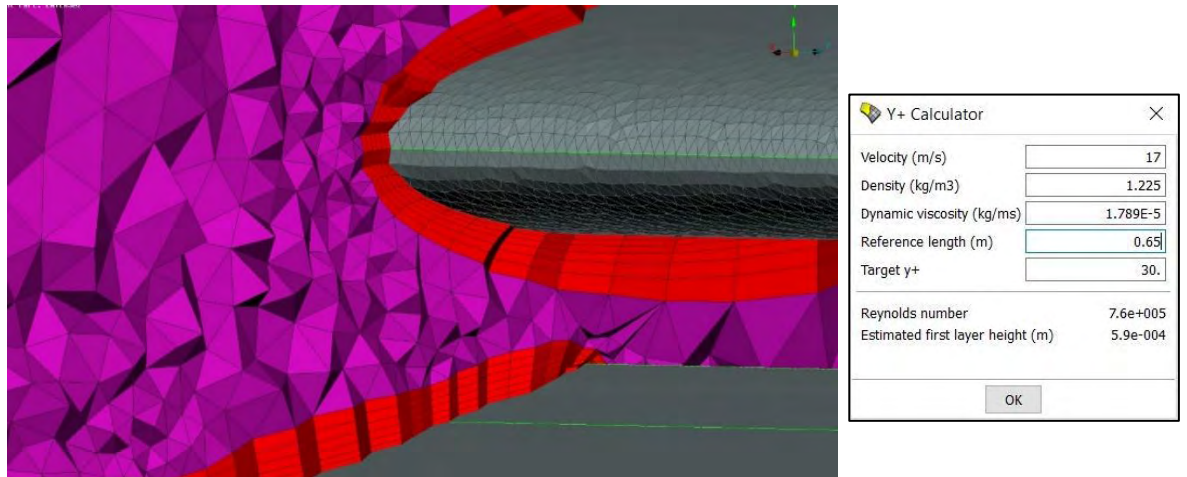

Figure 65: *Fluid Domain of front wing model*
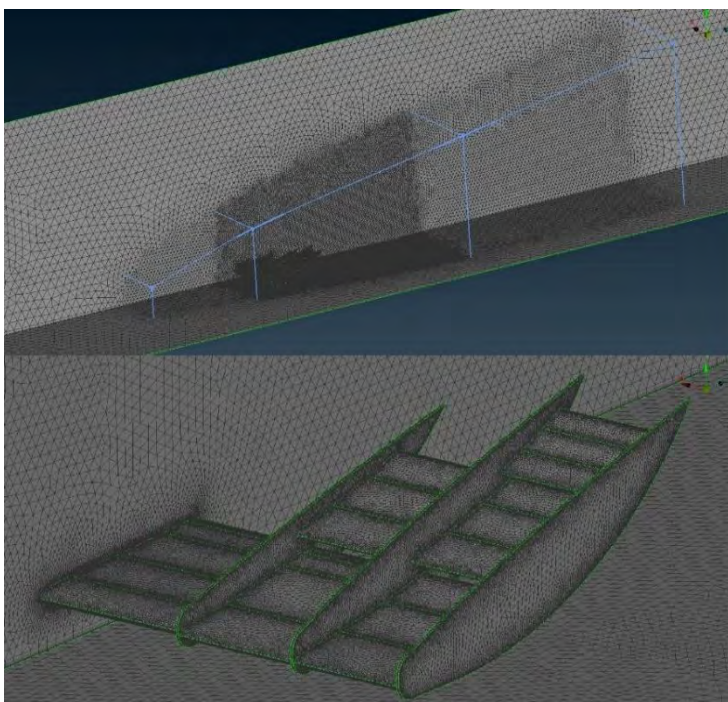
Figure 66: *Surface mesh used for the front wing model*

Shell Skewness Graph

Classes	Ranges		Elements
Class 1:	< 0.00	0.00%	0
Class 2:	0.00 - 0.10	95.78%	557423
Class 3:	0.10 - 0.20	3.43%	19983
Class 4:	0.20 - 0.30	0.57%	3313
Class 5:	0.30 - 0.40	0.10%	567
Class 6:	0.40 - 0.50	0.10%	557
Class 7:	0.50 - 0.60	0.01%	68
Class 8:	0.60 - 0.70	0.01%	34
Class 9:	0.70 - 0.80	0.00%	20
Class 10:	0.80 - 0.90	0.00%	5
Class 11:	0.90 - 0.92	0.00%	0
Class 12:	0.92 - 0.95	0.00%	0
Class 13:	0.95 - 0.98	0.00%	0
Class 14:	0.98 - 0.99	0.00%	0
Class 15:	0.99 - 1.00	0.00%	0
Class 16:	1.00 - 1.00	0.00%	0
Class 17:	> 1.00	0.00%	0
			Total: 581970

After the creation of the surface the mesh, layers are created. Using ANSA *Y+ Calculator* for a characteristic length of 0.65m and a velocity of 17m/s the estimated first layer height is about 5.9×10^{-4} m. So, a total number of six layers are created with the first four having an absolute height of 0.59mm and the next three a growth factor of 1.2. Finally, for the volume mesh tetras elements are created using ANSA *Tetra Rapid* algorithm with a growth rate of 1.2, while the maximum length for volume elements inside the three size boxes of is 35mm, 20mm and 35mm respectively resulting in a model with 7,947,126 volume elements.

Figure 68: *Layers created for front wing model*
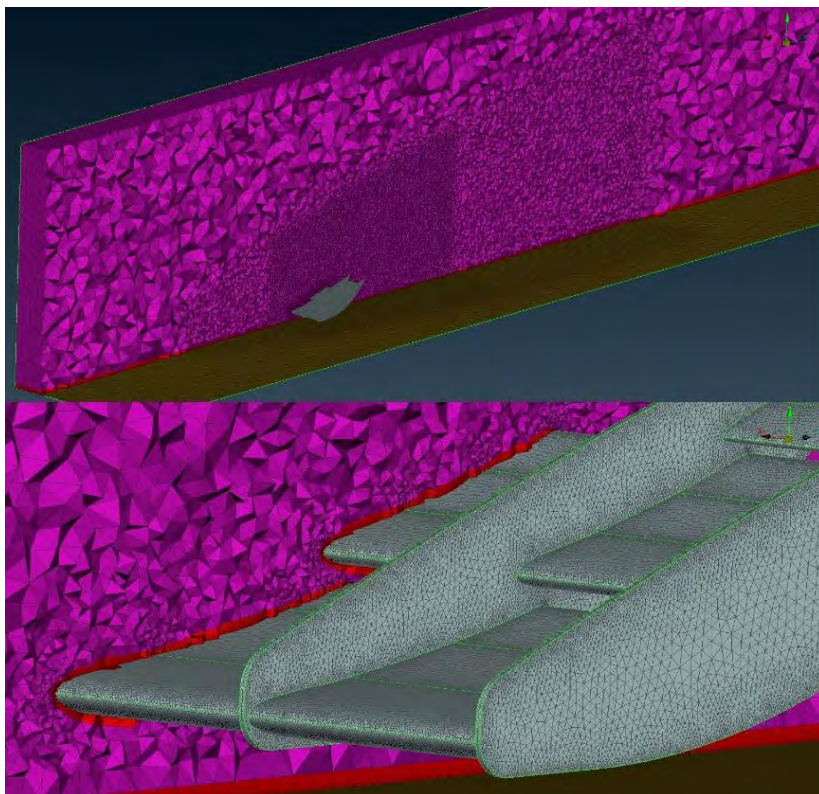
Figure 67: *Volume mesh element of the front wing model*
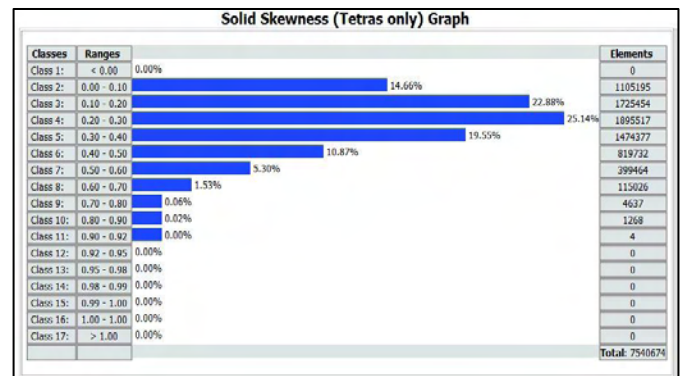
3.1.4.4. Rear Wing:

For the setup of the rear wing's CFD model, a Fluid Domain is created and extended ten times the characteristic length (8m) to the rear, five times to the front (4m) and three times to the sides (*2.5m*) assuming that the characteristic length of the whole model is about 0.8m. For the surface mesh of the model, ANSA CFD algorithm is used to create trias elements with a minimum target length of 50mm, a maximum target length of 150mm, a growth rate of 1.2, a distortion

Figure 69: *CAD model of the Rear wing*

angle of 10° and a 30° angle limit for the sharp edges. Three rectangular size boxes are also used to refine mesh around the rear wing's surface with a maximum length of 25mm, 15mm and 25mm each. Using these parameters and with respect to the quality criteria that were referred earlier the surface mesh has a total of 188,954 elements while all elements are compatible with skewness criterion.
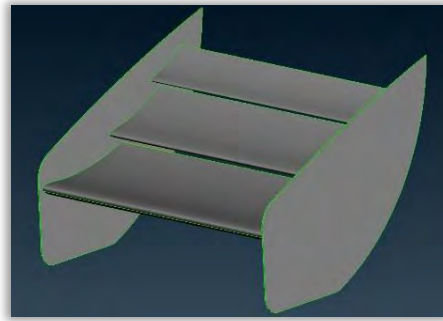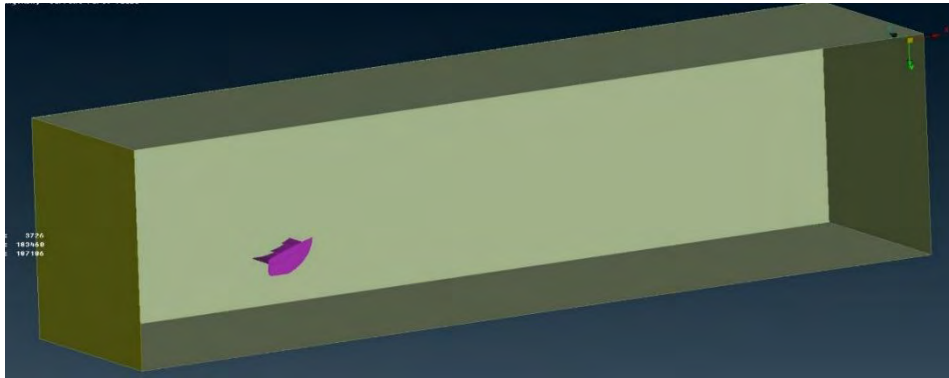
Figure 71: *Fluid Domain created for Rear wing model*
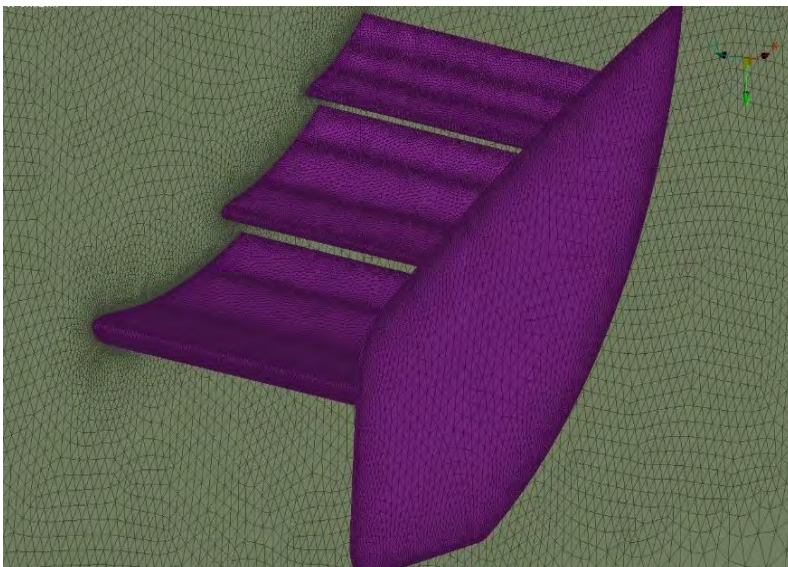
Figure 70: *Surface mesh created on the Rear wing's surface*

Shell Skewness Graph

Classes	Ranges		Elements
Class 1:	< 0.00	0.00%	0
Class 2:	0.00 - 0.10	99.06%	187174
Class 3:	0.10 - 0.20	0.92%	1741
Class 4:	0.20 - 0.30	0.02%	37
Class 5:	0.30 - 0.40	0.00%	2
Class 6:	0.40 - 0.50	0.00%	0
Class 7:	0.50 - 0.60	0.00%	0
Class 8:	0.60 - 0.70	0.00%	0
Class 9:	0.70 - 0.80	0.00%	0
Class 10:	0.80 - 0.90	0.00%	0
Class 11:	0.90 - 0.92	0.00%	0
Class 12:	0.92 - 0.95	0.00%	0
Class 13:	0.95 - 0.98	0.00%	0
Class 14:	0.98 - 0.99	0.00%	0
Class 15:	0.99 - 1.00	0.00%	0
Class 16:	1.00 - 1.00	0.00%	0
Class 17:	> 1.00	0.00%	0
			Total: 188954

After the creation of the surface the mesh, layers are created. Using ANSA *Y+ Calculator* for a characteristic length of 0.8m and a velocity of 17m/s the estimated first layer height is about 6×10^{-4} m. So, a total number of six layers are created with the first four having an absolute height of 0.6mm and the next three a growth factor of 1.2. Finally, for the volume mesh tetras elements are created using ANSA *Tetra Rapid* algorithm with a growth rate of 1.2, while the maximum length for volume elements inside the three size boxes of is 35mm, 20mm and 35mm respectively resulting in a model with 10,347,973 volume elements.
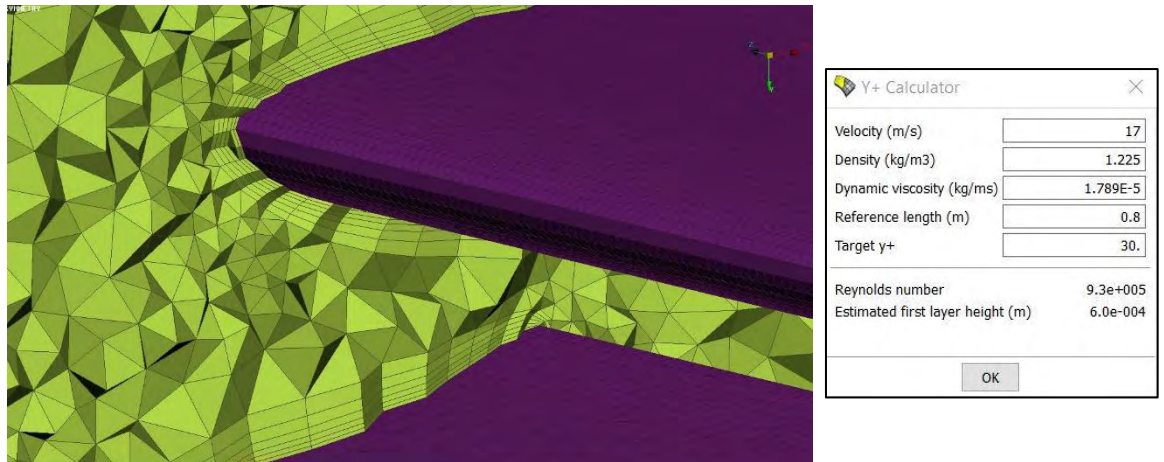
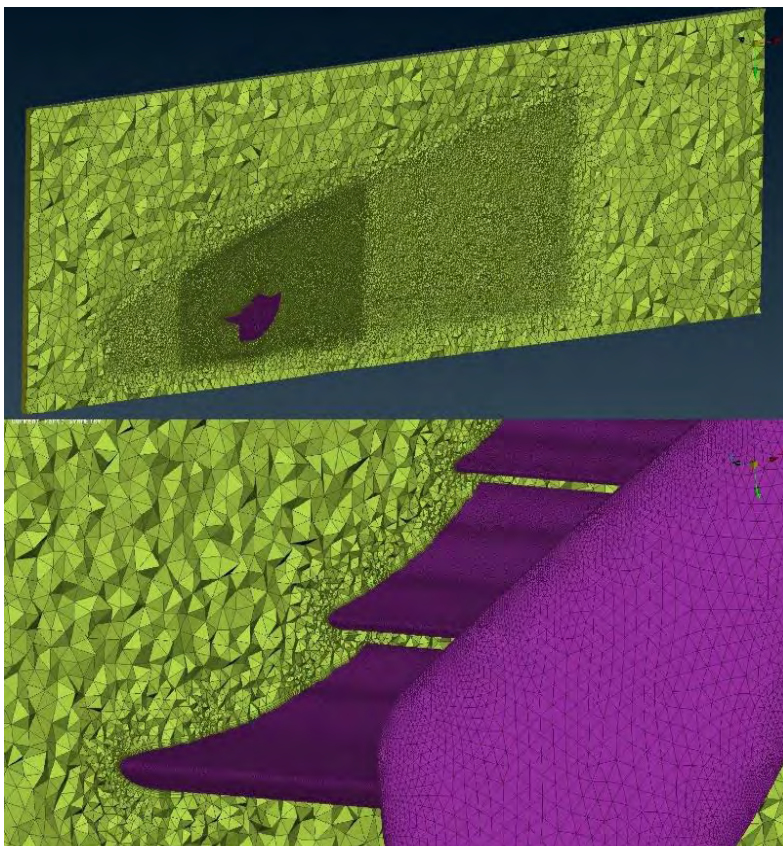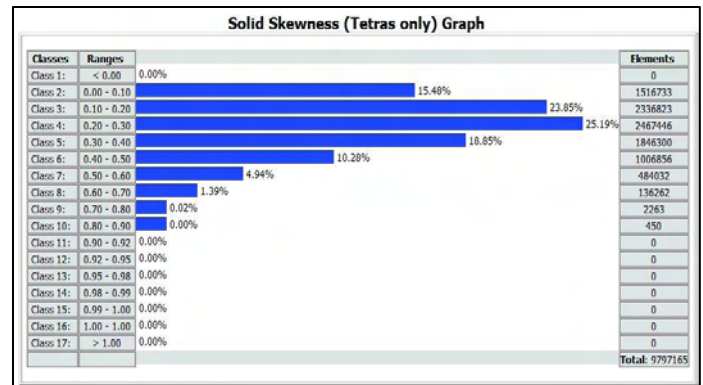**Figure 73:** *Layers of the Rear wing model*

Figure 72: *Volume mesh created for the Rear wing model*

3.1.4.5. Undertray & Sidepods:

The flow that reaches the sidepods and the undertray beneath the vehicle is totally different than a freestream flow, because it is disturbed from the body and the wheels of the car in front. So, in order to simulate these devices accurately it is necessary to build first a whole car model and test the different aerodynamic devices that are mounted on it. For the setup of the

Figure 74: *CAD of the model for Sidepods & Undertray*

CFD models for both devices, a Fluid Domain is created and extended ten times the characteristic length (27m) to the rear, five times to the front (14m) and three times to the sides (8m) assuming that the characteristic length of the whole model is about 2.7m. For the surface mesh of the model, ANSA CFD algorithm is used to create trias elements with a minimum target length of 50mm, a maximum target length of 250mm, a growth rate of 1.2, a distortion angle of 10° and a 30° angle limit for the sharp edges. Three rectangular size boxes are used to refine mesh around the car's surface with a maximum length of 50mm, 30mm and 40mm each. For these models an extra of four smaller size boxes are used to refine mesh around the sidepods and undertray to better estimate stall and drag for these devices. These four size boxes have a maximum length of 20mm and 15mm each. Using these parameters and with respect to the quality criteria that were referred earlier the surface mesh has a total of 626,484 elements while all elements are compatible with skewness criterion.
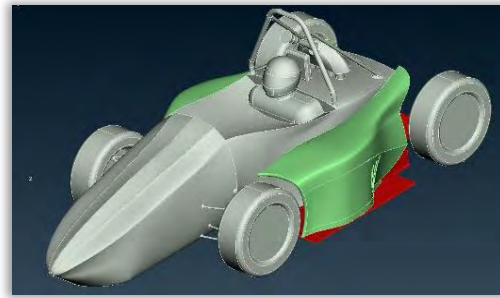

Figure 76: *Fluid Domain of the CFD model for Sidepods & Undertray*

Shell Skewness Graph

Classes	Ranges		Elements
Class 1:	< 0.00	0.00%	0
Class 2:	0.00 - 0.10	96.57%	605003
Class 3:	0.10 - 0.20	2.57%	16130
Class 4:	0.20 - 0.30	0.43%	2701
Class 5:	0.30 - 0.40	0.15%	921
Class 6:	0.40 - 0.50	0.14%	851
Class 7:	0.50 - 0.60	0.05%	326
Class 8:	0.60 - 0.70	0.04%	267
Class 9:	0.70 - 0.80	0.04%	233
Class 10:	0.80 - 0.90	0.01%	52
Class 11:	0.90 - 0.92	0.00%	0
Class 12:	0.92 - 0.95	0.00%	0
Class 13:	0.95 - 0.98	0.00%	0
Class 14:	0.98 - 0.99	0.00%	0
Class 15:	0.99 - 1.00	0.00%	0
Class 16:	1.00 - 1.00	0.00%	0
Class 17:	> 1.00	0.00%	0
			Total: 626484

Figure 75: *Surface mesh and size boxes used for the Sidepods & Undertray models*

After the creation of the surface the mesh, layers are next to be created. Using ANSA *Y+ Calculator* for a characteristic length of 2.7m and a velocity of 17m/s the estimated first layer height is about 6.7×10^{-4} m. So, a total number of six layers are created with the first four having an absolute height of 0.67mm and the next three a growth factor of 1.2. Finally, for the volume mesh tetras elements are created using ANSA *Tetra Rapid* algorithm with a growth rate of 1.2, while the maximum length for volume elements inside the size boxes is 50mm, 30mm, 40mm and 20mm respectively resulting in a model with 8,291,113 volume elements.
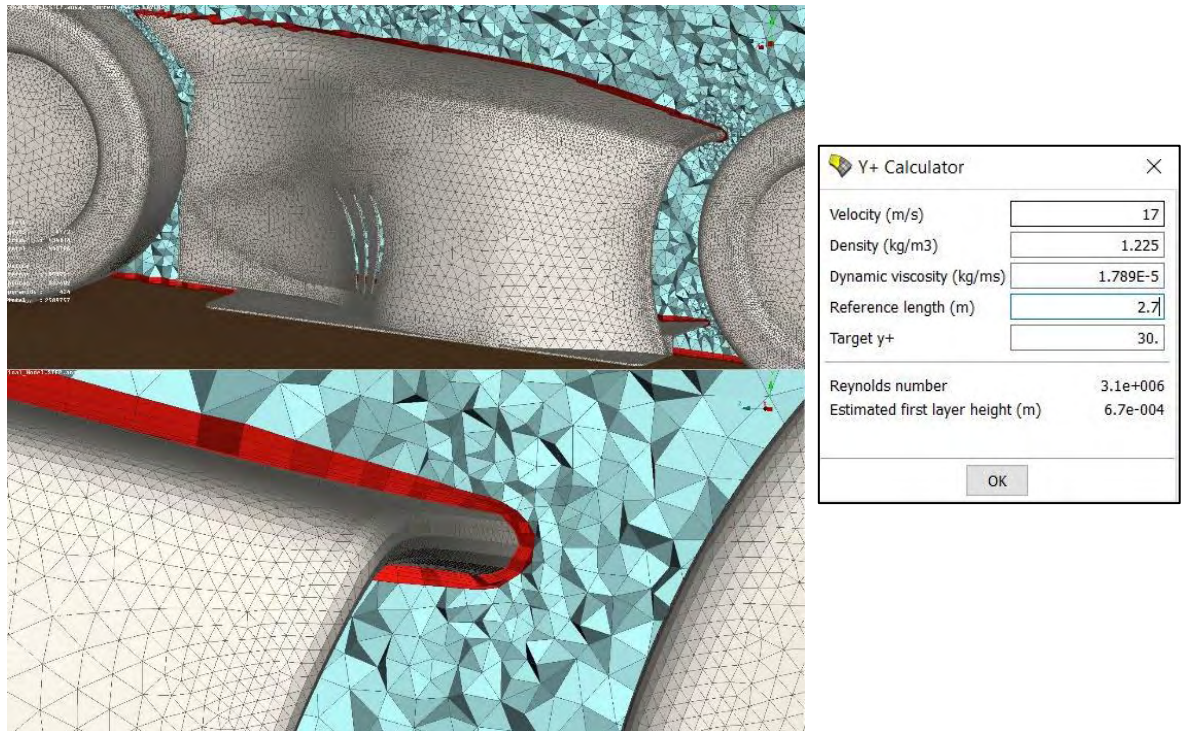

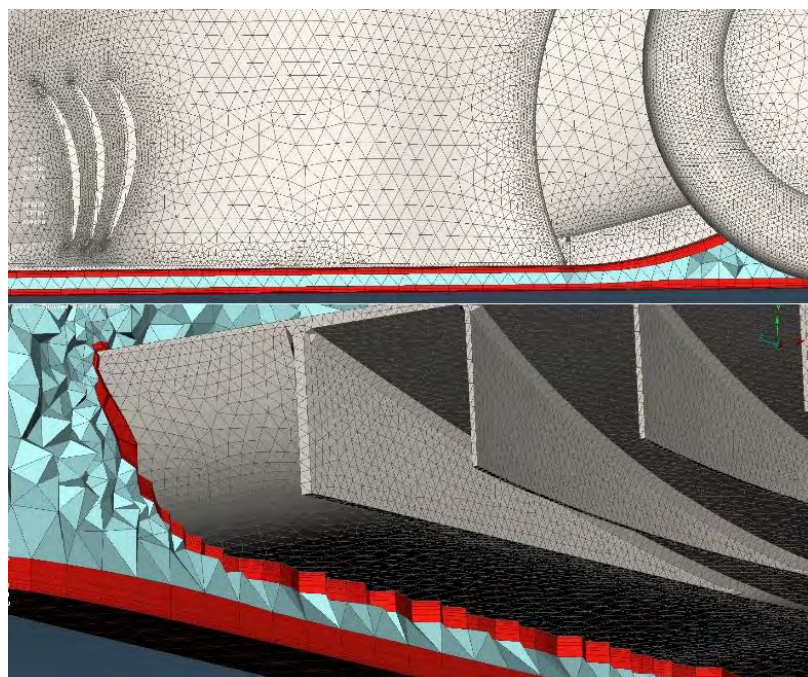**Figure 77:** *Layers used to predict stall on the Sidepods' surface*

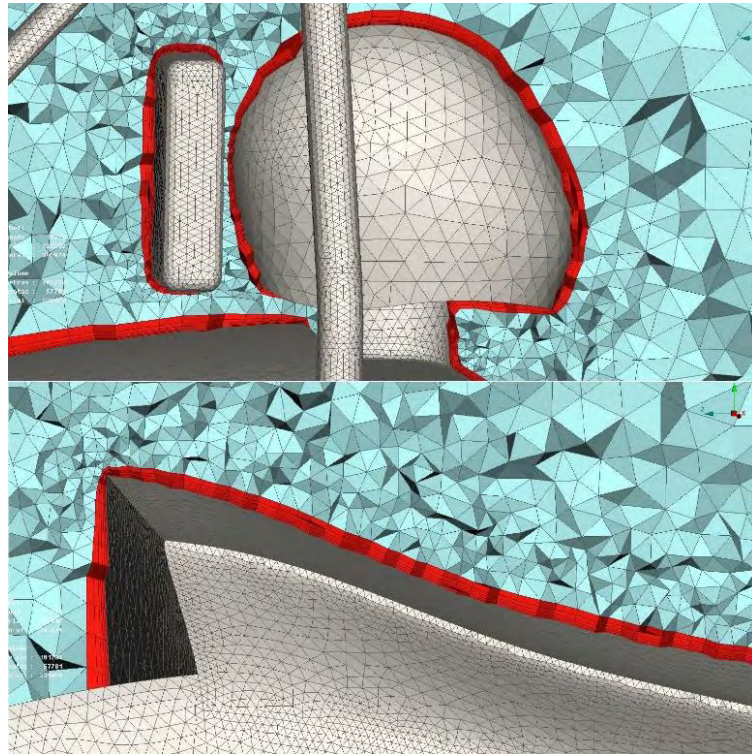**Figure 78:** *Layers created for the Undertray model to calculate stall accurately*

Figure 79: *Layers created both for Sidepods & Undertray car models*
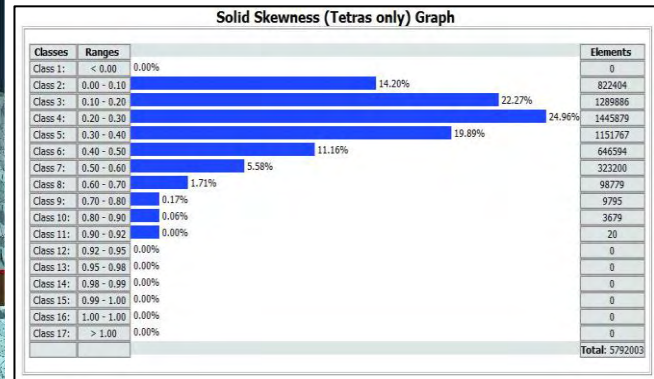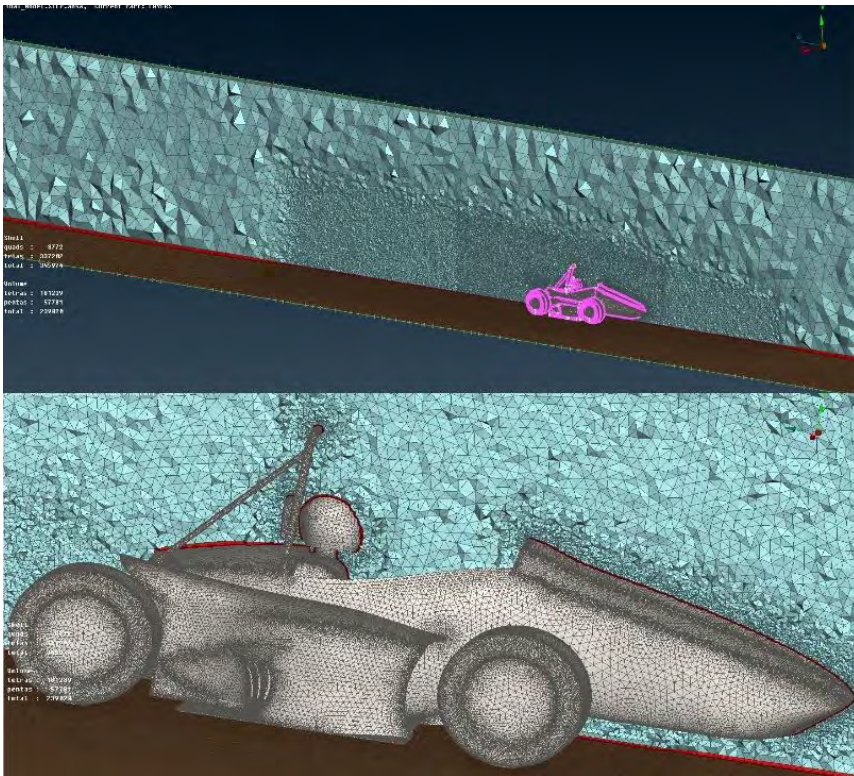

Figure 80: *Volume mesh elements created for the Sidepods & Undertray models*

3.1.4.6. Full Aerodynamic Package:

The final model to be tested is the car with all the aerodynamic devices mounted on it. This model is similar to that of the Sidepods & Undertray with only difference the front and rear wing that are also imported in the model, so many mesh parameters are in common. For the setup of the CFD model the Fluid Domain that is created, is extended ten times the characteristic length (31m) to the rear, five times to the front (16m) and three times to

Figure 81: *CAD model of the car with full aerodynamic package*

the sides (9m) assuming that the characteristic length of the whole model is about 3.1m. For the surface mesh of the model, ANSA CFD algorithm is used to create trias elements with a minimum target length of 50mm, a maximum target length of 250mm, a growth rate of 1.2, a distortion angle of 10° and a 30° angle limit for the sharp edges. Three rectangular size boxes are used to refine mesh around the car's surface with a maximum length of 50mm, 30mm and 40mm each. For the final model two extra size boxes are used to refine mesh around the front and rear wing to better estimate stall and drag for these devices. These two size boxes have a maximum length of 20mm and 15mm each. Using these parameters and with respect to the quality criteria that were referred earlier the surface mesh has a total of 543,181 elements while all elements are compatible with skewness criterion.

Figure 82: *Fluid Domain of the final CFD model*

Figure 83: *Surface mesh created for the final model*

After the creation of the surface the mesh, layers are next to be created. Using ANSA *Y+ Calculator* for a characteristic length of 3.1m and a velocity of 17m/s the estimated first layer height is about 6.9×10^{-4} m. So, a total number of six layers are created with the first four having an absolute height of 0.69mm and the next three a growth factor of 1.2. Finally, for the volume mesh tetras elements are created using ANSA *Tetra Rapid* algorithm with a growth rate of 1.2, while the maximum length for volume elements inside the size boxes is 50mm, 30mm, 40mm and 20mm respectively resulting in a model with 12,722,658 volume elements.
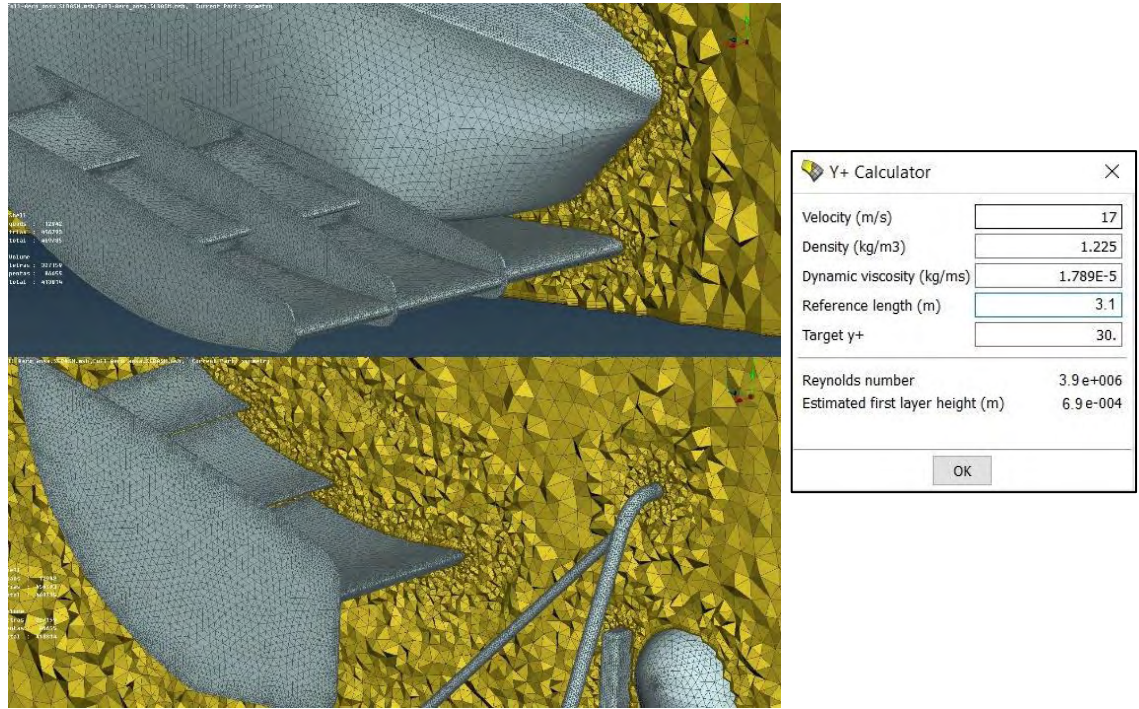

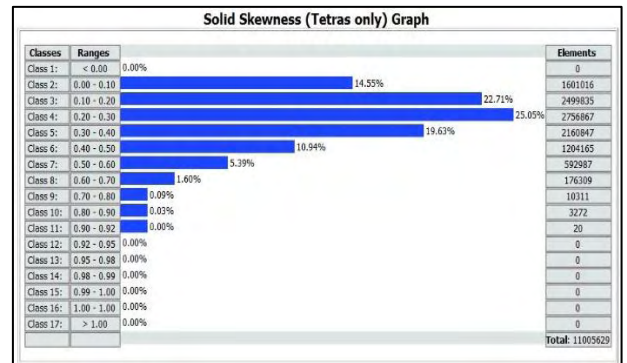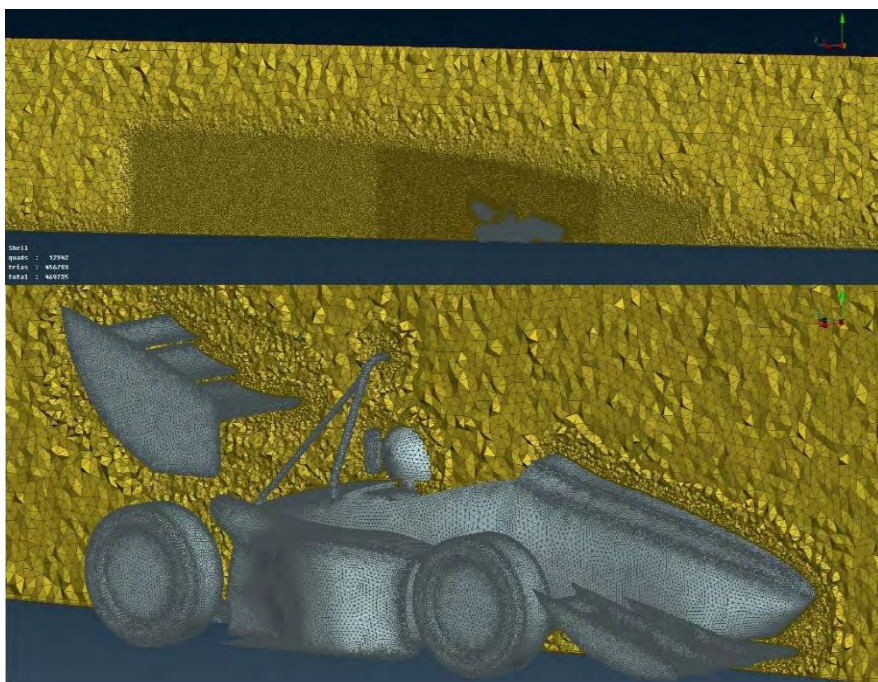**Figure 85:** *Layers created on front & rear wing of the final model*

Figure 84: *Volume mesh elements created for the final CFD model*

56

3.2. Solving Process

After the *pre*-Processing is completed and all the models are successfully meshed the CFD cases are ready to be solved, using ANSYS-*Fluent.* At this section are defined the numerical methods and the parameters of the CFD solver like the solving algorithms, the turbulence models, the boundary conditions, the convergence criteria, the monitors of interest, the number of iterations and anything else needed to properly solve each case. The governing equations for the time dependent three-dimensional fluid flow and heat transfer around a body are the continuity equation, momentum equations and energy equation. The general approach in road vehicle external aerodynamics is to assume incompressible and isothermal flow, as Ma < 0.3, which is in the vicinity of 100m/s at sea-level and it is unlikely that the flow will reach this velocity anywhere in the domain. Thus, the energy equation can be neglected and the momentum- and continuity equations can be written on incompressible form, neglecting the density terms. The same solver settings are used for all the models, so they are going to be described only once for all the cases. On the diagram bellow are shown the steps of the solving process as they are followed for all models, until the final results reach the desired accuracy.
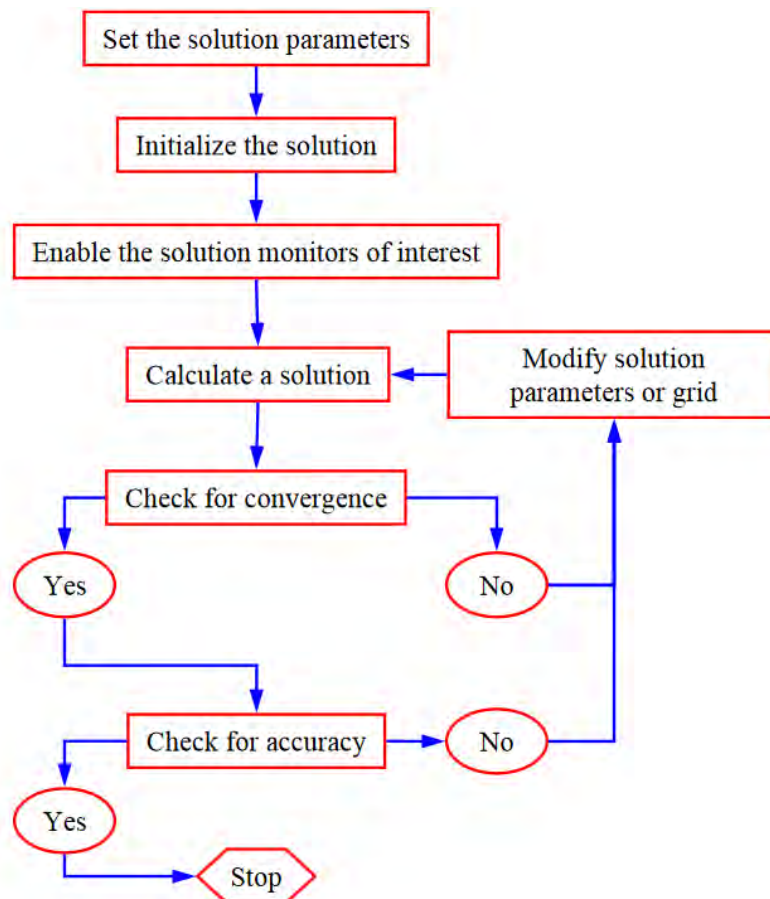

Figure 86: *Solving Process Steps*

3.2.1. General Settings

The first step when starting the solver is to define if the solving process is going to be *Serial* or *Parallel*. *Parallel* solving with *4 Processes* is used, while *Double Precision* is avoided for all the cases in order to reduce the CPU time needed. Note that the *Dimension* setting is already filled in *3D* and cannot be changed, since ANSYS Fluent automatically sets it based on the mesh or geometry for the current system.

Figure 87: *ANSYS-Fluent Launcher card settings*

After launching Fluent the *General* card is selected first in the navigation pane to perform the mesh-related activities and to choose a solver. All mesh parameters in ANSA are defined at mm, so when mesh files are imported from ANSA to ANSYS it necessary first to use a scale factor to convert the mesh length from mm to m, which is the units that ANSYS-Fluent operates.
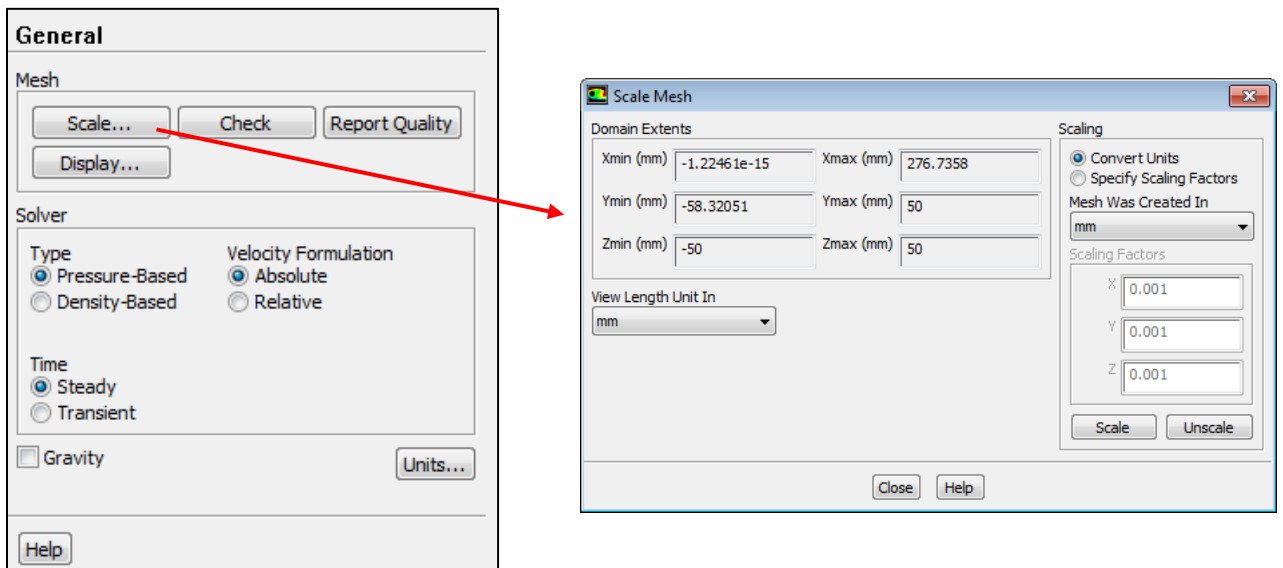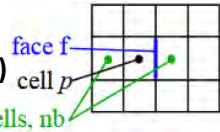

Figure 88: *General Settings card*

Fluent solvers are based on the finite volume method where the Fluid Domain is discretized into a finite set of control volumes or cells. The general transport equation (*3.1*) for mass, momentum, energy, etc. is applied to each cell and discretized and all equations are solved in or der to render the flow field.

$$\frac{\partial}{\partial t}\int_{V}\rho\phi\,dV + \oint\rho\phi\mathbf{V}\cdot d\mathbf{A} = \oint_{A}\Gamma\nabla\phi\cdot d\mathbf{A} + \int_{V}S_{\phi}\,dV \qquad \textbf{(3.1)}$$

$$\underbrace{\qquad}_{\text{Unsteady}} \quad \underbrace{\qquad}_{\text{Convection}} \quad \underbrace{\qquad}_{\text{Diffusion}} \quad \underbrace{\qquad}_{\text{Generation}}$$

Each transport equation is discretized into algebraic form (*3.2*). For a cell, P:

$$\frac{\left(\rho\phi_{p}\right)^{t+\Delta t}-\left(\rho\phi_{p}\right)^{t}}{\Delta t}\Delta V + \sum_{\text{faces}}\rho_{f}\,\phi_{f}\,V_{f}\,A_{f} = \sum_{\text{faces}}\Gamma_{f}\left(\nabla\phi\right)_{\perp,f}A_{f} + S_{\phi}\,\Delta V \qquad \textbf{(3.2)}$$

Discretized equations require information at both cell centers and faces. Field data (*material properties, velocities, etc.*) are stored at cell centers. Face values are interpolated in terms of local and adjacent cell values while the discretization accuracy depends on the "*stencil*" size. The discretized scalar transport equation contains the unknown scalar variable at the cell center as well as the unknown values in surrounding neighbor cells. This equation will, in general, be nonlinear with respect to these variables. The discretized equation (*3.3*) can be expressed simply as:

$$a_{P}\phi = \sum_{nb}a_{nb}\phi_{nb} + b \qquad \textbf{(3.3)}$$

where the subscript *nb* refers to neighbor cells, and α_p and α_{nb} are the linearized coefficients for φ and φ_{nb}. The above equation is written for every control volume in the domain resulting in equation sets which are solved iteratively. Coefficients α_p and α_{nb} are typically functions of solution variables (*nonlinear and coupled*), they are written to use values of solution variables from the previous iteration and they are updated with each outer iteration.

The *Pressure-Based* solver is selected by default on the Solver Type field and is used for all models. In this case, the coefficients α_p and α_{nb} are scalar values. This type of solver employs an algorithm which belongs to a general class of methods called the projection method. In the projection method, wherein the constraint of mass conservation (*continuity*) of the velocity field is achieved by solving a pressure (*or pressure correction*) equation. The pressure equation is derived from the continuity and the momentum equations in such a way that the velocity field, corrected by the pressure, satisfies the continuity. Since the governing equations are nonlinear and coupled to one another, the solution process involves iterations wherein the entire set of governing equations is solved repeatedly until the solution converges. The *Pressure-Based* solver takes momentum and pressure as the primary variables while pressure-velocity coupling algorithms are derived by reformatting the continuity equation. The *Pressure-Based* solver is applicable for a wide range of flow regimes from low speed incompressible flow to high-speed compressible flow and usually requires less memory (*storage*). It allows also flexibility in the solution procedure while the *Pressure-Based* coupled solver (*PBCS*) that is used, is applicable for most single-phase flows. Finally, all CFD simulations are done as *Steady* cases, at one moment without any timestep being used on the Time field.

3.2.2. Viscus Models

Since the airflow around a FSAE race car is turbulent, a model needs to be selected for simulation of the turbulent flow. There appears to be four major turbulence models that are used in the automotive industries: *k-ε, k-ω, Lattice-Boltzmann* and *Large Eddy Simulation (LES)*. Of these models the k-ε and k-ω are most widely used with the k-ε said to be the most stable. The fidelity of CFD predictions for turbulent flow is highly dependent upon the quality of the turbulence modeling. This is even more important for the flow around ground vehicles, whose salient flow features include three-dimensional boundary layers with strong streamline curvature, separation and strong vortices. These features require turbulence models that can properly account for *Non-Equilibrium* effects and anisotropy.

On the viscus model card that appears k-epsilon model is selected, which specifies turbulent flow to be calculated using one of three *k-epsilon* models bellow. For all the cases, *Realizable k-epsilon* model is used. Industrial applications of this model show that it is possible to achieve good results in terms of integral values (e.g., drag coefficient), which are within *2-5%*. Due to its implementation, it is very stable and fast converging. Therefore, it is perfectly suited for automated calculation processes, allowing a huge number of calculations in a relatively small time frame. The *Realizable k-ε* model is a relatively recent development and differs from the standard *k-ε* model in two important ways. The realizable *k-ε* model contains a new formulation for the turbulent viscosity and a new transport equation for the dissipation rate, *ε* has been derived from an exact equation for the transport of the mean-square vorticity fluctuation. The term "*Realizable*'' means that the model satisfies certain mathematical constraints on the Reynolds stresses, consistent with the physics of turbulent flows. Neither the standard *k-ε* model nor the RNG *k-ε* model is realizable.

Figure 89: *Viscous Models setting card*

An immediate benefit of the realizable *k-ε* model is that it more accurately predicts the spreading rate of both planar and round jets. It is also likely to provide superior performance for flows involving rotation, boundary layers under strong adverse pressure

gradients, separation, and recirculation. Both the *Realizable* and *RNG k-ε* models have shown substantial improvements over the standard *k-ε* model where the flow features include strong streamline curvature, vortices, and rotation. Since the model is still relatively new, it is not clear in exactly which instances the *Realizable k-ε* model consistently outperforms the *RNG* model. However, initial studies have shown that the realizable model provides the best performance of all the *k-ε* model versions for several validations of separated flows and flows with complex secondary flow features. One of the weaknesses of the *Standard k-ε* model or other traditional *k-ε* models lies with the modeled equation for the dissipation rate (ε) limitation of the *Realizable k-ε* model is that it produces non-physical turbulent viscosities in situations when the computational domain contains both rotating and stationary fluid zone. This is due to the fact that the *Realizable k-ε* model includes the effects of mean rotation in the definition of the turbulent viscosity. This extra rotation effect has been tested on single rotating reference frame systems and showed superior behavior over the S*tandard k-ε* model. However, due to the nature of this modification, its application to multiple reference frame systems should be taken with some caution.

To understand the mathematics behind the *Realizable k-epsilon* model, consider combining the *Boussinesq* relationship *(3.4)* and the *Eddy Viscosity (µt)* definition *(3.5)* to obtain the following expression (3.6) for the normal *Reynolds Stress* in an incompressible strained mean flow:

$$-\rho \overline{u_i' u_j'} = \mu_t \left(\frac{\partial u_i}{\partial x_j} + \frac{\partial u_j}{\partial x_i} \right) - \frac{2}{3} \left(\rho k + \mu_t \frac{\partial u_k}{\partial x_k} \right) \delta_{ij} \qquad \textbf{(3.4)}$$

$$\mu_t = \rho C_\mu \frac{k^2}{\varepsilon} \qquad \textbf{(3.5)}$$

$$\overline{u^2} = \frac{2}{3} k - 2 v_t \frac{\partial U}{\partial x} \qquad \textbf{(3.6)}$$

Using *3.5* equation for $v_t = \frac{\mu_t}{\rho}$, one obtains the result that the normal stress $\overline{u^2}$, which by definition is a positive quantity, becomes negative, that is, "*non-Realizable*", when the strain is large enough to satisfy *3.7* equation.

$$\frac{k}{\varepsilon} \frac{\partial U}{\partial x} > \frac{1}{3 C_\mu} \approx 3.7 \qquad \textbf{(3.7)}$$

The modeled transport equations for *k* and *ε* in the realizable *k-ε* model are:

$$\frac{\partial}{\partial t}(\rho k) + \frac{\partial}{\partial x_j}(\rho k u_j) = \frac{\partial}{\partial x_j}\left[\left(\mu + \frac{\mu_t}{\sigma_k} \right) \frac{\partial k}{\partial x_j} \right] + G_k + G_b - \rho \varepsilon - Y_M + S_k \qquad \textbf{(3.8)}$$

$$\frac{\partial}{\partial t}(\rho \varepsilon) + \frac{\partial}{\partial x_j}(\rho \varepsilon u_j) = \frac{\partial}{\partial x_j}\left[\left(\mu + \frac{\mu_t}{\sigma_\varepsilon} \right) \frac{\partial \varepsilon}{\partial x_j} \right] + \rho C_1 S \varepsilon - \rho C_2 \frac{\varepsilon^2}{k + \sqrt{v \varepsilon}} + C_{1\varepsilon} \frac{\varepsilon}{k} C_{3\varepsilon} G_b + S_\varepsilon \qquad \textbf{(3.9)}$$

Where:

$$C_1 = \max\left[0.43, \frac{\eta}{\eta+5}\right], \ \eta = S\frac{k}{\varepsilon}, \ S = \sqrt{2S_{ij}S_{ij}} \qquad \text{(3.10)}$$

The model constants C_2, σ_k and σ_ε have been established to ensure that the model performs well for certain canonical flows. The model constants are:

$$C_{1\varepsilon} = 1.44, \ C_2 = 1.9, \ \sigma_k = 1.0, \ \sigma_\varepsilon = 1.2 \qquad \text{(3.11)}$$

The next field to be filled is the *Near-Wall Treatment,* which specifies the near-wall treatment to be used for modeling turbulence. *Non-Equilibrium Wall Functions* is used for all the CFD cases. The key elements in the *Non-Equilibrium Wall Functions* are the Launder and Spalding's log-law for mean velocity is sensitized to pressure-gradient effects and the two-layer-based concept which is adopted to compute the budget of turbulence kinetic energy $(\overline{G_k}, \overline{\varepsilon})$ in the wall-neighboring cells. The log-law for mean velocity sensitized to the pressure gradients is:

$$\frac{\tilde{U}C_\mu^{1/4}k^{1/2}}{\tau_w / \rho} = \frac{1}{\kappa}\ln\left(E\frac{\rho C_\mu^{1/4}k^{1/2}y}{\mu}\right) \qquad \text{(3.12)}$$

$$\tilde{U} = U - \frac{1}{2}\frac{dp}{dx}\left[\frac{y_v}{\rho\kappa\sqrt{k}}\ln\left(\frac{y}{y_v}\right) + \frac{y-y_v}{\rho\kappa\sqrt{k}} + \frac{y_v^2}{\mu}\right] \qquad \text{(3.13)}$$

The non-equilibrium wall function employs the two-layer concept in computing the budget of turbulence kinetic energy at the wall-adjacent cells, which is needed to solve the k equation at the wall-neighboring cells. The wall-neighboring cells are assumed to consist of a viscous sublayer and a fully turbulent layer. The following profile assumptions for turbulence quantities are made:

$$\tau_t = \begin{cases} 0, & y < y_v \\ \tau_w, & y > y_v \end{cases} \quad k = \begin{cases} \left(\frac{y}{y_v}\right)^2 k_P, & y < y_v \\ k_P, & y > y_v \end{cases} \quad \varepsilon = \begin{cases} \frac{2vk}{y^2}, & y < y_v \\ \frac{k^{3/2}}{C_l^* y}, & y > y_v \end{cases} \qquad \text{(3.14)}$$

Using these profiles, the cell-averaged production of k, $\overline{G_k}$, and the cell-averaged dissipation rate $\bar{\varepsilon}$, can be computed from the volume average of and of the wall-adjacent cells. For quadrilateral and hexahedral cells for which the volume average can be approximated with a depth-average:

$$\overline{G_k} \equiv \frac{1}{y_n}\int_0^{y_n} \tau_t \frac{\partial U}{\partial y}\,dy = \frac{1}{\kappa y_n}\frac{\tau_w^2}{\rho C_\mu^{1/4}k_P^{1/2}}\ln\left(\frac{y_n}{y_v}\right) \qquad \text{(3.15)}$$

and

$$\bar{\varepsilon} \equiv \frac{1}{y_n}\int_0^{y_n} \varepsilon\,dy = \frac{1}{y_n}\left[\frac{2v}{y_v} + \frac{k_P^{1/2}}{C_l^*}\ln\left(\frac{y_n}{y_v}\right)\right]k_P \qquad \text{(3.16)}$$

3.2.3. Boundary Conditions

Boundary conditions specify the flow and thermal variables on the boundaries of τηε physical model. They are, therefore, a critical component of the CFD simulations and it is important that they are specified appropriately. The specification of boundary conditions should be geared as close as possible to the measurement conditions that would have been done during a real wind tunnel test. In the majority of cases, flow velocity and turbulent intensity of the wind tunnel are known.
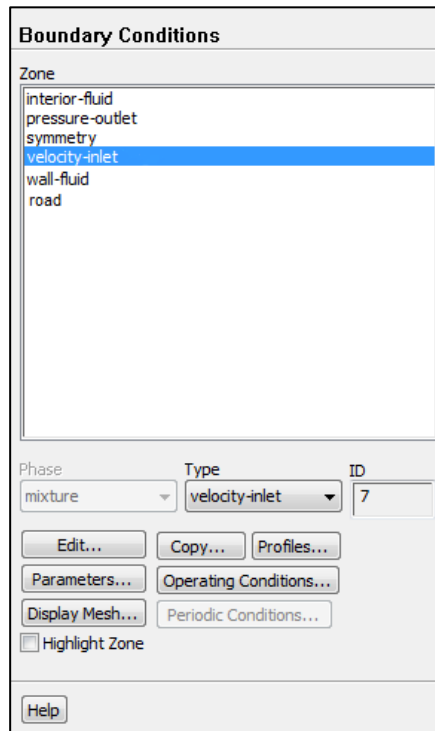
Figure 90: *Boundary Conditions settings card*

At the wind tunnel inlet, velocity inlet boundary conditions are used to define the free stream flow velocity in the computational wind tunnel. Therefore, a velocity inlet boundary condition is used to model the incoming flow. Velocity inlet boundary conditions are used to define the flow velocity, along with all relevant scalar properties of the flow, at flow inlets. The total (*or stagnation*) properties of the flow are not fixed, so they will rise to whatever value is necessary to provide the prescribed velocity distribution. This boundary condition is intended for incompressible flows, and its use in compressible flows will lead to a nonphysical result because it allows stagnation conditions to float to any level. The velocity inlet too close to a solid obstruction, since this could cause the inflow stagnation properties to become highly non-uniform. The velocity inlet boundary condition defines flow entering the physical domain of the model, *Fluent* uses both the velocity components and the scalar quantities that are defined as boundary conditions to compute the inlet mass flow rate, momentum fluxes, and fluxes of energy and chemical species. The mass flow rate entering a fluid cell adjacent to a velocity inlet boundary is computed as:

$$\dot{m} = \int \rho \vec{v} \cdot d\vec{A}$$

For all the CFD cases the *Components* velocity specification method is used and the inlet velocity is depending on the speed that each model of interest has to be tested with the CFD simulation. The inlet velocity values vary from 11m/s to 34m/s which is the final speed of the car. Usually the *Turbulence Intensity* ranges from 1-5% while for external flow problems the *Turbulent Viscosity Ratio* is between 1 - 10.
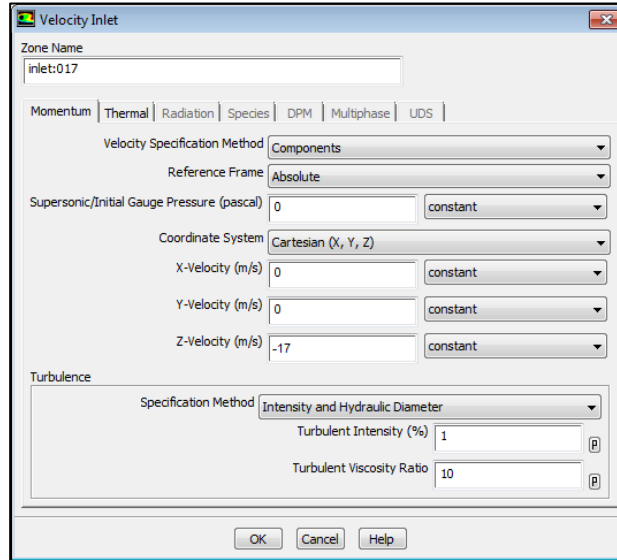

Figure 91: *Definition of Velocity Inlet boundary condition*

Pressure outlet boundary conditions are used to specify the static pressure at the computational wind tunnel outlet boundary. Pressure outlet boundary conditions require the specification of a static (gauge) pressure at the outlet boundary. The value of the specified static pressure is used only while the flow is subsonic. Should the flow become locally supersonic, the specified pressure will no longer be used and pressure will be extrapolated from the flow in the interior. All other flow quantities are extrapolated from the interior. To set the static pressure at the pressure outlet boundary, the appropriate value for Gauge Pressure in the Pressure Outlet panel is needed. This value will be used for subsonic flow only and is relative to the operating pressure set in the Operating Conditions panel.
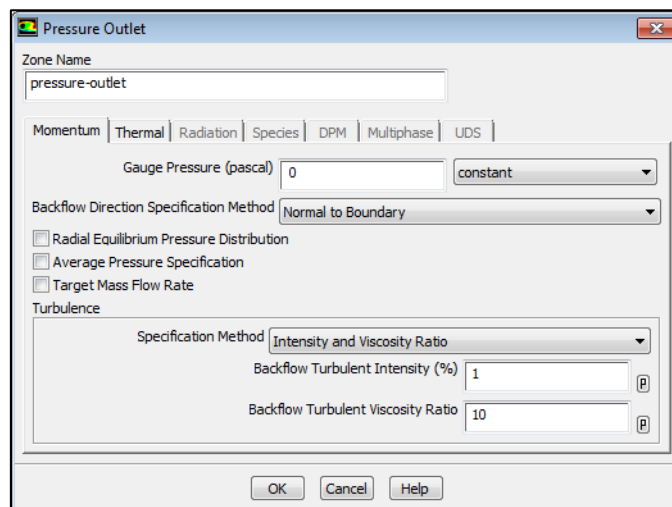
Figure 92: *Definition of Pressure Outlet boundary condition*

For all models that are tested, the reference geometry is defined with a stationary wall boundary condition. Wall boundary conditions are used to bound fluid and solid regions. In viscous flows, the no-slip boundary condition is enforced at walls by default, but it can be specified aa tangential velocity component in terms of the translational or rotational motion of the wall boundary, or as "slip" wall by specifying shear. The stationary boundary condition specifies a fixed wall, whereas the moving boundary condition can be used to specify the translational or rotational velocity of the wall, or the velocity components. In viscous flows, the no-slip boundary condition is enforced at walls by default and is used in all CFD cases.
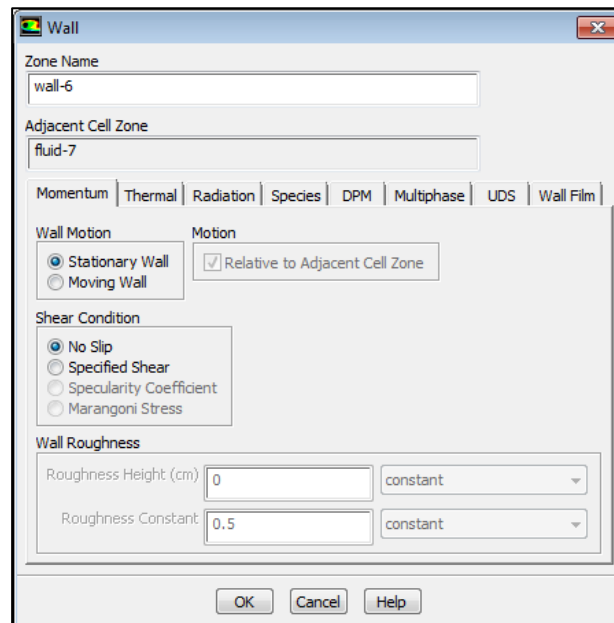
Figure 93: *Definition of Stationary wall boundary condition*

Effects like rotating wheels and moving road where is needed have to be modeled using the Rotating/Moving Wall Boundary Conditions respectively. This adds tangential velocity to the selected walls. Wall motion conditions are entered in the Momentum section of the Wall panel. The Wall panel will expand, to show the wall velocity conditions. Note that the moving wall condition cannot be used to model problems where the wall has a motion normal to itself. *Fluent* will neglect any normal component of wall motion that is defined either with *Absolute* or *Relative to Adjacent Cell Zone* method which is used by default. For the CFD cases were the road is included in the simulation, it is defined with a linear translational motion and the wall's Speed and Direction has to be specified. To define non-linear translational motion, the *Components* option can be used. For problems including the whole vehicle with the wheels, the surfaces of the wheels include rotational wall motion and have to be defined as *Rotational* walls with a specific rotating Speed about a specified rotation axis which. This axis is independent of the axis of rotation used by the adjacent cell zone, and independent of any other wall rotation axis. For 3D problems, the axis of rotation is the vector passing through the specified Rotation-Axis Origin and parallel to the vector from (0,0,0) to the (X,Y,Z) point specified under Rotation-Axis Direction. Note that the modeling of tangential rotational motion will be correct only if the wall bounds a surface of revolution about the prescribed axis of rotation (e.g., a circle or cylinder). Note also that rotational motion can be specified for a wall in a stationary reference frame. The no-slip condition is the default, and it indicates that the fluid sticks to the wall and moves with the same velocity as the wall, if it is moving.
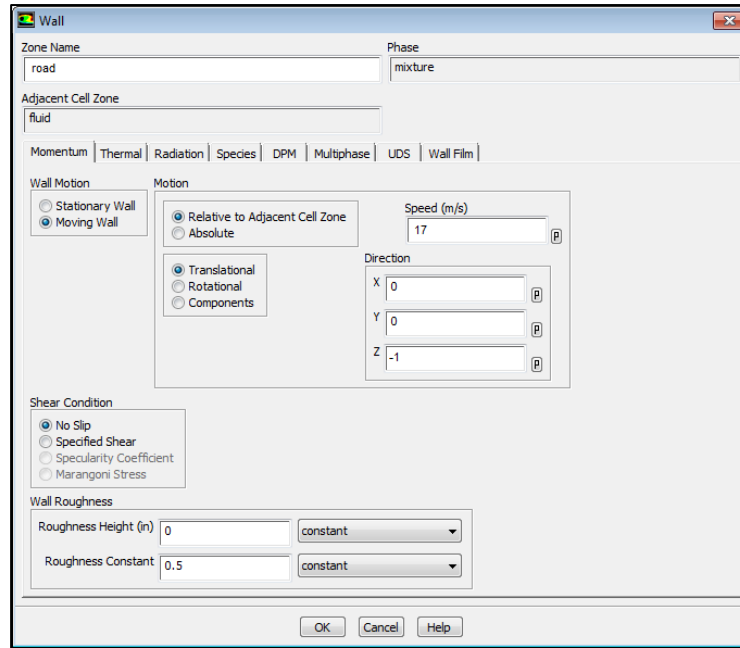
Figure 94: *Definition of Moving wall boundary condition for road*

Symmetry Boundary Condition is defined for the rest walls of the domain (*wind tunnel's top and sides*). Symmetry boundary condition is used for all cases where the half geometry is used and reflects an equally symmetric flow solution. As such, symmetry boundary conditions can reduce computational costs significantly a and do not require specification of any flow variable. *Fluent* assumes a zero flux of all quantities across a symmetry boundary. There is no convective flux across a symmetry plane: the normal velocity component at the symmetry plane is thus zero. There is no diffusion flux across a symmetry plane: the normal gradients of all flow variables are thus zero at the symmetry plane. The symmetry boundary condition can therefore be summarized as a zero-normal velocity and a zero normal gradients of all variables at a symmetry plane. As stated above, these conditions determine a zero flux across the symmetry plane, which is required by the definition of symmetry. Since the shear stress is zero at a symmetry boundary, it can also be interpreted as a "*slip*" wall when used in viscous flow calculations.
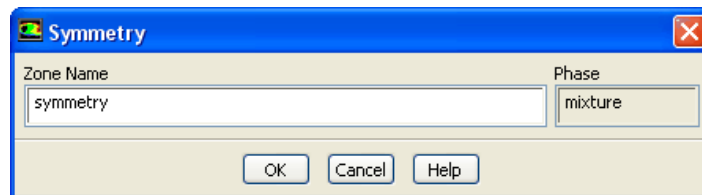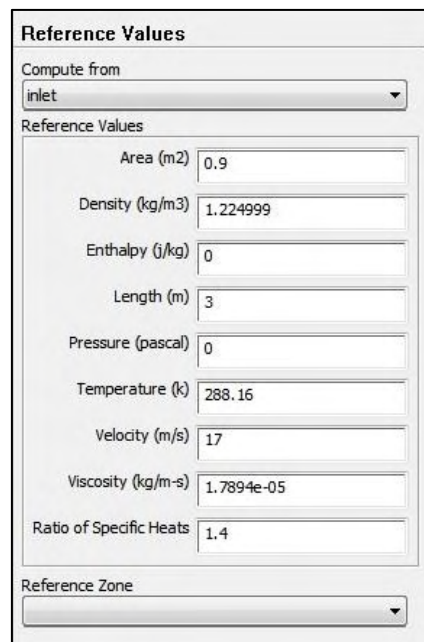

Figure 95: *Symmetry boundary condition default card*

3.2.4. Reference Values

At this card are defined the physical parameters of the problem that is examined each time. These *Reference Values* are used in the computation of derived physical quantities and non-dimensional coefficients, like the Drag and Lift coefficients. The first parameter that is defined for all cases is the frontal *Area* of each geometry, which can be easily calculated using the *Projected Surface Area* tool. Next the characteristic length of each model is defined on the *Length* field, as it was calculated for ANSA models, while on the *Velocity* field is defined the inlet velocity of each CFD case. All the other fields use their default values or they just change according to the rest reference values. Force coefficients use the reference area, density, and velocity. In addition, the pressure force calculation uses the reference pressure. Moment coefficients use the reference length, area, density and velocity. Reynolds number uses the reference length, density, and viscosity. Pressure and total pressure coefficients use the reference pressure, density, and velocity, while Skin friction coefficient uses the reference density and velocity. These reference values are used only for postprocessing.
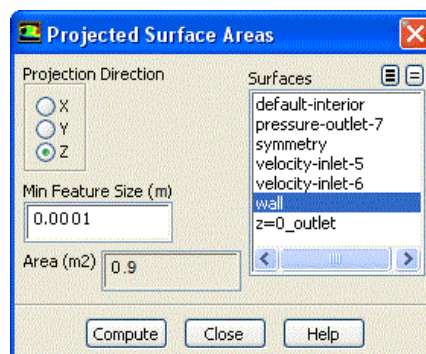

Figure 96: *Reference Values settings card*

Figure 97: *Projected Surface Areas calculator*

67

3.2.5. Solution Methods

Scheme provides a drop-down list of the available pressure-velocity coupling schemes while as previously mentioned, the *Pressure-Based* solver allows to solve flow problems in either a *Segregated* or *Coupled* manner. The *Coupled* algorithm is selected because it obtains a robust and efficient single phase implementation for steady-state flows, with superior performance compared to the *Segregated* solution schemes.
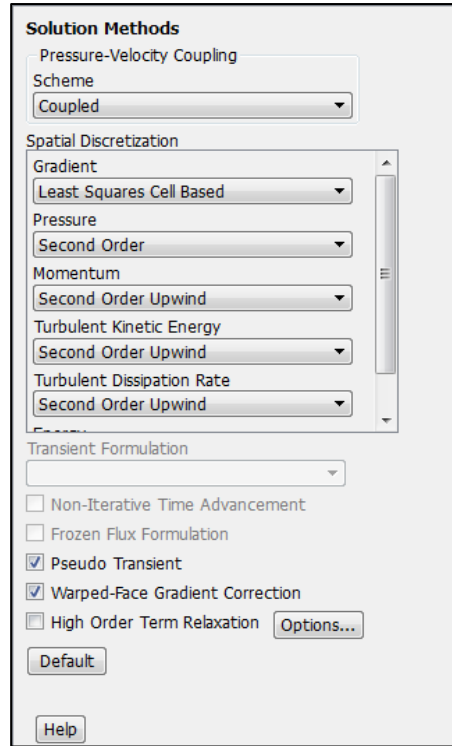

Figure 98: *Solution Methods settings card*

The *Pressure-Based Segregated* algorithm solves the momentum equation and pressure correction equations separately, but this semi-implicit solution method results in slow convergence. The *Coupled* algorithm on the other hand, solves the momentum and pressure-based continuity equations together. However, the memory requirement increases by 1.5 - 2 times that of the segregated algorithm since the discrete system of all momentum and pressure-based continuity equations must be stored in the memory when solving for the velocity and pressure fields (*rather than just a single equation, as is the case with the segregated algorithm*). The full implicit coupling is achieved through an implicit discretization of pressure gradient terms in the momentum equations, and an implicit discretization of the face mass flux, including the Rhie-Chow pressure dissipation terms.

In the momentum equations, the pressure gradient for component *k* is of the form:

$$\sum_f p_f A_k = -\sum_j a^{u_k p} p_j \qquad \textbf{(3.17)}$$

Where $a^{u_k p}$ is the coefficient derived from the Gauss divergence theorem and coefficients of the pressure interpolation schemes. Finally, for any i^{th} cell, the discretized form of the momentum equation for component u_k is defined as:

$$\sum_j a_{ij}{}^{u_k u_k} u_{kj} + \sum_j a_{ij}{}^{u_k p} p_j = b_i{}^{u_k} \qquad \textbf{(3.18)}$$

In the continuity equation, the balance of fluxes is replaced using the flux expression, resulting in the discretized form:

$$\sum_k \sum_j a_{ij}{}^{pu_k} u_{kj} + \sum_j a_{ij}{}^{pp} p_j = b_i{}^{p} \qquad \textbf{(3.19)}$$

As a result, the overall system of equations (*3.18*) and (*3.19*), after being transformed to the *δ-form*, is presented as:

$$\sum_j [A]_{ij} \vec{X}_j = \vec{B}_i \qquad \textbf{(3.20)}$$

where the influence of a cell *i* on a cell *j* has the form:

$$A_{ij} = \begin{bmatrix} a_{ij}^{pp} & a_{ij}^{pu} & a_{ij}^{pv} & a_{ij}^{pw} \\ a_{ij}^{up} & a_{ij}^{uu} & a_{ij}^{uv} & a_{ij}^{uw} \\ a_{ij}^{vp} & a_{ij}^{vu} & a_{ij}^{vv} & a_{ij}^{vw} \\ a_{ij}^{wp} & a_{ij}^{wu} & a_{ij}^{wv} & a_{ij}^{ww} \end{bmatrix} \qquad \textbf{(3.21)}$$

In some cases, using porous jump boundary conditions, the *Coupled* scheme may suffer from convergence instability that do not respond to changes in the coupled solver settings. This behavior depends on the specific flow configuration and porous jump boundary condition values and it is recommended to change the pressure-velocity coupling to one of the segregated schemes. For transient flows, using the *Coupled* algorithm is necessary when the quality of the mesh is poor, or if large time steps are used.
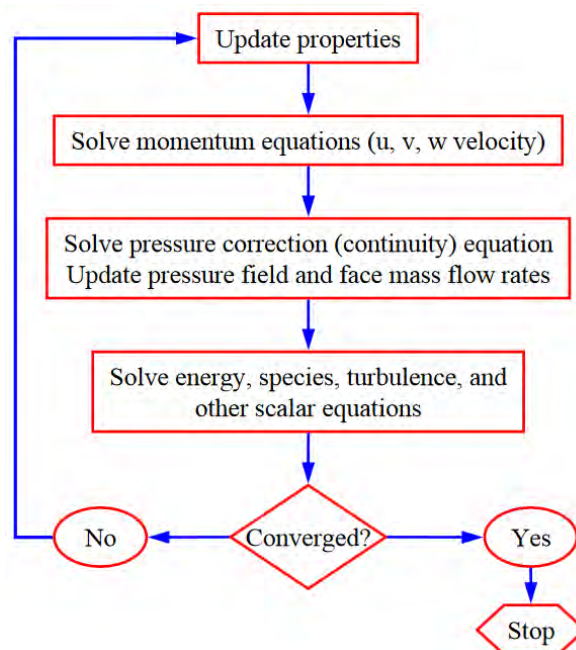

Figure 99: *Pressure-Based Coupled algorithm diagram*

Spatial Discretization contains settings that control the spatial discretization of the convection terms in the solution equations. *Gradient* contains a drop-down list of the options for setting the method of computing the gradient. Gradients are needed not only for constructing values of a scalar at the cell faces, but also for computing secondary diffusion terms and velocity derivatives. The gradient $\nabla\varphi$ of a given variable φ is used to discretize the convection and diffusion terms in the flow conservation equations. The *Least Squares Cell-Based* gradient method t is selected and used for all the CFD models. In this method, the solution is assumed to vary linearly. In Cell Centroid Evaluation, the change in cell values between cell c_0 and c_i along the vector r_i from the centroid of cell c_0 to cell c_i, can be expressed as:

$$\left(\nabla\phi\right)_{c0}\cdot\Delta r_i=\left(\phi_{ci}-\phi_{c0}\right) \qquad \textbf{(3.22)}$$

If similar equations are used for each cell surrounding the cell c_0 and assuming that J is the coefficient matrix that is purely a function of geometry, the following system is written in a compact form as:

$$[J]\left(\nabla\phi\right)_{c0}=\Delta\phi \qquad \textbf{(3.23)}$$

The objective here is to determine the cell gradient $(\nabla\varphi_0)$ by solving the minimization problem for the system of the non-square coefficient matrix in a least-squares sense. The above linear-system of equation is over-determined and can be solved by decomposing the coefficient matrix using the Gram-Schmidt process. This decomposition yields a matrix of weights $\left(W_{i_0}^x, W_{i_0}^y, W_{i_0}^z\right)$ for each cell. Thus, for our cell-centered scheme this means that the three components of the weights () are produced for each of the faces of cell c_0. Therefore, the gradient at the cell center can then be computed by multiplying the weight factors by the difference vector $\Delta\varphi = \left(\varphi_{c_1} - \varphi_{c_0}\right)$ as:

$$\left(\phi_x\right)_{c0} = \sum_{i=1}^{n}W^x{}_{i0}\cdot\left(\phi_{ci}-\phi_{c0}\right) \qquad \textbf{(3.24)}$$

$$\left(\phi_y\right)_{c0} = \sum_{i=1}^{n}W^y{}_{i0}\cdot\left(\phi_{ci}-\phi_{c0}\right) \qquad \textbf{(3.25)}$$

$$\left(\phi_z\right)_{c0} = \sum_{i=1}^{n}W^z{}_{i0}\cdot\left(\phi_{ci}-\phi_{c0}\right) \qquad \textbf{(3.26)}$$

On irregular (*skewed and distorted*) unstructured meshes, the accuracy of the least-squares gradient method is comparable to that of the node-based gradient. However, it is less expensive to compute the least-squares gradient than the node-based gradient. Therefore, it has been selected as the default gradient method in the ANSYS-*Fluent* solver. The next field is *Pressure* (*for the pressure-based solver only*) which contains a drop-down list of the discretization schemes available for the pressure equation where *Second Order* is used by default. Finally, *Momentum, Turbulent Kinetic Energy* and *Turbulent Dissipation Rate* are the names of the other convection-diffusion equations being solved and in the drop-down lists that appears for these fields, the *Second Order Upwind* discretization scheme is used in all cases.
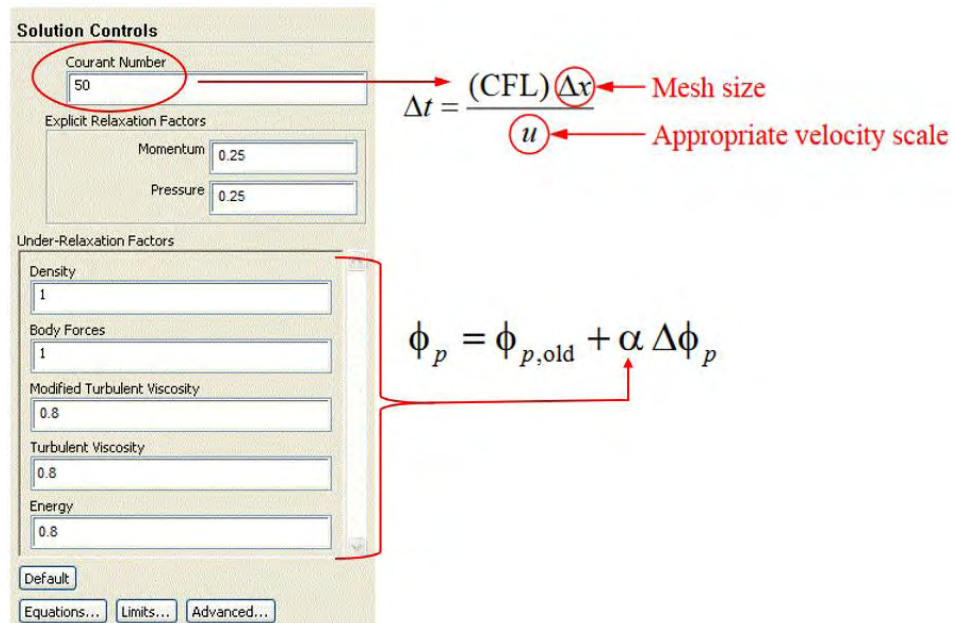
3.2.6. Solution Controls

At this card are defined solution parameters like the *Courant Number* and the *Relaxation Factors* that are used. When the *Pressure-Based* solver and the *Coupled* pressure-velocity scheme is used for time-independent flows, the *Courant Number* is used to stabilize the convergence behavior and a value of 50 is settled for all the cases. The under-relaxation of equations, also known as implicit relaxation, is used in the pressure-based solver to stabilize the convergence behavior of the outer nonlinear iterations by introducing selective amounts of φ in the system of discretized equations. This is equivalent to the location-specific time step:

$$\frac{a_p \phi}{\alpha} = \sum_{nb} a_{nb} \phi_{nb} + b + \frac{1-\alpha}{\alpha} a_p \phi_{old} \qquad \textbf{(3.27)}$$

The *Courant Number* (*CFL*) in terms of a on the above equation, can be written as:

$$\frac{1-\alpha}{\alpha} = \frac{1}{CFL} \qquad \textbf{(3.28)}$$

Explicit Relaxation Factors for the *Coupled* scheme defines the explicit relaxation of variables between sub-iterations for *Momentum* and *Pressure*. Both values of *Momentum* and *Pressure* are settled as 0.25. The *Under-Relaxation Factors* field contains the under-relaxation factors for all equations that are being solved with the *Pressure-Based* solver. The *Pressure-Based* solver uses under-relaxation of equations to control the update of computed variables at each iteration. This means that all equations solved using the *Pressure-Based* solver, will have under-relaxation factors associated with them. Under-relaxation factor a, is included to stabilize the iterative process for the *Pressure-Based* solver. The default under-relaxation parameters for all variables are set to values that are near optimal for the largest possible number of cases. These values are suitable for many problems, but for some particularly nonlinear problems it is prudent to reduce the under-relaxation factors initially. Typically, an increase in the under-relaxation factors brings about a slight increase in the residuals, but these increases usually disappear as the solution progresses. If the residuals continue to increase after the first 4 or 5 iterations, the under-relaxation factors should be reduced.

Figure 100: *Solution Controls settings card*

71

3.2.7. Monitors

At the end of each solver iteration, the residual sum for each of the conserved variables is computed and stored, thus recording the convergence history. By default, residual values for all relevant variables are printed in the text (*console*) window after each iteration. Residual plots show when the residual values have reached the specified tolerance. On a computer with infinite precision, these residuals will go to zero as the solution converges. On an actual computer, the residuals decay to some small value (*"round-off"*) and then stop changing (*"level out"*). For single-precision computations (the default for workstations and most computers), residuals can drop as many as six orders of magnitude before hitting round-off. Double-precision residuals can drop up to twelve orders of magnitude. There are no universal metrics for judging convergence. Residual definitions that are useful for one class of problem are sometimes misleading for other classes of problems. For most problems, the default convergence criterion in ANSYS-*Fluent* is sufficient. This criterion requires that the scaled residuals must decrease to 10^{-3} for all equations except the energy and P-1 equations, for which the criterion is 10^{-6}.
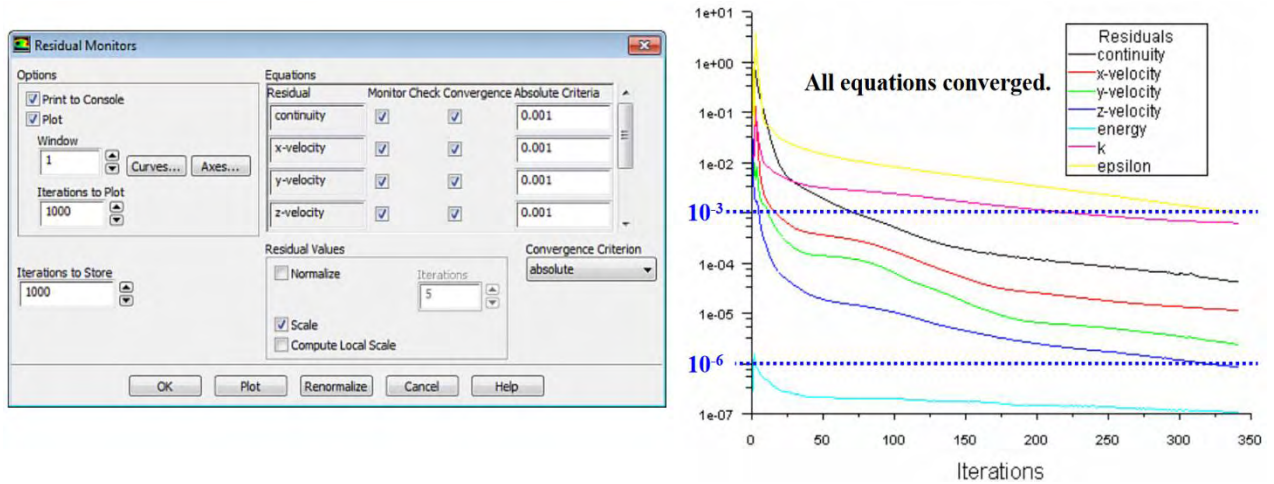

Figure 101: *Residual Monitors settings for convergence criteria*

Therefore, to judge convergence it is not only enough to examine residual levels, but also to monitor relevant integrated quantities such as the *Drag* and *Lift* coefficients and check if they reach steady values. So, for all cases two extra monitors are created for Drag and Lift coefficient respectively and are also plotted to have a clear view of their convergence behavior.
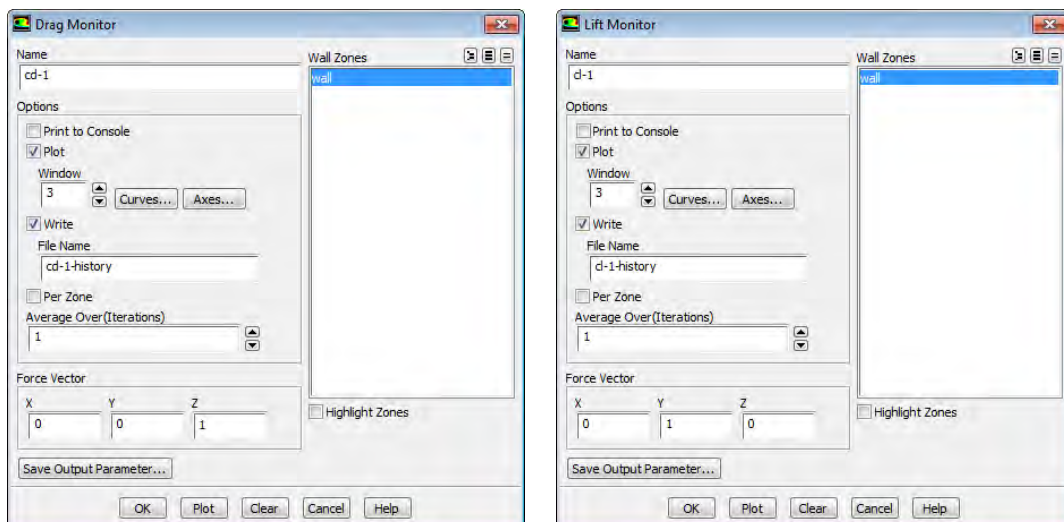

Figure 102: *Drag and Lift monitors*

3.2.8. Solution Initialization

Before starting any CFD simulation, the *Fluent* solver needs an initial "guess" for the solution flow field. In many cases, you must take extra care to provide an initial solution that will allow the desired final solution to be attained. The *Solution Initialization* task page defineσ values for flow variables and initialize the flow field to these values. The default initialization method for single phase steady-state flows is the *Hybrid Initialization* method and is used for all the CFD cases.
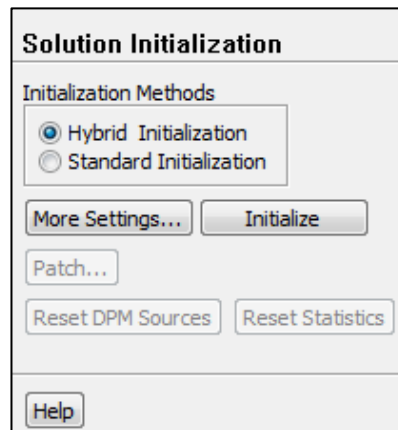

Figure 103: *Solution Initialization card*

Hybrid initialization is a collection of recipes and boundary interpolation methods. It solves Laplace's equation to determine the velocity and pressure fields. All other variables, such as turbulence, species fractions, volume fractions, and so on, will be automatically patched based on domain averaged values or a particular interpolation recipe. These recipes are shown in detail below:

- **Velocity Field:** Laplace's equation is solved with appropriate boundary conditions to produce the velocity field in the domain $\nabla^2 \varphi$, where φ is the velocity potential. The velocity components are given by the gradient potential $\vec{V} = \nabla \varphi$.
  The Velocity potential is expressed as follows for the various boundary conditions:

  - *Wall Boundaries*: The velocity normal to the wall is zero.

  $$\frac{\partial \varphi}{\partial n}\bigg|_{wall} = 0$$

  - *Inlet Boundaries*: The velocity normal to the inlet boundaries are computed from the user-specified boundary values.

  $$\frac{\partial \varphi}{\partial n}\bigg|_{inlet} = V_\perp$$

  - *Far Field Boundaries*: At the far-field boundaries the velocity normal to the boundaries is computed from the user-specified free stream conditions. Far away from the body the flow approaches the free stream conditions:

$$\frac{\partial \varphi}{\partial x}\bigg|_{\infty} = u_{\infty}$$

$$\frac{\partial \varphi}{\partial y}\bigg|_{\infty} = v_{\infty}$$

$$\frac{\partial \varphi}{\partial z}\bigg|_{\infty} = w_{\infty}$$

- *Outlet Boundaries***:** They are specified as zero potential $\varphi = 0$

- **Pressure Field:** An additional Laplace equation is solved with the appropriate boundary condition to produce the smooth pressure field in the domain, only if the pressure information is available in at least one inlet and one outlet in the domain. Otherwise, the pressure field will be initialized with the averaged constant value from all the boundaries $\nabla^2 P = 0$, where P is expressed as follows for the various boundary conditions:

  - *Pressure inlet boundaries*: P is computed as *1%* less than the specified Total Pressure.

  - *Pressure outlet boundaries*: P is computed as 1% more than the specified Gauge Pressure at this boundary.

  - *Velocity/Mass flow inlet boundaries*: P uses the value of the specified Supersonic/Initial Gauge Pressure.

  - *Wall Boundaries*: the normal gradient of P is set to zero.

$$\frac{\partial p}{\partial n}\bigg|_{wall} = 0$$

- **Turbulent Parameters:** By default, turbulent parameters are initialized with constant values (*domain averaged*).

- **Species Fractions:** By default, secondary species mass/mole fractions are initialized with a 0.0 value.

4. CFD SIMULATIONS RESULTS ANALYSIS

4.1. Nosecone

The first part of the aerodynamic package to be tested is the nosecone of the car. Three main types of nosecones are designed and tested, that are also the most common in use. One with horizontal edge, one with vertical and one with an angled edge. Three extra variant models are created for each one of these types, having a different design of their top surface like peaked lines, side channels and a lifted cockpit deflector which are the most common aerodynamic design technics used in hoods of different race cars. The main idea behind the design of the nosecone is the minimization of the drag, as this device is not used to produce downforce. However, the aim is to avoid the generation of lift and achieve at least neutral situation. Numerous CFD simulations are done for all these 13 models at the speed of 60km/h, which is the average speed of a FSAE car, in order to calculate their aerodynamic coefficients (C_L & C_D) and compare them until the most efficient type is selected.

4.1.1. Horizontal Nosecone

The first type of nosecone that is tested is the *Horizontal edge* nosecone. The purpose of this design is to use the round horizontal edge in order to "feed" the undertray of the car with even more air as it creates a larger opening on the underside. However, that design leads to a sharp form of the side edges which could easily affect the air directing to sidepods. Also, the pressure being created on the stagnation point is quite low and that can be also seen on the Drag coefficient value (0.282) on the table below, while the lift coefficient is at -0.196 which results in an aerodynamic efficiency of 0.71.
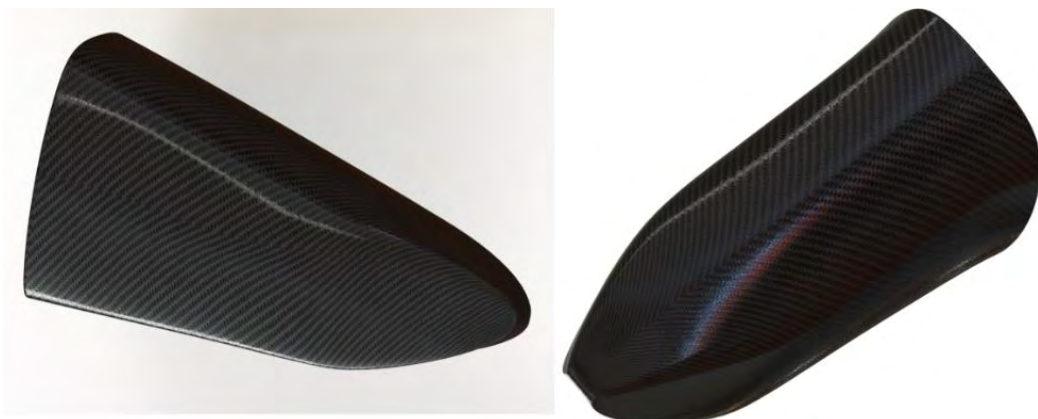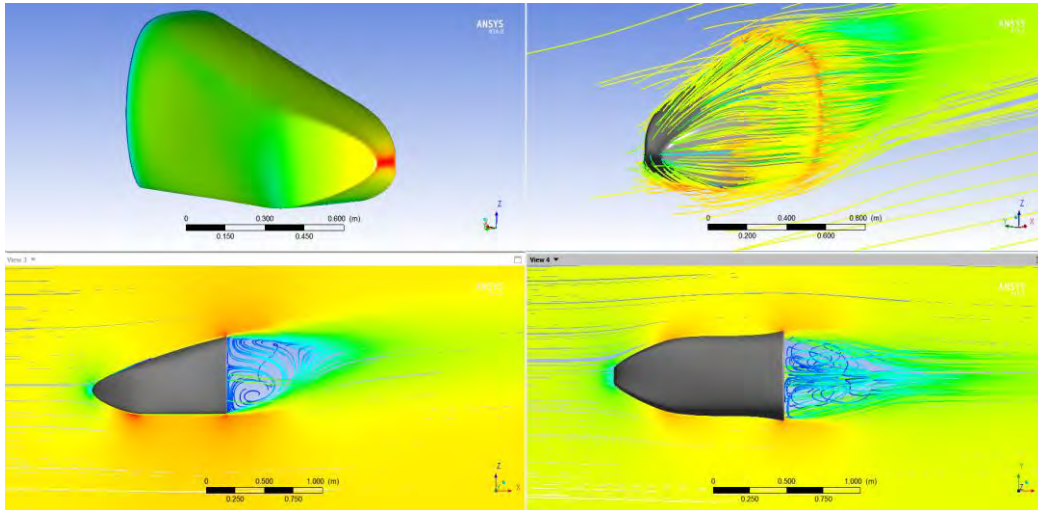

Figure 104: *Horizontal nosecone CAD design*

Characteristics	
Lift Coefficient *(C_L)*	*-0.196*
Drag Coefficient *(C_D)*	*0.282*
Efficiency *(C_L / C_D)*	*0.71*

Figure 105: *Pressure distribution and streamlines around the horizontal nosecone*

4.1.2. Vertical Nosecone

The next design of nosecone is the *Vertical edge* nosecone. The purpose of this design is to use the round vertical edge in order to "*split*" the incoming air to the sides in order to direct it to the sidepods. However, that design leads again to a sharp form of the upper and underside edges of the nosecone, which affect the undertray and can easily lead to a flow separation, which begins from the leading edge of the nosecone as shown in the *Figure* below. The pressure being created on the stagnation point is significantly higher on that type and that can be also seen on the increase of the Drag coefficient (0.289) on the table below, while the lift coefficient is also increased at -0.21 which results in an aerodynamic efficiency of 0.73.

Figure 106: *Vertical nosecone CAD designs*

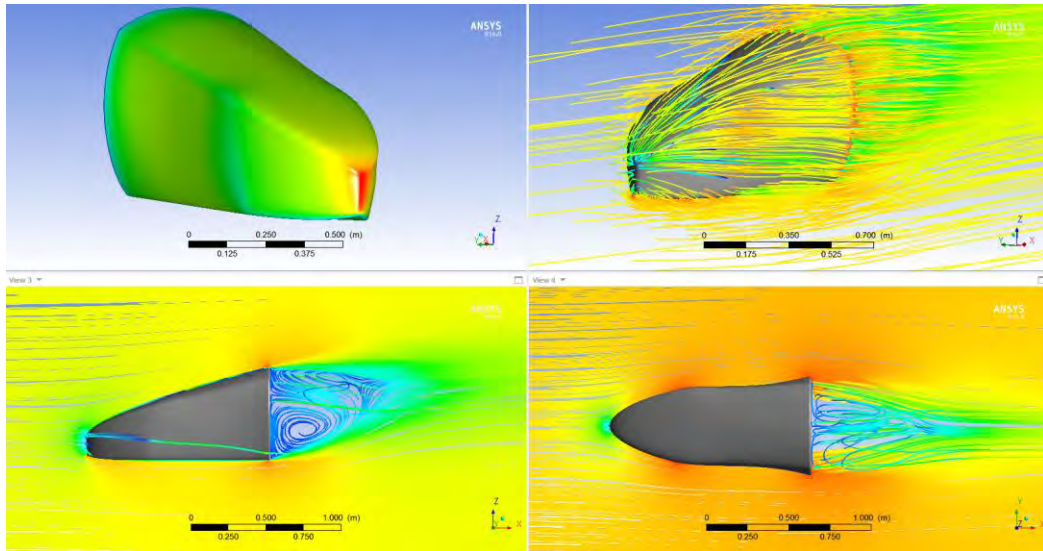| Characteristics	
Lift Coefficient *(C_L)*	*-0.21*
Drag Coefficient *(C_D)*	*0.289*
Efficiency (C_L / C_D)	*0.73*

Figure 107: *Pressure distribution and streamlines around the vertical nosecone*

4.1.3. Angled Nosecone

The last design of nosecone is the one with the *Vertical edge*. The purpose of this design is to use again a vertical edge in order to "*split*" the incoming air to the sides for the sidepods and use the angle of that edge in order to reduce the pressure of the stagnation point and give more space to the underside of the nosecone to "feed" the undertray. The pressure being created on the stagnation point is significantly lower comparing to the previous type. The Drag coefficient is 0.292 as shown on the table below, while the lift coefficient is at -0.202 which results in an aerodynamic efficiency of 0.69. Although the drag coefficient is slightly higher for that type of nosecone, the models that occurred with the combination of peaked lines and cockpit deflector on the top surface, were more efficient comparing to the rest models.
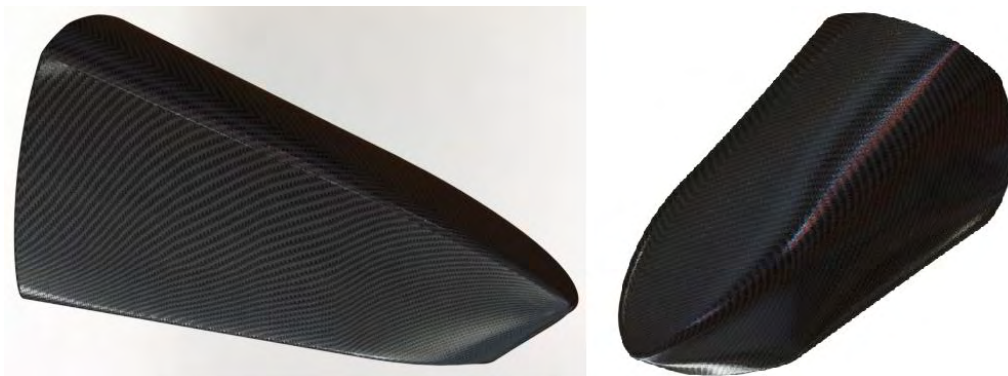

Figure 108: *Angled nosecone CAD design*

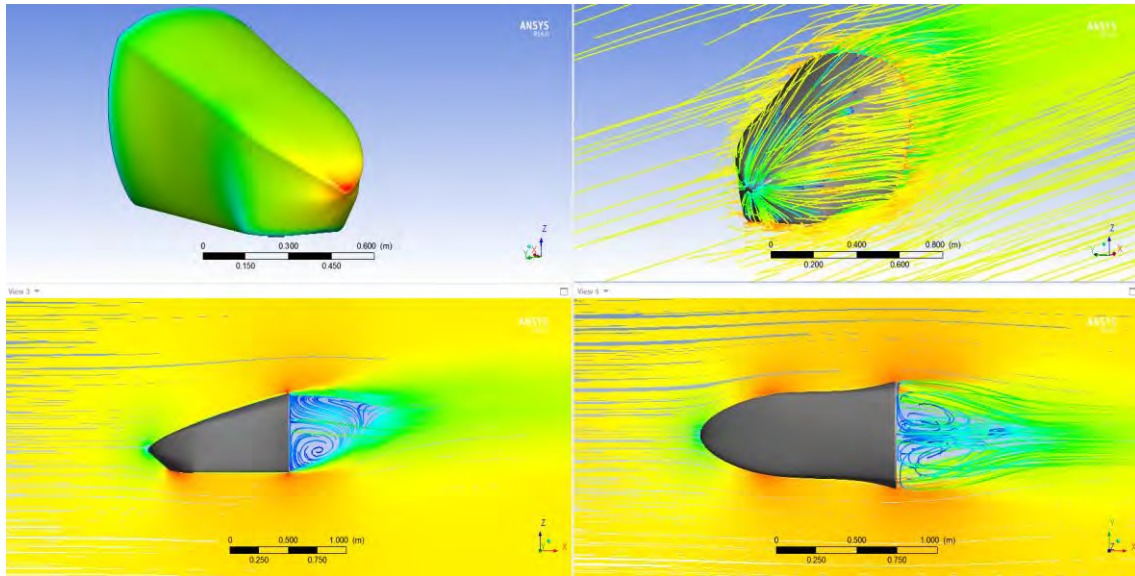| Characteristics	
Lift Coefficient *(C_L)*	*-0.202*
Drag Coefficient *(C_D)*	*0.292*
Efficiency (C_L / C_D)	*0.69*

Figure 109: *Pressure distribution and streamlines around the vertical nosecone*

4.1.4. Final Nosecone

The final design of nosecone that was selected is the one with the *Vertical edge* and a combination of peak lines and a cockpit deflector. These extra aids o the top surface of the nosecone seem to improve significantly its efficiency. The pressure being created on the stagnation point is even lower comparing to the simple angled model. The Drag coefficient is slightly increased at 0.305 as shown on the table below, but the lift coefficient is now at -0.238 which results in the best aerodynamic efficiency of 0.78.
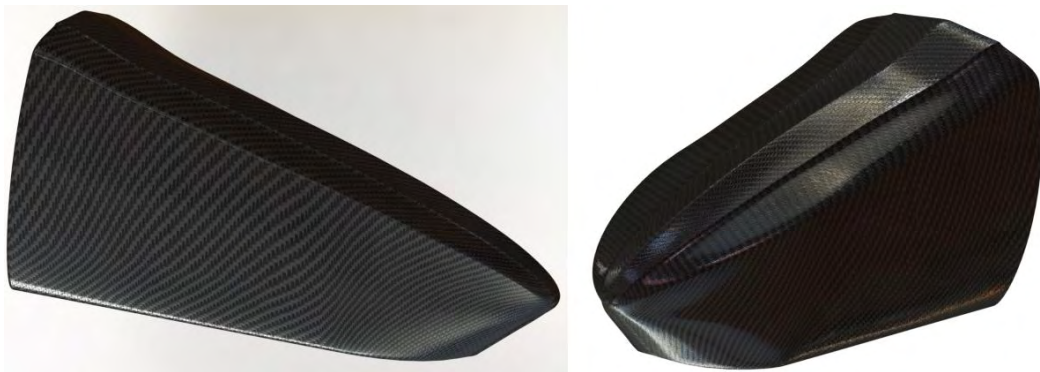

Figure 110: *Final nosecone CAD designs*

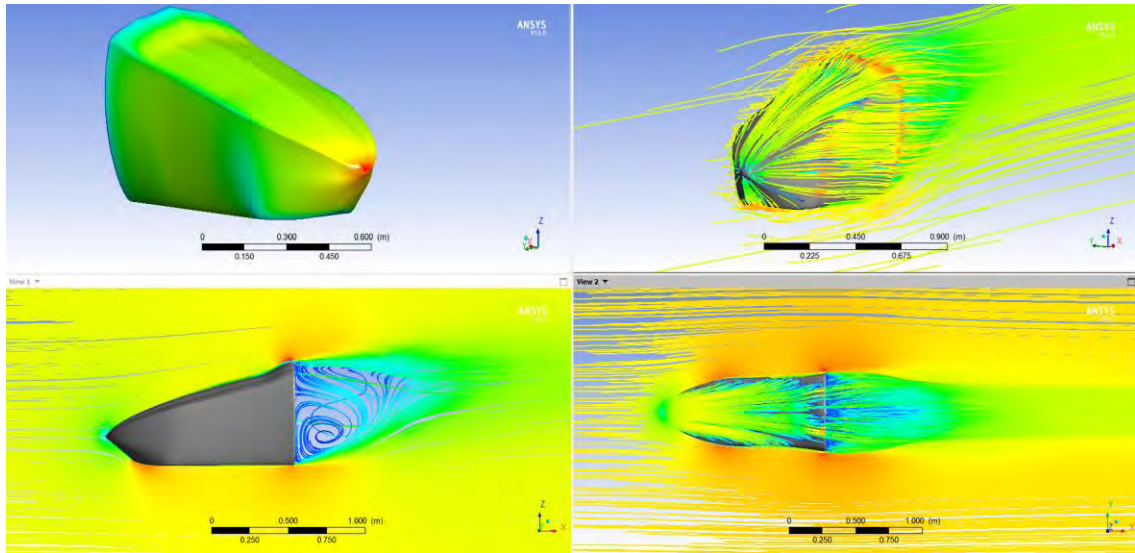| Characteristics	
Lift Coefficient *(C_L)*	-0.238
Drag Coefficient *(C_D)*	0.305
Efficiency (C_L / C_D)	0.78

Figure 111: *Pressure distribution and streamlines around the final nosecone*

4.1.5. Results Comparison

On the table below are shown in summary the results that occurred from the CFD simulations that were done for all the combinations of nosecone models. For all cases Drag, Lift coefficients, downforce and drag are calculated, while the most crucial factor is the ratio C_L / C_D *which is known as the aerodynamic efficiency.* As it is shown on the table, the use of peaked lines increases slightly the drag coefficient and affect the lift coefficient more. The side channels on the other hand can easily increase lift coefficient but it also has a big impact on the increase of drag coefficient. Furthermore, the cockpit deflector seems to increase a lot the lift coefficient for the vertical and angled models and if combined with peaked lines gives the best results. Although the aim of the nosecone's design is the minimization of drag the final model that is selected has a high drag coefficient but considering that it has also one of the highest lift coefficients its aerodynamic efficiency is satisfactory.

Nose Cone Types				Drag Coefficient(C_D)	Lift Coefficient(C_L)	Ratio CL/CD	Drag(N)	Downforce(N)
	–	–	–	0,282	-0,196	0,700	17,57	12,47
	✓	–	–	0,315	-0,209	0,660	20,06	13,3
	✓	✓	–	0,287	-0,218	0,760	18,16	13,81
	✓	–	✓	0,329	-0,186	0,570	20,9	11,83
	–	–	–	0,289	-0,21	0,730	18,68	13,61
	✓	–	–	0,279	-0,204	0,730	18,6	13,59
	✓	✓	–	0,277	-0,174	0,630	21,2	13,32
	✓	–	✓	0,296	-0,229	0,770	19,7	15,25
	–	–	–	0,292	-0,202	0,690	18,97	13,36
	✓	–	–	0,304	-0,23	0,760	19,09	14,47
	✓	✓	–	0,385	-0,268	0,700	24,29	16,92
	✓	–	✓	0,305	-0,238	0,780	19,18	14,96
	✓	✓	✓	0,367	-0,312	0,850	23,23	19,6

Figure 112: *CFD Results for each combination of Nosecone types*

4.2. Undertray

The next step after the selection of the final nosecone is the creation of a CFD model with the whole car and wheels, in order to simulate and test properly the different types of undertrays that were designed. Five main types of undertray are designed and simulated at the speed of 60km/h while the ride height from the ground is 4cm for all cases, in order to select the most efficient device at these conditions. The aim of all designs is to achieve the highest amount of downforce, while keeping drag as low as possible and avoid stall at the outlet od the diffusers. The weight of each undertray is also taken under consideration in order to estimate the aerodynamic efficiency of each type comparing to its mass.

4.2.1. Single Diffuser *(Undertray_1)*

The first undertray model has a large single diffuser at the rear of the undertray. Its dimensions are restricted from the rules which set a standard safe distance from the wheels. The maximum available space for the angle of the diffuser at the rear side of the chassis is also restricted from the bulk-head, so the maximum angle is settled at 8°. Seven vertical flaps are placed along the exit of the diffuser to keep the flow attached and avoid stall, while there is not any ground effect device used at the underside. Along the sides of the undertray side-skirts are placed to prevent air from escaping and as it can be seen from the floor plan there is a narrowing of the undertray which aims to guide all the incoming air directly to the diffuser. However, this type of undertray produce only a total downforce of *28.7 N,* but it has the least amount of drag (*61.87 N*) due to the small angle of the diffuser and weighs about 6.15kg.

Figure 113: *Single diffuser undertray CAD designs*

Characteristics	
Number of Diffusers	*1*
Diffuser Angle	*8°*
Ground Effect Device	✗
Downforce	*28.7 N*
Drag	*61.87 N*
Weight	*6.15 Kg*

As it can be seen on the Figure bellow, the flow stays attached along the undertray's surface. Although, the narrowing of the undertray seems to work and guide the air directly to the diffuser the side-skirts on the other hand cannot prevent much of the incoming air

from escaping due to their low height which is restricted from the FSAE rules. Finally, the pressure distribution is low (*green regions*) at the entrance of the diffuser an even lower just at the outlet of the diffuser where flow seems to accelerate more (*red streamlines*).
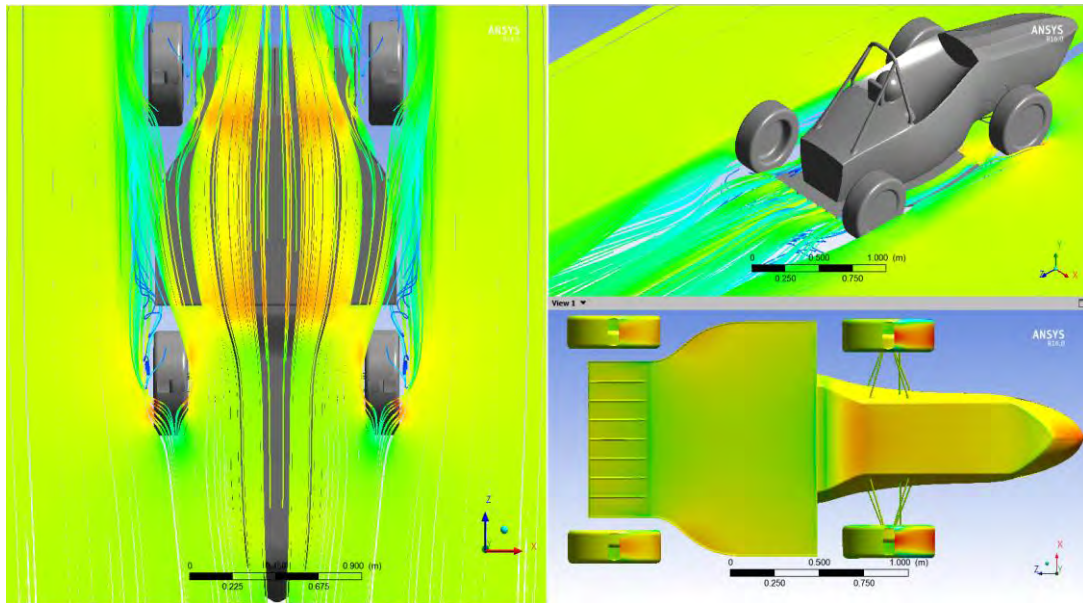

Figure 114: *Streamlines and pressure distribution for the single diffuser undertray*

4.2.2. Separated Rear Diffusers with Splitter *(Undertray_2)*

The second type of undertray has the same designing with the previous one until the inlet of the diffuser which is now different. The restriction of the diffuser's angle from the bulk-head of the chassis has a direct impact on the downforce that is generated, as it is shown on the previous type. An easy solution to increase the diffusers angle is to design two separated diffusers that are extending at the rear of the car, within the FSAE regulations. These two extended diffusers have an angle of 10.5° each and two long flaps are also placed to avoid flow separation due to the higher angle. This type of undertray has also a triangular bump at the center of the undertray which works as a splitter in order to separate the oncoming air and send it directly in to the two rear extended diffusers. This bump works also as a ground effect device as it is the lowest surface of the undertray and closer to the ground than any other part and interact with the moving ground. Finally, a curvature fillet has been placed at the exit edge of that bump in order to take advantage of the outcoming air and work as a small diffuser. This undertray produce a total downforce of *31.4 N* and its drag is increased up to 71.58 *N,* while the addition of the new diffuser resulted in a weight of 9.81kg which is inacceptable comparing with the downforce that is being generated.

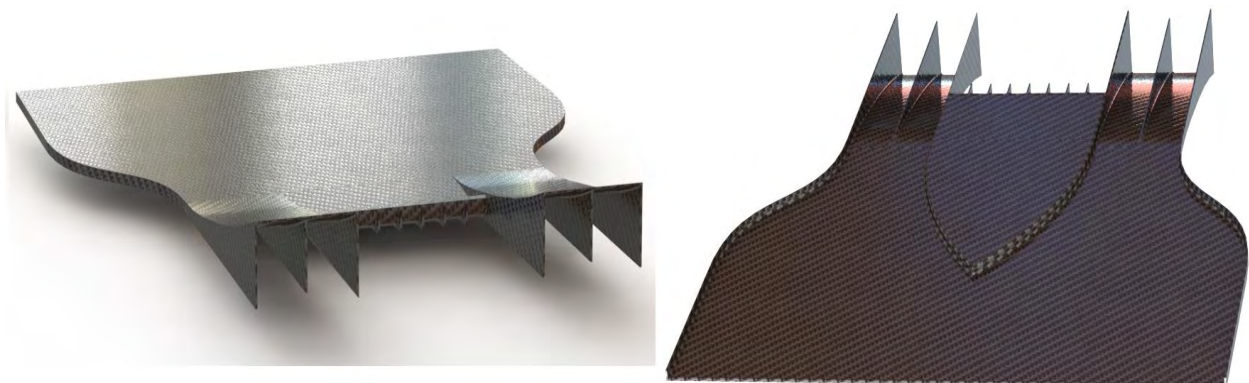**Figure 115:** *Separated rear diffuser CAD designs*

Characteristics	
Number of Diffusers	3
Diffuser Angle	10.5°
Ground Effect Device	✓
Downforce	31.4 N
Drag	71.58 N
Weight	9.81 Kg

As it can be seen on the Figure bellow, the flow stays again attached along the undertray's surface. The bump on middle of the undertray seems to successfully split the air and send it to the diffusers, however it is not so effective as a ground effect device, as the pressure on its surface is not as low as it was expected. The narrowing of the undertray is the same as on the previous type, however due the separated oncoming air from the splitter, it seems that there is also an amount of air escaping from the sides. Finally, from the pressure distribution, it is shown that the center of pressure has been transferred to the longer diffusers at the rear and is again low at both the entrance and the outlet of the undertray.
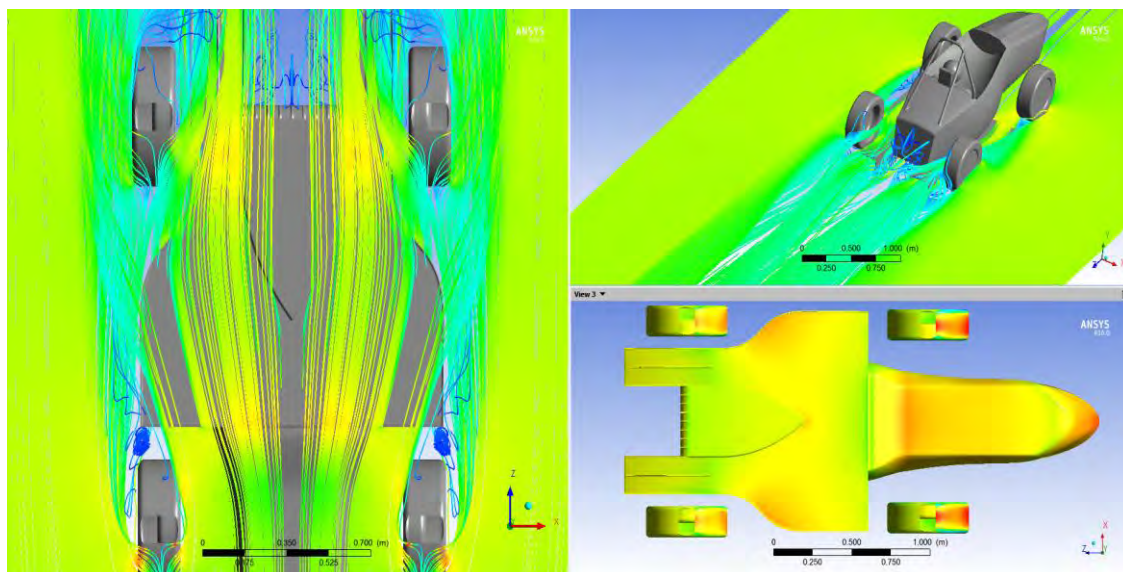

Figure 116: *Streamlines and pressure distribution for the separated diffusers undertray*

4.2.3. Separate Rear Diffusers *(Undertray_3)*

The third type of undertray has again the same designing with the previous two until the inlet of the diffuser and with the triangular bump splitter having been replaced by a small diffuser just under the bulk-head with an angle of 8°, in order to take advantage of the oncoming air in the middle of the undertray. The two rear extended diffusers have again an angle of 10.5° each and two long flaps are also placed to avoid flow separation. This undertray produce a total downforce of *44.72 N* and its drag is increased up to 66.84 *N,* while the removal of the new diffuser resulted in a total weight of 7.41kg which is 2kg lower than the previous type but again high enough comparing to the generated downforce.

Figure 117: *Separated diffusers CAD designs*

Characteristics	
Number of Diffusers	*3*
Diffuser Angle	*10.5°*
Ground Effect Device	✗
Downforce	*44.72 N*
Drag	*66.84 N*
Weight	*7.41 Kg*

As it can be seen on the Figure bellow, the flow stays again attached along the undertray's surface. Although, the narrowing of the undertray is the same as on the previous types, it seems that at this case less air is escaping from the sides is however due to the lower pressure that is created in the diffusers' inlet and sucks more air in. Furthermore, the streamlines show that the air is clearly accelerating even more along the whole underside of the car which is also the reason why it generates higher amounts of downforce. Finally, from the pressure distribution it is shown that the center of pressure has been transferred more to the rear due to the middle diffuser and is also lower both at the entrance and the outlet of the diffusers.
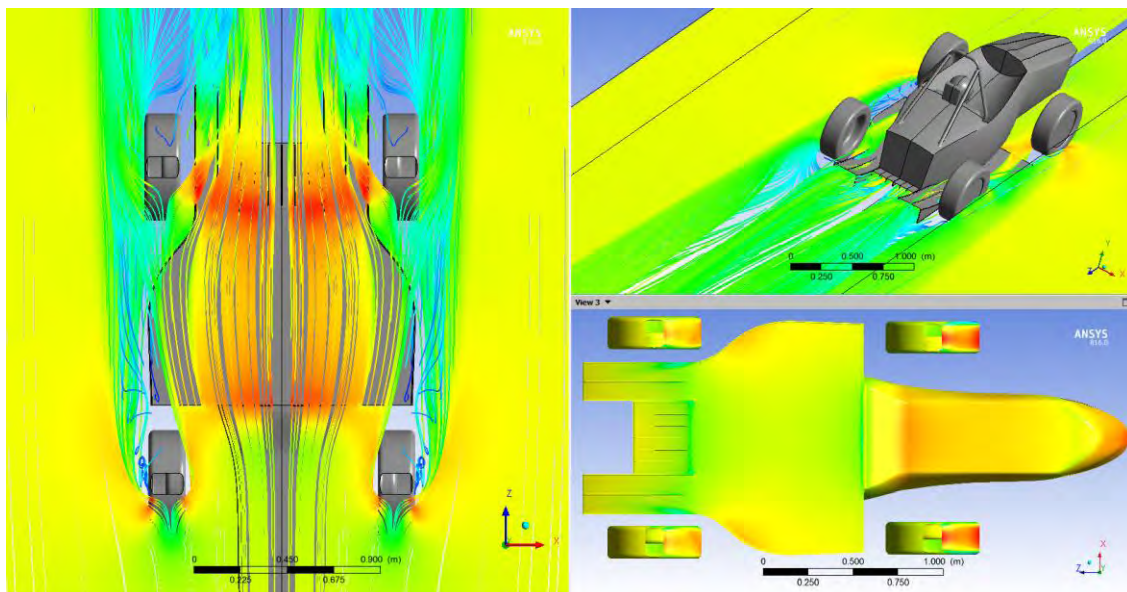

Figure 118: *Streamlines and pressure distribution for the separated diffusers undertray*

4.2.4. Side Diffusers *(Undertray_4)*

The next type of undertray is completely different than the previous designs. In order to reduce the weight of the undertray the rear long diffusers are replaced by two side diffusers which have an angle of 17.5° each. This gave more space for the central diffuser too, which was also replaced from a curvature fillet with vertical flaps due to the lack of space for a bigger diffuser with higher angle.
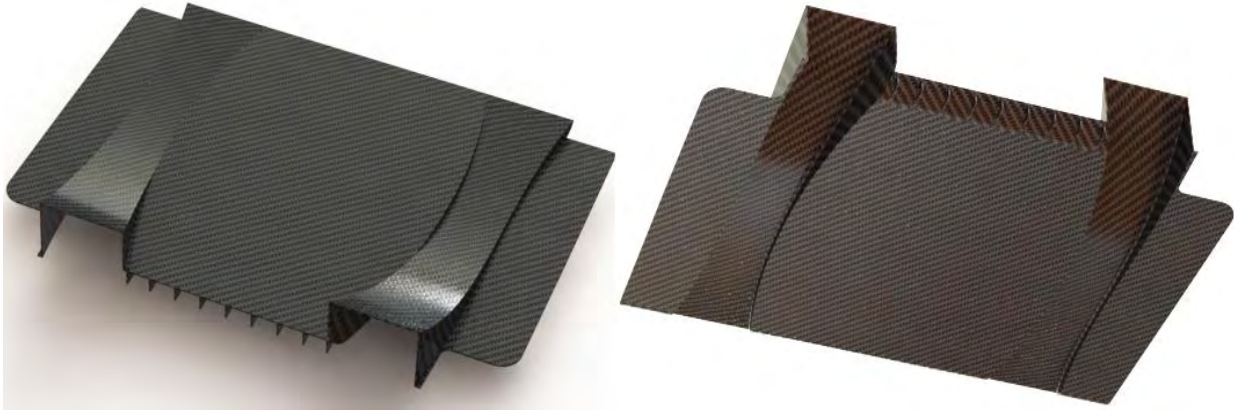

Figure 119: *Side diffusers CAD designs*

However, at that case, the angle of the side diffusers is restricted from the suspension dumpers that are located just above the diffusers' exits. To overcome this problem and increase the downforce without increasing the diffusers' angles, the diffuser tunnels are designed in such a way that they can take advantage of the Venturi effect in two dimensions, vertically and horizontally. As it is shown from the floor plan of the undertray, the shape of the diffuser tunnels is similar to that of a Venturi tube. The inlets are shaped like nozzles which are getting thinner on the middle of the undertray and end up to the diffusers in order to accelerate the air even more along the whole surface, as it is shown in the *Figures* bellow.
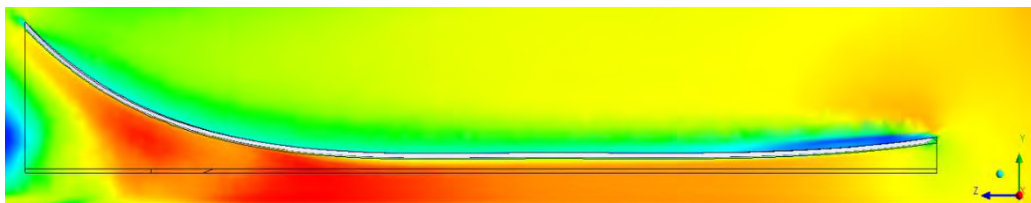

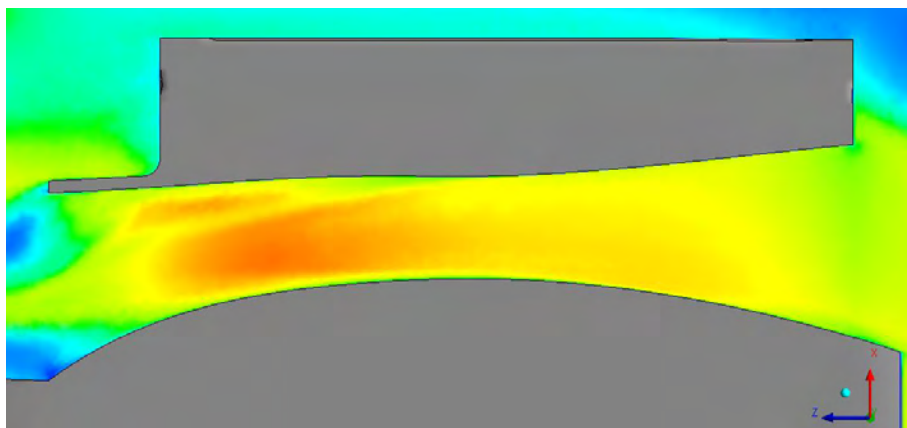**Figure 120:** *Venturi effect taking place on vertical axis Y, due to the angle of the diffuser*

Figure 121: *Venturi effect taking place of the horizontal axis X, due to the shape of the undertray*

84

This type of undertray produce even more downforce at about *48.62 N,* but its drag is increased up to 80.6 *N* which is higher than in previous models*.* However, the total weight of this undertray is reduced at 6.63 kg.

Characteristics	
Number of Diffusers	2
Diffuser Angle	17.5°
Ground Effect Device	✗
Downforce	48.62 N
Drag	80.6 N
Weight	6.63 Kg

The *Figure* bellow shows that, the flow stays attached along the whole undertray's surface. Although, on this type of undertray there is no narrowing at the rear, the low pressure that is created along the underside of the car prevents the air from escaping from the sides. The fact that the diffuser tunnels are extended along the whole underside of the car and they are not just placed between the rear wheels at the end of the undertray seems that it makes the air to accelerate even more along the whole underside of the car which is also the reason why it generates higher amounts of downforce. Finally, from the pressure distribution it is shown that the center of pressure has been transferred more to the front, while the pressure has been distributed equally at the whole surface and it seems to be lower at the entrance of the undertray which is not desired.
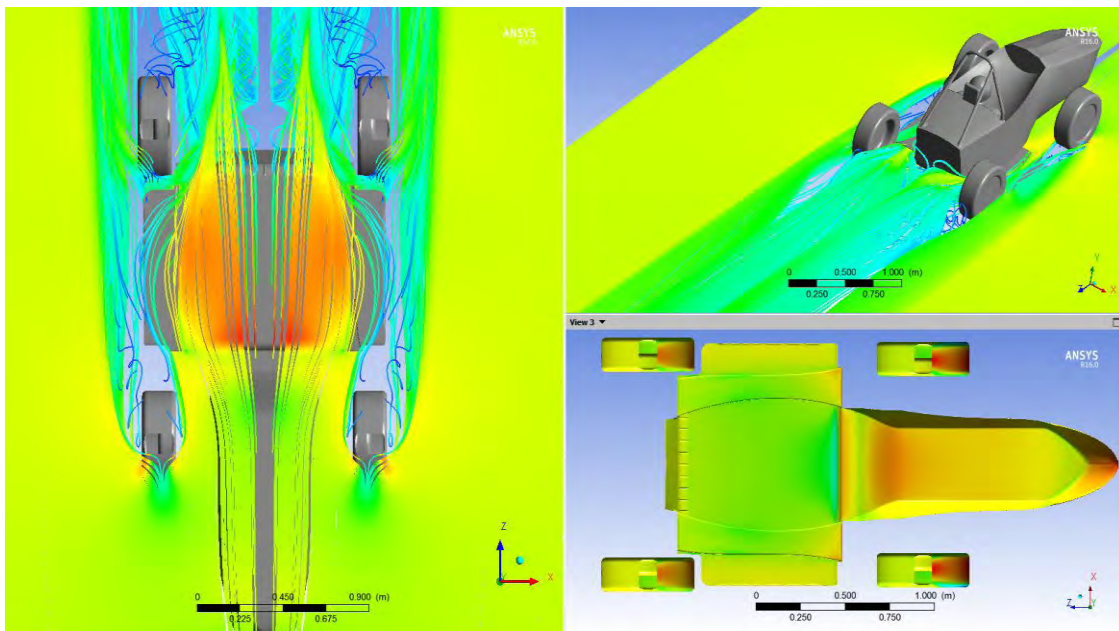
Figure 122: *Streamlines and pressure distribution for the side diffusers undertray*

4.2.5. Side & Double Diffusers *(Undertray_5)*

The final type of undertray that is designed is based on the previous model with some extra modifications in order to improve the aerodynamic efficiency. More specifically the diffusers' inlets and outlets are redesigned in order take advantage of the available space from the dumpers and chassis, while the tunnels are longer to shift the center of pressure more to the rear. Furthermore, the sharp inlet of the previous undertray is now replaced from a smooth curvature surface which accelerates the air beneath the nosecone and guides the air smoothly to the diffusers' inlets. At the rear side of the undertray a double diffuser with a ground effect device on the middle is placed in order to take advantage of the oncoming air on the center. The vertical flaps that are placed on these diffusers are designed with a specific curvature in order to deflect the air exiting the undertray and send it directly in the low-pressure area just behind the rear wheels, in order to reduce the drag that is created there. Similar vertical flaps are placed at the outlets of both side diffusers in order to avoid flow separation and guide the air on the upper surface of the central diffuser and use it to generate more downforce.
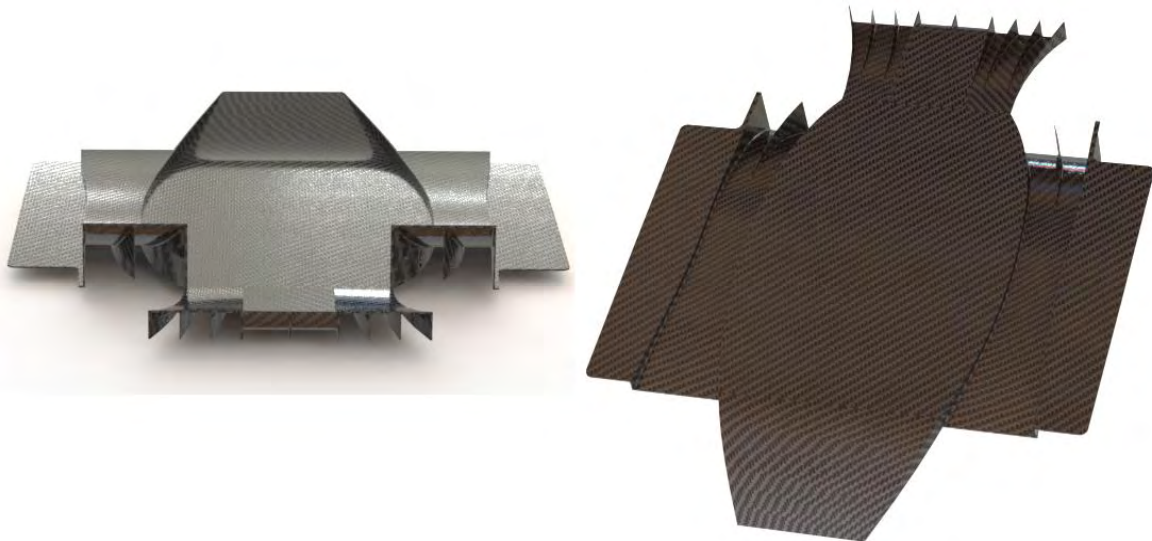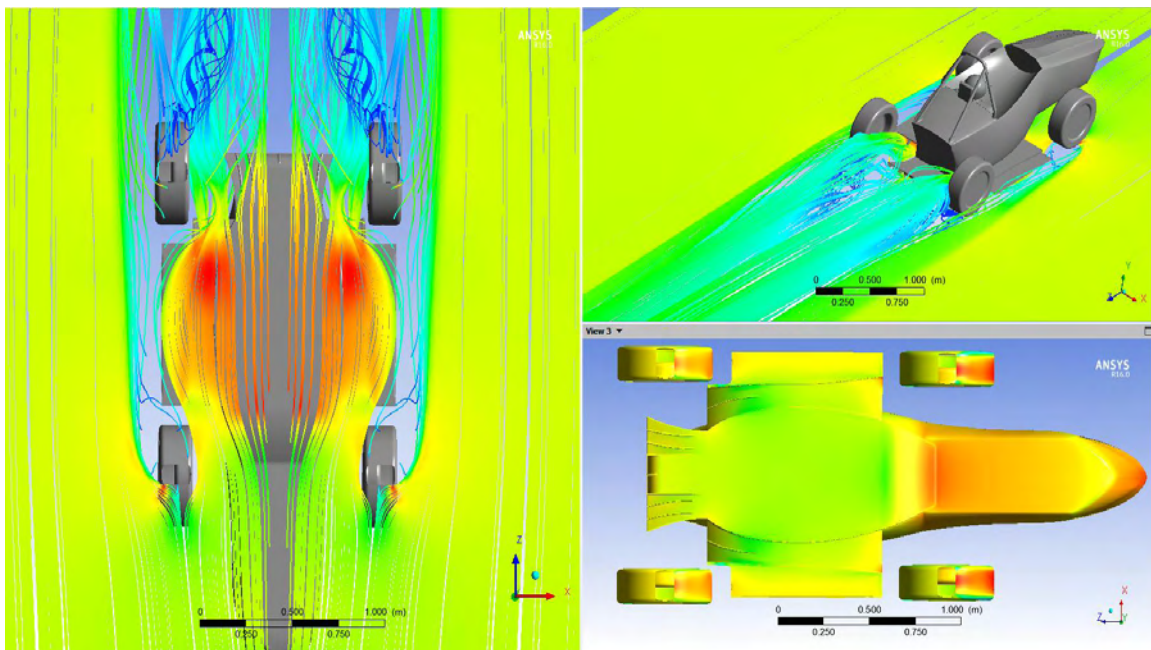

Figure 123: *Side & double diffusers CAD designs*

This final type of undertray produce about double as much downforce as any previous type and reaches an amount of 86.34 *N,* while its drag has fallen to 77.64 *N* which is an acceptable value comparing to its increased efficiency. Although, that the total weight of this undertray is at 7.36 kg which is heavier than some previous types, the generated amount of downforce is higher than its own weight so it is the most efficient one.

Characteristics	
Number of Diffusers	*3*
Diffuser Angle	*15.5˚*
Ground Effect Device	✔
Downforce	*86.34 N*
Drag	*77.64 N*
Weight	*7.36 Kg*

On the *Figure* bellow it shown that, the flow is attached along the whole undertray's surface. The low pressure that is created at the outlets of the side diffusers sucks the oncoming air and prevents it from escaping from the sides. Again, due to that the diffuser tunnels are extended along the whole underside of the car seems that it makes the air to accelerate more along the whole underside of the car but especially at the rear end of the undertray which is also the reason why it generates higher amounts of downforce. Additionally, from the pressure distribution it is shown that the center of pressure has been clearly transferred more to the rear of the car due to the longer diffusers, while the pressure has been distributed equally at the whole underside surface. Finally, due to the curvature surface on the undertray's inlet, the extremely low pressure region that occurred on the previous model seems to have been disappeared and the pressure is now smoother, allowing the air to flow directly to the rear diffusers.

Figure 124: *Streamlines and pressure distribution for the side & double diffusers undertray*

As it has been already mentioned, the CFD simulations for all the undertray types were done in a ride height of 4cm from the ground. However, the undertray is an aerodynamic device which is strictly connected with the ground effect, thus the distance from the moving road has a direct impact to the aerodynamic efficiency of the undertray. So, the next step after the selection of the best type of undertray is the definition of the ideal ride height which should compatible with the FSAE regulations. Two extra CFD simulations are done for a ride height of 3 and 2cm and the results are summarized on the table below.

Ride Hight	Lift Coefficient(C_L)	Drag Coefficient(C_D)	Downforce(N)	Drag(N)	Ratio C_L/C_D
4cm	-0,578	0,517	86,34	77,64	1,12
3cm	-0,658	0,521	102,42	78,41	1,26
2cm	-0,675	0,528	137,88	80,04	1,28

Figure 125: *CFD results for different ride heights of the final undertray*

At the ride height of 3cm the lift coefficient is significantly increased from *-0.578* to *-0.658* with just a small increase in drag coefficient from *0.517* to *0.521*, which both resulted in a total downforce of *102.42 N* and a drag of *78.41 N* respectively. For the 2cm ride height on the other hand, the lift coefficient is shown to be just a bit higher at -0.675 which may be due to the fact that less air is entering on the underside of the car, while the drag coefficient increased to 0.528 giving a total drag of 80.04 N and a downforce of 137.88 N. Although, the aerodynamic efficiency and downforce reach their peak at the 2cm ride height, the undertray was finally placed 3cm from the ground due to the FSG 2016 regulations which set a minimum ride height of 3cm for all cars and also due to the "*soft*" suspension setup which could easily led to a collision between the undertray and the ground. On the diagram bellow is shown the change of drag and lift coefficient at the three different ride heights that were tested.
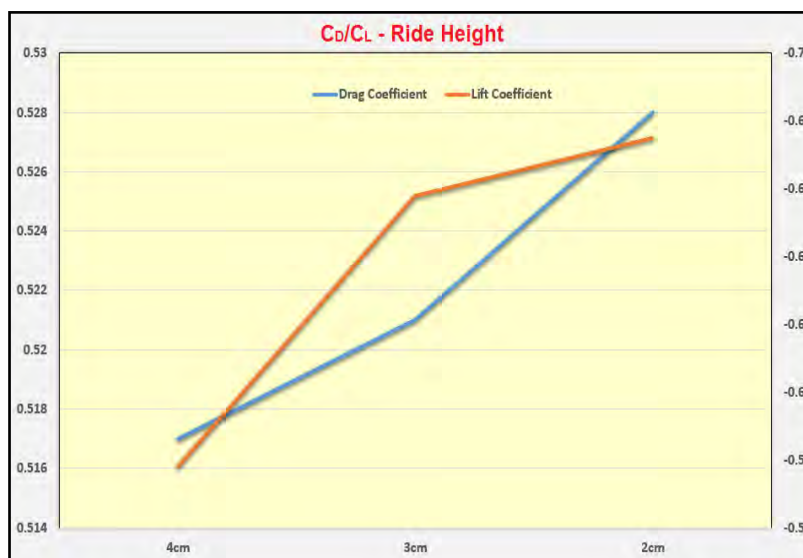

Figure 126: *Drag & Lift coefficients variation with ride height for the final undertray*

After the definition of the optimal ride height for the undertray, four more CFD simulations are done at different speeds of air from 40 – 120km/h in order to test how the undertray operates at these speeds and the affect that it has on the flow field around the vehicle. It is interesting how downforce and drag change almost exponential as the speed increases, while at the final speed of the car the undertray can generate up to 367.22 N of downforce which is about three times its weight.

Speed	Lift Coefficient(C_L)	Drag Coefficient(C_D)	Downforce(N)	Drag(N)	Ratio C_L/C_D
40 km/h	-0,632	0,508	42,39	34,22	1,24
60km/h	-0,658	0,521	102,42	78,41	1,26
80km/h	-0,661	0,512	167,29	126,12	1,29
100km/h	-0,674	0,514	210,85	186,17	1,31
120km/h	-0,682	0,518	367,22	267,08	1,32

Figure 127: *CFD results of the final undertray at different speeds and a ride height of 3cm*
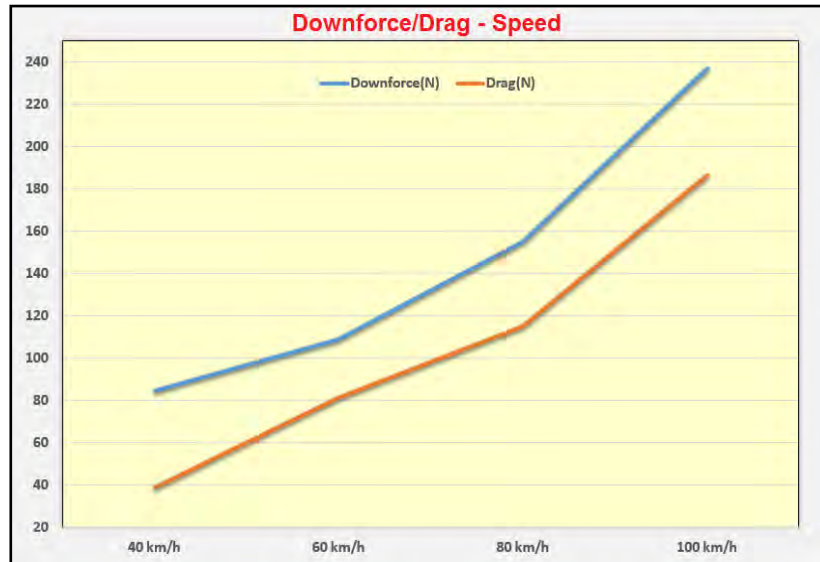
Figure 128: *Drag & Lift coefficients variation with the increase of speed*

4.2.6. Results Comparison

Finally, on the table below are shown the results of the CFD simulations for each type of undertray. It interesting how the final type of undertray has the double efficiency comparing to the first one, while their weight is about the same and there are small differences between the drag. The final undertray was also tested first without the vertical flaps but the results shown that drag is higher due to the flow separation that occurs on the diffusers which also results in lower downforce.

Undertray Type	Lift Coefficient(C_L)	Drag Coefficient(C_D)	Downforce(N)	Drag(N)	Ratio C_L/C_D
Undertray_1	-0,239	0,465	28,7	61,82	0,51
Undertray_2	-0,254	0,499	31,4	71,58	0,51
Undertray_3	-0,342	0,481	44,72	66,84	0,71
Undertray_4	-0,471	0,519	48,62	80,6	0,91
Undertray_5(without *flaps*)	-0,557	0,527	73,56	82,09	1,06
Undertray_5(*with flaps*)	-0,578	0,517	86,34	77,64	1,12

Figure 129: *CFD results in summary for all types of undertrays*
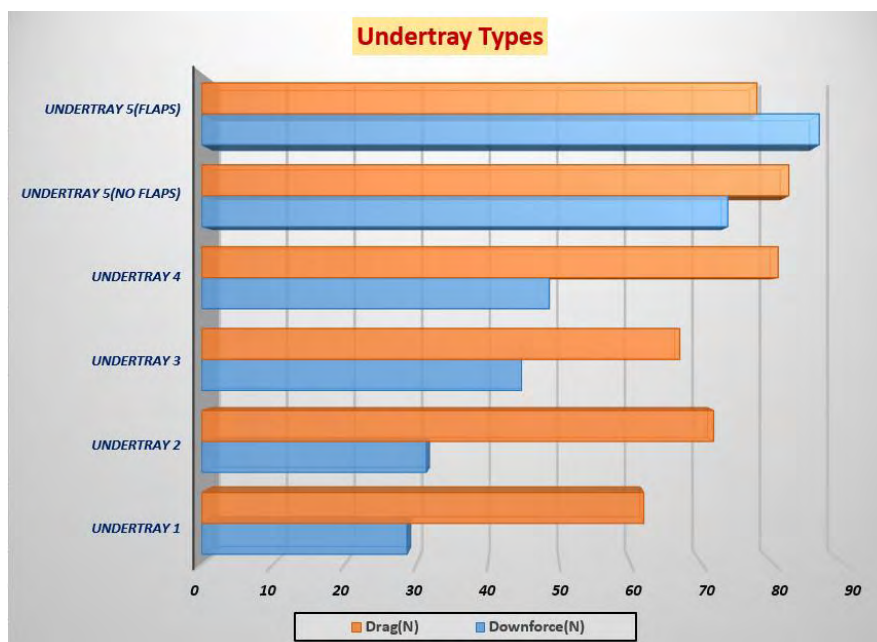

Figure 130: *Downforce and Drag comparison for all the undertrays*

89

4.3. Sidepods

After the selection of the most efficient undertray, sidepods are the next aerodynamic devices to be tested in order to set a complete car CFD model and estimate the final results. Sidepods are used to provide enough air for the cooling system through the radiator, while normalizing the turbulent flow coming from the front wheels and slow down the air in order to be more time for the convection to take place within the radiator's fins. In order to properly design the sidepods to be efficient, it is first necessary to estimate the required amount of mass flow for the radiator in different conditions. Depending on the speed that the car moves, the RPMS of the engine can be significantly different, which means that the engine has different cooling needs at different speeds. After a short calculation based on the average RPMS of the engine for speeds between 40-100km/h, the specifications of the radiator's fan and the dimensions of the radiator, the mass flow requirements of the radiator are estimated approximately for each speed. The graph below highlights in summary these data and was used in order to design all the types of sidepods and test their efficiency.
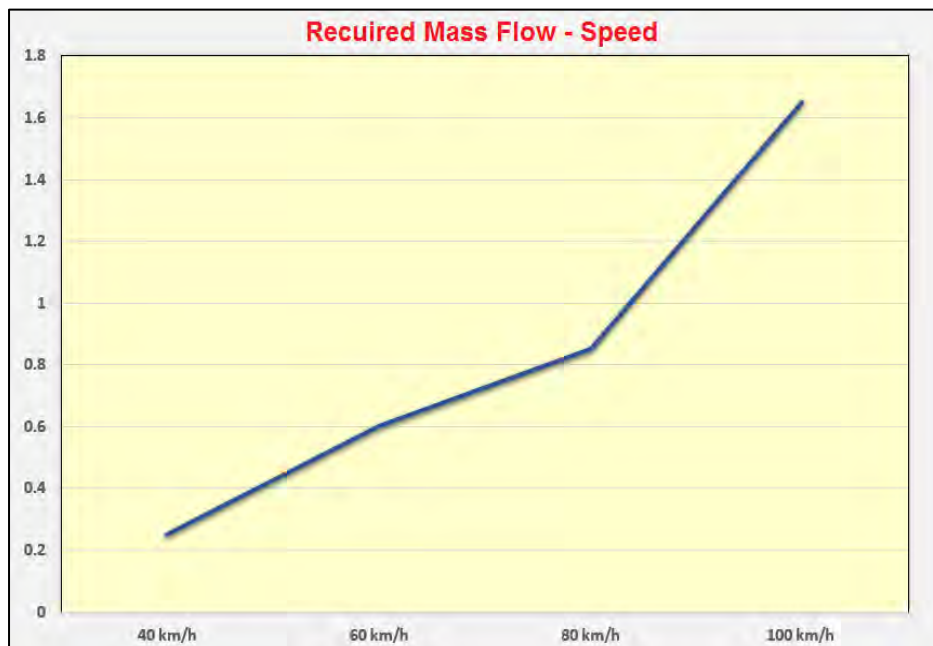

Figure 131: *Required mass flow of air (in kg/s) for the radiator in speeds between 40-100km/h*

Except of the mass flow of air, drag and lift coefficients must again be considered during the designing of the sidepods as their aerodynamic efficiency too. Furthermore, stall should definitely be avoided both on the inner and outer surface of the sidepods not only for the reduction of drag but also because of the huge impact that it has on the efficiency of the radiator inside the sidepod. Due to boundary layer effects, generally at sharp leading edges, the flow separates from the surface and forms strong vortex. In sidepods this stall usually occurs on the sidepod's inlets when the leading edge is designed too sharp and the vortices that are created affect the pressure distribution in front of the radiator. To avoid this undesired situation the inlets of the sidepods have to be designed with a specific curvature radius in order to keep the flow attached on the sidepod walls

and make turbulent flow of the wheels laminar. Numerous CFD simulations of sidepods' inlets are done at the speed of 60km/h, with different radius for their leading edges in order to predict stall and select the identical fillet radius to use for the design of all the types of sidepods.

Firstly, a sidepod model is created with a sharp leading edge on the inlet in order to test if stall can occur at any speed between 40-100km/h, which are the speeds that an FSAE car can reach during a race. On the figure below it is shown that at the speed of 60km/h and with a sharp leading edge, the flow can easily separate and generate vortices either on the interior or the exterior of the sidepod. On that case, the flow is separated at the outer surface of the sidepod, which can increase the drag of the car and even worse affect other aerodynamic devices like the rear wing. The model with the sharp edge resulted in a drag coefficient of *0.157*.
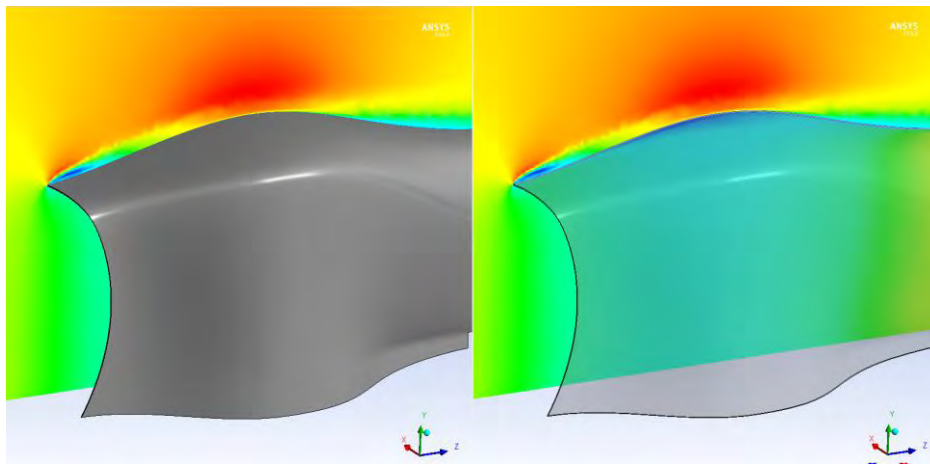
Figure 132: *Separation occurring on the inlet of the sidepod due to the sharp leading edge*

Four sidepods models are created next with leading edge radius between 1-4cm. After the CFD simulations at 60km/h it resulted that stall stops at a radius of 2cm or above and the flow stays attached both in the interior and exterior of the sidepod as it shown on the figure below. For the 2cm radius model a drag coefficient of *0.134* occur which is significantly improved comparing to the sharp edge model. So, the leading edge radius on the inlets of all the sidepods types are selected to be 2cm as the minimum permitted radius to avoid stall on the inlet.
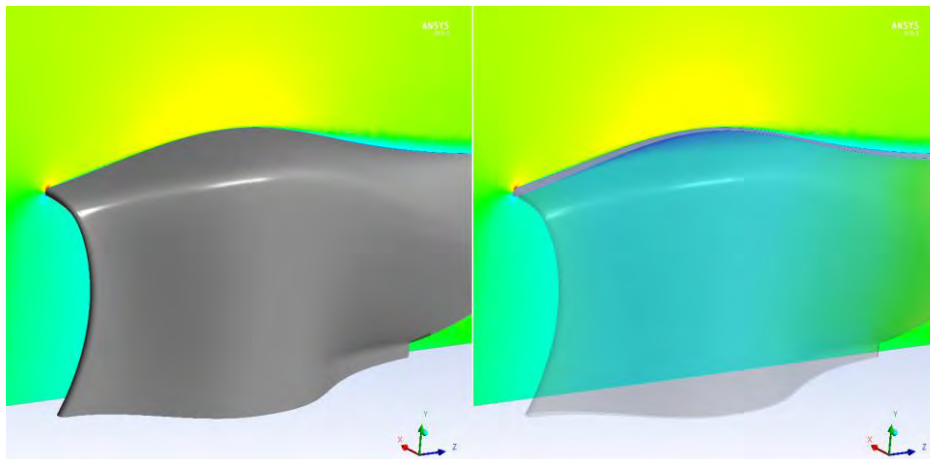
Figure 133: *Stall is eliminated for leading edge's radius above 2cm*

4.3.1. No Sidepods

Before proceeding to the design of the sidepods it is first necessary to simulate the car model without any sidepods in order to take a first idea of how the flow field is formed behind the front wheels and how would the radiator operate in these conditions. The CFD simulation is done at 60km/h and the aim is to calculate the pressure distribution in the frontal area of the radiator. The radiator is placed in the position that is designed on the side of the chassis close to the main hoop. The results of the CFD simulation show that the region between the front and rear wheels is a region with a high turbulent flow field due to the strong vortices that are created behind the front wheels. These vortices are directing straight in to the radiator's inlet and have a huge impact on the pressure field in front of it. As it is shown on the figure below the pressure distribution at the lower right side of the radiator is low due to the vortices and that means that this region of the radiator would not let the air to flow in to the fins as it happens on the rest surface. This situation is surely undesired for the correct operation of the sidepod as it essentially reduces the active area of the radiator.
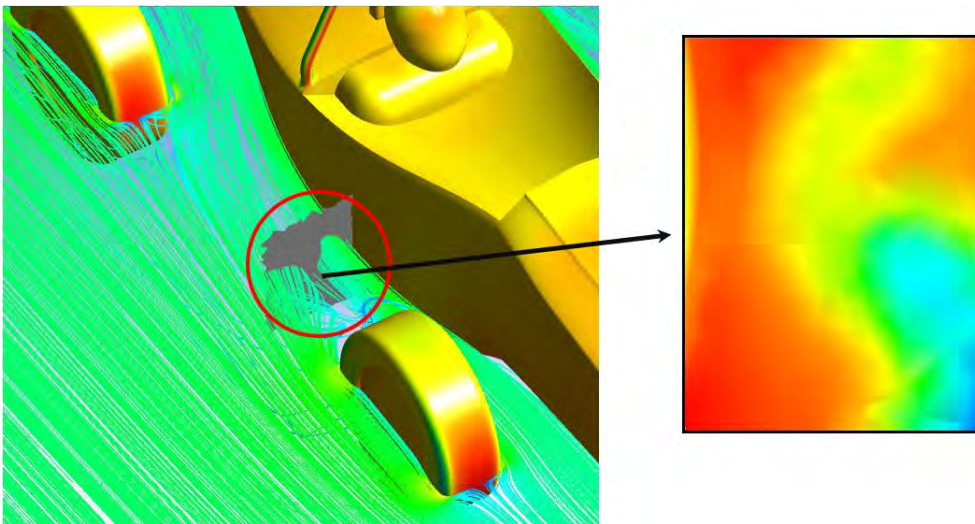
Figure 134: *Pressure distribution on the frontal surface of the radiator, for the model without sidepods*

At that case, the mass flow of air passing through the radiator is about 0.892 kg/s. Although this mas flow is higher than the required amount of air (*0.63kg/s*) at the speed of 60km/h, the flow passing throw the radiator is basically turbulent which is also shown by the non-uniform pressure distribution in front of the radiator. The lift coefficient at that case is *0.286*, while the drag coefficient is low as expected at *0.426.* Note that at this case the lift coefficient has a positive value which means that the car without any aerodynamic device mounted on it generates lift.

Characteristics	
Mass flow	*0.892 Kg/s*
Lift Coefficient (*C_L*)	*0.286*
Drag Coefficient (*C_D*)	*0.426*

4.3.2. Lowered Sidepods

From the previous simulation, it is clear that the use of a sidepod is necessary in order to protect the radiator from the turbulent flow behind the wheels and improve its efficiency. So, the aim is to design a sidepod in such a way that it can eliminate turbulent flow on the inlet and create an equally distributed pressure field on the radiator's surface. The first type of sidepods have a lowering at the side of the outlet in order to work as a nozzle and accelerate the air coming out in order to drop pressure and create a greater pressure difference between the front and rear of the radiator.

Figure 135: *CAD designs of the first type of sidepods*

However, this type of sidepods seems to create a very low pressure region in front of the radiator. There is a peak for the pressure distribution between the front and rear side of the radiator, after which it seems that a region with extremely low pressure behind the radiator can significantly affect the radiator, the same way as when this low pressure is occurring on the radiator's surface. Considering also that just beneath the outlet of the sidepod there is also the outlet of the diffuser the pressure drops even more, so the outlet of the sidepods should be designed is such a way that will not lead to such a high pressure drop. The use of a sidepod resulted in an increase of the mass flow up to *0.969kg/h,* while drag coefficient occur at *0.527* and lift coefficient at *-0.601.*
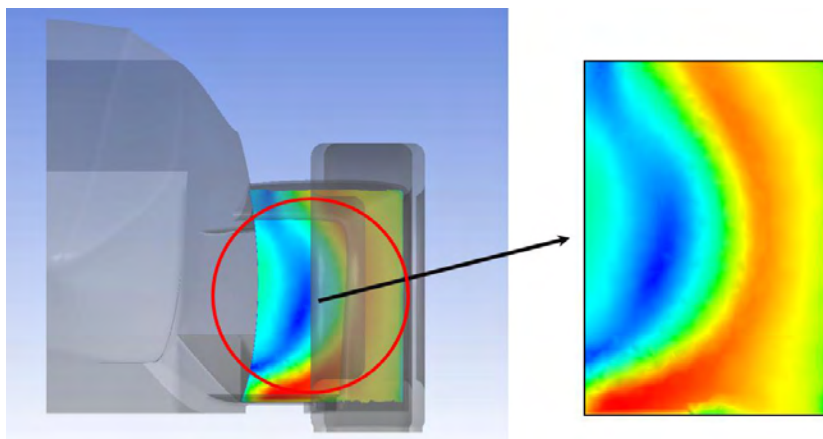

Figure 136: *Pressure distribution on the frontal surface of the radiator, for the lowered sidepods model*

Characteristics	
Mass flow	0.969 Kg/s
Lift Coefficient (C_L)	-0.601
Drag Coefficient (C_D)	0.527

4.3.3. Lifted Sidepods

To improve the previous undesired situation with the low-pressure region at the rear of the radiator, the new sidepods are designed with a lifted rear surface which leaded to a bigger opening at the outlet of the sidepods. However, the outlet should stay small enough in order for the pressure to remain lower that the pressure in front of the radiator. In addition, this lifted surface of the sidepods should be designed according to that and avoid also any flow separation on the outer surface of the sidepod due to high angle.
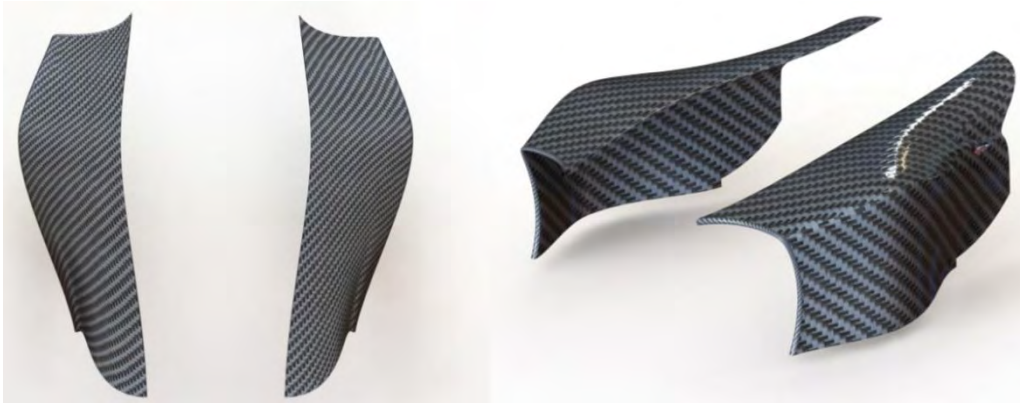
Figure 137: *CAD designs of the second type of sidepods with lifted upper surface*

At that case, it seems that the pressure distribution in the radiator's surface is much more improved and equally distributed. However, there are again some regions around the radiator that still have low pressure but doesn't affect the flow. This type of undertray provide to the radiator a mass flow of *0.946 kg/s*, which might be slightly lower than the previous type but with such uniform pressure distribution the efficiency of the radiator is higher.
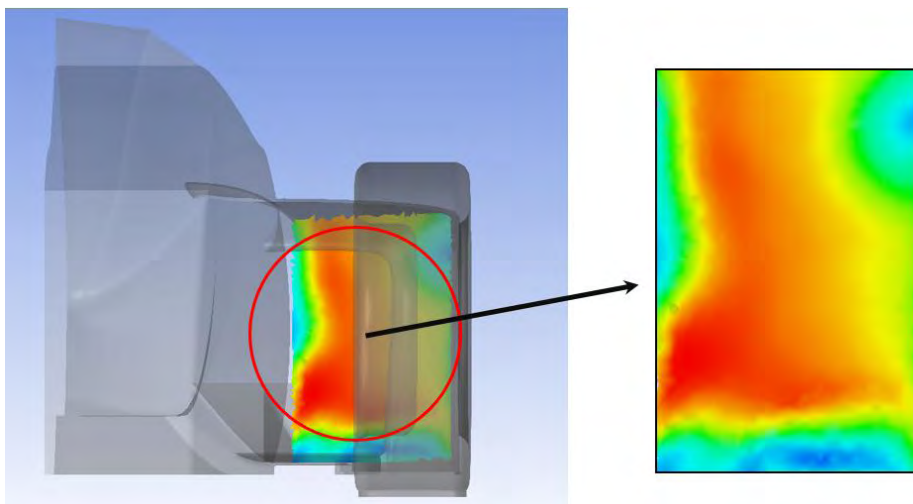
Figure 138: *Pressure distribution on the frontal surface of the radiator, for the lifted sidepods model*

Characteristics	
Mass flow	*0.946 Kg/s*
Lift Coefficient (C_L)	*-0.642*
Drag Coefficient (C_D)	*0.538*

4.3.4. Final Sidepods

From the previous case, it is clear that the most appropriate type of sidepods for the flow field between the wheels is the one with a lift surface on the outlet. The final type of sidepods is similar to that model, with some extra improvements. The rear lifted surface at the rear is redesigned to take advantage of that surface in order to generate extra downforce without any flow separation. At the same time, the sides of the sidepods are now thinner in order to make the outlet small enough to keep the pressure in desired low limits and due to FSAE regulations. Three gills are placed at the side of each sidepod working as openings for the stalled air which is trapped behind the radiator and affects the pressure difference, in order to reduce the total, drag and let the air flow easier through the sidepod.
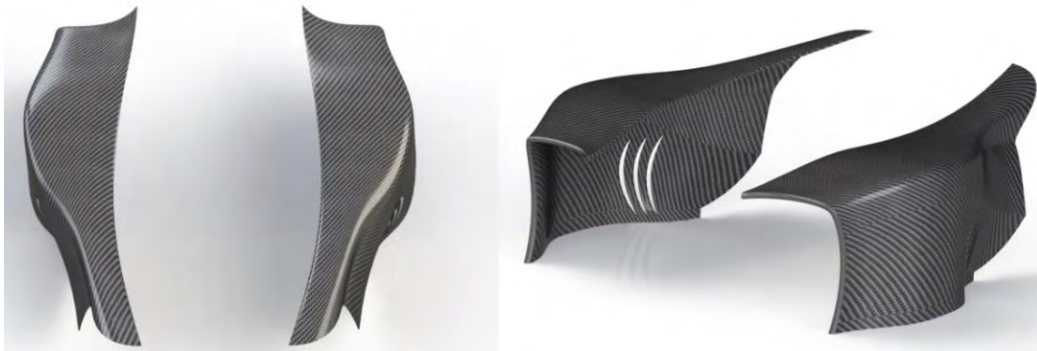
Figure 139: *CAD designs of the final type of sidepods with lifted upper surface*

As it is shown on the figure below, the pressure distribution at the final sidepods models is equally distributed and the low-pressure regions at the edges of the radiator are now eliminated. Some small regions with low pressure do not affect the efficiency of the radiator as they are not in front of the fins of the radiator. These final sidepods provide a mass flow of air up to 0.958kg/s which is improved comparing to the previous model, while lift coefficient is increased up to *-0.668* and drag coefficient is declined at *0.532*.
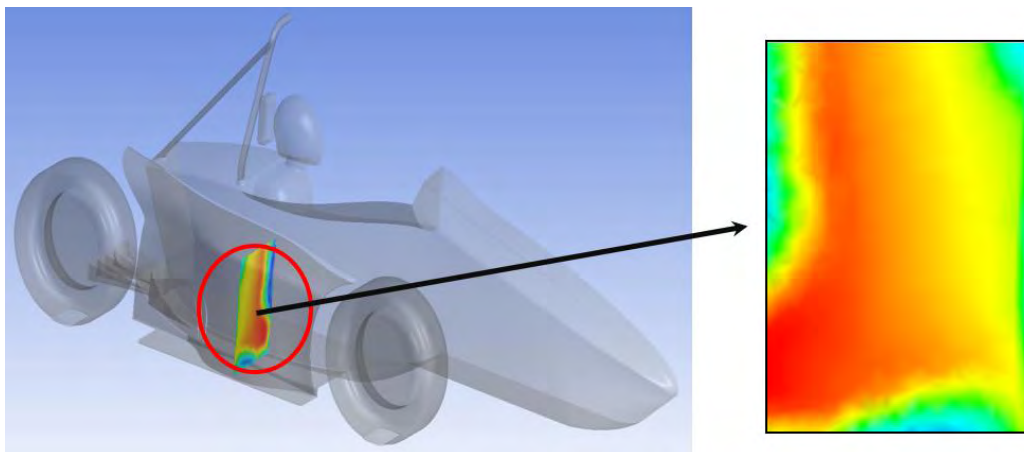

Figure 140: *Pressure distribution on the frontal surface of the radiator, for the final sidepods model*

Characteristics	
Mass flow	*0.958 Kg/s*
Lift Coefficient (C_L)	*-0.668*
Drag Coefficient (C_D)	*0.532*

As it is shown on the figure below, the flow field between the front and rear wheels is now clearly laminar. The use of the sidepod protects the radiator from the turbulent flow that is created behind the front wheels and it also slows down the flow entering the sidepod in order to give more time to the convection to take place inside the radiator's fins. The side gills on the sidepods let also the excessive amount of air to flow out of the sidepods, keeping with that way the pressure on the outlet to stay on the desired limits.
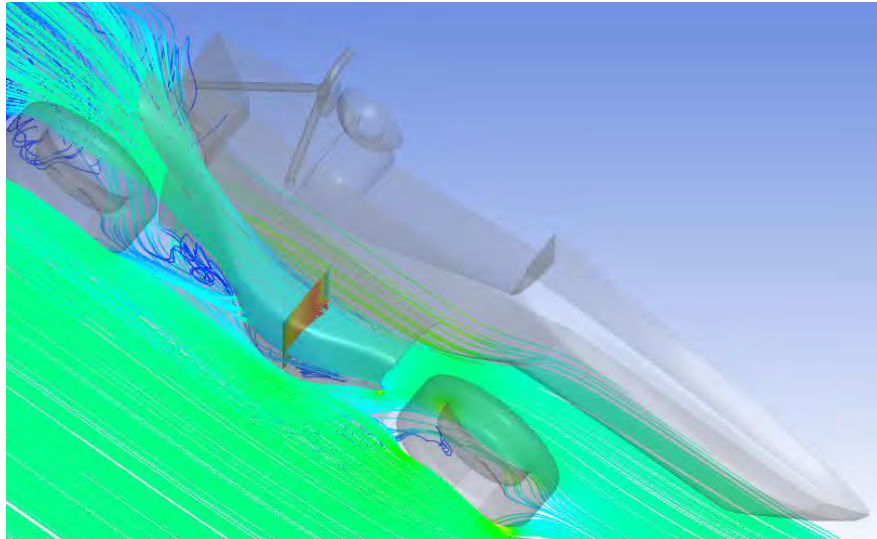
Figure 141: *Improved flow field inside the final sidepods*

The lifted inlet of the undertray, which is just beneath the inlet of the sidepods, causes a slight separation of the flow at the bottom of the sidepod. However, this separation doesn't affect the efficiency of the radiator because it is direct to the end cap at the underside of the radiator and not to the radiator's fins. Considering also that in reality there is also the fan of the radiator which sucks even more air, these low-pressure regions in front of the radiator would probably disappear.
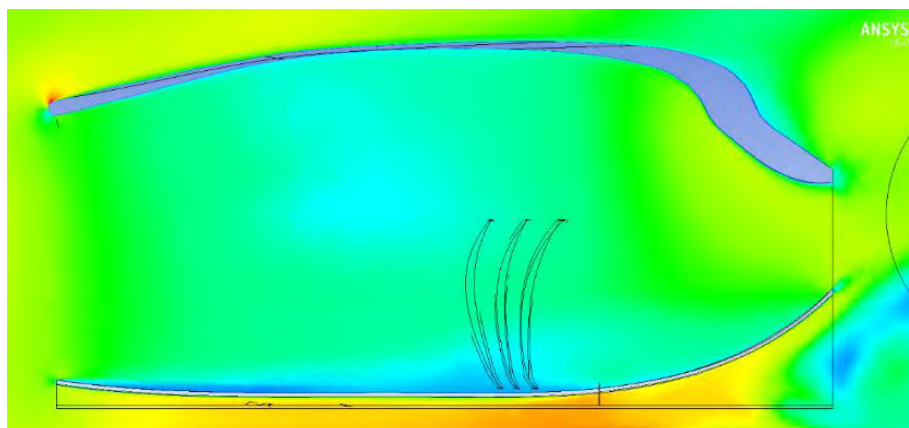

Figure 142: *Pressure distribution inside the final sidepods*

The model with the final sidepods have to be tested in all possible speeds between 40-100km/h in order to estimate if the mass flow of air entering the sidepods and passing through the radiator is enough, comparing to the required mass flow that was calculated in the first place. As it Is shown on the table below, the mass flow gradually increases at higher speeds reaching up to 1.652kg/s of air at the final speed of the 100km/h. Drag and lift coefficients have also the same trend, but drag coefficient seems to increase with a higher rate, for speeds above 80km/h. This can be seen also from the aerodynamic efficiency (C_L / C_D), which increases steadily up to a peak of 1.4 at the speed of 80km/h and above that speed the significant increase of drag drops the efficiency at 1.27.

Sidepods 3				
Speed	Mass flow(kg/s)	Lift Coefficient(C_L)	Drag Coefficient(C_D)	Ratio C_L/C_D
40 km/h	0,686	-0,546	0,506	1,08
60 km/h	0,958	-0,668	0,532	1,26
80 km/h	1,298	-0,871	0,623	1,4
100 km/h	1,652	-0,939	0,738	1,27

Figure 143: *Mass flow and aerodynamic characteristics of the final sidepods model at speeds from 40-100km/h*

The diagram below shows that the mass flow of air with the final sidepods exceeds of the required mass flow that was estimated for the correct operation of the radiator, for all the speeds from 40km/h to 100km/h. In some speeds, also the estimated mass flow seems to be double as the required mass flow, which is very positive for safety reasons. At the final speed of 100km/h however, the real mass flow is slightly higher than the required mass flow, but this is not a big problem while the time period that the car reaches and stays at its final speed during the race is negligent.
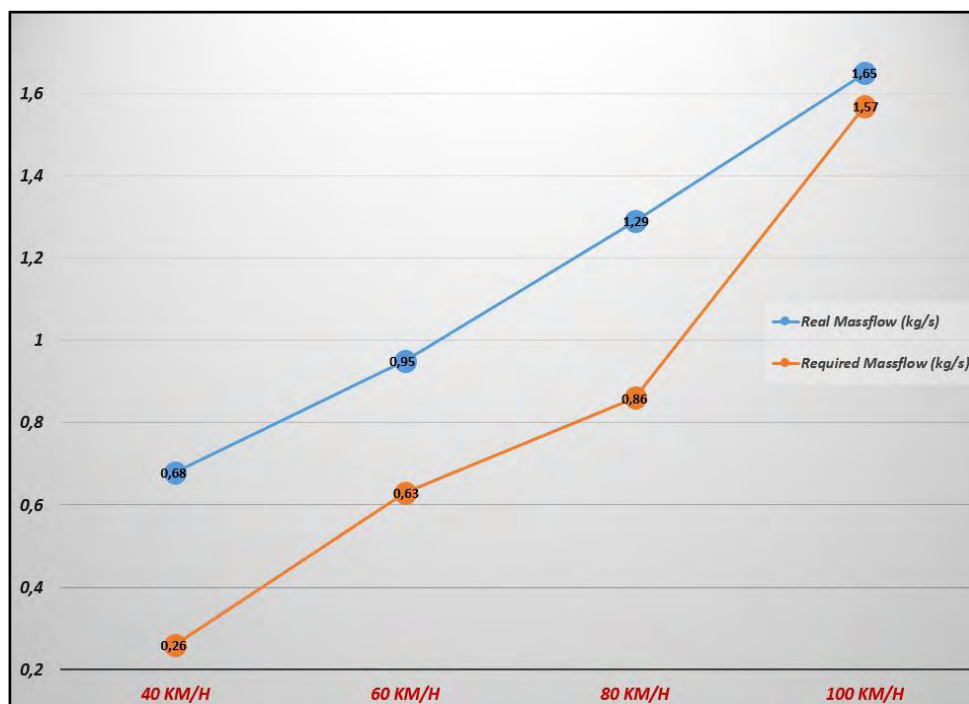
Figure 144: *Real mass flow at the finals sidepod, comparing to the estimated required mass flow at different speeds*

4.4. Wings

4.4.1. Front Wing

In order to properly design the front wing of the aerodynamic package of the car, it is necessary first to select the appropriate NACA airfoil type to assembly the front wing and estimate also their identical angle of attack, number of elements and their dimensions. Furthermore, three different types of front wings are designed and tested in order to select the most efficient one and determine the correct ride height to be placed. All the CFD simulations are done at the speed of 60lm/h.

4.4.2.1. NACA Airfoil selection

The first step before proceeding to the design of a complete front wing model is the selection of the most efficient type of NACA airfoil. Due to the lack of time there were not tested different types of NACA airfoil profiles, but the selection process was based on the airfoils theory and on a bibliography research for the designing of different front wings from other FSAE teams. The conclusion of this research is that the most efficient and appropriate type of airfoil for the design of a front wing of a FSAE car is the *NACA-6412* considering the low speeds that the cars move and the fact that the front wing should not generate big amounts of drag which can affect other aerodynamic devices on the rear.
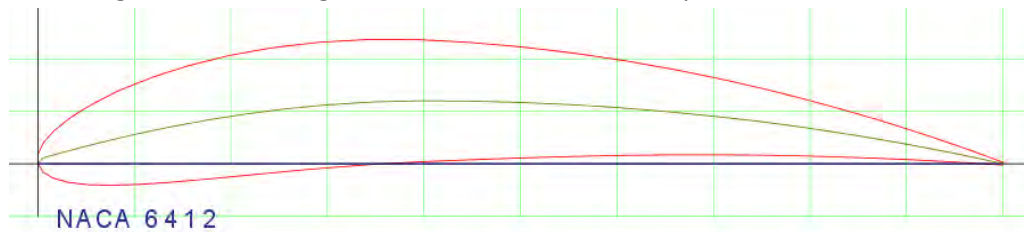
NACA 6412

Figure 145: *NACA 6412 airfoil used on the front wing*

After having select the airfoil that is going to be used for the assembly of the front wing, the next step is selection of the most efficient angle of attack for these airfoils. For the front wing the number of elements that are used depends on their position on the wing. For the main elements which is the central airfoil beneath the nosecone most times is used a single element, while for the region between the front wheels and the nosecone are usually placed two to three elements or in some cases even four, depending on the design of the front wing and the wheels' diameter. In order to determine the angle of attack for the elements three models are created tested with 3D CFD simulations. The first model is a single NACA 6412 airfoil with 20cm width and 30cm chord length and is tested for angles from 4° to 14°.

1st Element - *NACA 6412*			
Angle of Attack	Lift Coefficient(C_L)	Drag Coefficient(C_D)	Ratio C_L/C_D
4°	-1.443	0.317	4.55
6°	-1.521	0.341	4.46
8°	-1.591	0.373	4.27
10°	-1.659	0.413	4.02
12°	-1.72	0.46	3.74
14°	-1.777	0.511	3.48

Figure 146: *CFD results of the single airfoil model for angles between 4° and 14°*

The single element is selected to be placed with an angle of attack of 10°, having a lift coefficient of -1.659, a drag coefficient of 0.413 and an efficiency of 4.02. The second model has two elements, with the first being the element of the previous model with the new angle of attack and the second one being a NACA 6412 airfoil with 20cm width and 25cm chord length. At this model only the angle of attack of the second airfoil is tested for angles between 10° and 20°. According to the results of the table below, the second airfoil is placed at an angle of 18°, where it has a lift coefficient of -1.708, a drag coefficient of 0.583 and the efficiency is at 2.93.

2nd Element - NACA 6412			
Angle of Attack	Lift Coefficient(C_L)	Drag Coefficient(C_D)	Ratio C_L/C_D
10°	-1.52	0.471	3.23
12°	-1.569	0.491	3.2
14°	-1.618	0.517	3.13
16°	-1.664	0.548	3.04
18°	-1.708	0.583	2.93
20°	-1.748	0.621	2.81

Figure 147: *CFD results of the double airfoils model for angles between 10° and 20°*

The third model is consisted of three elements, which are going to be the part of the wing which is placed just in front of the front wheels. The third airfoil that is placed is again a NACA 6412 airfoil with a width of 20cm and a chord length of 15cm. The previous two airfoils remain with their selected angles of attack of 10° and 18° respectively and only the third airfoil is tested in different angles of attack from 20° to 30°. The results of the simulations for the three airfoils models shown that the optimal angle of attack for the third airfoil is at 28° were the lift coefficient is up to -1.782, the drag coefficient is at 0.729 and the efficiency is at 2.44.

| 3rd Element - NACA 6412			
Angle of Attack	Lift Coefficient(C_L)	Drag Coefficient(C_D)	Ratio C_L/C_D
20°	-1.67	0.641	2.61
22°	-1.702	0.661	2.57
24°	-1.732	0.684	2.53
26°	-1.756	0.709	2.48
28°	-1.782	0.729	2.44
30°	-1.809	0.75	2.41

Figure 148: *CFD results of the three airfoils mode for angles between 20° and 30°*

However, the selection process of the most appropriate angle of attack was not only based on the drag and lift coefficients. Velocity and pressure were also taken under consideration in order predict the angle of attack above of witch the flow is separated and stall occurs. The more elements are used the higher the angle of attack can be, but drag increases rapidly to which is an undesired situation. On the figure below it shown the velocity field around the airfoils for all the models and angles of attack that were tested.
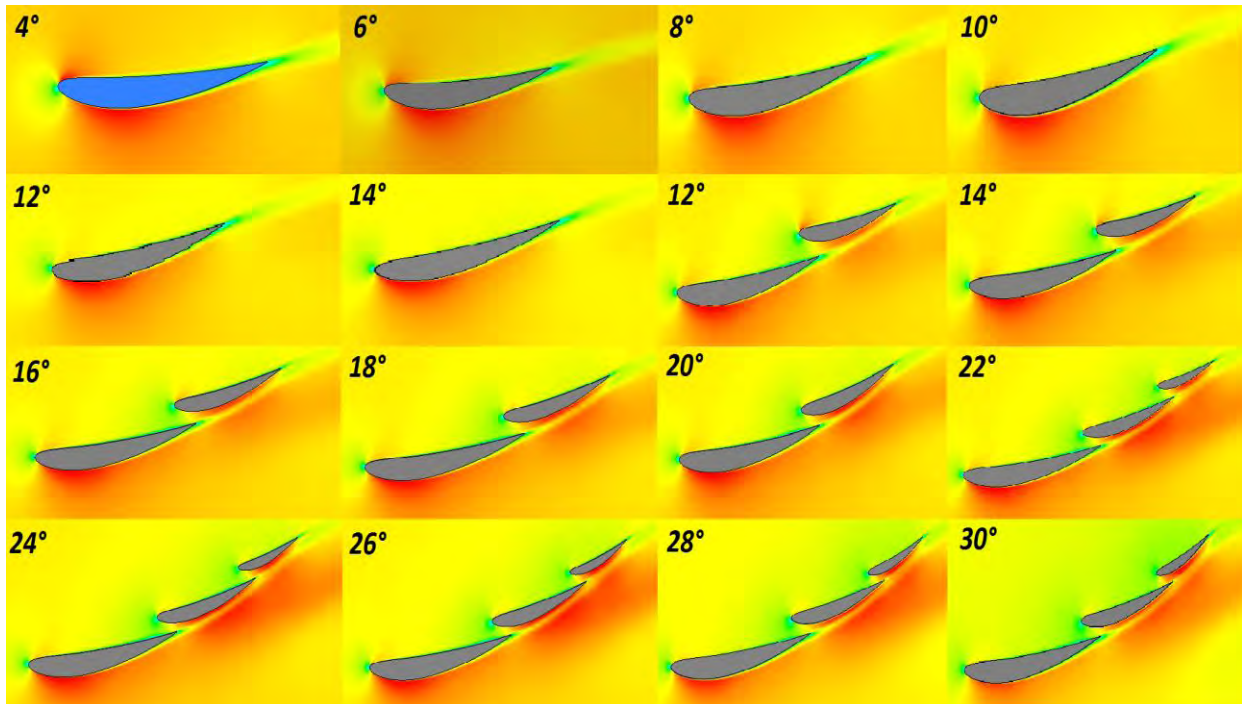
Figure 149: *Velocity field for the three NACA 6412 airfoils models, for angles between 4° and 30°*

For the main airfoil of the front wing, which is the element that is placed on the center of the wing under the nosecone it usually used a symmetric airfoil in order to let the air pass unobstructed to the undertray's inlets. However, the NACA 4412 airfoil is selected as the main airfoil because of its less aggressive shape and the fact that is an airfoil which can take a great advantage of ground effect at low speeds without any flow separation and generate higher amount of downforce comparing to the symmetric airfoil which can sometimes even produce lift.
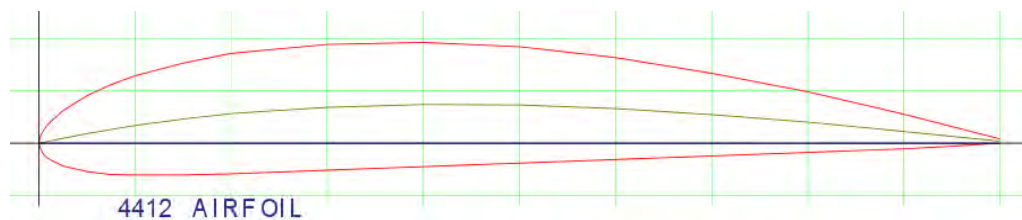
Figure 150: *NACA 4412 airfoil used as the main element of the front wing*

The main airfoil NACA 4412 is always used as a single element and only in small angles of attack in order to generate low drag and avoid stall to feed the undertray with a laminar flow and improve its efficiency. Again, a single element with 20cm width and a chord length of 35cm is tested with 3D CFD simulations for angles between 2° and 8°. The

main airfoil is selected to be placed with an angle of attack of 6**°** where the lift coefficient is at -1.318 and the drag coefficient is at 0.272, resulting in a high efficiency of 4.85. In comparison with the NACA 6412, it is interesting how the NACA 4412 is increasing its efficiency as the angle of attack is getting higher which is due to the low amount of drag that is generating and which is the main reason that was selected as the main airfoil of the front wing.

Main Element - *NACA 4412*			
Angle of Attack	**Lift Coefficient(C_L)**	**Drag Coefficient(C_D)**	**Ratio C_L/C_D**
2°	-1.104	0.251	4.4
4°	-1.225	0.256	4.79
6°	-1.318	0.272	4.85
8°	-1.402	0.299	4.69

Figure 151: *CFD results of the main airfoil model for angles between 2° and 8°*

Except of the aerodynamic characteristics of the main airfoil for all these angles, there are also tested the velocity and pressure contours that occur around the airfoil in order to estimate when stall occurs and how the separated flow is guiding to the undertray. It is also clear from the velocity field, how much less drag is produced with this type of airfoil comparing to the previous one. On the figures below are shown both the velocity field and pressure distribution around the airfoil for all cases with angles from 2*° to 8°.*
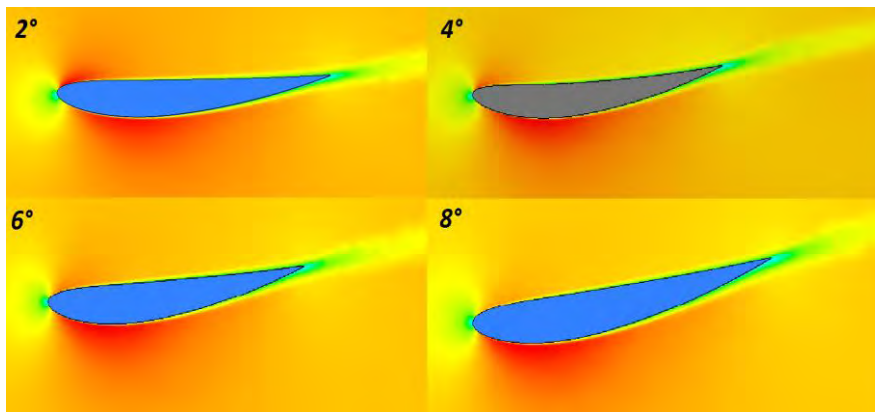
Figure 152: *Velocity field of NACA 4412 main airfoil model, for angles between 2° and 8°*
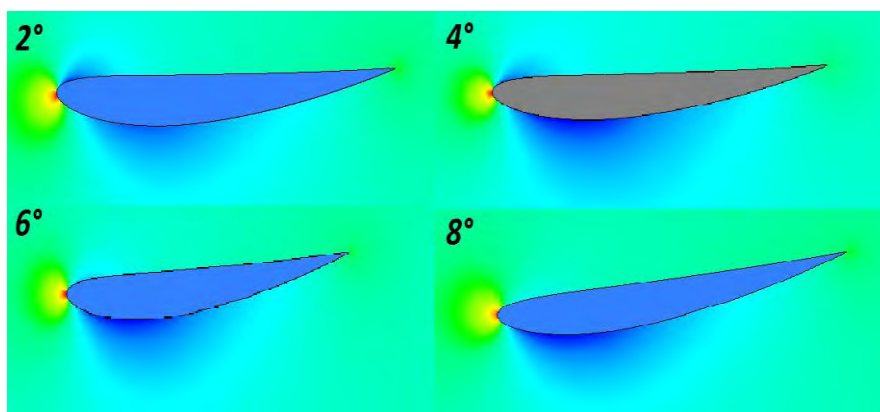
Figure 153: *Pressure distribution of NACA 4412 main airfoil model, for angles between 2° and 8°*

4.4.2.2. Front Wing

After the definition of the most efficient angle of attack for the two, three and main element, the front wing is ready to be designed. The previous three models are now redesigned with different dimensions in order to assembly the front wing and be compatible with FSAE rules. In more detail, the main element NACA 4412 has now a width of 60cm and its position will be just under the nosecone. The two elements NACA 6412 have a width of 30cm, while their position on the front wing is between the inner side of the front wheels and the main element. The reason that these two airfoils are placed on this specific position is to send the oncoming air directly to the sidepods in comparison with the three airfoils which would deflect the air above the sidepods. Finally, the three NACA 6412 elements are place at the outer side of the front wing, just in front of the front wheels and have the same width as the wheels 25cm. The aim of these three airfoils in front of the wing is to deflect air above or by the sides of the front wheels in order to avoid flow separation and reduce the drag.
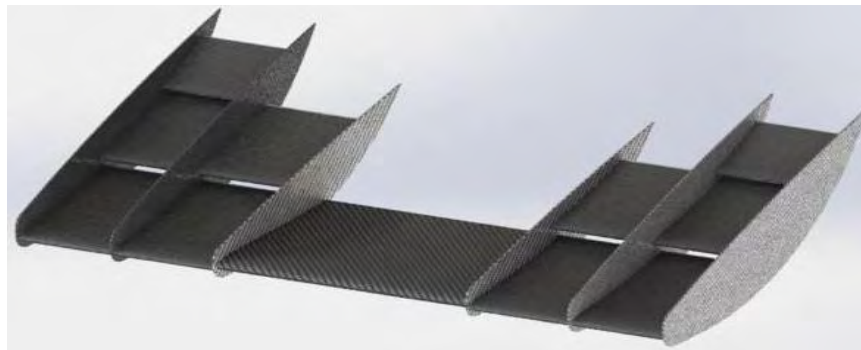
Figure 154: *CAD Design of the front wing*

The CFD results of the front wing at 60km/h shown that the wing at a ride height of 3cm has a lift coefficient of -5.88 and a drag coefficient of 1.012 which result in a total efficiency of 5.81. Although the lift coefficient is high the small distance of the ground can lead to flow separation at the first elements of the wing thus the drag is increasing significantly. This can be also seen by the velocity field on the figure below, where the blue color shows regions where stall has occurred and it is clear that stall begins below the two elements and affect also the flow beneath the main element.
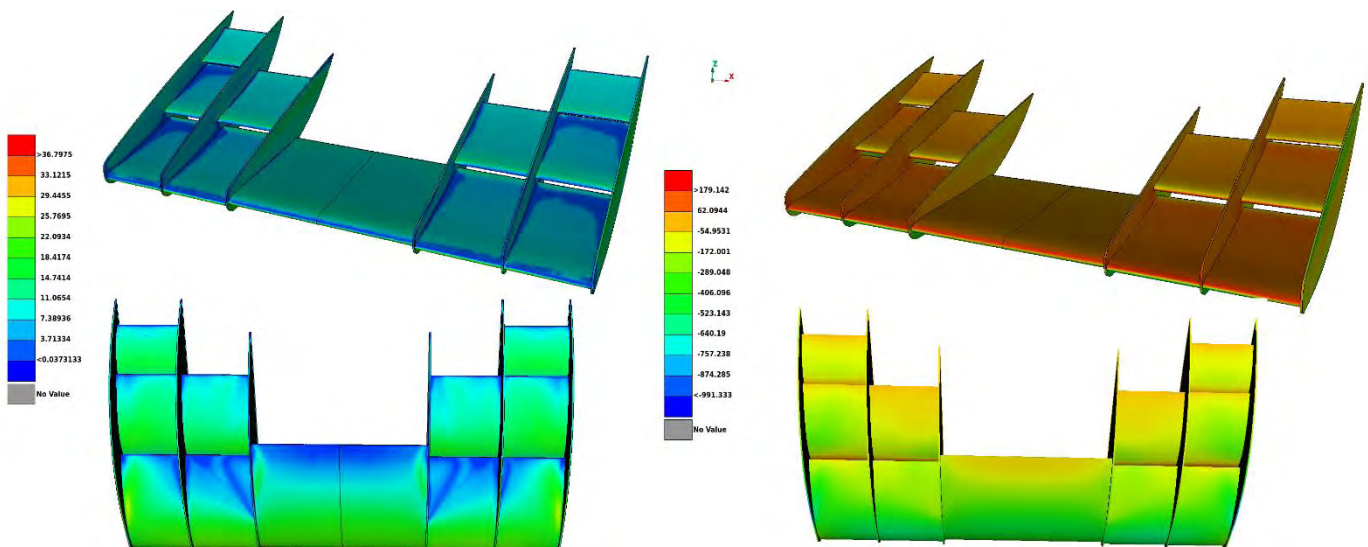

Figure 155: *Velocity field and Pressure distribution of the front wing at a ride height of 3cm*

Due to the small distance between the front wing and the ground the efficiency of the wing is strictly connected with the ride height of the moving road. That means that when the front wing is placed close to the ground, the ground effect takes place and so, the final step is to select the appropriate ride height to place the front wing in order to increase its efficiency and avoid stall at any cost. Five CFD simulations of the front wing are done at a speed of 60km/h, for five different ride heights from 3cm to 6cm. The front wing is finally placed 6cm from the ground were the lift coefficient is at -5.692 and drag coefficient has dropped at 0.917 resulting in a 6.21 efficiency.

Ride Height	Lift Coefficient(C_L)	Drag Coefficient(C_D)	Downforce(N)	Drag(N)	Ratio C_L/C_D
3cm	-5.88	1.012	198.93	33.84	5.81
4cm	-5.733	0.973	188.93	32.33	5.89
5cm	-5.68	0.948	181.41	30.23	5.99
6cm	-5.692	0.917	184.96	29.23	6.21

Figure 156: *CFD Results of the front wing at ride heights from 3 - 6cm*

On the figures below it shown how the velocity field around the airfoils is affected by the ride height at each simulation. For the part of the wing with the two airfoils it is shown that at the 4cm there is a large flow separation at the first airfoil which affects significantly the second one and increases drag, which at the ride height of 6cm seems to have been eliminated and the flow stays attached on the airfoils. The same situation, can be seen for the velocity field of the three airfoils, were again at 4cm there is a green region behind the airfoils were the flow is separated, which again at 6cm has disappeared improving the efficiency and the drag coefficient as it shown on the table. Finally, the streamlines of the front wing confirm this situation, as at 4cm are shown the strong turbulences that are created behind the wing due to the stall, while at 6cm the flow is more laminar and the streamlines are straight.
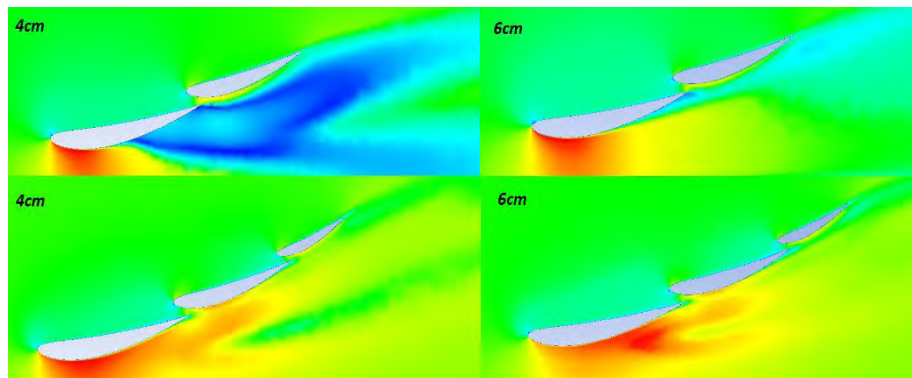
Figure 158: *Velocity field around the front wing for 4 and 6cm ride height*
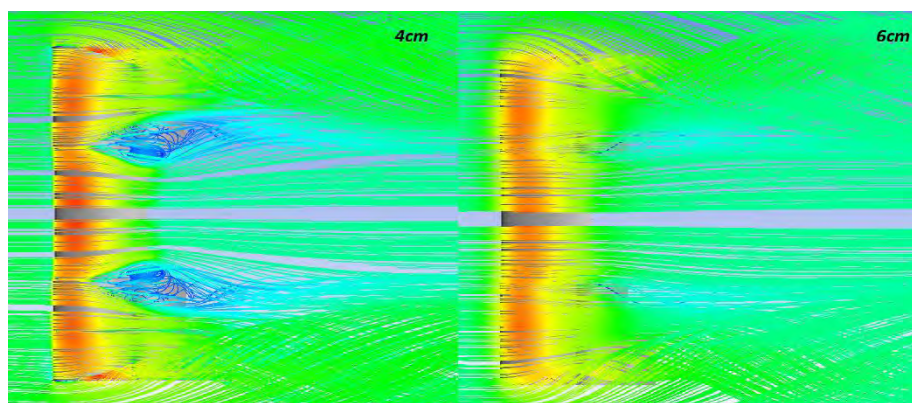
Figure 157: *Streamlines of the front wing for 4 and 6cm ride height*

4.4.2. Rear Wing

In order to properly design the rear wing of the aerodynamic package, it is first necessary to select the most appropriate type of airfoil to be used in order to achieve the highest possible efficiency for the rear wing. The aim of the rear wing is to produce high amounts of downforce in order to push the rear tires to the road and balance the aerodynamic forces acting on the car. For that reason, high lift airfoils are preferable, but again the amount of drag being produced has to stay in logically low levels.

4.4.2.1. NACA Airfoil selection

For the selection of the NACA airfoil to be used for the assembling of the rear wing, a bibliographic research was done again based on other FSAE teams and on the aerodynamics theory for high lift and low speed airfoils instead of testing different types of NACA airfoils, due to the lack of time. This research resulted in the selection of the EPLER-E423 high lift airfoil, due to its aggressive save which can lead to high amounts of downforce with small angles of attack, while keeping drag at low levels.
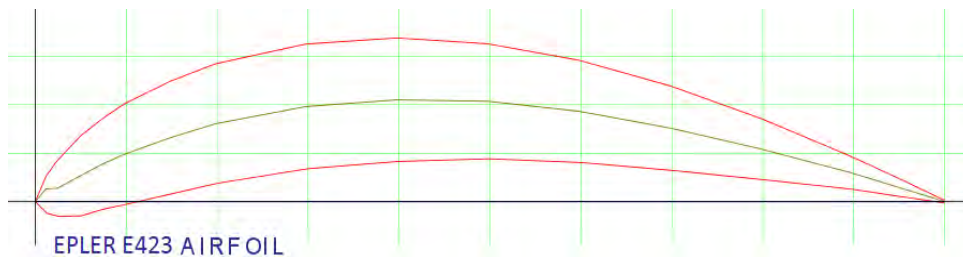
EPLER E423 AIRFOIL

Figure 159: *EPLER-E423 airfoil used for the assembly of the rear wing*

After the selection of the type of airfoil it is again necessary to test it and estimate the identical angle of attack, the number of elements and their dimensions. Usually, rear wings are consisting from two to four airfoils which in some case can be up to five depending on the design. For this rear wing however, three elements are selected to be used and the process to define their angle of attack is the same as previous. The first model consists of a single EPLER-E423 airfoil with 20cm width and 35cm chord length, while it is tested for angles from 1° to 13°.

1st Element - *Eppler E423*			
Angle of Attack	**Lift Coefficient(C_L)**	**Drag Coefficient(C_D)**	**Ratio C_L/C_D**
1°	-1.684	0.454	3.71
3°	-1.773	0.475	3.73
5°	-1.849	0.509	3.63
7°	-1.916	0.555	3.45
9°	-1.97	0.599	3.29
11°	-2.021	0.658	3.07
13°	-2.067	0.709	2.92

Figure 160: *CFD results of the single airfoil model for angles between 1° and 13°*

The second model consists of two EPLER-E423 airfoils, with the first element being the one that was tested on the previous model with the final selected angle of attack. The second airfoil has a width of 20cm and a chord length of 30cm and the aim is to test it different angles of attack in order to achieve higher amounts of downforce. This airfoil is tested for higher angles of attack between 15° and 25°, while it is selected to be placed with an angle of 23° achieving a lift coefficient of -1.995, a drag coefficient of 0.893 and a efficiency of 2.23.

2nd Element - Eppler E423			
Angle of Attack	Lift Coefficient(C_L)	Drag Coefficient(C_D)	Ratio C_L/C_D
15°	-1.853	0.733	2.53
17°	-1.881	0.757	2.48
19°	-1.931	0.805	2.4
21°	-1.964	0.847	2.32
23°	-1.995	0.893	2.23
25°	-2.023	0.941	2.15

Figure 161: *CFD results of the double airfoils model, for angles between 15° and 25°*

The third model consists of three elements in total, which is going to be also the final shape of the rear wing. The previous two airfoils are exactly the same as the final model that was selected in the previous case, with an angle of 23° for the second element, while the third airfoil that is added at this model is again an EPLER-E423 with 20cm width and 250cm chord length. This airfoil has to be place in even higher angle of attack to keep the flow attached for the whole rear wing, so it is tested at angles between 22° and 30°. After the 3D CFD simulations at those angles, the third element is placed at an angle of 28° and the final model has a lift coefficient of -1.979, a drag coefficient of 1.02 and an aerodynamic efficiency of 1.92. Although the fact that drag coefficient is significantly high, it is not a problem as the adding of the rear wing's endplates will correct this undesired situation and will improve the total efficiency.

3rd Element - Eppler E423			
Angle of Attack	Lift Coefficient(C_L)	Drag Coefficient(C_D)	Ratio C_L/C_D
22°	-1.911	0.951	2.01
24°	-1.933	0.974	1.98
26°	-1.956	1	1.96
28°	-1.979	1.029	1.92
30°	-2.003	1.061	1.89

Figure 162: *CFD results of the three airfoils model, for angles between 22° and 30°*

However, in order to select the suitable angle of attack for the airfoils, the velocity field around the airfoils has also to be taken under consideration. As it is shown on the figures below, for the single element the flow seems to accelerate significantly after the angle of 7° and that's why it was placed at 9°, because after that drag is rising high. For the double elements model, it is clear how the second airfoil accelerates the air even more

and helps the flow to stay longer attached increasing downforce. Finally, the third element increases the region of the accelerating air and helps the flow to stay attached along on the whole chord of the second element, while the openings between the airfoils let the excessive air to pass through, reducing drag.
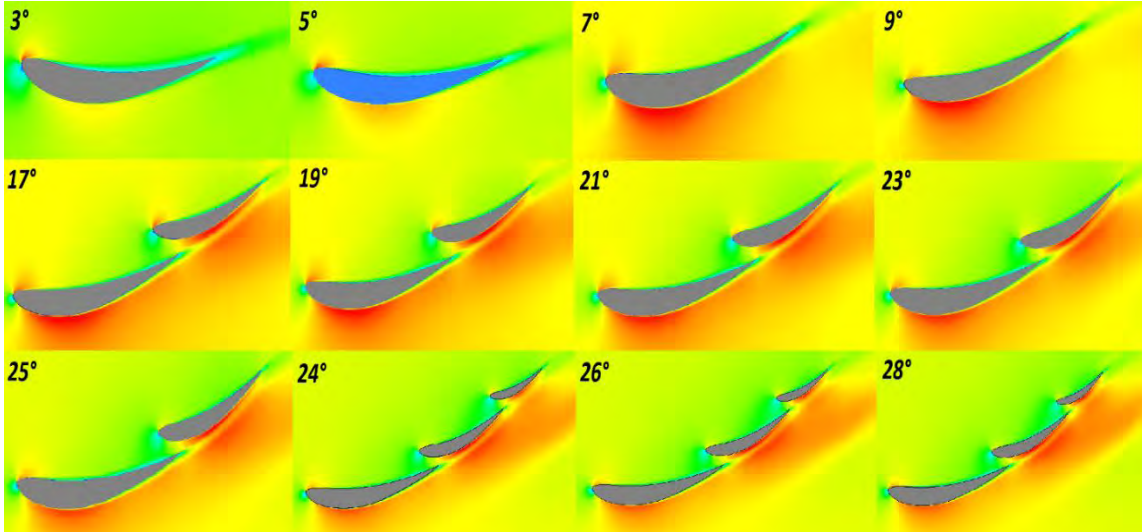

Figure 163: *Velocity field of the three EPLER-E423 airfoils models, for angles between 3° and 28°*

4.4.2.2. Rear Wing

The design of the rear wing is much more simple comparing to that of the front wing while there are no any parts behind the rear wing which affect its efficiency. The final model of the three EPLER-E423 airfoils is used with the selected angles of attack at 9°, 23° and 28°, but their width is now 80cm, which is the distance between the rear wheels and it is the area where the rear wing is placed, as it is defined by FSAE Regulations. Two large endplates are added at the both sides of the airfoils and are extending to the ground and to the rear in order to keep the low pressure that is created beneath the wing. The CFD simulation is done at 60km/h but an inaccuracy in the results is expected due to the fact that the flow reaching at the rear wing in reality is completely different from the free laminar flow that is tested at this case. However, the whole aerodynamic package mounted on the car is tested on the next section where the final results of the car are examined.
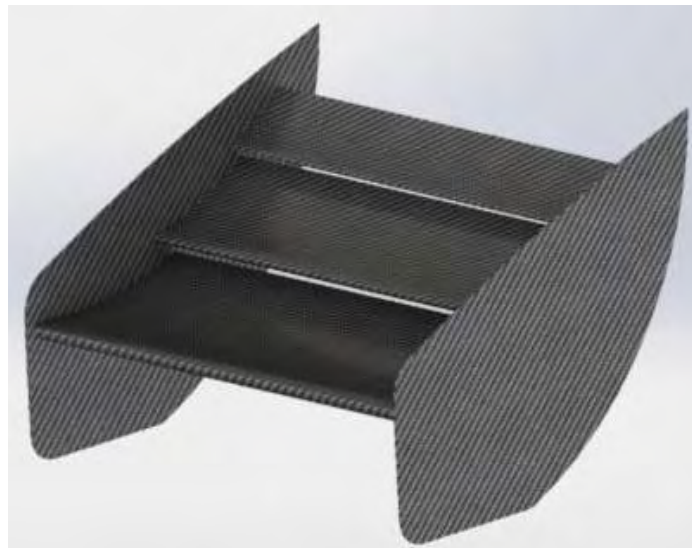
Figure 164: *Rear wing CAD design*

The CFD results for the rear wing on a freestream flow showed that it has a lift coefficient of -4.571 and a drag coefficient of 1.174 which result in an efficiency of 3.89 and a total downforce of 208N. The figures below show the velocity field and pressure distribution on the surface of the rear wing, where it can be seen that the air speed above the wing is lower than under it where the pressure is also significantly lower especially under the first element. Furthermore, a small flow separation can be seen on the outer sides of the endplates which due to the sharp edges and the high vortices that are also created there.
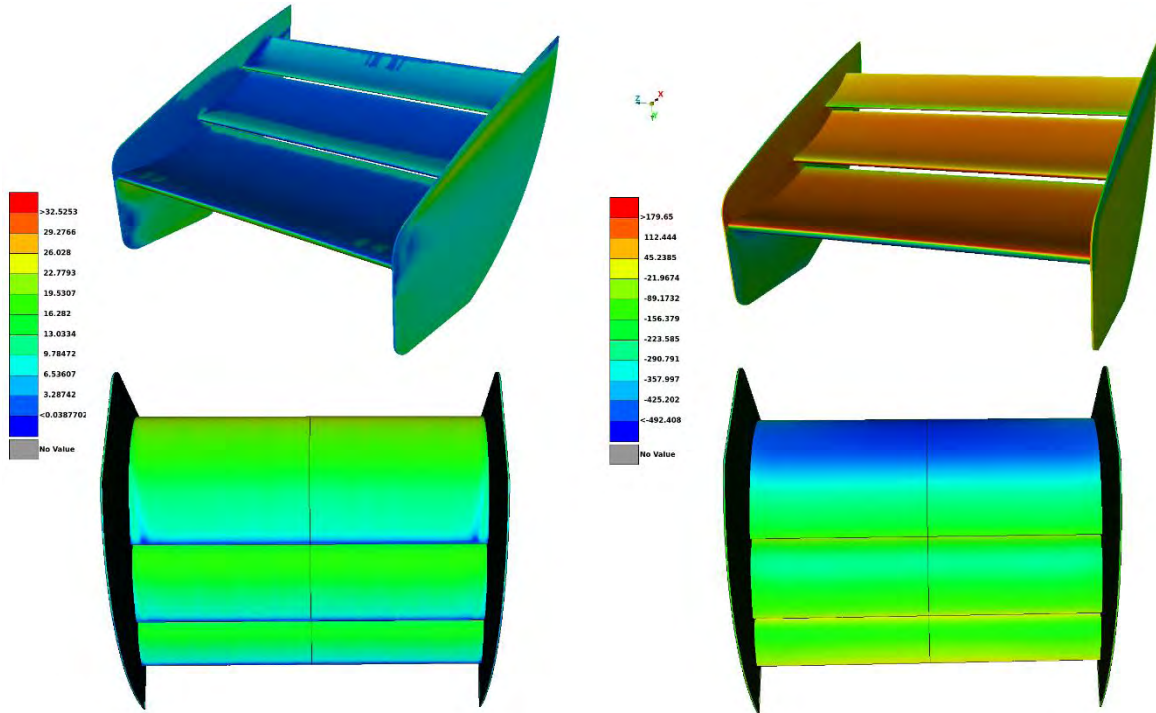
Figure 165: *Velocity field and Pressure distribution on the surface of the rear wing*

Finally, the figure below shows the velocity streamlines around the rear wing. It is clear that the flow stays attached along the upper surfaces of the airfoils and accelerates beneath the main element, reaching a peak of 32km/h. This figure can be also confirmed from the velocity field contour shown on the plane below, where the flow reaches its maximum speed under the main element and creates small stall regions only at the openings between the airfoils.
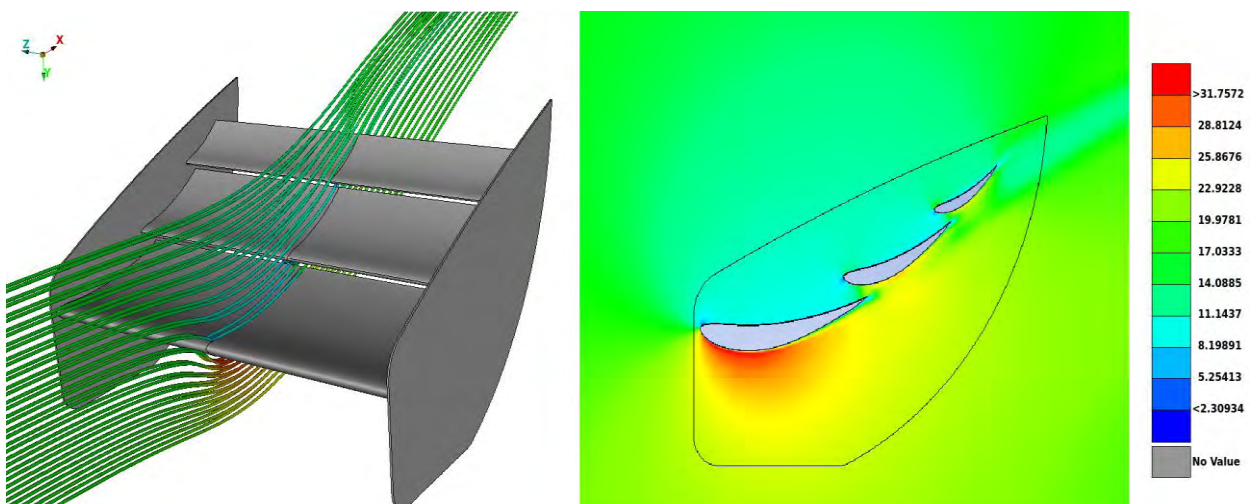
Figure 166: *Streamlines and Velocity field contour around the rear wing*

107

4.5. Whole Car Models

After the completion of all the CFD simulations for each part of the aerodynamic package, the final step is the CFD simulation of the models with the whole car and the moving road, in order to calculate the final aerodynamic characteristics of each model and make an estimation of their efficiency. Three car models are situated, one with no aerodynamic devices, one with the sidepods and undertray mounted on it and the final one with a full aerodynamics package including front and rear wings too. All CFD simulations are done at the speed of 60km/h, with a moving road while for the comparison of the final results, all models are tested in speeds from 40km/h to 100km/h.

4.5.1. Model without an Aerodynamic Package

The first model to be tested, is the car without any aerodynamic device mounted on it. The aim of this simulation is to determine the efficiency of the car without aerodynamic devices and calculate its aerodynamic characteristics like the drag and lift coefficient in order to estimate how much will the aerodynamic devices improve this situation. As it was already calculated at the study for the sidepods, this model produce lift which means that the aerodynamic package that is going to be used at each case should also overcome first this amount of generated lift in order to produce downforce. The model is simulated at 60 km/h with a moving road at the same speed and more details are added in order to estimate the drag coefficient more accurately.
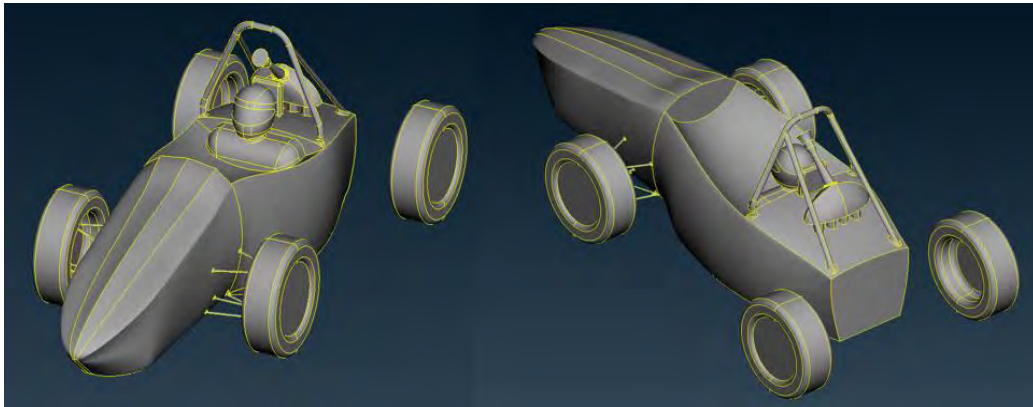
Figure 167: *CFD model of the car without any aerodynamic devices*

This model is expected to heave the least amount of drag due to the smaller frontal area of 0.728m² and the lack of aerodynamic devices producing downforce. The drag coefficient is calculated at 0.426, the lift coefficient is 0.286, producing a drag force of 58.42N, and a lift force of 38.42N while resulting in a total aerodynamic efficiency of 0.67. The figure below show the pressure distribution created on a contour plane along the vehicle. There is an expected flow separation at the end of the nosecone just in front of the driver which is due the cockpit opening. It is also clear that on the underside of the car the pressure is higher comparing to the pressure on the top, which is the reason why the car produces lift, while the high-pressure region behind the car is the reason why the drag is so low.
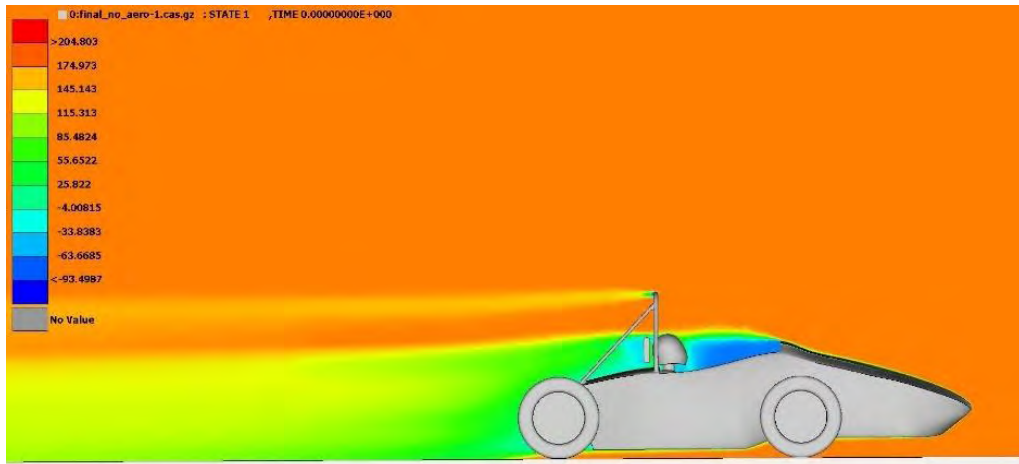
Figure 168: *Pressure distribution contour of the model without any aerodynamic devices*

The pressure distribution on the car's surface also confirms the aerodynamic characteristics that were calculated. The higher-pressure points (*193.5 Pa*) appear on the frontal areas of the front and rear wheels, on the stagnation point of the nosecone, on the driver's head and on the main hoop. On the underside of the car, the pressure distribution along the car's surface is between 79.5 Pa and -376 Pa, which is significantly high and considering the moving road there is no ground effect taking place as there are no aerodynamic devices to take advantage of it. Finally, the center of pressure seems to be transferred to front of the car which also an undesired situation which can result in oversteering issues.
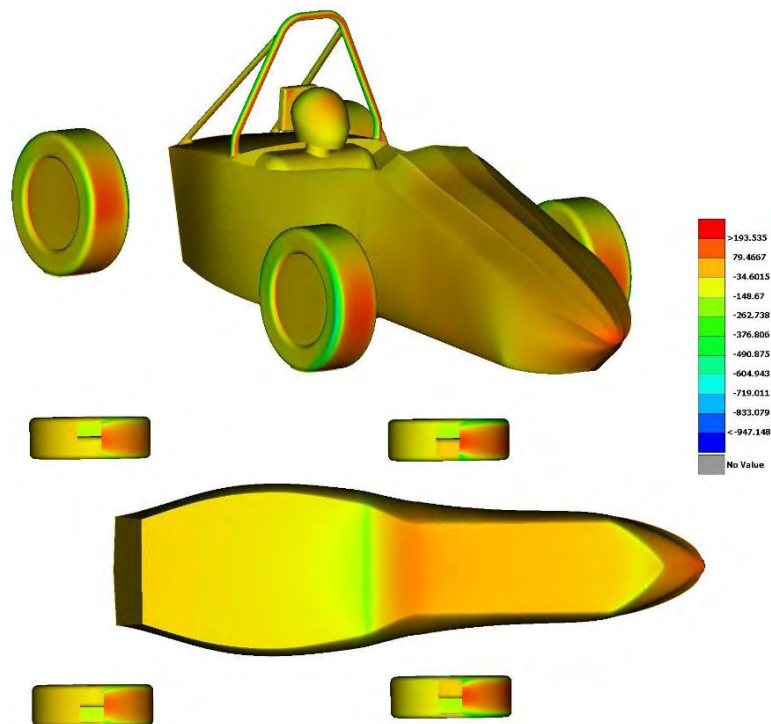
Figure 169: *Surface pressure distribution of the model without any aerodynamic devices*

Next the velocity field around the car is calculated and projected on a contour plane along the car. The blue color show the regions were the speed of air is significantly low, which is evidence that the flow there is separated and drag is increased. At this contour can be seen in more detail that the large flow separation is on the cockpit and behind the head restrain, while also on the sides of the front wheels the stall is greater that the rear wheels.
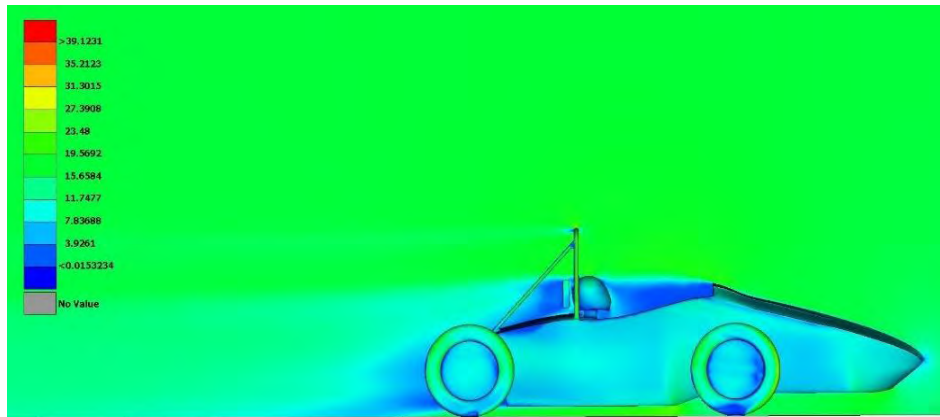
Figure 170: *Velocity field around the model without any aerodynamic devices*

Streamlines are also used in order to visualize the air flow around the vehicle. On the figure below are shown the velocity streamlines, where the red color represents higher speeds and the blue ones represent the low. It seems that the air flow smoothly at the front side of the car, while the bump of the nosecone directs the air above the driver's head. At the underside of the car the flow is again laminar along the whole surface and accelerates at just 22.5m/s on the front of the car, while a large amount of air is escaping from the sides and rear of the car, increasing the pressure beneath the car.
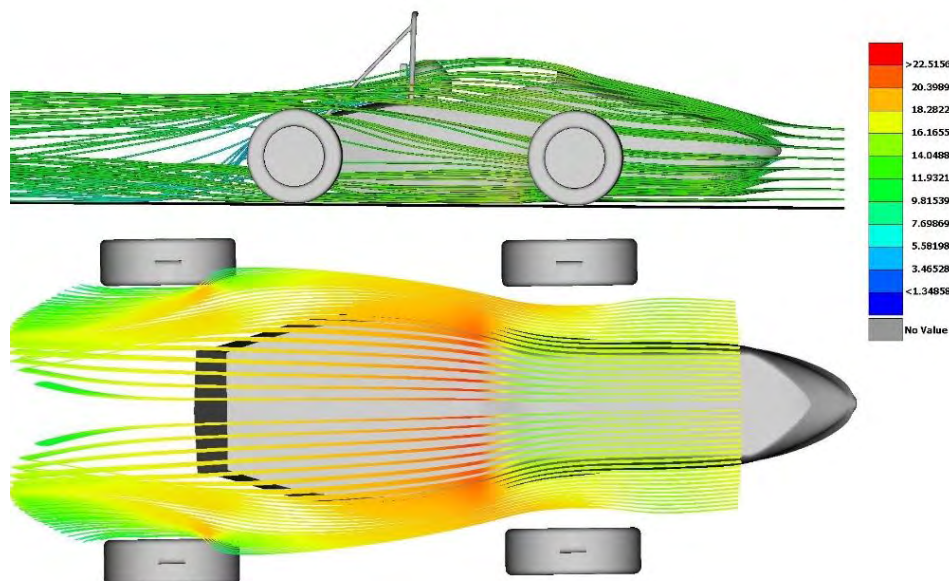
Figure 171: *Velocity streamlines of the model without any aerodynamic devices*

Furthermore, flow velocity vectors are used to show in more detail the magnitude of the velocity in each region of the car's surface. The blue vectors represent the points were velocity is close to zero and pressure is respectively high, while the green and red vectors show the regions were the magnitude of velocity is high. Regions like the nosecone's stagnation point, the cockpit and the frontal areas of wheels are characterized by vectors with zero velocity while on the wheels' sides and main hoop the magnitude is higher and separation may occur easier.
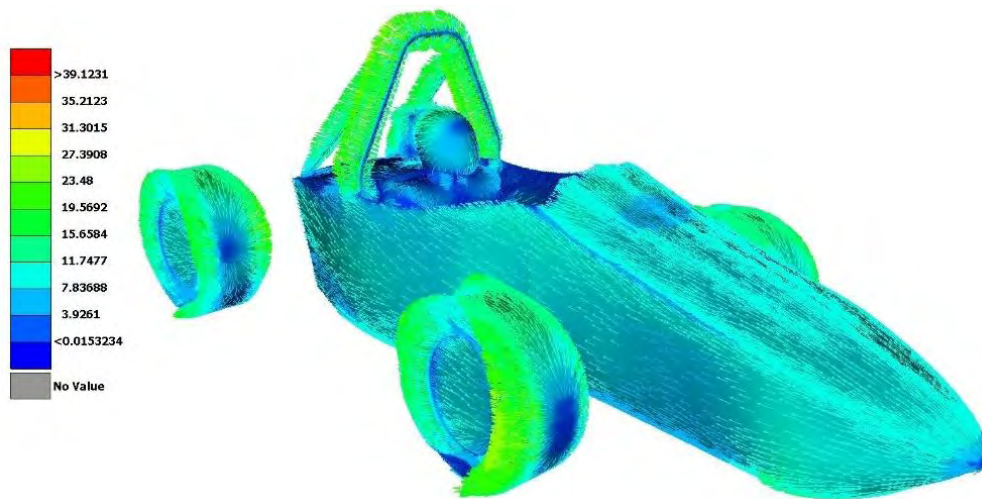
Figure 172: *Velocity vectors on the surface of the model without any aerodynamic devices*

Finally, turbulence intensity is used to visualize areas around the car where strong vorticities and stall occurs. The figure below represents with green volume mesh elements the regions were turbulence intensity is higher than 1.5%. This figure confirms again that the highest turbulence regions are behind the wheels and behind the car. This situation makes clear the need of a front wing in order to make the air avoid the wheels and direct it to the sidepods and undertray.
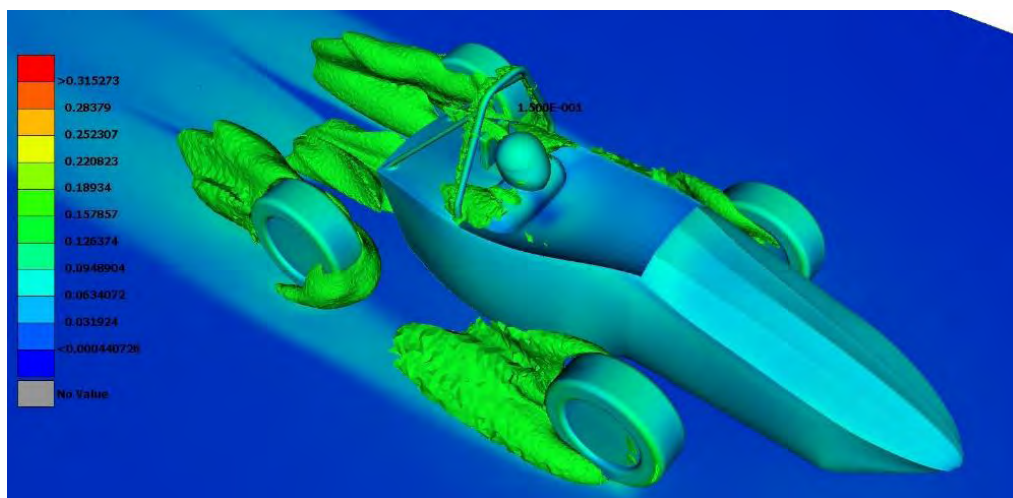
Figure 173: *Turbulence Intensity higher than 1.5% for the model without any aerodynamic devices*

4.5.2. Model with Undertray & Sidepods

The next model to be tested is the car with the final sidepods and final undertray that were selected earlier, mounted on it. The car with this aerodynamic package is exactly how the car *Thireus 277* participated at the FS Germany and FS Hungary competition at 2016. The CFD simulation is done again at 60km/h, with a moving road too, in order to calculate the aerodynamic characteristics of the car and compare them with these that resulted for the car without any aerodynamic device and estimate if the efficiency of the car is improved.
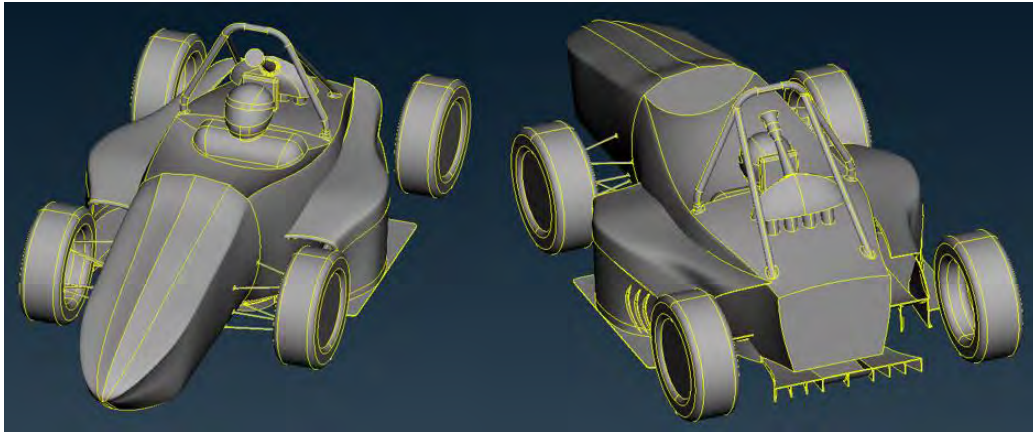
Figure 174: *CFD model of the car with undertray & sidepods*

The addition of the undertray and sidepods resulted in a slightly increased frontal area of $0.8m^2$ and due these devices drag and downforce are expected to be higher too. The CFD simulation resulted in a drag coefficient of 0.532, a lift coefficient of -0.668 which gave a drag force of 81.21N, and a downforce of 108.87N while the total aerodynamic efficiency at 1.26. Considering that the model with the naked car without any devices generated a lift force of 58.42N, the undertray and sidepods package overcome that lift and produces a total downforce of 167.3N. The pressure distribution on the contour plane below does not differs much from the previous, while again the highest stall region is at the driver's cockpit and the increased drag of the model can be also seen at the light blue region behind the vehicle.
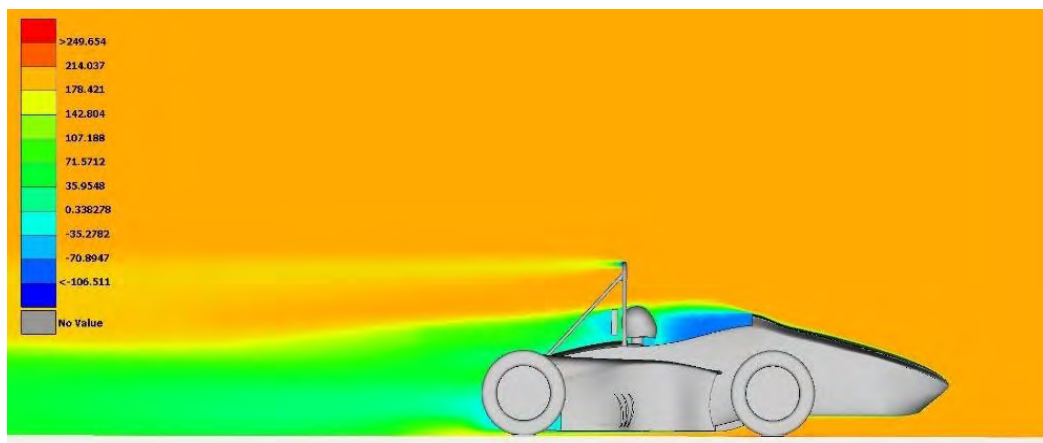

Figure 175: *Pressure distribution contour of the model with undertray & sidepods*

The pressure distribution on the car's surface is shown on the figure below. On the top surface of the car it seems that the points where the highest pressure (*185 Pa*) occurs are the nosecone's stagnation point, the frontal areas of the wheels and some region at the sides of the sidepods. At the underside of the car the figure is completely different, as at this model the pressure is fluctuated between 106 Pa and -370 Pa which is significantly lower comparing to the previous model. Furthermore, the center of pressures is now transferred more to the rear at the diffusers' outlets, avoiding the creation of oversteering.
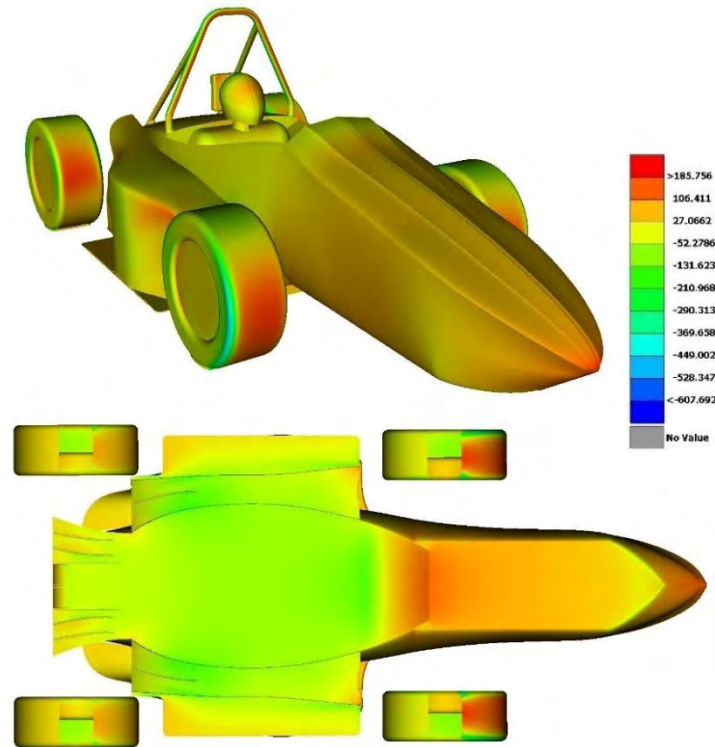
Figure 176: *Surface pressure distribution of the model with undertray & sidepods*

The velocity field is also calculated and projected on a contour plane along the car. It seems again that the low velocity regions are the cockpit and the area behind the head restrain and the wheels. However, at the sides of the sidepods at the gills outlets it seems that the air's speed is significantly low but the air coming out of the gills seems to slightly improve this undesired situation, while the region with separated flow behind the car is bigger.
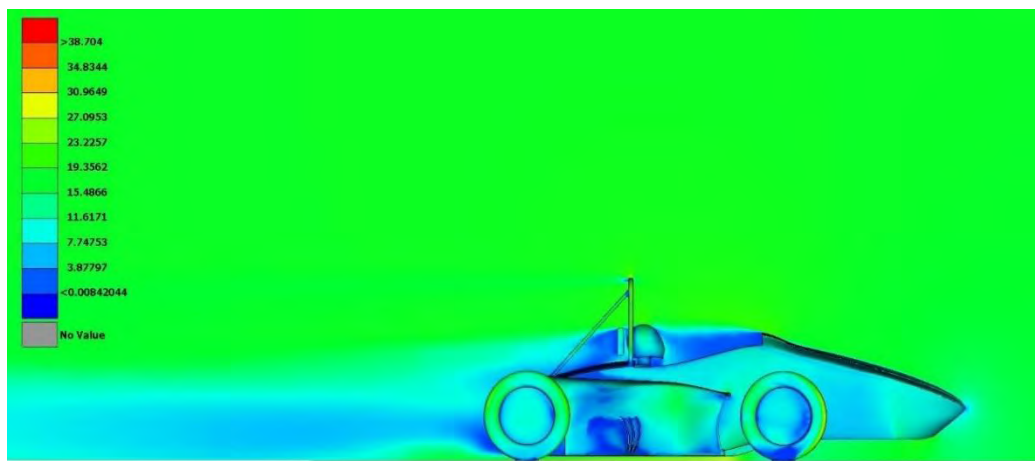
**Figure 177:** *Velocity field around the model with undertray & sidepods*

Next streamlines are used to visualize the flow of air around the vehicle. As it is shown on the figures below the flow is laminar at the front of the car, while it is also clear how the lifted surface of the sidepods generate downforce and there is an amount of air escaping out of the sidepods' gills. From the figure at the underside of the vehicle the air clearly accelerates along the whole surface and reaches a peak of 27m/s at the undertray's diffusers. It can be also seen how the middle diffuser's vertical flaps direct a small amount of air behind the rear wheels to reduce drag.
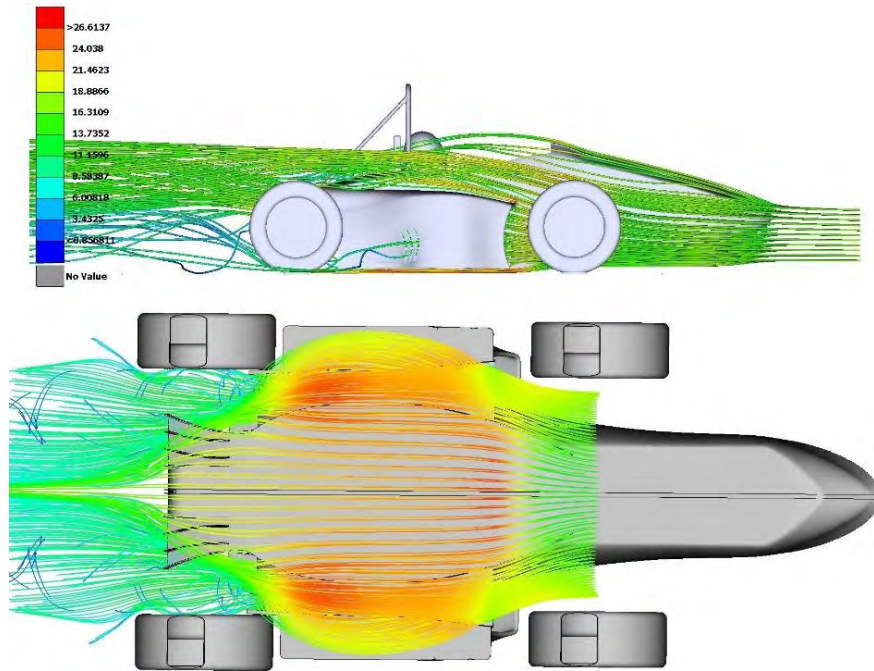
Figure 178: *Velocity streamlines of the model with undertray & sidepods*

Furthermore, the figure below show how the nosecone splits the oncoming air and send it directly to the sidepods. The streamlines are laminar and the turbulence flow behind the front wheels is eliminated which is due to the low-pressure region inside the sidepods which sucks more air in and prevents it from creating strong vortices.
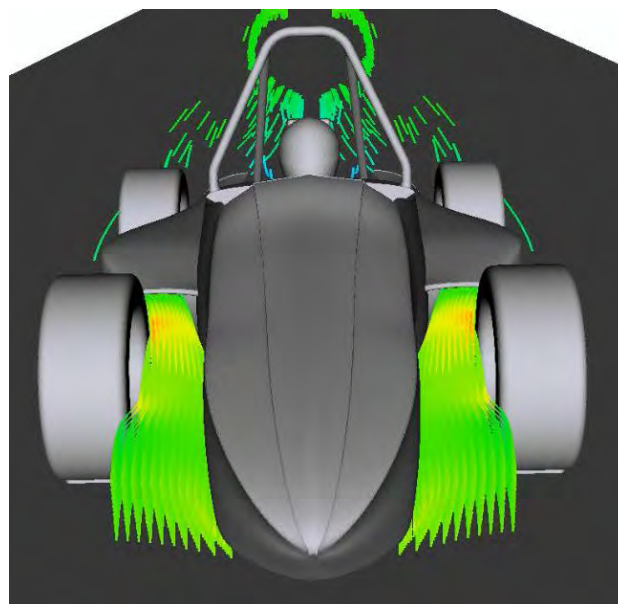

Figure 179: *Velocity Streamlines passing through the sidepods*

On the figure below it is shown the velocity magnitude in vectors projected on the car's surface. The blue vectors show again the point where velocity is close to zero while the greener vectors highlights points where velocity is higher that 19m/s. Again, the stagnation point of the nosecone, the frontal areas of the wheels and the area of the cockpit are characterized by low magnitude of velocity, while areas as the side of the wheels, the main hoop and the upper surface of the nosecone have higher magnitude of velocity which reaches a peak of 39m/s.
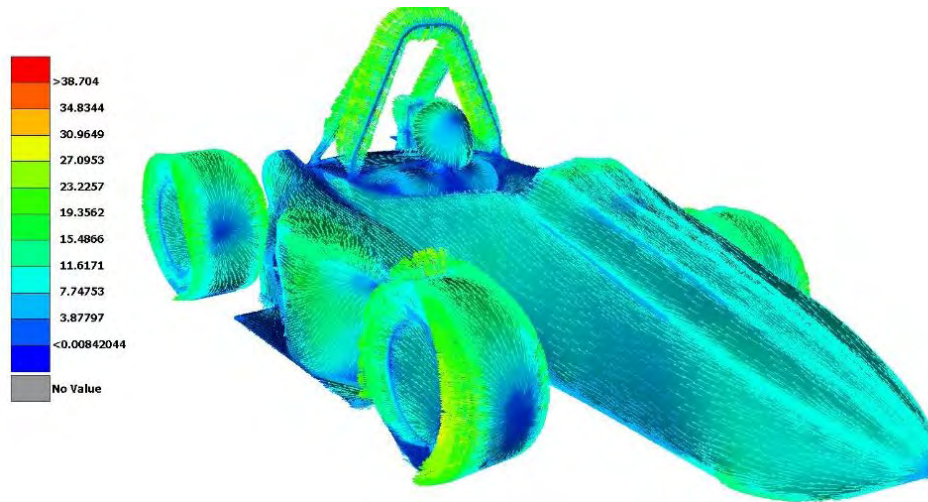
Figure 180: *Velocity vector on the surface of the model with undertray & sidepods*

Finally, turbulence intensity higher than 1.5% is visualized with green volume mesh elements in order to predict the regions where high vortices occur and the flow is highly turbulent. As it is shown on the figure below, again the regions behind the wheels and the driver are area where high turbulence occurs. It is also clear that there are strong vortices starting from the inner side of the front wheels and directing straight into the upper side of the sidepods, while vortices with lower intensity occur also at the outlet of the gills and the upper surface of the sidepod without having any significant impact.
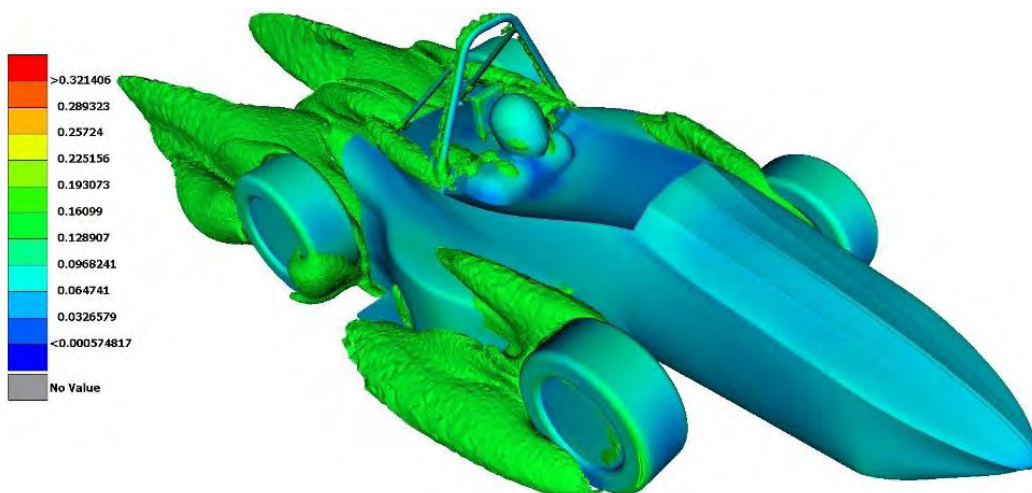
Figure 181: *Turbulence Intensity higher than 1.5% of the model with undertray & sidepods*

4.5.3. Model with a Full Aerodynamic Package

The final model to be tested is the car with complete aerodynamic package mounted in it. The model is same as the previous with the sidepods and undertray, with only difference the addition of the front and rear wing that were selected earlier. The CFD simulation is done at the speed of 60km/h with a moving road at the same speed. The aim of this simulation is to test the impact of using a front and rear wing on the aerodynamic efficiency of the car and estimate if it can improve the flow field around the vehicle. Furthermore, it is necessary to test also the efficiency of the front and rear wing respectively as they are mounted on the car and the flow reaching at them is completely different.
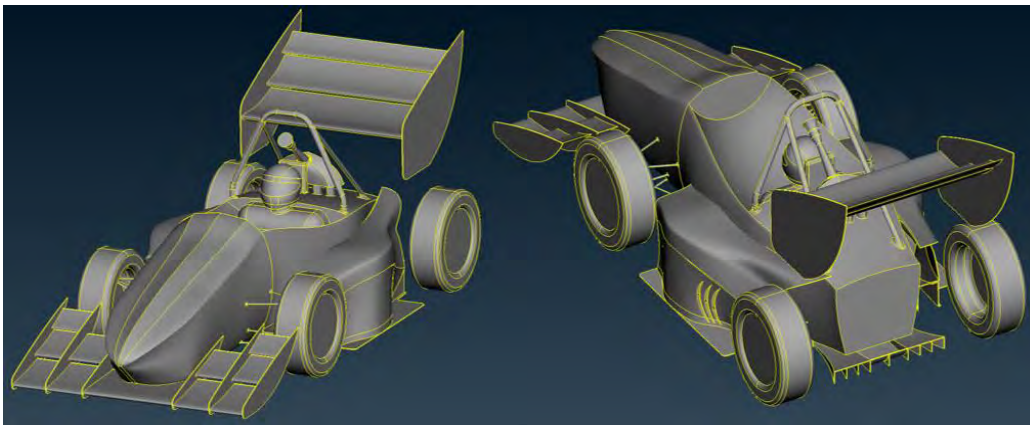
Figure 182: *CFD model of the car with a full aerodynamic package*

The new model with the addition of the front and rear wing has obviously, the highest frontal area of $1.02m^2$, comparing to the previous models. The CFD results shown that the car with a full aerodynamic package has a lift coefficient of -1.898, a drag coefficient of 0.82 which result in a high efficiency of 2.31. The model generates a total downforce of 342N which is three times higher than the previous model, while the drag has significantly rise as expected at 148N. From the pressure contour on the plane below it can be seen that the pressure distribution has completely changed comparing to the previous models. The low and high peaks of pressure are significantly higher now but due to scale of that is used they are not clear. Again, the area of the cockpit has the greatest stall, while the rear wing has a huge impact on the pressure distribution behind the car and it is also clear how the small flow separation of the main hoop affects the flow reaching the rear wing. On the front of the car it can be seen how the pressure is significantly lower at the underside of the nosecone which can surely improve the efficiency of the undertray.
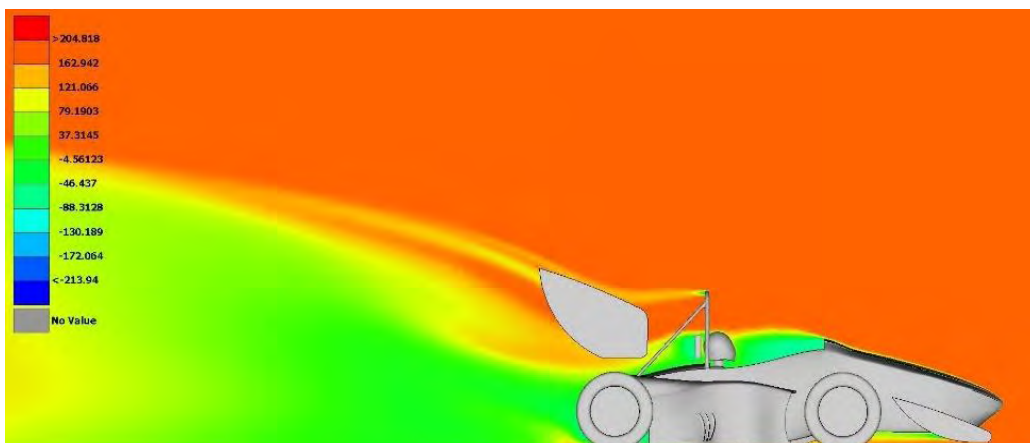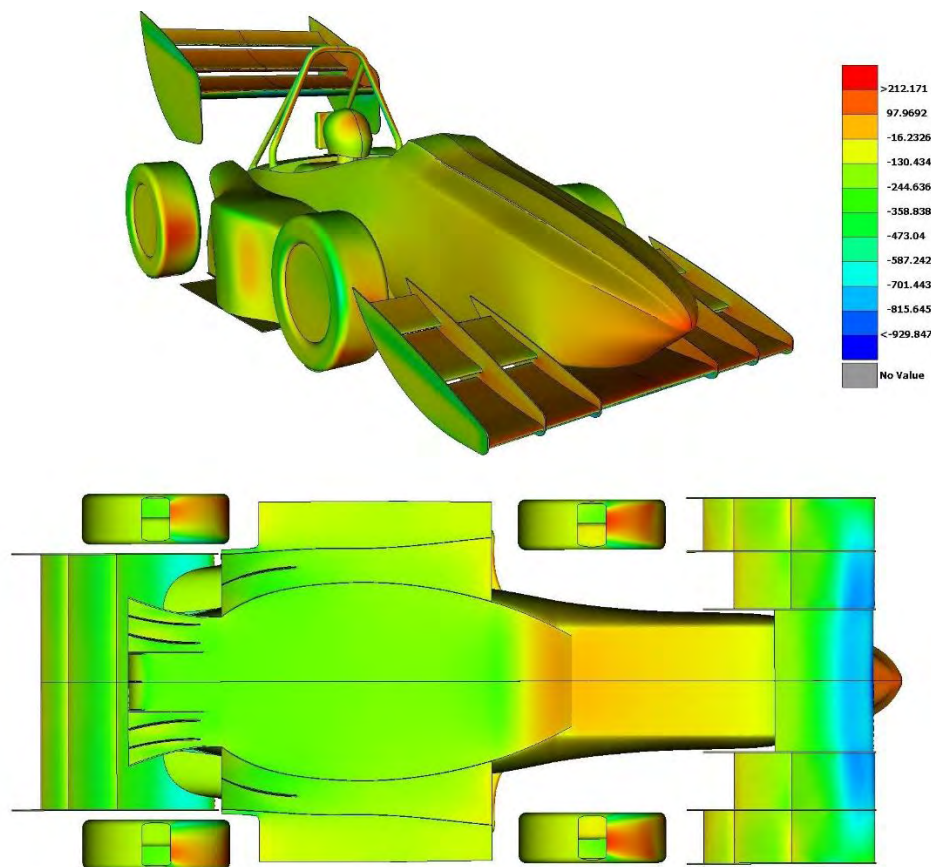

Figure 183: *Pressure distribution contour of the model with a full aerodynamic package*

116

Pressure distribution is also calculated and visualized on the surface of the car. As it can be seen from the figure below, the stagnation point of the nosecone, the frontal area of the rear wheels and the upper sides of the wings deal with the highest pressure between *97Pa* and *212Pa*. It is interesting how the addition of the front wing has eliminated the high pressure that is created on the frontal area of the front wings, which means that it successfully deflects the oncoming air from hitting the wheels. At the underside of the car the peak of low pressure is about -930Pa and it can be seen at the undersides of the front and rear wings, while along the whole surface of the undertray the pressure distribution is below of *-358Pa*. The center of pressure is now transferred more to the front due to the low-pressure region that is created at the front wing from the ground effect taking place, but the addition of the rear wing and the diffuser keep the center of pressure close to the center of mass just under the driver avoiding any oversteering on understeering situation.

Figure 184: *Surface pressure distribution of the model with a full aerodynamic package*

The velocity field around the car is visualized with a contour plane where the blue color represents the areas where velocity is lower than 3m/s and the red color represents regions where velocity is higher than 23m/s and flow is accelerating. As it can be seen on the figure below flow separation occurs on the cockpit area, on the region behind the driver and on the sides of the sidepods. It is interesting how flow separation at the sides of the front wheels is eliminated due to the front wing and it has been transferred to the sides of the sidepods. Other regions where stall occurs are the side of the rear and front wings which is due to the thin endplates that split the flow. Finally, the flow is accelerating immediately under the front wing where it reaches a peak of 33m/s while keeping the high speed at 20m/s along the whole surface of the undertray and dropping pressure.
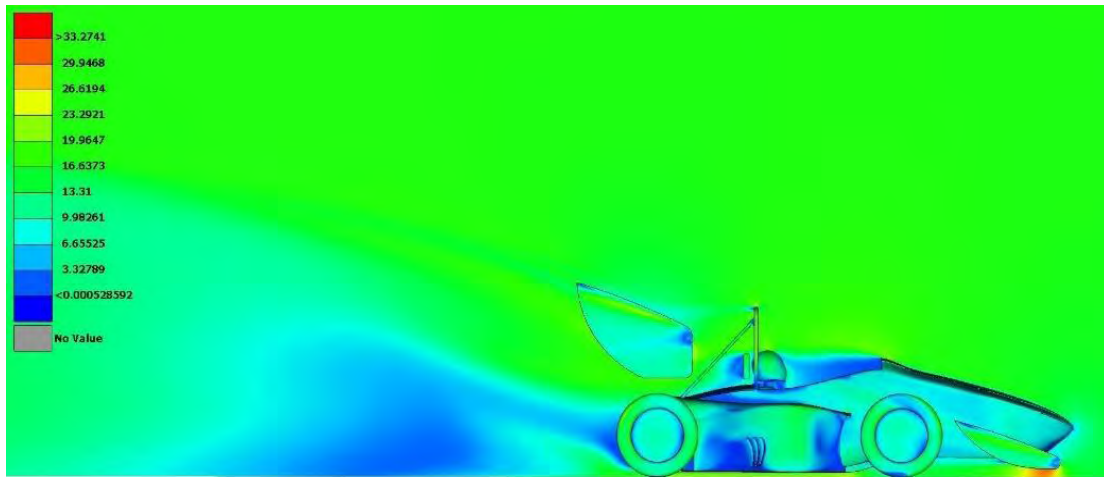
Figure 185: *Velocity field around the model with a full aerodynamic package*

The streamlines below are used to visualize the path that follows the air flow around the car. Red streamlines represent the points where the speed of the air is higher than 33m/s while the blue ones represent points where the speed is below 7m/s. It is clear that the front wing takes advantage of the ground effect and the flow there is accelerating and reaching the peak of 33m/s while the air flowing to the undertray is significantly higher comparing to the previous cases. The front wing directs also an amount of air to the inner side of the rear wing which can rapidly improve its efficiency. Finally, the rear wing it self seems to receive the biggest amount of air at the rear and accelerate it at 20m/s, while creating strong vortices which are the main reason for the increase in drag.
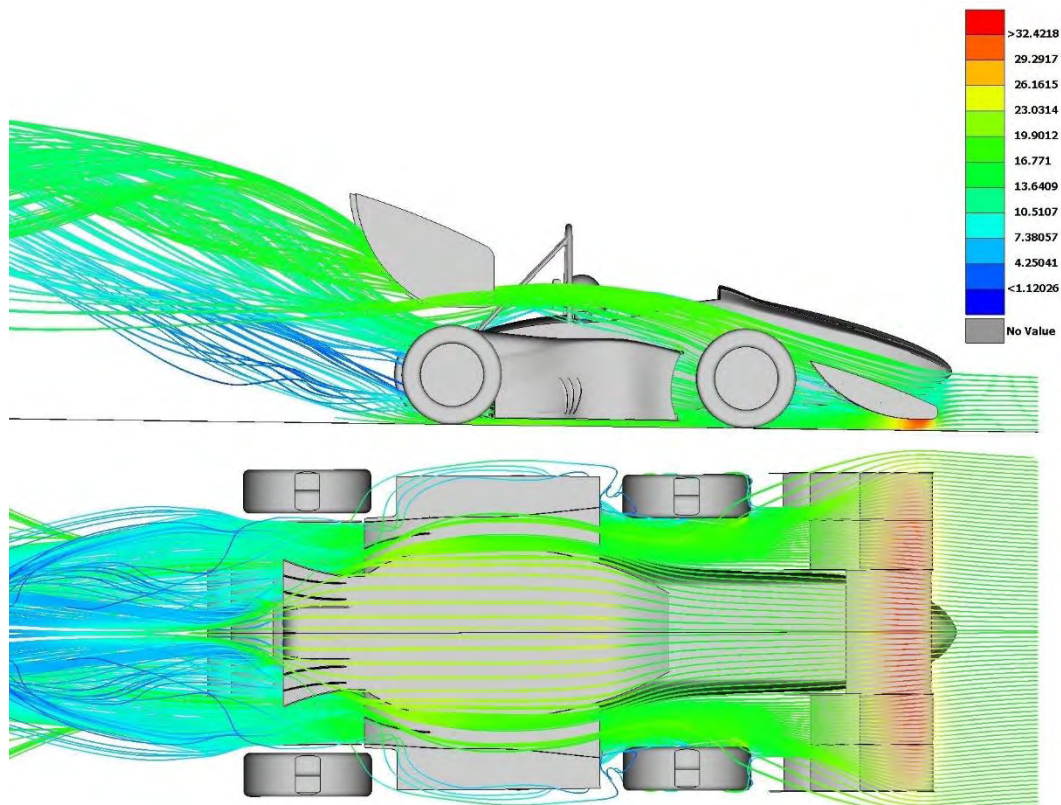

Figure 186: *Velocity streamlines of the model with a full aerodynamic package*

On the figure below are shown in more detail the streamlines of the front wing. It is clear how the part with the three elements in front of the front wheels works efficiently as it creates strong vortices that are avoiding the contact with the front wheels and protect the flow from being separated and turbulent. These vortices are directing just in the region behind the front wheels, reducing this way the drag that is formed there, while when they reach the rear of the car they are sucked from the significantly low pressure region under the rear wing and improve its efficiency as even more air is accelerating under the wing's airfoils.
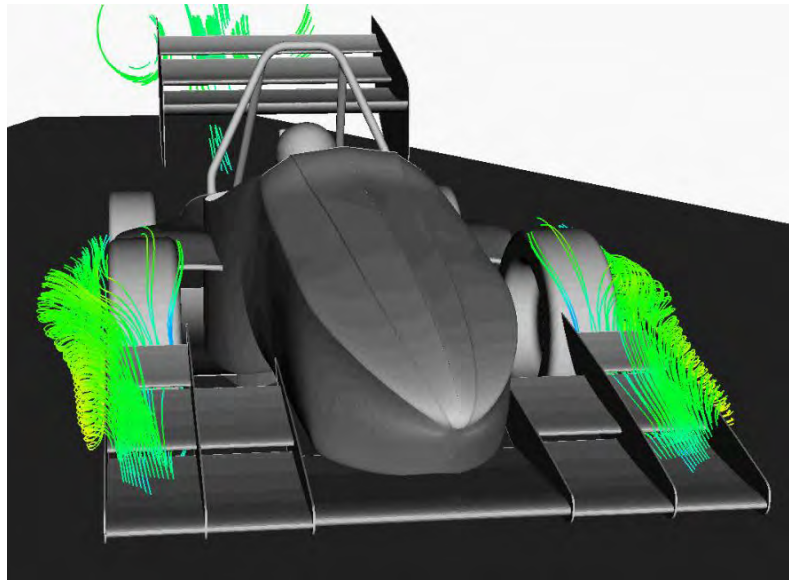

Figure 187: *Streamlines of the front wing*

Furthermore, the figure below shows the shape of the flow reaching at the rear wing. This figure confirms that the flow of the rear wing is influenced by many parts of the car that are located at the front and that has a huge impact on the efficiency of the rear wing. It is clear how the flow is strongly affected by the cockpit area, the driver and the head restrain and is separated by creating vortices that are directing under the rear wing and interact with the freestream flow there which decreases its speed.
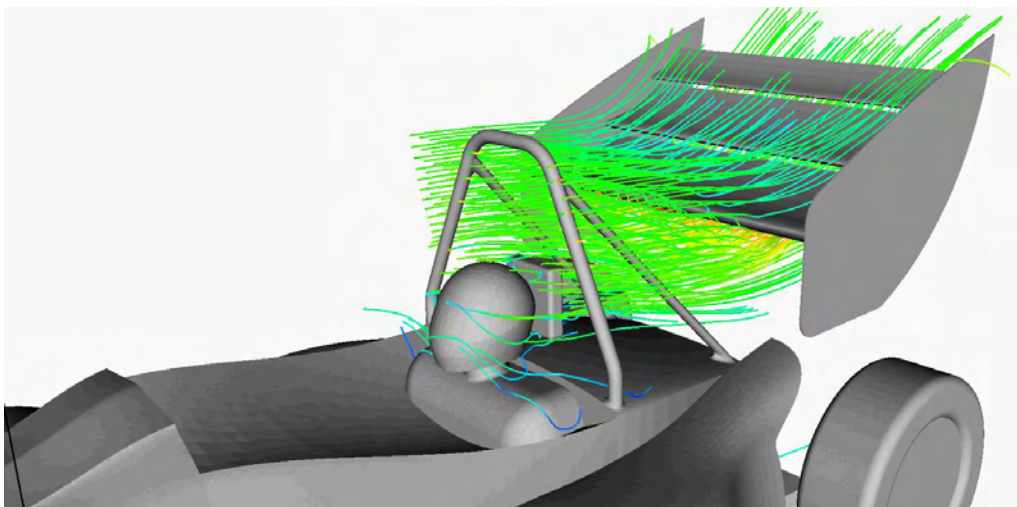

Figure 188: *Velocity streamlines reaching at the rear wing*

Velocity vectors are representing the resultant force of X, Y and Z direction and the color shows the magnitude. Vectors with blue color represent points were the resultant magnitude of the velocity is lower than 6m/s while red vectors show points where velocity is between 16 - 33m/s. According to the figure below at the front edge of the front wing velocity vector reach their maximum magnitude, while it also clear that the vectors are pointing at the underside of the car which means that the air passing under the front wing is directing to the undertray. At the endplates' sides of the front wing it can be seen that strong vortices are generated, as the vectors there are yellow and their direction is fluctuated. The velocity vectors at the frontal area of the front wheels are now pointing at the same direction and their color show that the flow there is less interacted as the front wheel deflects the air and prevent him of coming in contact with the wheels. On the stagnation point of the nosecone all vectors are blue, as the flow has almost zero speed while also velocity at the upper side of the front wing's main element is again low as the biggest amount of air is directing beneath the airfoil.
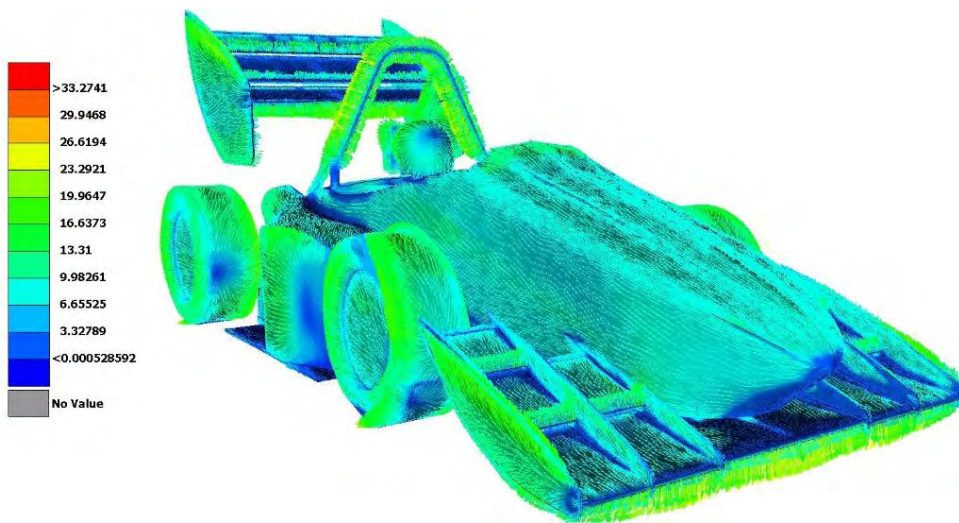
Figure 189: *Velocity vectors on the surface of the model with a full aerodynamic package*

Finally, the figure below show with green volume elements the regions where the turbulence intensity is higher than 1.5%. As it can be seen, the front wing has reduced the turbulences behind the front wheels and at the outer surface of the sidepods while the highest intensity is at the rear side of the car where the weak of the rear wing contributes in the creation of large vortices with intensity higher than 3%.
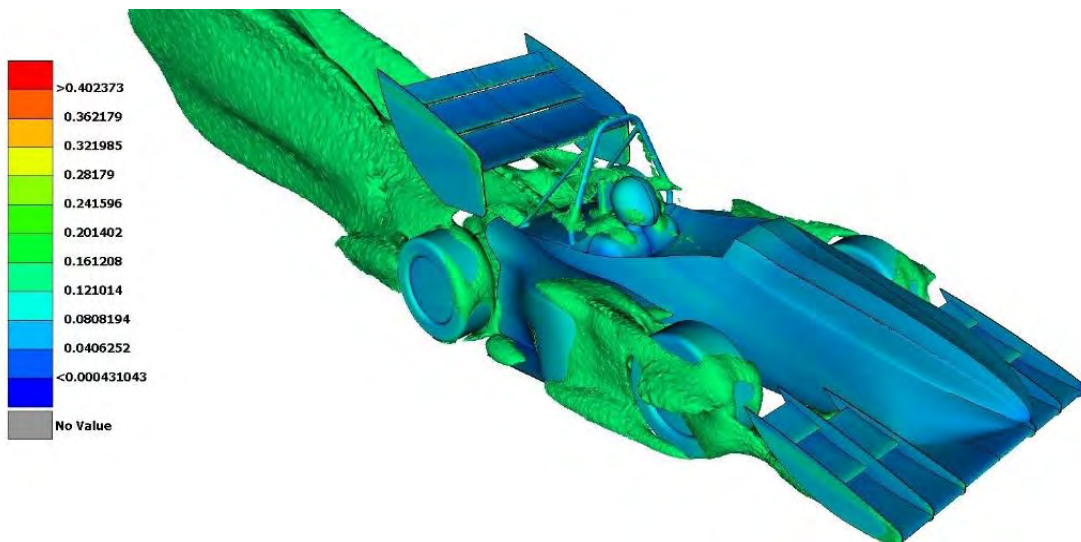
Figure 190: *Turbulence Intensity higher than 1.5% of the model with a full aerodynamic package*

4.5.4. Results Comparison

The final step is a comparison of the CFD results between the previous car models in order to make a conclusion for the efficiency of each aerodynamic package. As it is shown on the table below the car with a full aerodynamic package has the highest efficiency of 2.31 which is about double as much as the efficiency with only an undertray and sidepods and three times higher comparing to the car without any devices. This can be also seen from the drag and lift coefficients and the amount of downforce and drag that each model generates.

Final Models	Frontal Area(m²)	Lift Coefficient(C_L)	Drag Coefficient(C_D)	Downforce(N)	Drag(N)	Ratio C_L/C_D
No Aerodynamic Devices	0.728	0.286	0.426	-38.42	58.42	0.67
Undertray & Sidepods	0.799	-0.668	0.532	108.87	81.24	1.26
Front & Rear Wings	1.019	-1.898	0.82	342.46	148.04	2.31

Figure 191: *CFD Results of each car model*

In order to test furthermore the efficiency of each model at different speeds, CFD simulations are done for speeds between 40 - 100km/h and the chart below highlights the produced amount of downforce for each case. According to this chart the car without any aerodynamic device generates lift for all these speeds as its lift coefficient is positive and reaches a peak of -100N at the final speed. Next the model with undertray and sidepods has a gradual increase for the generated downforce which start at 150N for 40km/h and reaches a peak of 240N at the speed of 100km/h. Finally, the model with a full aerodynamic package has clearly a gradual increase in downforce as from 150N at 40km/h it is rocketed at the peak of 870N at the final speed of 100km/h and is about five times higher than the previous model.
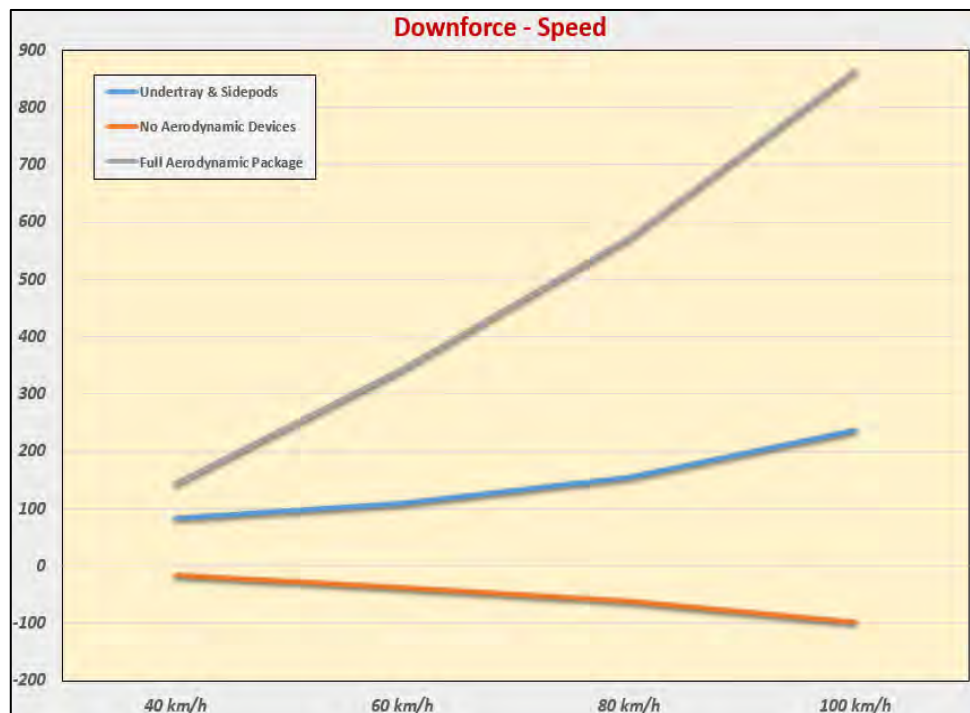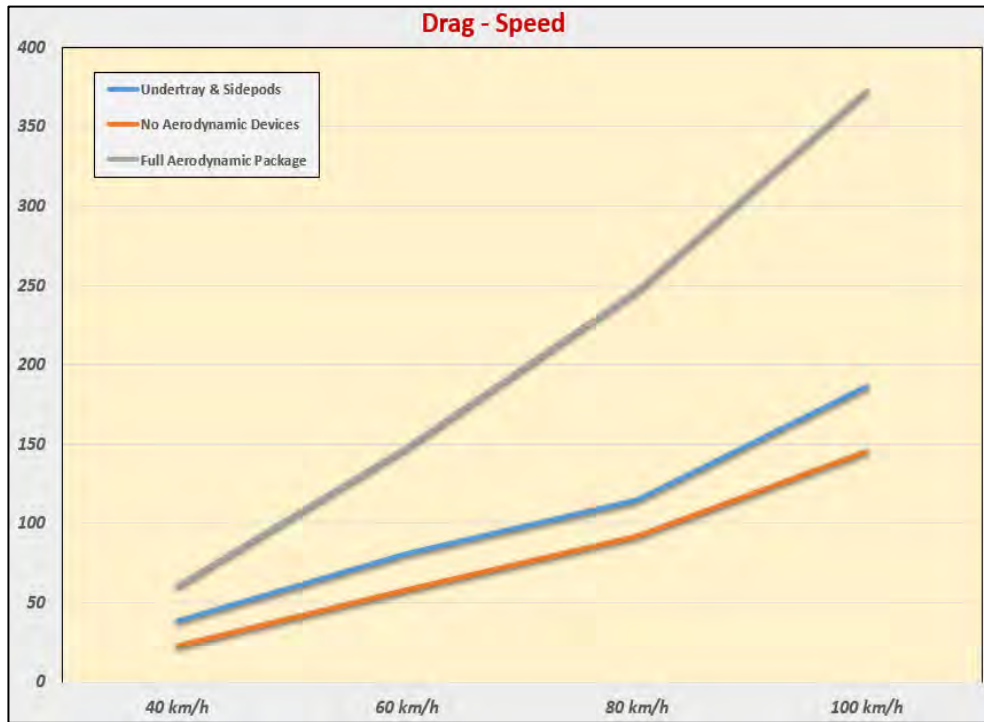

Figure 192: *Downforce generated at each case for speeds between 40-100km/h*

Although the model with a full aerodynamic package generates the highest amount of downforce at all speeds, it is expected that this model will produce also big amounts of downforce. The chart below highlights data for the drag force of each model for speeds from 40 - 100km/h. Both models of the car without any aerodynamic device and with undertray have the same gradual increasing tendency, starting with a drag force under 50N at 40km/h and reaching a peak value of 140N for the first model and a value of 180N for the undertray model. On the other hand, the model with a full aerodynamic package generates a significantly higher amount of drag at all speeds, as it starts with a drag close to the previous models at 60N and then rapidly increases and reach its peak of 375N for the final speed of the car at 100km/h. The generated drag of the full aerodynamic model is about doubled comparing to the rest models, however this happens only for speeds over 80km/h and it is an acceptable situation as at the average speed of the car at 60km/h the amount of drag is as much higher as it was expected according to the generated downforce that was referred earlier.

Figure 193: *Drag generated at each case for speeds between 40-100km/h*

5. LAP-TIME SIMULATIONS & VALUATION OF THE RESSULTS

Although that the CFD simulations of all models of the aerodynamic package are completed and their results have been analyzed, it is necessary to test these results in real time lap simulations, in order to make a conclusion about the efficiency of each aerodynamic package and its impact on the track performance of the car. OptimumLap is used in order to simulate the performance of the car on the track by using data for the tires, engine and aerodynamics as inputs. The vehicle model used in OptimumLap is a point mass, quasi-steady state model which mathematically is overly simplistic, but, in reality, this model is very powerful at analyzing the global performance trends of a vehicle without having to capture or model more detailed effects. The advantage of this is that a vehicle can be characterized by very few inputs, requiring very little time to setup and conduct a simulation. Even though the model is a point-mass model, meaning that no weight transfer or transient effects are taken into account, the simulated results still correlate well with logged data. All the lap-time simulations are done for the FS Germany 2016 Endurance Track.
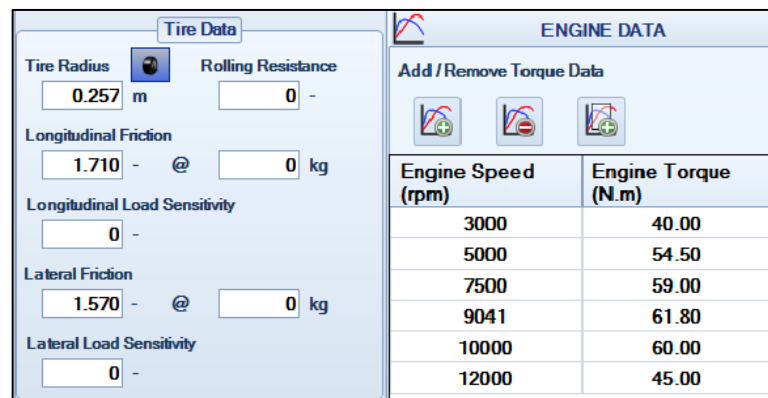

Figure 194: *Tire & Engine Data used for the lap-time simulation model*

The tire and engine data of *Thireus 277* that are inserted as it is shown on the figure above, resulted in an engine torque and power trend as it is shown on the diagram below. The engine torque increases rapidly with the engine speed and reaches a peak of 62N·m at 9041rpm and then drops sharply, while the engine power is rising gradually until the peak of 84hp at 10,000 rpm and then is slightly declined.
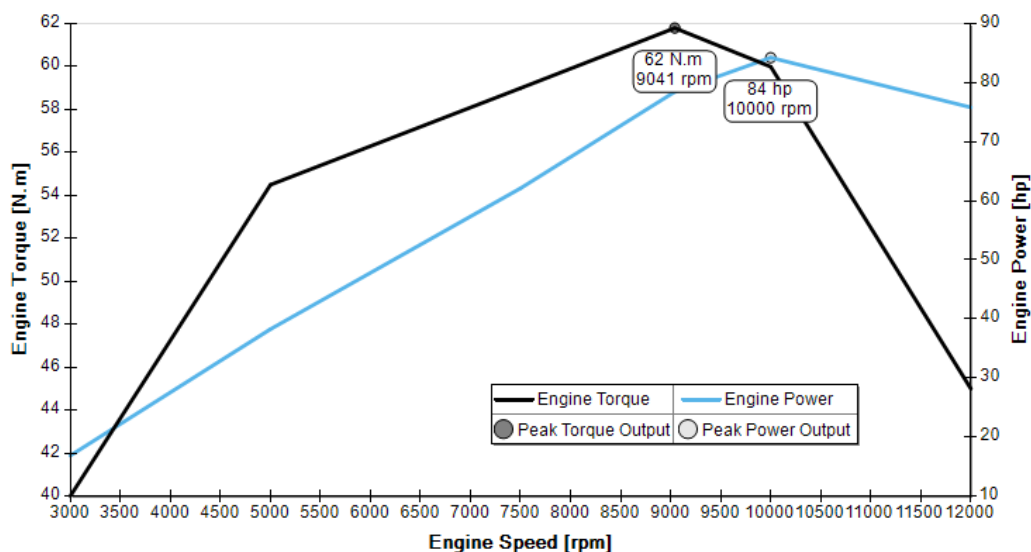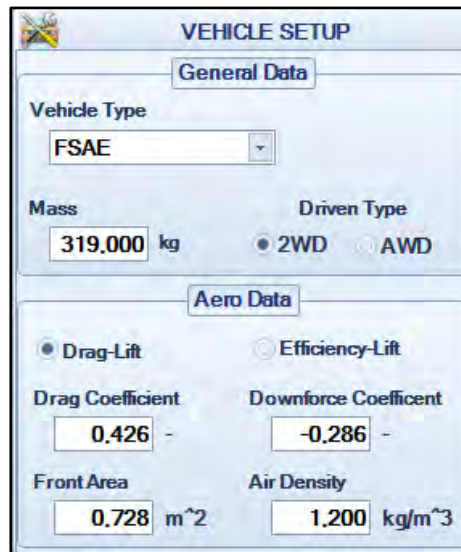

Figure 195: *Engine Torque & Power versus Engine Speed*

123

5.1. Without Aerodynamic Devices

The first model that is simulated is the car without any aerodynamic devices. On the figure below are shown the general and Aerodynamics data that are used. The total mass of this model resulted at about 319kg with a 70kg driver on it, 2WD driven type and FSAE vehicle type are also selected. For the Aerodynamics data, the values are imported exactly as they were calculated on the section 4. Note that the lift coefficient in OptimumLap is referred as downforce coefficient and as this model was calculated with a positive lift coefficient, it has to be imported with a minus sign.

Figure 196: *General & Aero Data used for the model without aerodynamics devices*

The simulation of the car with these characteristics at the FS Germany 2016 Endurance Track resulted in a total lap-time of **48.50sec**. The figure below shows the speed of the car at each part of the track. The blue color represents speeds below 56km/h while the red color show speeds above 70km/h. The maximum speed of the car at the straight line of the track is calculated at 111km/h, while the average speed of the car during corners is calculated at 42km/h.
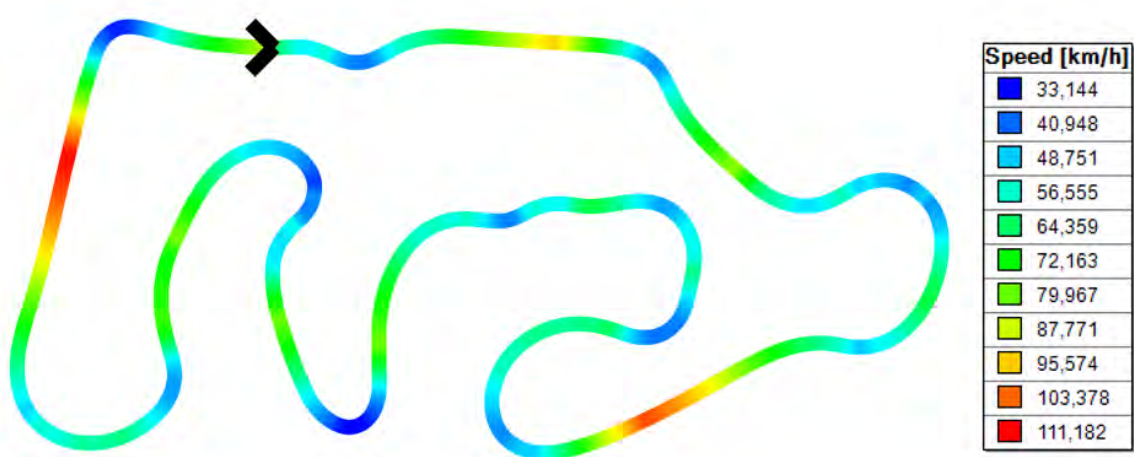

Figure 197: *Speed of the car without aerodynamic devices along the track*

The next figure shows the downforce that the car generates along the whole track. As the CFD results shown on section 4, the car without any aerodynamic devices generates lift at all speeds, thus all the values of downforce below have a minus sign. So, at that case the blue color represents values of lift above 85N, while the red color shows values of lift below 40N. Although this model generated lift at all parts of the track it is interesting how at the minority of the track the lift force is not exceeding the value of 65N, which means that the car without any aerodynamic devices generates a small amount of lift which can be easily overcome with a use of an aerodynamic package.
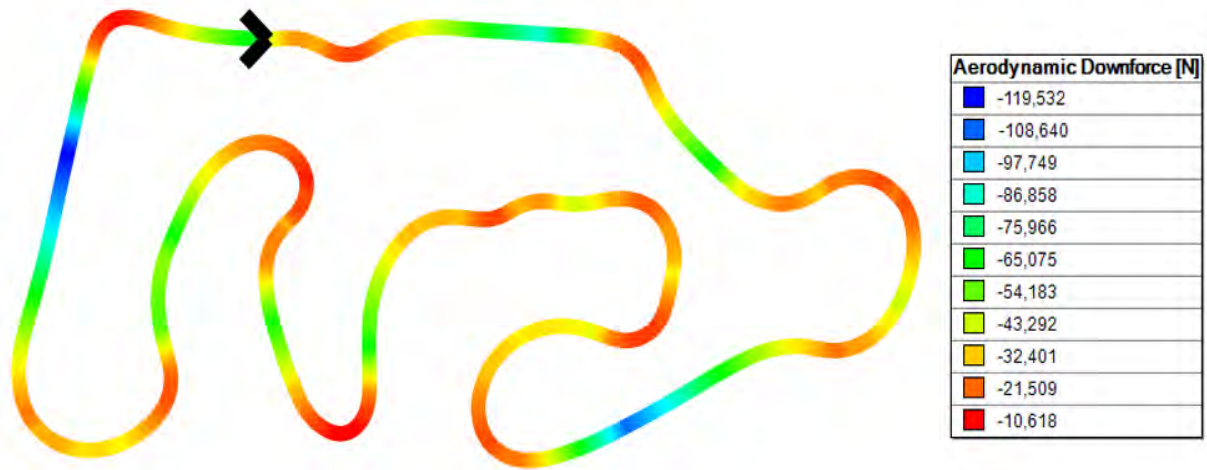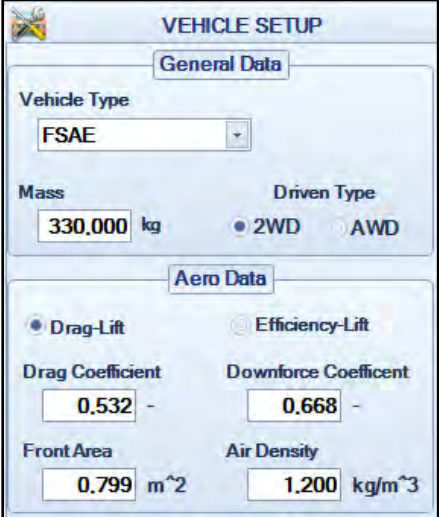

Figure 198: *Generated Downforce of the car without aerodynamic devices along the track*

5.2. Undertray & Sidepods

The next model to be simulated in the Endurance track of FS Germany 2016 is the car with the undertray and sidepods. The aerodynamic package that is mounted at this model add an extra weight of 11kg, which resulted in a total vehicle mass of 330kg. Again, the FSAE vehicle type and 2WD Driven type is used. The rest aerodynamic data are imported exactly as they were calculated at section 4. Note that at this case the lift coefficient of -0.668 is inserted as a positive value while it is referred as Downforce coefficient and the frontal area has also changed.

Figure 199: *General & Aero Data used for the model with undertray & sidepods*

125

The simulation of this model with OptimumLap at the Endurance track resulted in a total lap-time of **47.84sec** which is about 0.7sec faster comparing to the previous model. The final speed of the car at the straight line of the track is about the same as previous, but the average cornering speed of the vehicle is now slightly increased at 43km/h. Considering that at this case the car is by 11kg heavier it seems that with an addition of only an aerodynamic undertray with a lift coefficient of -0.668 the car can increase its corner speed and reduce lap-time by half a second. However, if the undertray could be constructed in a more efficient way with better handling of the composite materials its total weight could be about the half and the results would be significantly improved.
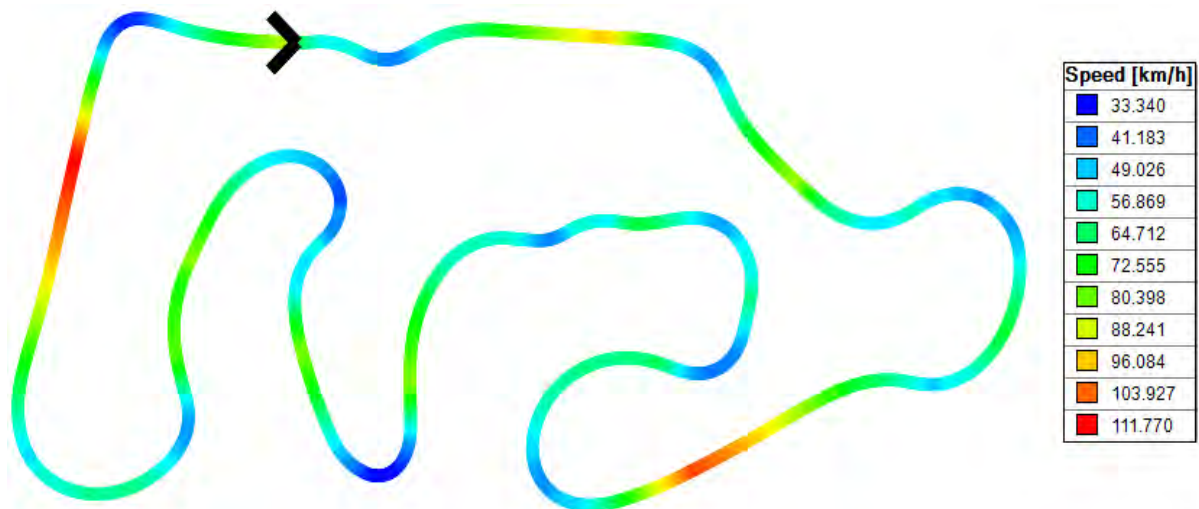

Figure 200: *Speed of the car with undertray & sidepods along the track*

The next figure shows again the amount of downforce that is generated at each point of the track during the race. The color distribution is completely different than the previous model, as now the car generates downforce and not lift. The blue color shows values of downforce below 111N, which the car reach them only the corners of the track where it is moving with the average speed of 4km/h. The red color on the other hand represents values of downforce from 168N and above, which are reached when the car its moving on the straights and reaches speeds higher than 70km/h.
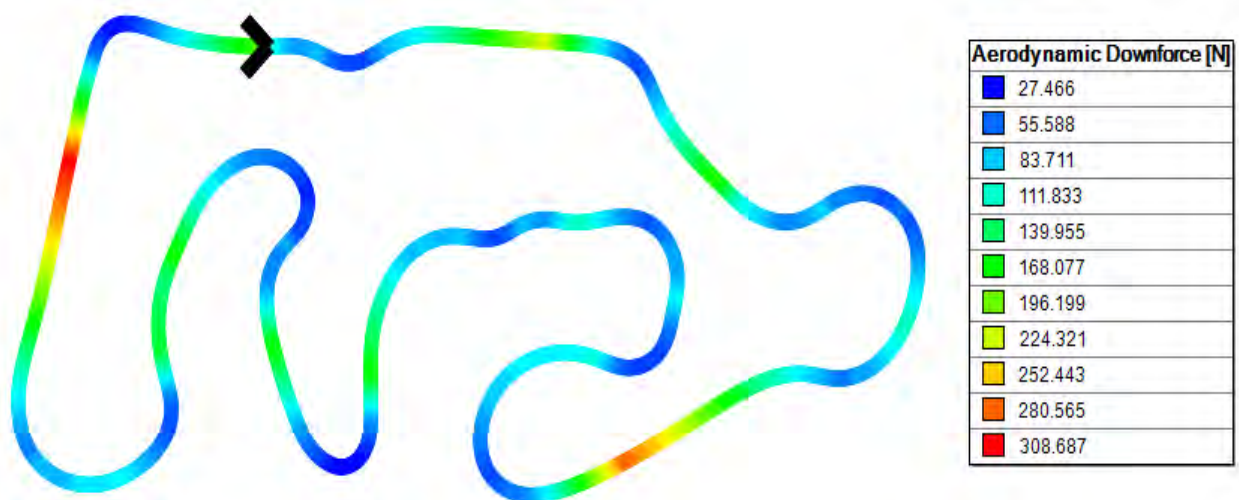

Figure 201: *Generated Downforce of the car with undertray & sidepods along the track*

5.3. Full Aerodynamic Package

The final model to be tested and analyzed is the car with a full aerodynamic package mounted on it. The addition of the front and rear wing resulted in a total vehicle mass of 338kg, while again the vehicle type is situated as FSAE and the driven type is selected 2WD. The aerodynamics data that are inserted are according to the CFD results that were calculated earlier. The frontal area is significantly increased at 1.019m^2 while the lift coefficient of 1.898 is inserted again with a positive sign.

Figure 202: *General & Aero Data used for the model with a full aerodynamic package*

The simulation of the car with a full aerodynamic package at the endurance track of FS Germany 2016 resulted in a total lap-time of **46.67sec** which is 1.2sec quicker than the previous model. The figure below shows the different values of speed that the car is fluctuated at along the whole track. With blue color are represented the values of speed that are beneath 57km/h and are mainly shown at the corners of the track. The average speed of the vehicle along the corners is about 46km/h which is significantly higher than in the previous models and this is due to the extra downforce that is acting on the tires. The red color on the other hand shows values of speed over 75km/h which are shown at the straights of the track, where the car reaches also its final speed of 112km/h.
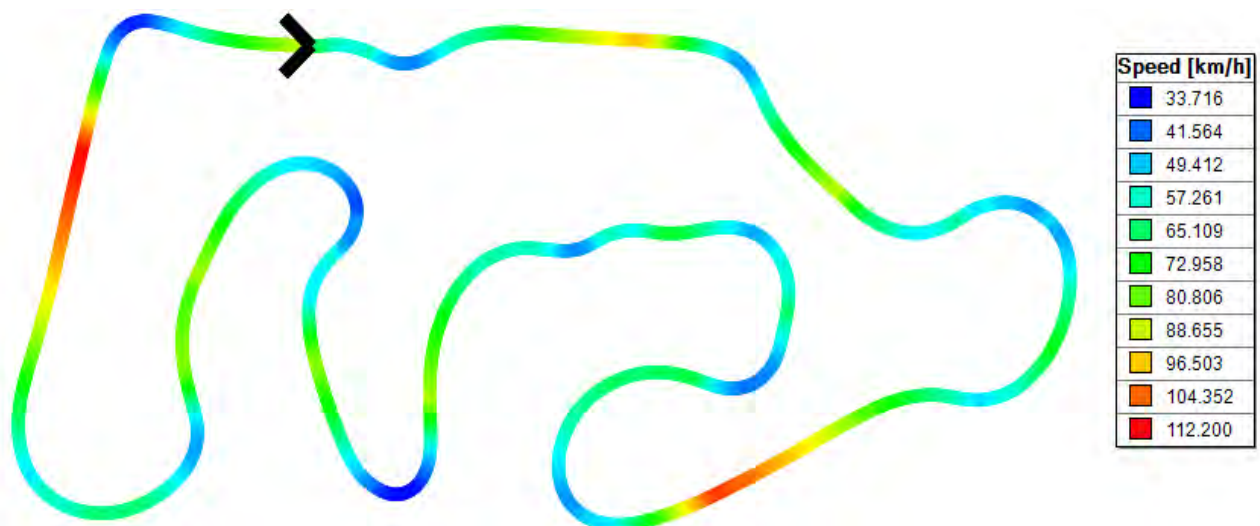

Figure 203: *Speed of the car with a full aerodynamic package along the track*

Finally, the figure below shows the amount of downforce that the car produces as its passes from different parts of the track. The blue color is used for values of downforce that are lower than 400N and is found mainly on the corners of the track where the car moves with its average speed of 46km/h. The red color represents downforce values that are higher than 600N and are shown on the straight lines of the track where the car reaches speeds over 80km/h. It is interesting how this model can produce the same amount of downforce (*100N*) at its lower speed of 30km/h, with the previous model on its average speed of 43km/h, while the maximum amount of downforce at 112km/h is three times higher (*1,128N*) than it was on the model with the undertray. So, it can be clear how the downforce can significantly affect the performance of the car and improve its efficiency.
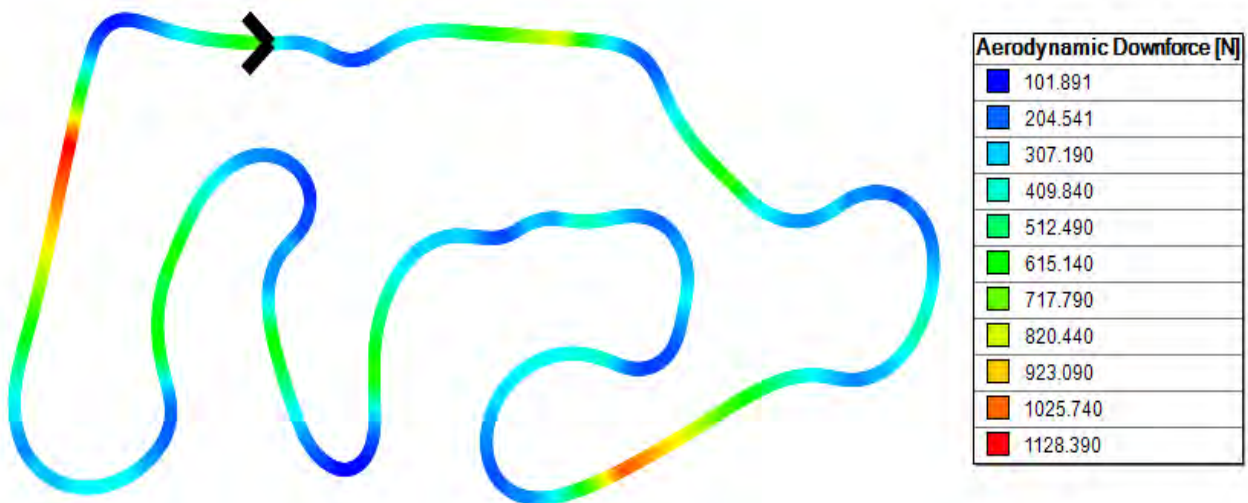

Aerodynamic Downforce [N]	
■	101.891
■	204.541
■	307.190
■	409.840
■	512.490
■	615.140
■	717.790
■	820.440
■	923.090
■	1025.740
■	1128.390

Figure 204: *Generated Downforce of the car with a full aerodynamic package along the track*

5.4. Track Results Comparison

At this section are presented numerous graphs and charts for different characteristics of the models on the track, like the generated downforce and drag, the corner speed and engine throttle and power versus a variety of other factors. These charts can help the user to make better conclusions in detail for the efficiency of each model and compare the advantages of each case. Furthermore, some graphs are used in order to compare the CFD results that were calculated for each model with the real-time track data. Every model is represented with a different color in all charts. The purple color is used for the car with a full aerodynamic package, the orange color is used for the model with the undertray and sidepods, while the blue color represents the car without any aerodynamic devices as it is shown on the figure below.

| Selected Results	
——	[46.67] Thireus 2016 (1), FSAE Endurance Germany 2010
——	[47.84] Thireus 2016 (1), FSAE Endurance Germany 2010
——	[48.50] Thireus 2016 (1), FSAE Endurance Germany 2010

Figure 205: *Colors used to represent each model on the next charts*

The first graph highlights the variance of the generated amount of downforce with speeds between 30 - 115km/h. This chart can confirm the accuracy of the CFD results, as according to the graph it can be seen that the variance line of each model follows the same tendency as it was predicted with the CFD calculations. In more detail the values of downforce of all the models at each speed along the track are really close to the calculated values of the CFD simulations, at 60km/h the model without devices generates a downforce at about -35N (*CFD prediction: -38N*), the undertray model generates about 100N (*CFD prediction: 108N*), while the full aero model generates 350N (*CFD prediction: 342N*). Furthermore, at the final speed of 100km/h the model without devices generates a downforce of -98N (*CFD prediction: -101N*), the undertray model generates about 226N (*CFD prediction: 220N*), while the full aero model generates 847N (*CFD prediction: 852N*).
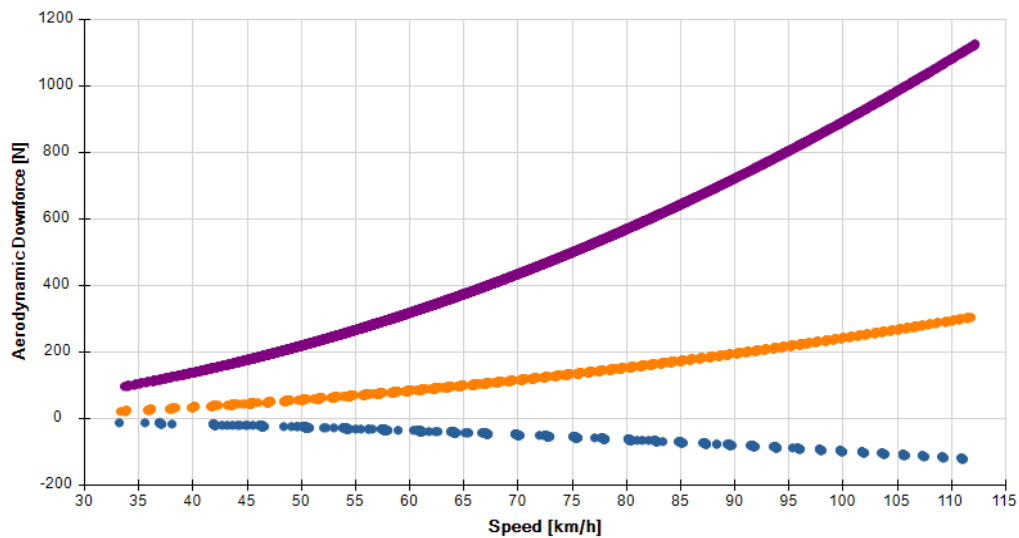
Figure 206: *Downforce generated at each case for speeds between 30 - 115km/h*

The same figure can be seen for the drag, where the tendency is similar to the CFD predictions. In detail, at 60km/h the model without devices generates a drag force at about 51N (*CFD prediction: 58N*), the undertray model generates about 78N (*CFD prediction: 81N*), while the full aero model generates 350N (*CFD prediction: 342N*). Furthermore, at the final speed of 100km/h the model without devices generates a downforce of -98N (*CFD prediction: -101N*), the undertray model generates about 226N (*CFD prediction: 220N*), while the full aero model generates 146N (*CFD prediction: 148N*).
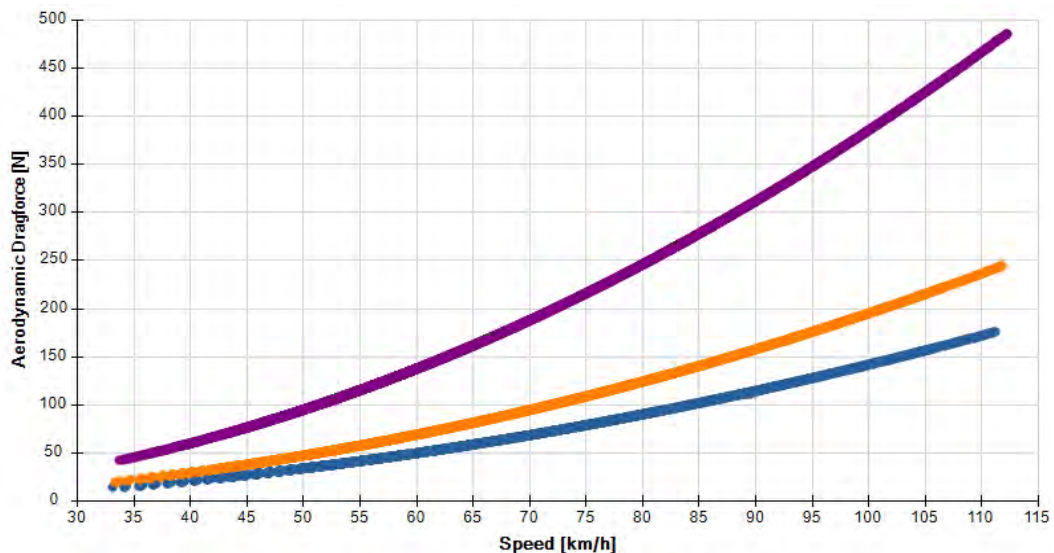
Figure 207: *Drag generated at each case for speeds between 30 - 115km/h*

The next graph, highlights data about the aerodynamic downforce of each model, as the car passes from different radius corners and straights along the track. It is clear again how the car with a full aerodynamic package generates the highest amount of downforce during the corners while on the straight line (*0m Radius*) it a reaches an amount of downforce about three times higher than the model with the undertray. For corners with radius between 200 - 1500m this difference in downforce is still the same and is the reason why the car with a full aerodynamic package reaches higher speeds while cornering.
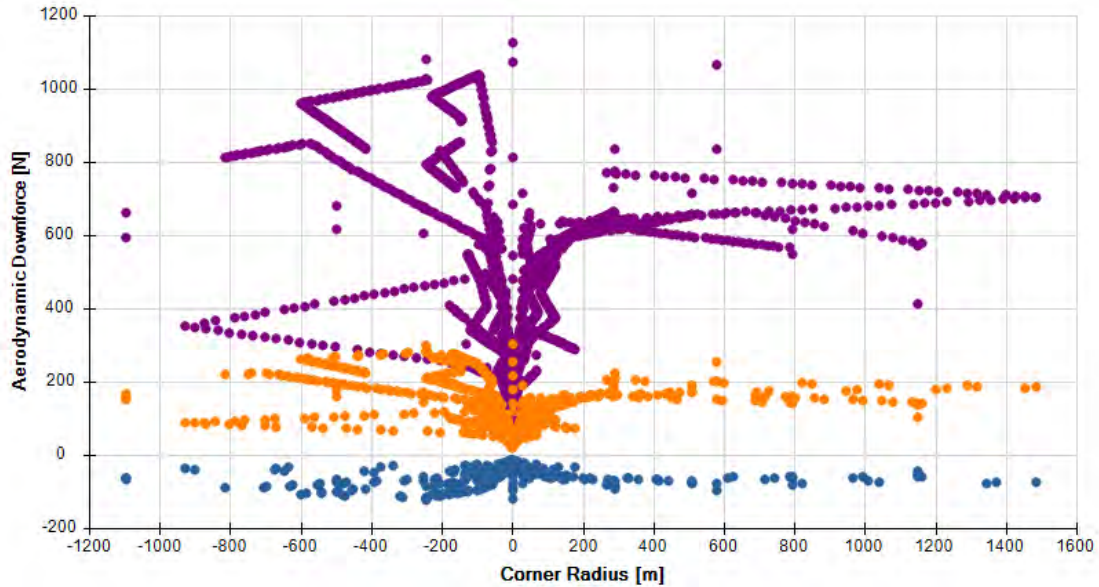

Figure 208: *Downforce generated at different corner radius for each case*

The graph below has again data about the generated downforce of each model, but at this case it shows values of downforce along the whole distance of the track. At this diagram, the differences between the amount of downforce at each case can be seen in more detail, as it is clear that at each part of the track either on straights or corners the car with a full aerodynamic package generates significantly higher amounts of downforce. It also interesting how more rapidly increases the downforce of the full aero model as the car exits the corners, comparing to the other two cases.
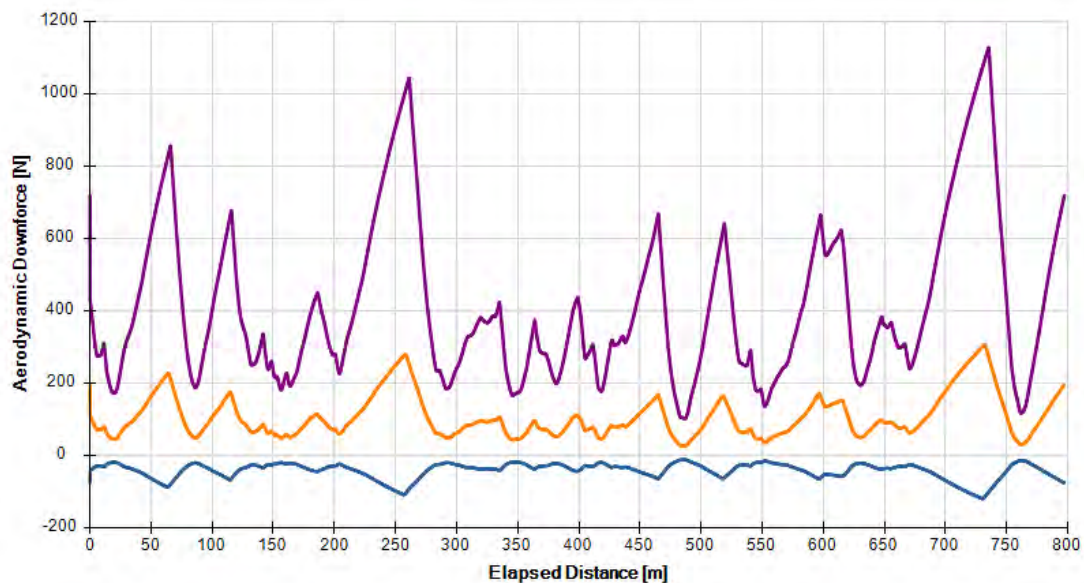

Figure 209: *Downforce generated at different parts of the track for each case*

130

On the two charts below, it is shown the impact of the higher amount of downforce in the performance of the vehicle and the engine too. The first graph show the variation of the vehicle speed with the corner radius for each model. This figure confirms that the extra generated amount of downforce at the full aero model car really increase the performance of the tires, which results in an increase of the cornering speed. As it shown below for corners with radius between 200 - 1500m the full aero model reaches speeds that are about 3-5km/h higher than in the other models and which is the main reason why this model has the fastest lap time, as the whole track is mainly consisted of corners.
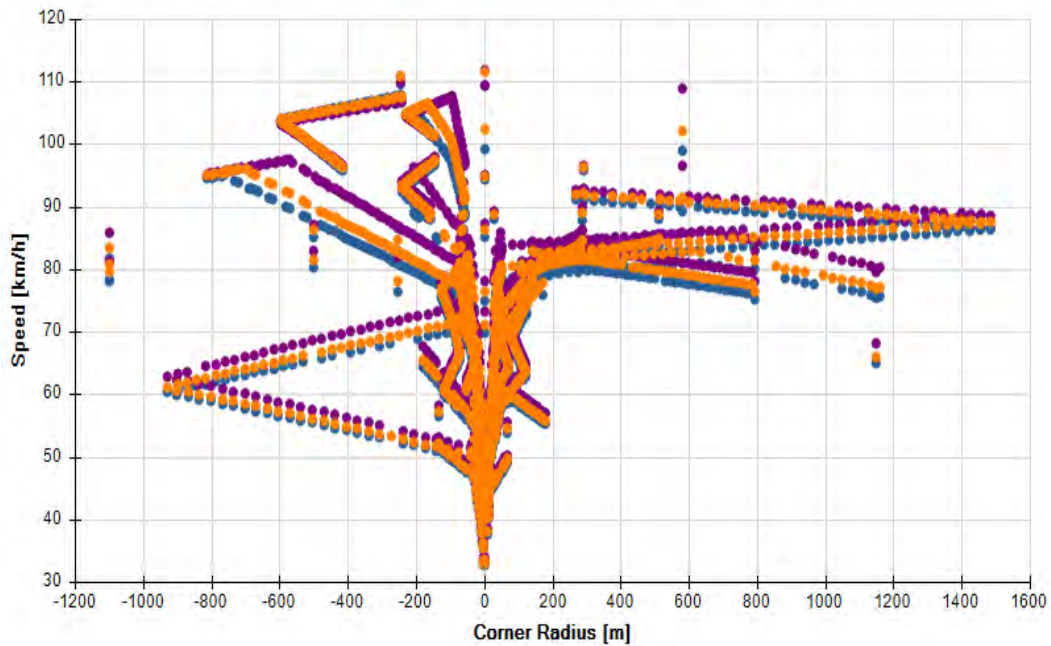
Figure 210: *Vehicle speed at different corner radius for each case*

Finally, the last graph below highlights data about the percent of the engine throttle along the different radius corners. It can be seen that again the model with a full aerodynamic package requires the least percent of throttle during corners, in comparison to the other two case were the equivalent percent is about 8-10% higher. This difference in throttle is due to the fact that in the case of the full aero model, the increased downforce improves significantly the performance of the tires, thus with less throttle the car can keep its cornering speed at higher levels.
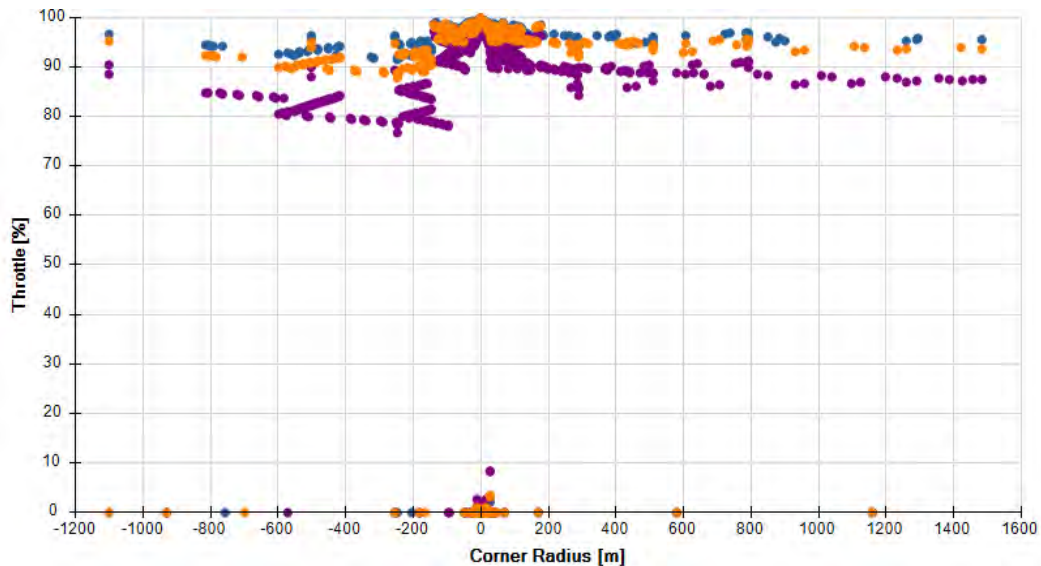
Figure 211: *Percent of Engine Throttle at different corner radius for each case*

131

6. BIBLIOGRAPHY

1. Ansys I. *"ANSYS Fluent User's Guide 16.2"*, 2015.

2. Borello G., Ferro S., Limone S., Ferro G., Bergamini P., and Quagliotti F.B. *"The Role of the Moving Ground for Automotive Wind Tunnel Testing on Race Cars"*, 1999.

3. Cooper K. R**.**, Syms, J., and Sovran, G. *"Selecting Automotive Diffusers to Maximize Underbody Downforce"*, SAE World Congress, Detroit, Michigan, 2000.

4. De Silva, C.M., Nor Azmi, M., Christie, T., Abou-saba, E., Ooi, A., *"Computational flow modeling of formula-SAE sidepods for optimum radiator heat management"*, 2011.

5. Dimitriou, I., and Garry, K. P. *"Use of Narrow Belt for Moving Ground Simulation and its Effects on the Aerodynamic Forces Generated on a Formula 1 Car"*. SAE Motorsports Engineering Conference and Exhibition, Indianapolis, 2002.

6. Doddegowda, P., Bychkovsky, A., George, A. *"Use of computational fluid dynamics for the design of formula SAE race car aerodynamics"*. SAE Technical Paper, 2006.

7. George, A. R. *"Aerodynamic Effects of Shape, Camber, Pitch and Ground Proximity on Idealized Ground-Vehicle Bodies"*, 1981.

8. Gibson M. M. and Launder B. E. *"Ground Effects on Pressure Fluctuations in the Atmospheric Boundary Layer"*, J. Fluid Mech.*,* 1978.

9. Huminic, A., Chiru, A., *"On CFD investigations of vehicle aerodynamics with rotating wheels simulation"*, SAE Technical Paper, 2006.

10. I. Oxyzoglou, I. Nerantzis, *"Weight Optimization of a F1 Composite Front Wing"*, 7th International Conference of BETA CAE Systems S.A., 2017

11. Jenson K. *"Aerodynamic Undertray Design for Formula SAE"*. Oregon State University, 2010.

12. Joseph Katz. "*Race Car Aerodynamics Designing for Speed*". Inc, Bentrey Publishers. 1995.

13. Katz J. *"New Directions in Race Car Aerodynamics",* MA: Bentley Publishers, 2006.

14. Katz, J. *"High Lift Wing Design for Race-Car Applications"*, Aerotech '95, Los Angles, California, 1995.

15. Milliken,W., F., Milliken, D., L. *"Race Car Vehicle Dynamics"*, Inc., Society of Automotive Engineers*,* 1995.

16. McBeath S., Sparkford, Yeovil, Somerset. *"Competition Car Aerodynamics",* UK: Haynes Publishing*,* 2006.

17. SAE International, *"2016 Formula SAE Rules"*, 2016.

18. Shih T. H., Liou W., WShabbir A., Yang Z. and Zhu J. *"A New Eddy Viscosity Model for High Reynolds Number Turbulent Flows Model Development and Validation"*, Computers Fluids*,* 1995.

19. Stollery J. L., and Burns W. K. *"Forces on Bodies in the Presence of the Ground",* The City University, London.

20. Wordley S. and Saunders J. *"Aerodynamics for Formula SAE: Initial design and performance prediction*", SAE International*,* 2005.

21. Wordley S. and Saunders J. *"Aerodynamics for Formula SAE: A Numerical, Wind Tunnel and On-Track Study",* SAE International, 2005.

22. *W. Seibert*, *"Some Remarks and Techniques for handling Autom. Ext. Aerodynamic Set-up and Simulation"*.

23. *W. Seibert, "CFD in Aerodynamic Design Process of Road and Race Cars"*, European Automotive Congress, Slovakia, 2001.

SOFTWARE USED

QUOTE

«If you can keep your head when your boss is wrong
and blaming it on you.
If you can trust your CFD predictions when everyone doubt you,
but make allowance for their ignorance too.
If you can wait for residuals to fall and not be tired of waiting
or when experimentalists lie about you, don't deal in lies,
or on getting good predictions don't give way to pride
and yet your pressure contours don't look too good, nor appear too pretty.
If you can do a transient calculation and not let it be your master.
If you can plan the next project and not make dates your aim.
If you can meet with Convergence and Divergence and treat these two imposters
just the same.
If you can bear to hear the truth you've spoken twisted by non-specialists to
make a trap for fools
or watch a geometry and meshing session you gave your life to …crash, broken,
and stop and build it up again with the next Release.
If you can make a billion cell automotive simulation,
and risk it all on a 1000 core parallel run.
And on crashing start again at the beginning,
and never breathe a word about the cost.
If you can force your heart and nerve to understand CFD jargon,
and comprehend when there is nothing in you,
except the will which says "what does it mean?".
If neither SST, K-omega nor Direct Navier-Stokes can hurt you.
If you can fill all your CPU's
with 100 Gigabyte's worth of simulations to run.
You must be using a suite of CFD software and everything that's in it,
and what is more… you are a CFD Engineer my son!»

Then just iterate, iterate, iterate, make one change at a time, study
your results carefully and remember, when it comes to Aerodynamics,
common sense doesn't work…